Cell-Matrix Interactions: Collagen-GAG Scaffold Fabrication, Characterization, and Measurement of Cell Migratory and Contractile Behavior via Confocal Microscopy

by

Brendan A. Harley

S.M., Mechanical Engineering
Massachusetts Institute of Technology, 2002

S.B., Engineering Sciences
Harvard College, 2000

Submitted to the Department of Mechanical Engineering in Partial Fulfillment of the Requirements for the Degree of

Doctor of Science in Mechanical Engineering

at the

Massachusetts Institute of Technology

June 2006

Signature of Author .....
Department of Mechanical Engineering
May 12, 2006

Certified by .....
Lorna J. Gibson
Matoula S. Salapatas Professor of Materials Science and Engineering
Thesis Supervisor

Accepted by .....
Lallit Anand
Chairman, Department Committee on Graduate Students
Department of Mechanical Engineering

Dedicated to:

My family, friends, colleagues, and all those who have taught, inspired, and shared the experience with me along the way.

Cell-Matrix Interactions: Collagen-GAG Scaffold Fabrication, Characterization, and Measurement of Cell Migratory and Contractile Behavior via Confocal Microscopy

by

Brendan A. Harley

Submitted to the Department of Mechanical Engineering
On May 12, 2006 in Partial Fulfillment of the
Requirements for the Degree of Doctor of Science in
Mechanical Engineering

Abstract

Three-dimensional, collagen scaffolds are an analog of the extracellular matrix and are used for many tissue engineering applications. While material and microstructural properties significantly affect overall scaffold bioactivity, the specific influence of construct mechanical properties, composition, and pore microstructure is unknown. In this thesis, experimental and theoretical approaches are employed to systematically examine the independent effect of extracellular features on cell behavior within a series of standardized, well-characterized, collagen-glycosaminoglycan (CG) scaffolds, providing valuable information for designing biomaterials with improved physiological relevance. This thesis also aims to provide experimental and theoretical approaches appropriate for characterizing and describing a wide range of porous biomaterials and for quantifying the effect of extracellular cues on cell behavior within these biomaterials.

CG scaffolds are fabricated via freeze drying. Novel thermal processing conditions were developed to produce two homologous series of uniform, mechanically isotropic CG scaffolds, one with varying pore size and constant stiffness and the other with constant pore size and varying stiffness. The thermal processing conditions and the resultant scaffold microstructure have been modeled using an isothermal coarsening heat transfer model within a conductive mold with interface resistance, allowing fabrication of future scaffolds with engineered microstructures. The mechanical properties, specific surface area, and permeability of the scaffolds have been experimentally measured and theoretically described using a cellular solids framework appropriate for modeling many porous biomaterials. This thesis research has produced a standardized series of CG scaffolds appropriate for quantitative *in vitro* cell behavior assays. An experimental methodology for measuring cell-generated contractile forces and cell motility is described and implemented; the independent effect of scaffold pore size and stiffness on the magnitude and kinetics of cell motility within the scaffolds was determined via confocal microscopy. Slight changes in the extracellular environment appreciably influence cell behavior. Significant effects of cell density, cell type, scaffold microstructure, and scaffold stiffness were observed: cell migration speed increased with decreasing pore size or increasing cell density and increased asymptotically with scaffold stiffness. An improved measurement of the contraction force generated by single dermal fibroblasts (F_c = 26 ± 13 nN) within the CG scaffold has also been made.

Thesis Supervisor: Lorna J. Gibson
Title: Matoula S. Salapatas Professor of Materials Science and Engineering

Acknowledgements

At the conclusion of this thesis it is important to acknowledge that there have been many people along the way who have enriched and made this work possible. I have enjoyed and truly relished my time at MIT and this has been in no small part due to all those who I have shared the experience with. The nature of my research and thesis has been highly collaborative so there are a multitude of people, facilities, and resources that have made significant contributions.

I first wish to express my deepest gratitude to Prof. Lorna Gibson, who has served as my advisor, doctoral thesis committee chair, and mentor. She gave me the resources and freedom to explore this research topic and guided the development of my experimental, theoretical, and analytical skills. Her experience, insight, and guidance were critical components of my development as an engineer and academic and I truly appreciate the commitment she made to my intellectual and academic maturation.

I would also like to thank Prof. Ioannis Yannas who served as the advisor of my master's thesis and then served as a second advisor and as an active member of my doctoral thesis committee. He constantly reminded me of the importance of understanding the clinical applications of my research and has been one of my most trusted resources throughout my graduate experience.

I am also grateful to Prof. Paul Matsudaira and Prof. Peter So, who served as members of my thesis committee. Although I've only managed to absorb a fraction of their knowledge of biology and imaging, I appreciate their insight and the resources they made available to me throughout this project. I have also been extremely lucky to have the presence of Dr. Myron Spector as a third advisor throughout my time at MIT; his advice and expertise contributed significantly to the development of my experimental and analytical skills. Additionally, I would like to thank Prof. Merton Flemings and Prof. Chris Schuh for their assistance in creating the thermal models to describe CG scaffold fabrication (Chapter 3); what started as a small class project blossomed into a significant technical portion of this thesis with their assistance and encouragement.

A number of collaborators contributed significantly to the technical content of this thesis. I would like to thank Prof. Fergal O'Brien (Royal College of Surgeons in Ireland, Ireland) for his assistance with the initial fabrication, microstructural characterization, and experimental measurements of the specific surface area and permeability of the CG scaffolds (Chapters 2 and 4); Dr. Andrew Lynn (University of Cambridge, UK) for originating and spearheading the mineralized CG scaffold project (Appendix B); and Prof. Alessandro Sannino (University of Lecce, Italy) for helping to develop the spinning protocol to fabricate tubular CG scaffolds (Appendix A). All three have been, are, and will be friends, colleagues and trusted resources. I truly look forward to all we can cook up together over a generation of research and collaboration.

I owe special thanks to Hyung-Do Kim and Dr. Muhammad Zaman for their assistance with all things biological (and moving!) in this thesis (Chapter 6); their help in designing the fluorescent staining protocols, running the confocal microscope, and performing the three-dimensional image processing made the 3D cell tracking experiments possible. I would also like to acknowledge Prof. Krystyn Van Vliet, Kristin Myers, Alan Schwartzman, Prof. Simona Socrate, and the NanoMechanical Technology Laboratory for the facilities and assistance that aided in the mechanical characterization of the CG scaffolds (Chapter 5). Their work, eagerness to help, and friendship have been invaluable and have played a significant role in both this thesis and my academic experience.

I would also like to thank the members of the Fiber and Polymers Lab, Cellular Solids Lab, and the Socrate Lab at MIT as well as the V.A. Tissue Engineering Lab. Particularly, Debbie, Scott, Ramille, Abel, Eric, Karolina, Ricardo, Zach, Asha, Anastassia, Casey, Mark, Toby, Matt, Janet, Juwell, and Yihvan for their friendly conversations, technical assistance, and invaluable support throughout my six years at MIT.

The DuPont-MIT Alliance, the National Institutes of Health (Grant No. DE-13053), the Cambridge-MIT Institute, and the MIT-Whitaker Health Science Fund Fellowship provided financial support for this research.

As much as I have enjoyed my time in lab, I am truly fortunate to have received so much support from my family. I want to thank my parents, Karen and Brendan, for playing an active role in my education, for providing the opportunity to continue my education to this point, and for assisting me along the way: from help learning my multiplication tables in the third grade to help proofreading my doctoral thesis. I also want to thank my brothers Peter and Colin for the hours of Lego fun and other adventures we had together as we grew up. It would have been impossible to reach this point without their help and support.

Most of all, I want to thank my wife, Kathryn Clancy, for being my partner, counselor, and cheerleader. It is so easy to bury your head in work and not notice or appreciate the humanity and world around you. This is my third dissertation we have been through together and I truly notice and appreciate all that she has done over the years to help me become the academic and human I am proud to be. Not only have you read virtually everything – including this tome – I have written and acted as my most trusted resource, confidant, and sounding board for things academic and not, you have also lead by example as a gifted academic, union organizer, campaigner for social justice, and partner. Thank you for your support, kindness, friendship and, most of all, for helping me realize that work was not nearly the most important facet of my life.

Table of Contents

List of Figures

List of Tables

List of Equations

$$E_{scaffold} = E_s \cdot \left(\frac{\rho^*}{\rho_s}\right)^2$$

Equation 5.12. $E_{hole} = 0.2 \cdot E_{scaffold}$ 191

$$V_{scaffold} = x$$

$$V_{hole} = 1 - x$$

Equation 5.13. $$E^*_{compression} = \frac{E_1 \cdot E_2}{E_1 \cdot V_2 + E_2 \cdot V_1} = \frac{E_1 \cdot E_2}{E_1 \cdot \frac{3.2 \cdot b \cdot l}{3.4 \cdot b \cdot l} + E_2 \cdot \frac{0.2 \cdot b \cdot l}{3.4 \cdot b \cdot l}}$$ 195

Equation 5.14. $E^*_{compression} = 208Pa = E_2$ 195

$$E^*_{tension} = 2000Pa = E_1 \cdot V_1 + E_2 \cdot V_2$$

Equation 5.15. $$E^*_{tension} = E_1 \cdot \frac{0.2 \cdot b \cdot l}{3.4 \cdot b \cdot l} + 208 \cdot \frac{3.2 \cdot b \cdot l}{3.4 \cdot b \cdot l}$$ 196

$$\sigma_{cr} = 0.57 \cdot (E_1)^{1/3} \cdot (E_2)^{2/3}$$

$$\sigma_{cr} = 0.57 \cdot (30.7kPa)^{1/3} \cdot (208Pa)^{2/3}$$

Equation 5.16. $\sigma_{cr} = 630Pa$ 197

$$\varepsilon_{cr} = \frac{\sigma_{cr}}{E_1} = \frac{630Pa}{30.7kPa} = 0.02$$

$$\varepsilon_{rr} = \frac{\Delta d}{\cdot d_o} = \frac{d_o - d}{d_o}$$

Equation 6.1. $$\varepsilon_{\theta\theta} = \frac{\pi \cdot d_o - \pi \cdot d}{\pi \cdot d_o} = \frac{d_o - d}{d_o} = \varepsilon_{rr}$$ 213

$$\varepsilon_{zz} = \frac{\Delta t}{t_o} = \frac{t_o - t}{t_o}$$

Equation 6.2. $\varepsilon_{zz} = \varepsilon_{rr} = \frac{d_o - d}{d_o}$ 214

$$\varepsilon_{rr} = \varepsilon_{zz} = \varepsilon_{\theta\theta}$$

Equation 6.3. $e = 1 - (1 - \varepsilon)^3 = \frac{\Delta V}{V} = \frac{3 \cdot (1 - 2 \cdot \nu)}{E} \cdot p$ 214

Equation 6.4. $F = p \cdot l^2 = \frac{E \cdot e}{3 \cdot (1 - 2 \cdot \nu)} \cdot l^2$ 214

Equation 6.5.

$$0 < \varepsilon \le 0.1 : \_F = \frac{0.83 \cdot E^* \cdot e}{3 \cdot (1 - 2 \cdot \nu^*)} \cdot l^2 \quad \text{\_\_\_(6.5a)}$$

$$\varepsilon > 0.1 : \_F = \frac{0.83 \cdot E^* \cdot e_{el}^*}{3 \cdot (1 - 2 \cdot \nu^*)} \cdot l^2 + \frac{0.83 \cdot E_c \cdot (e - e_{el}^*)}{3 \cdot (1 - 2 \cdot \nu_c)} \cdot l^2 \quad \text{\_\_\_(6.5b)}$$

..... 216

Equation 6.6. $F_c = \dfrac{F}{\frac{1}{3} \cdot N}$ 216

Equation 6.7. $F_c = \dfrac{n^2 \cdot \pi^2 \cdot E_s \cdot I}{l^2}$ 219

Equation 6.8.

$$F_c = \frac{n_{hydro}^2 \cdot \pi^2 \cdot E_s \cdot I}{l^2}$$

$$F_c = \frac{0.34 \cdot \pi^3 \cdot E_s \cdot d^4}{64 \cdot l^2}$$

..... 220

Equation 6.9.

$$D_{jxn} = l = \frac{d}{2.785} = \frac{d}{C_1}$$

$$\rho_{jxn} = \frac{6(jxn/UC)}{11.31 \cdot \left(\frac{d}{2.785}\right)^3 (vol/UC)} = \frac{11.459}{d^3} = \frac{C_2}{d^3}$$

..... 251

Equation A.1. $\dfrac{SA}{V} = \dfrac{10.15}{d}\left(\dfrac{\rho^*}{\rho_s}\right)^{1/2}$ 274

Equation C.1. $M_{EDAC} = (\#\,samples) \cdot M_{scaffold} \cdot \left(0.0012 \dfrac{mol_{COOH}}{gm_{collagen}}\right) \cdot \left(\dfrac{5mol_{EDAC}}{1mol_{COOH}}\right) \cdot \left(\dfrac{191.7gm_{EDAC}}{1mol_{EDAC}}\right)$ ... 324

Equation C.2. $M_{NHS} = (\#\,samples) \cdot M_{scaffold} \cdot \left(0.0012 \dfrac{mol_{COOH}}{gm_{collagen}}\right) \cdot \left(\dfrac{2mol_{NHS}}{1mol_{COOH}}\right) \cdot \left(\dfrac{116.0gm_{NHS}}{1mol_{NHS}}\right)$ 324

Equation C.3. $a = \dfrac{1}{\sqrt{C_0 + \sqrt{C_1^2 + C_2^2}}}$ 331

Equation C.4. $b = \sqrt{\dfrac{\sqrt{C_1^2 + C_2^2}}{C_0 \cdot \sqrt{C_1^2 + C_2^2} + C_2^2 - C_1^2}}$ 331

Equation C.5. $AspectRatio = \dfrac{a}{b}$ 331

Equation C.6. $d = 1.5 \cdot 2 \cdot \sqrt{\frac{a^2 + b^2}{2}}$ 331

CHAPTER 1. *Introduction and Background: Measurement of Cell Traction, Contraction, and Motility*

1.1. The extracellular matrix and extracellular matrix analogs

The extracellular matrix (ECM) is a complex organization of structural proteins such as collagen, elastin, adhesive proteins including fibronectin and laminin, proteoglycans (PG), and glycosaminoglycans (GAGs) including chondroitin sulfate (CS), keratin sulfate (KS), dermatin sulfate, and hyaluronic acid (HA) (**Figure 1.1**).

The ECM defines the local environment of cells within tissues and organs, and acts as an insoluble regulator of cell behavior. However, the nature, kinetics, and mechanics of cell-ECM interactions have not been elucidated. Three-dimensional scaffolds are an analog of the extracellular matrix (ECM), acting as a physical support structure and as an insoluble regulator of biological activity that affects cell processes such as motility, applied traction force, cell-mediated contraction, and proliferation. A variety of materials, synthetic and organic, have been used as analogs of the ECM for many TE applications, where the ECM analog compositional,

mechanical, and microstructural properties have been observed to significantly affect overall scaffold bioactivity. Additionally, it has been observed that a single construct variant is not suitable for all applications. What isn't well understood is what is responsible for this phenomena; that is whether construct bioactivity is defined by architecture, stiffness, composition, degradation characteristics, or some combination of these or potentially many other variables.

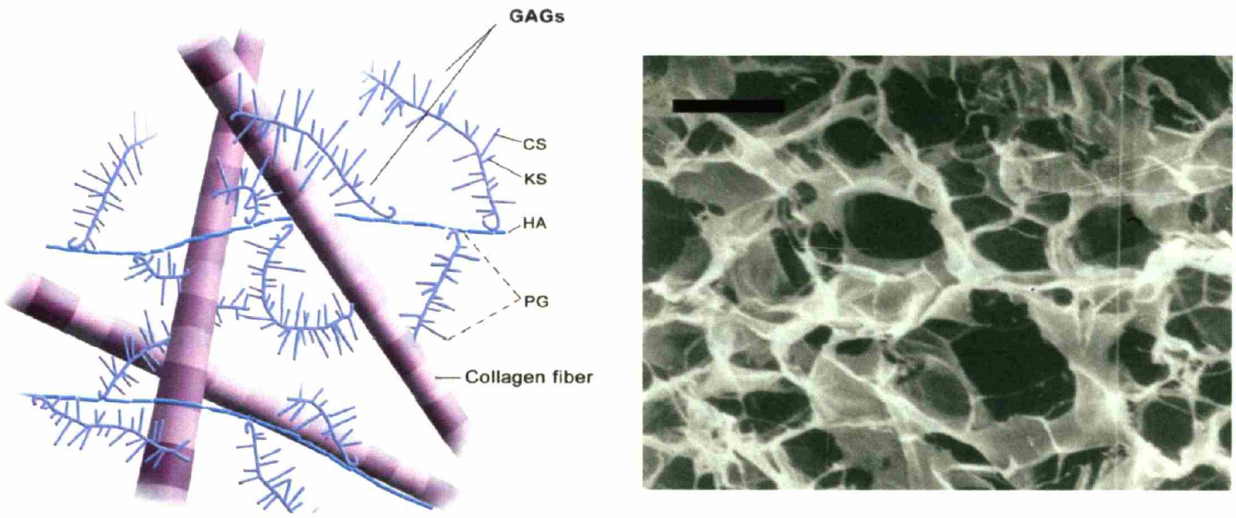

Figure 1.1. Characteristic organization of the extracellular matrix in tissues and organs (left). Collagen-glycosaminoglycan tissue engineering scaffold (ECM analog, right). Scale bar: 100 μm. (Yannas, Lee, et al., 1989; Yannas, 2001).

The question under consideration in this thesis is how do cells detect and respond to their environments and what are the critical cues? While many experiments have begun to probe cell-substrate interactions on two-dimensional surfaces (Pelham and Wang, 1997; Lo, Wang, et al., 2000; Wang, Dembo, et al., 2000; Beningo, Dembo, et al., 2001; Munevar, Wang, et al., 2001; Wang, Dembo, et al., 2001; Wang, Wan, et al., 2001), the critical biochemical and biophysical

parameters that affect cell behavior in three-dimensional constructs such as scaffolds and gels have not been quantitatively investigated.

The objective of this thesis is to use collagen-glycosaminoglycan (CG) scaffolds as an experimental tool to systematically study the effect of the extracellular environment on cell behavior. The approach is threefold: First to develop, characterize, and model new fabrication techniques to produce isotropic, three-dimensional CG scaffolds with a homogeneous pore microstructure. Secondly, to characterize and model the pore microstructure, specific surface area, permeability, and mechanical properties of these scaffold variants, thereby characterizing the local extracellular environment of cells within the scaffold variants. Thirdly, to systematically investigate the independent effect of CG scaffold microstructure and mechanical properties on cellular migratory and contractile behavior.

1.2. Mammalian response to injury

The goal of achieving *in vivo* induced regeneration for a variety of tissue and organs following severe injury remains at the forefront of current tissue engineering investigations and provides the motivation for this thesis. Typically, an analog of the extracellular matrix is utilized as a template that, when properly formulated, induces regeneration of lost or damaged tissue. Currently, successful regeneration has been induced in the skin and peripheral nerves (Yannas, 2001), while progress has been made in developing appropriate extracellular matrix analogs to alter the typical organismic response to injury in a variety of tissues, including kidney, cartilage, bone, central nervous system, and brain dura. These investigations, active for the previous three decades, have primarily focused on identifying the optimal extracellular matrix analog

components to block organized wound contraction and scar tissue formation while inducing regeneration of physiological tissue (Yannas, 2001). The rationality and historical background of developing bioactive scaffolds for tissue engineering applications, which served as the motivation for identifying critical extracellular parameters within the scaffold which influence cell behavior and construct bioactivity, will now be introduced.

1.2.1. Defect Scale

Treatment options for organ injury depend significantly on the scale of the defect. Microscopic defects can be treated using a wide variety of soluble factors (*i.e.*, herbs, potions, pharmaceuticals, vitamins, hormones, and antibiotics). However, organ-scale defects present a significantly larger wound site, require considerably different treatment practices, and constitute the focus of this article. These defects, primarily created by disease or by an acute or chronic insult that result in millimeter or centimeter scale wounds, cannot be treated with drugs because the problem is the failure of a mass of tissue including cells, soluble proteins and cytokines, and insoluble extracellular matrix (ECM). Significant loss of function in the affected tissue or organ, termed the "missing organ," leads to consequences such as lack of social acceptance in cases of severe burns and facial scars, loss of mobility and sensory function in the case of neuroma, and life-threatening symptoms in cases such as cirrhotic liver, large-scale severe burns, and ischemic heart muscle.

1.2.2. Regeneration versus Repair

Certain organisms have the ability to regenerate significant portions of damaged tissue. An example is the amphibian newt that regenerates functional limbs following amputation. The

mammalian fetus has displayed the ability to regenerate damaged organs and tissue spontaneously up to the third trimester of gestation; however, adult mammals do not typically exhibit spontaneous regeneration following severe organ injuries (Mast, Nelson, et al., 1992; Yannas, 2001). Instead, the adult mammal response to severe injury is closure of the wound by contraction and scar tissue formation, a process termed repair. Cell-mediated contraction of the wound site is observed in many different species to varying degrees at many organ sites (Yannas, 2001). Compared to the tissue which it replaces, scar tissue is mechanically weaker (Levenson, Geever, et al., 1965), physically disfiguring, and can lead to the restricted motion of joints. Regeneration is characterized by synthesis of a physiological (normal, functional) replacement tissue in the wound site that is structurally and functionally similar to the original tissue.

The contractile fibroblast phenotype, termed the myofibroblast, plays a critical role in determining the nature (repair or regeneration) of mammalian wound healing; the ubiquity of fibroblast activity during wound healing and the use of scaffolds to modify their behavior *in vivo* prompted their study in this investigation. During adult repair, myofibroblast-mediated organized wound contraction and scar tissue synthesis is observed (Yannas, 2001). During early fetal healing characterized by regeneration, differentiation of myofibroblasts has not yet occurred and regeneration occurs in the absence of contraction. The data suggest that induced organ regeneration in the adult may be encouraged by developing techniques to stimulate partial reversion to early fetal healing. Additionally, the transforming growth factor-β (TGF-β) family of molecules has been implicated in this ontogenetic transition between fetal regeneration and adult repair response to injury. TGF-βs are multifunctional cytokines with widespread effects on cell growth and differentiation, embryogenesis, immune regulation, inflammation, and wound

healing (Border, Noble, et al., 1995). In terms of their relationship with repair processes, TGF-β1 and TGF-β2 are known to promote scar, while TGF-β3 may reduce scar (Lin, Sullivan, et al., 1995; Shah, Foreman, et al., 1995). As such, deficient levels of TGF-β1 and -β2 and increased levels of TGF-β3 are observed in early gestational ("fetal" regenerative healing response) compared to late gestational ("adult" repair healing response) mice. These results implicate increased TGF-β1, -β2, and decreased TGF-β3 expression along with myofibroblast activity in late gestation and post-partum fetal scar formation (Soo, Beanes, et al., 2003). The available evidence suggests future experiments utilizing procedures for control of TGF-β in conjunction with other tissue engineering constructs that modify myofibroblast behavior, such as bioactive scaffolds, to induce regeneration of tissues that are known to be non-regenerative.

1.2.3. Tissue Triad

There are three distinct tissue types, termed the tissue triad, which together define the structure of most organs: the epithelial layer, the basement membrane layer, and the stroma (**Figure 1.2**) (Martinez-Hernandez, 1988; Yannas, 2001).

Developmental and functional similarities between this triad in a variety of tissues and organs such as skin and peripheral nerves have been observed, suggesting that it can be used as an illustrative device to understand injury response in other organs as well (Yannas, 2001). A layer of epithelial cells (the epithelial layer) cover all surfaces, tubes, and cavities of the body; this layer is cell-continuous and avascular; unlike the basement membrane and stroma, the epithelial layer does not comprise a significant amount of extracellular matrix (ECM). The basement membrane is an acellular, avascular, continuous layer of ECM components separating the

epithelial layer and the stroma. The stroma is cellular, contains ECM and connective tissue components, is heavily vascularized, and provides a reservoir for nutrient uptake to and waste removal from the basement membrane and epithelia.

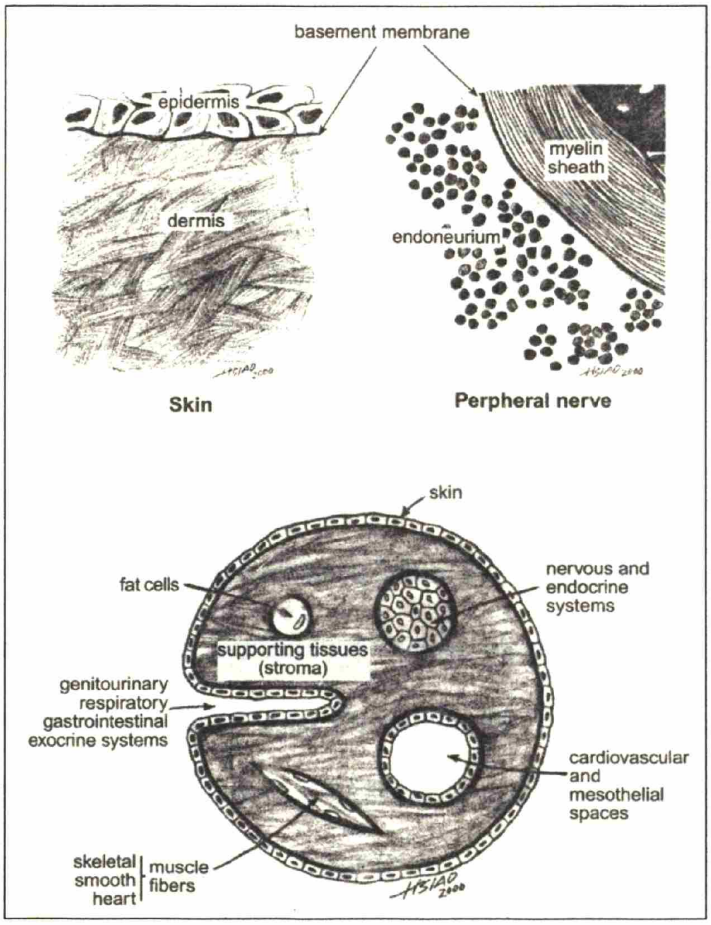

Figure 1.2. Schematic of the tissue triad structure observed in mammalian tissue (Yannas, 2001).

Following injury to a variety of tissues such as the skin, peripheral nerves, blood vessels, lung, kidney, and pancreas, the epithelial and basement membrane layers regenerate spontaneously when the stroma remains intact, while the damaged stoma heals through repair-mediated contraction and scar formation processes (Oliver, 1953; Lehv and Fitzgerald, 1968; Vracko, 1972; Stemerman, Spaet, et al., 1977; Haber, Hanna, et al., 1985; Ikeda, Oda, et al., 1989;

Yannas, Lee, et al., 1989; Stenn and Malhotra, 1992; Ferdman and Yannas, 1993; Uitto, Mauviel, et al., 1996; Fu and Gordon, 1997; Yannas, 2001).

Understanding the injury response of the tissue triad has suggested a paradigm for inducing regeneration in non-regenerative tissues: the repair mechanisms appear to be activated by disruption of the stromal architecture, and proper replacement of the stromal layer is critical for any regeneration to occur. As such, development of materials to replace the lost stromal architecture has been a primary focus of studies of regenerative medicine over the past two decades.

1.2.4. Methods to Treat Loss of Organ Function

Six approaches have been used to restore some level of functionality to a damaged tissue or organ: transplantation, autografting, implantation of a permanent prosthetic device, use of stem cells, *in vitro* synthesis of organs, and induced regeneration. The last three techniques are often collectively referred to as "tissue engineering" (Lanza, Langer, et al., 1997).

1.2.4.1. Transplantation

Transplantation is widely used to replace complex tissues and organs, but is limited by two significant factors. While transplantation of a select few tissues such as the eye and testis occur without rejection, a significant challenge facing transplantation is the immunological barrier between the donor and host. After transplantation, the donor organ is attacked and rejected by the host's immune system. The primary clinical method for preventing such rejection is the use of immunosuppressive drugs for the remainder of the host's life to suppress their immune system.

However, immunosuppression also makes the host vulnerable to infections (Wickelgren, 1996). A second major obstacle is the difficulty in finding immunocompatible donors and the shortness of supply of suitable organs (Lanza, Cooper, et al., 1997).

1.2.4.2. Autografting

With autografting, the donor and the recipient are the same individual; a fraction of the tissue or organ is harvested from an uninjured site and grafted at the nonfunctional site (Medawar, 1944). Autografting removes issues related to immune response, but necessitates the creation of a second wound site (donor site), subjecting the patient to a second severe trauma and additional loss of functionality. Therefore, autografting is utilized only when sufficient autograft tissue is available and when the loss of functionality or morbidity at the primary wound site outweighs that at the harvest site, giving it limited applicability; typical applications of autografting are following severe burns and peripheral nerve injuries in the hand.

1.2.4.3. Permanent Prosthetic Device

Permanent, prosthetic devices are typically fabricated from biologically inert materials such as metals, ceramics, and synthetic polymers that do not provoke the immune response problems inherent to many transplanted tissues. Even though these devices are fabricated from bio-inert materials, interactions between the prosthesis and the surrounding biological environment still lead to a number of unfavorable physical and biological manifestations. Specific examples are the formation of a thick, fibrous scar tissue capsule around the implant (Rudolph, Van de Berg, et al., 1992), stress-shielding of the surrounding tissue (Spector, Heyligers, et al., 1993), platelet aggregation to implanted surfaces (Snyder, Watach, et al., 2002), and accumulation of wear

particles both at the site of implantation and in the lymphatic system (Urban, Jacobs, et al., 2000). The spontaneous remodeling process of the tissues surrounding the implant can also be significantly altered, leading to further tissue degradation (Willert, 1977). These often-serious side effects illustrate the difficulty of replacing bioactive tissues with bio-inert implants fabricated from materials possessing drastically different material and mechanical properties.

1.2.4.4. Stem Cells

The pluripotent nature of stem cells offers a multitude of therapeutic possibilities (Kondo, Wagers, et al., 2003; Lerou and Daley, 2005). Current efforts in stem cell research have focused on understanding stem cell plasticity and ways of controlling stem cell differentiation (Wagers, Christensen, et al., 2002; Wagers and Weissman, 2004). Previously, mesenchymal (Pittenger, Mackay, et al., 1999), epithelial (Slack, 2000), and neural stem cells (Gage, 2000) have been grown *in vitro* and studied. More recently, experimental investigations of stem cells have also focused on utilizing hematopoietic and embryonic stem cells. In particular, techniques to harvest and identify them (Christensen, Wright, et al., 2004; Surdez, Kunz, et al., 2005), expand and differentiate them in culture (Wagers, Christensen, et al., 2002; Sherwood, Christensen, et al., 2004; Daley, 2005; Lengerke and Daley, 2005; Passegue, Wagers, et al., 2005; Udani, Santarelli, et al., 2005; Wang, Yates, et al., 2005), and re-implant them at an injury site (Udani, Santarelli, et al., 2005; Kunisaki, Fuchs, et al., 2006) have been at the forefront of stem cell research

While few significant advances have been made to this point, stem cell technologies present a great deal of promise. However, improved understanding of stem cell behavior and development of stem cell-based technologies also raise a number of important ethical questions (Daley, Sandel,

et al., 2005), consideration of which will play a significant role in the development of stem cell-based tissue engineering solutions.

1.2.4.5. In Vitro Synthesis

In vitro synthesis requires the growth of a functional volume of tissue *in vitro*. *In vitro* synthesis allows for total control over the culture environment such as soluble regulator content (*i.e.*, growth factors, cytokines), insoluble regulator content (*i.e.*, ECM proteins), and a variety of cell culture medium and loading conditions. In order to develop large (critical dimension >1 cm), bioactive scaffolds, it is important to metabolically support the cells within these constructs. There are two mechanisms available for transport of metabolites to and waste products from cells in a scaffold: diffusion, and with *in vivo* applications, transport through capillary networks formed in the scaffold via angiogenesis. While angiogenesis becomes the limiting factor *in vivo*, significant angiogenesis is not observed for the first few days after implantation, and is not present at all *in vitro*. As a result, current tissue engineering constructs are size limited (<1 cm) due to diffusion constraints. Improving metabolite influx is critical for larger, more complex scaffolds. Additionally, the complexity of biological systems, specifically cytokine, growth factor, and inter-cellular signaling needs throughout the volume of developing tissue have to date precluded, with few exceptions such as *in vitro* culture of replacement heart valves (Rabkin-Aikawa, Mayer, et al., 2005) and epithelial sheets for severe burn patients (Woodley, Peterson, et al., 1988), the formation of complex tissues *in vitro*.

1.2.4.6. Induced In Vivo Organ Synthesis (Induced Regeneration)

Induced organ synthesis *in vivo* relies on the processes inherently active in the wound site to regenerate lost or damaged tissue and is the only methodology to date that has modified the adult mammalian wound healing response to induce regeneration. A highly porous analog of the ECM, also termed a scaffold, is utilized to induce regeneration at a wound site where the organism would normally respond via repair processes. Induced organ synthesis was made possible by the development of fabrication techniques to produce ECM analogs with well-defined pore microstructure, specific surface area, chemical composition, and degradation rate (Yannas, Lee, et al., 1989; Yannas, 2001). Its first application was the use of a collagen-glycosaminoglycan (CG) scaffold (termed dermal regeneration template – DRT) that induced skin regeneration following severe injury. The DRT displayed high biological activity when implanted into a full-thickness skin wound and was capable of inducing regeneration of the underlying dermal layer of skin as well as the epidermal and basement membrane layers (Burke, Yannas, et al., 1981; Yannas, Lee, et al., 1989).

1.3. Biological length scales

When studying cell-biomaterial interactions, it is important to consider a wide range of length scales and understand the relative contributions of each length scale. This is especially important when designing and fabricating a standardized series of three-dimensional platforms for tissue engineering applications. Like many biological entities, this range of prominent length scales for biomaterials covers 10 orders of magnitude ($1 - 10^{-10}$ m), where different structural features influence distinct functional characteristics.

At the angstrom and nanometer scale, the primary chemical structure and higher order organization such as protein or crystal structure of the ECM or biomaterial influences protein adsorption and cell attachment via integrin–ligand interactions and complexes. At the micron scale, the local microstructural and mechanical environment surrounding individual cells provides critical cues affecting individual cell behavior and construct bioactivity. At the millimeter scale, interactions between the biomaterial and populations of cells as well as with the entire tissue or organ influence construct bioactivity and cell behavior.

1.4. Studies of cell motility, traction forces, and contraction

Developing and utilizing appropriate constructs to measure cell motility and contraction is the focus of this thesis. Cell contraction plays a critical role in organized wound contraction and scar synthesis following injury while cell migration plays a critical role in many physiological systems. Notably, migration of fibroblasts and vascular endothelial cells during wound healing, metastatic tumor cells migration from the tumor mass to the circulatory system, and active cell motility as a crucial component of embryonic development.

Cell motility into and within 3D tissue engineering constructs is a useful model system for studying cell migration relevant to both physiological and pathological conditions. However, such studies are also especially important to aid the design of future bioactive constructs because the initially acellular scaffold must be rapidly cellularized either *in vitro* or *in vivo*; understanding and controlling this process is a critical feature for the development of the next generation of tissue engineering scaffolds.

1.4.1. Cell motility and traction forces on 2D substrates

On two-dimensional substrates, migration speed and traction forces of individual cells have been measured using a variety of experimental arrangements. Two-dimensional substrates allow easy optical interrogation of cell behavior using light and fluorescent microscopy techniques to track cell movement and measure the traction forces exerted on the underlying substrate. The nature and strength of cell traction forces, for example are typically calculated from the observed local deformation of the underlying substrate (**Figure 1.3**) while cell motility is assayed using time-lapse imagine techniques that calculate the temporal movement of individual cells (Beningo and Wang, 2002; Tan, Tien, et al., 2003).

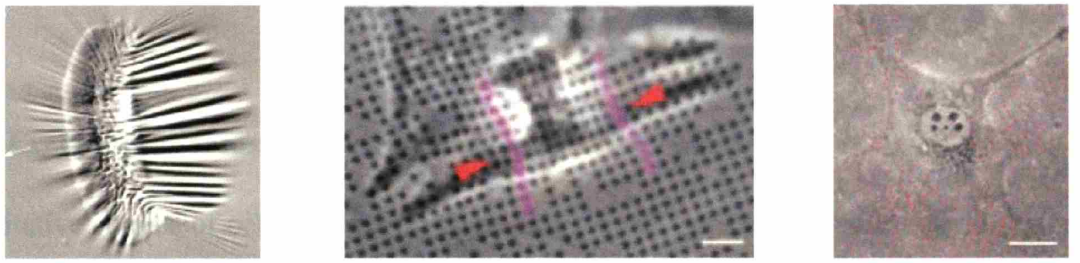

Silicone membrane | Silicone membrane with a regular dot pattern | Polyacrylamide membrane with fluorescent microspheres

Fig. 1.3a

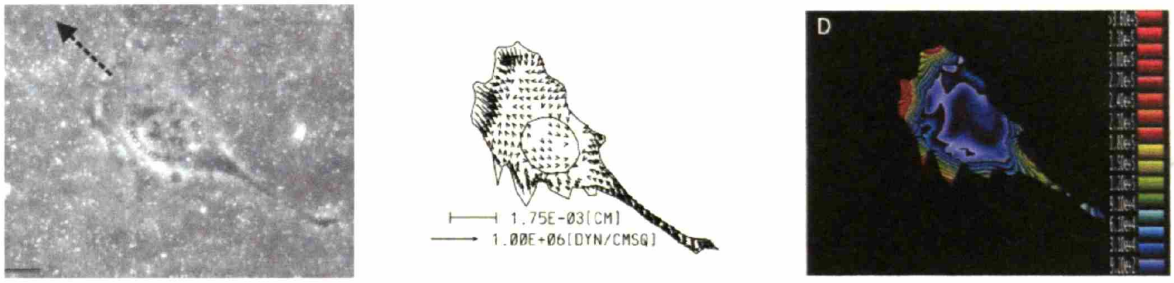

Cell on membrane | Deformation vectors | Field of traction stresses

Fig. 1.3b

Figure 1.3. Experimental measurement of cell traction forces on flexible substrates from local substrate deformation (Beningo and Wang, 2002).

Substrate stiffness has been observed to significantly affect many cellular processes on two-dimensional surfaces; in particular, migration speed, directional persistence, generated traction force, DNA synthesis, and apoptosis have all been observed to be modified by substrate stiffness and morphology (Pelham and Wang, 1997; Dembo and Wang, 1999; Pelham and Wang, 1999; Lo, Wang, et al., 2000; Wang, Dembo, et al., 2000; Beningo, Dembo, et al., 2001; Munevar, Wang, et al., 2001; Wang, Dembo, et al., 2001; Beningo and Wang, 2002; Tan, Tien, et al., 2003). Such experiments measuring cell behavior and processes on two-dimensional substrates have provided valuable information concerning cell-ECM interactions; however, in order to quantitatively interrogate the biochemical and biophysical parameters that affect cell behavior in 3D, a new generation of three-dimensional constructs needs to be developed.

1.4.2. Experimental measurement of cell behavior in 3D constructs

Quantitative studies of cell behavior in three-dimensional constructs require careful control over substrate characteristics and the cell behavior assays. Cell mediated contraction experiments using three-dimensional constructs (*i.e.*, scaffolds, gels) have predominantly been made by calculating an average cell-mediated contractile force from the gross deformation of a larger construct due to a large cell population (Delvoye, Wiliquet, et al., 1991; Kolodney and Wysolmerski, 1992; Eastwood, McGrouther, et al., 1994; Brown, Talas, et al., 1996; Chapuis, Lucarz-Bietry, et al., 1996; Eastwood, Porter, et al., 1996; Brown, Prajapati, et al., 1998; Eastwood, Mudera, et al., 1998; Jenkins, Redwood, et al., 1999; Freyman, Yannas, et al., 2001; Freyman, Yannas, et al., 2001; Freyman, Yannas, et al., 2001; Freyman, Yannas, et al., 2002; Sethi, Yannas, et al., 2002). These investigations have reported individual cell-generated contractile forces ranging from 0.1 – 200 nN for a number of different fibroblast populations.

Recently, three-dimensional cell motility has been investigated using a variety of tissue engineering constructs (**Figure 1.4**) (Zaman, Trapani, et al., In preparation, 2006), typically amorphous gels. Confocal microscopy is used to track cell position in three-dimensional space in order to calculate cell motility; experimental results are then reported in terms of experimental variables such as construct density or the density of ligands within the construct.

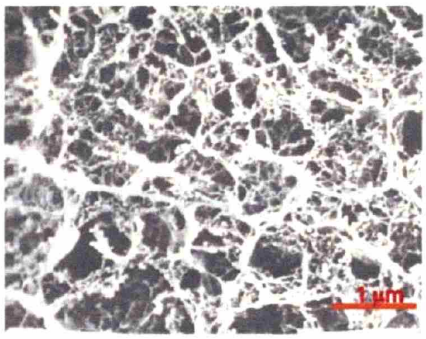

Fig. 1.4a

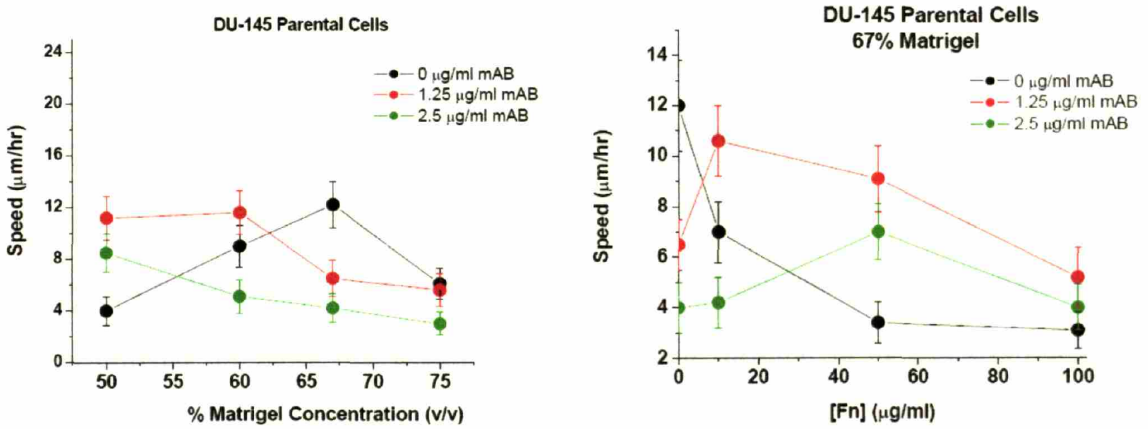

Fig.1.4b

Figure 1.4. Study of cell motility in a 3D Matrigel construct (Zaman, Trapani, et al., In preparation, 2006).

These constructs have begun to allow study of cell behavior in three-dimensions. However, the specific influence of construct parameters such as mechanical properties, composition,

degradation characteristics, microstructure, as well as the influence of environmental factors such as soluble regulator (*i.e.*, growth factor, cytokine) content, cell culture conditions, and exogenous loading is unknown. Standardized construct variants with well-characterized material, microstructural, and mechanical properties present a platform appropriate for such quantitative assays of cell behavior.

1.5. Measuring cell-mediated contraction and migration in 3D collagen-GAG scaffolds

Quantitative and system-wide understanding of the independent and cooperative mechanisms by which the ECM environment influences cell behaviors (*i.e.*, contraction, motility, substrate adhesion, viability, and remodeling) and by which intracellular mechanisms and structures influence the ECM environment and surrounding cells provides a pathway for developing advanced tissue engineering constructs. Current studies of cell behavior in 3D constructs have provided a multitude of information regarding many different cell processes, but what is really missing is a technique to independently control the compositional, mechanical, and microstructural extracellular environment. The lack of standardization and characterization of the constructs utilized for these investigations have made it difficult to extrapolate the results of individual studies. Such a platform would make possible systems-biology type studies and development of resultant quantitative models of cell behavior, providing an elegant framework for designing future bioactive scaffolds.

1.5.1. Choice of experimental construct

Collagen-based scaffolds provide a platform for quantitative studies of *in vitro* cell behavior. These low-density, open-cell foams are biodegradable and are characterized by an interconnected pore network defined by struts, providing an appropriate environment for *in vitro* and *in vivo* tissue engineering applications.

Collagen is a significant constituent of the natural extracellular matrix (ECM), and scaffolds made from collagen have been used in a variety of applications due to a number of useful properties. Collagen scaffolds possess requisite hemostatic properties, low antigenicity, and appropriate mechanical characteristics for use in tissue engineering applications (Yannas, 1972; Yannas and Huang, 1972; Yannas, Burke, et al., 1975; Comninou and Yannas, 1976; Huang and Yannas, 1976; Huang and Yannas, 1977; Silver, Yannas, et al., 1978; Silver, Yannas, et al., 1979). Additionally, collagen scaffolds have been observed to promote cell and tissue attachment and growth (Yannas, Lee, et al., 1989; Yannas, 1990; Howe, Aplin, et al., 1998; Freyman, Yannas, et al., 2001; Schoof, Apel, et al., 2001; Yannas, 2001; van Tienen, Heijkants, et al., 2002).

In designing bioactive collagen scaffolds, four physical and structural properties must be controlled to critical levels: the periodic banding of the collagen fiber structure must be selectively abolished to prevent platelet aggregation, the chemical composition must incorporate ligands appropriate for the binding of cells specific to the area of study, the mean pore size must be bounded within lower and upper limits, and the degradation rate must allow the scaffold to remain insoluble for a critical period (Yannas, 1997; Yannas, 2001).

Scaffolds manufactured from a copolymer of collagen and glycosaminoglycan (CG copolymers) possess a number of useful qualities for use as tissue engineering constructs: they can be sterilized by both dry heat and chemical treatments, they have degradation rates that can be adjusted within a wide range, and they can be fabricated from a number of macromolecular constituents with a variety of pore structures. The work in this thesis has fabricated a series of new type I collagen-glycosaminoglycan (CG) scaffolds. Distinct versions of this scaffold have been used to regenerate skin and the conjunctiva, and have greatly enhanced peripheral nerve regeneration across long gaps (Yannas, Lee, et al., 1989; Chang and Yannas, 1992; Chamberlain, Yannas, et al., 1998; Yannas, 2001).

The original fabrication protocol for collagen-glycosaminoglycan scaffolds used for *in vivo* tissue regeneration studies (Yannas, Lee, et al., 1989) results in a structurally heterogeneous scaffold structure inappropriate for detailed *in vitro* studies of cell behavior. In order to utilize the collagen-glycosaminoglycan scaffold as a construct for quantitative, *in vitro* investigations of cell motility and contraction process, it is critical to produce a series of standardized scaffold variants with a well-defined, uniform (homogeneous) pore structure characterized by equiaxed (spherical) pores. Such a structure will present a consistent pore microstructure as well as a uniform distribution of ligands to all cells within the experimental volumes under study, making quantitative measurement of cell behavior possible.

1.5.2. Choice of cell types

Fibroblasts were primarily studied in this thesis due to the major role they play in the migratory and contractile wound healing response. Ideally, human dermal fibroblasts would be used, but

issues associated with obtaining human cells and the concern of infectious disease transmission made their use impractical. Fibroblasts obtained from an animal source were also impractical for quantitative studies of cell behavior within standardized CG scaffold variants due to the large number of cells that were required for this study and the non-uniformity of the primary fibroblasts obtained from animal to animal. Extensive culture of a single primary fibroblast cell population to obtain a large enough cell stock was also impractical due to the instability of the primary fibroblast phenotype during long terms culture (Freyman, 2001).

The use of a dermal fibroblast cell-line provided the ideal cell source for this investigation because of the uniformity of the cell population and the stability of the fibroblast phenotype over long periods of culture. The parental NR6 mouse fibroblast cell line, a 3T3 fibroblast-derivative which lack endogenous receptors (Chen, Gupta, et al., 1994; Chen, Xie, et al., 1994) was utilized for the majority of the cell behavior assays. The parental human DU-145 prostate carcinoma cell line, a highly invasive and metastatic cell line, was utilized for one experiment comparing the behavior of two cell types with known differences in motility and metabolic activity (Mamoune, Luo, et al., 2003).

1.6. Thesis organization

The thesis is organized in the following manner:

- Chapter 2 presents the development of a new fabrication protocol for producing a series of CG scaffolds with distinct mean pore sizes, each with a homogenous pore microstructure. An in-depth description of the lyophilization process applicable for fabricating a wide range of porous biomaterials will also be presented.

§ Chapter 3 examines the validity and sensitivity of thermal models to predict the final pore structure of the CG scaffold from the thermal processing conditions. An isothermal coarsening model incorporating a conductive mold with interface resistance will be described.

§ Chapter 4 presents experiments, computations utilizing cellular solids theory, and analyses of the specific surface area and permeability of a series of CG scaffold variants under a variety of physiological conditions.

§ Chapter 5 details experiments, computations, and analyses of the mechanical properties of a series of CG scaffold variants examining the effect of pore size, relative density, crosslinking treatment, and hydration. Cellular solids modeling techniques will be further used to illustrate its applicability for describing microstructural and mechanical properties of porous biomaterials.

§ Chapter 6 makes use of the scaffold variants fabricated and characterized in the previous three chapters to measure individual cell-mediated contractile forces generated within the scaffold strut network and to determine the independent effect of scaffold stiffness and microstructure on *in vitro* cell motility.

§ Chapter 7 presents a summary of the conclusions from this thesis as well as an outline of outstanding questions and corresponding research directions which can build upon the results of the present work.

§ Appendices A and B describe the development of a series of collagen-based scaffolds with engineered chemical and microstructural characteristics for peripheral nerve and orthopedic tissue engineering applications. The scaffold fabrication design rules developed in Chapters 2 and 3 will be used in detail to engineer specific microstructures.

CHAPTER 2. *Fabrication of Collagen-GAG Scaffolds with Uniform, Controllable Microstructures*

2.1. Introduction

Porous, three-dimensional scaffolds have been used extensively as biomaterials in the field of tissue engineering for *in vitro* study of cell-scaffold interactions and tissue synthesis and *in vivo* study of induced tissue and organ regeneration (Yannas, Lee, et al., 1989; Chang and Yannas, 1992; Nehrer, Breinan, et al., 1997; Chamberlain, Yannas, et al., 1998; Freyman, 2001; Freyman, Yannas, et al., 2001; Freyman, Yannas, et al., 2001; Yannas, 2001; Zmora, Glicklis, et al., 2002). Biologically active scaffolds used for these applications must meet a number of biophysical and biochemical constraints. They must be biocompatible and, for *in vivo* applications, degrade in the body at a rate that allows the scaffold to remain insoluble for the duration of the critical cellular processes, a time period particular to each biological system; the products of degradation must also be biocompatible. The chemical composition must incorporate ligands appropriate for the binding of cells specific to each application. The average pore diameter must be large enough for cells to migrate through the pores and small enough to retain a critical total surface area for appropriate cell binding. And to allow for transport of cells and metabolites, the scaffold must

have a high specific surface and large pore volume fraction (generally greater than 90%) as well as an interconnected pore network (Yannas, 2001). These microstructural characteristics are especially critical as they define the total surface area and special distribution of ligands presented to cells.

Scaffold pore size has been shown to influence cellular activity. The optimal scaffold pore size that allows maximal entry of cells (Chvapil, 1977) as well as cell adhesion and matrix deposition has been shown to vary with different cell types (Doillon, Whyne, et al., 1986; Tsuruga, Takita, et al., 1996), but typically ranges between 5 and 500 μm. Scaffold pore size has been observed to influence adhesion, growth, and phenotype of a wide variety of cell types, notably endothelial cells, vascular smooth muscle cells, fibroblasts, osteoblasts, rat marrow cells, chondrocytes, preadipocytes, and adipocytes (LiVecchi, Tombes, et al., 1994; Wake, Patrick, et al., 1994; Nehrer, Breinan, et al., 1997; Zeltinger, Sherwood, et al., 2001; Kuberka, von Heimburg, et al., 2002; Salem, Stevens, et al., 2002; Borden, El-Amin, et al., 2003; Claase, Grijpma, et al., 2003). A key component in defining overall construct bioactivity is scaffold microstructural homogeneity or heterogeneity. Scaffold heterogeneity has been shown to lead to variable cell adhesion and to affect the ability of the cell to produce a uniform distribution of extracellular matrix proteins (Zeltinger, Sherwood, et al., 2001).

The shape of the pores that make up the porous scaffold must also be considered. Cells have been observed to be extremely sensitive to the mechanical properties of the underlying substrate (Lo, Wang, et al., 2000), and slight changes in the mean shape of the pores can result in significant variation in the extracellular mechanical properties (Gibson and Ashby, 1997; Harley

and Gibson, In preparation, 2006) and overall construct bioactivity (Chang and Yannas, 1992). Changes in mean pore shape may also play a role in defining the areas of the scaffold available or unavailable for binding and the predominant direction of cell migration as well as in the geometrical organization of cells within the scaffold. As scaffold microstructural heterogeneity has been observed to significantly influence scaffold bioactivity, the uniformity of the size and shape of the individual pores that define the scaffold microstructure can also significantly influence overall construct bioactivity. Tissues synthesized in a scaffold with non-uniform pore architecture have shown inferior biomechanical properties compared to tissue synthesized in a scaffold with a more uniform pore structure (Hollister, Maddox, et al., 2002). In some scaffolds with equiaxed pores, cells aggregate into spherical structures, while in some scaffolds with a more elongated (ellipsoidal as opposed to spherical) pore shape, cells align with the pore axis (Zmora, Glicklis, et al., 2002). Because the scaffold pore microstructure significantly affects cell behavior and overall construct bioactivity, it is important to be able to manufacture scaffolds with a well-defined pore structure.

The objective of this study was to develop a technique to produce a series of CG scaffolds with uniform and controllable pore microstructure in order to present cells in each scaffold variant a uniform and consistent extracellular environment. To produce such scaffolds, the lyophilization fabrication process (freeze-drying) was modified to improve scaffold microstructural homogeneity. A detailed review of the prominent features of freeze-drying will help motivate these modifications.

2.2. Freeze-drying: A Technological Overview

Porous, collagen-glycosaminoglycan (CG) scaffolds are primarily manufactured using a freeze-drying process (Yannas, 2001). The conceptual underpinning of freeze-drying is similar to many techniques currently used to produce porous, open-cell materials: the pore microstructure is defined by a removable phase that is distributed in three-dimensional space, termed a removable template. The scaffold material is then distributed around the removable template which is then eliminated from the construct using any number of steps appropriate for the template and scaffold materials, resulting in the open-cell microstructure. Examples of this technique include salt-leaching (RoyChowdhury and Kumar, 2006), colloidal crystal templating (Blanco, Chomski, et al., 2000; Jiang, Bertone, et al., 2001; Yin, Lu, et al., 2001; Stachowiak, Bershteyn, et al., 2005), and lost wax casting (Ott, 1994); these technologies have been utilized to produce many different open-cell foam materials, including scaffolds for tissue engineering applications.

To fabricate CG scaffolds via freeze-drying, a collagen-glycosaminoglycan suspension is first produced. Microfibrillar type I collagen is first mixed with acetic acid (0.05M); the low-pH (pH 3.2) acetic acid acts to swell the collagen fibers, destroying the quaternary structure as well as the periodic banding of the collagen fibers. These structural modifications remove a large component of the immunological markers on the collagen surface, reducing host immunological response, and prevent platelet aggregation to the CG scaffold surface (Yannas, Burke, et al., 1975; Yannas and Silver, 1975; Silver, Yannas, et al., 1978; Silver, Yannas, et al., 1979). A glycosaminoglycan (GAG), typically chondroitin 6-sulfate, is then added to the swollen collagen-acetic acid mixture. Spontaneous crosslinks are formed between the swollen collagen

fibrils and the newly-added GAG, resulting in precipitation of the collagen-GAG content out of solution and the formation of a collagen-GAG suspension in the aqueous acetic acid phase.

Fabrication of porous, CG scaffolds is best described using a graphical illustration of the phase diagram of the CG suspension (**Figure 2.1**). In the chamber of a commercial freeze dryer, the aqueous CG suspension is solidified (*i*: red arrow, **Figure 2.1**) at atmospheric pressure (P_{atm}) to a specified final freezing temperature (T_f) in a mold designed to define the final overall geometry of the CG scaffold. For this investigation, stainless steel pans were used to make sheets of scaffold. During solidification, the collagen-GAG content is localized between the growing ice crystals in the aqueous (0.05M acetic acid) phase. Once complete, the solidification process produces a continuous, interpenetrating network of ice crystals surrounded by fibers of collagen and GAG (Hobbs, 1974; Kurz and Fisher, 1989; Freyman, Yannas, et al., 2001). Upon application of a low enough pressure (P_{sub}) via an applied vacuum, direct sublimation removes the solidified aqueous phase (ice crystal) content (*ii*: green arrow, **Figure 2.1**), leaving a highly porous scaffold structure where the scaffold microstructure is defined by the ice crystals formed during solidification (**Figure 2.1**). The pore volume fraction and final pore microstructure of a CG scaffold variant depends on the volume fraction of the precipitate in the CG suspension and the underlying solidification processes during fabrication.

The formation of ice crystals in the CG suspension is influenced by the nucleation rate and the rate of heat and protein diffusion. These processes are primarily influenced by the final freezing temperature (T_f) and the heat transfer processes associated with freezing. The rate of nucleation and diffusion are mediated by the degree of undercooling required to initiate solidification (Hobbs, 1974). A larger undercooling temperature increases the rate of ice crystal nucleation and

decreases the rate of heat and protein diffusion relative to the point of nucleation, leading to the formation of smaller ice crystals and resulting in a CG scaffold with a smaller mean pore size (Hobbs, 1974; Michel, 1978; Kurz and Fisher, 1989; Loree, Yannas, et al., 1989; Chang, Yannas, et al., 1990; Chang and Yannas, 1992).

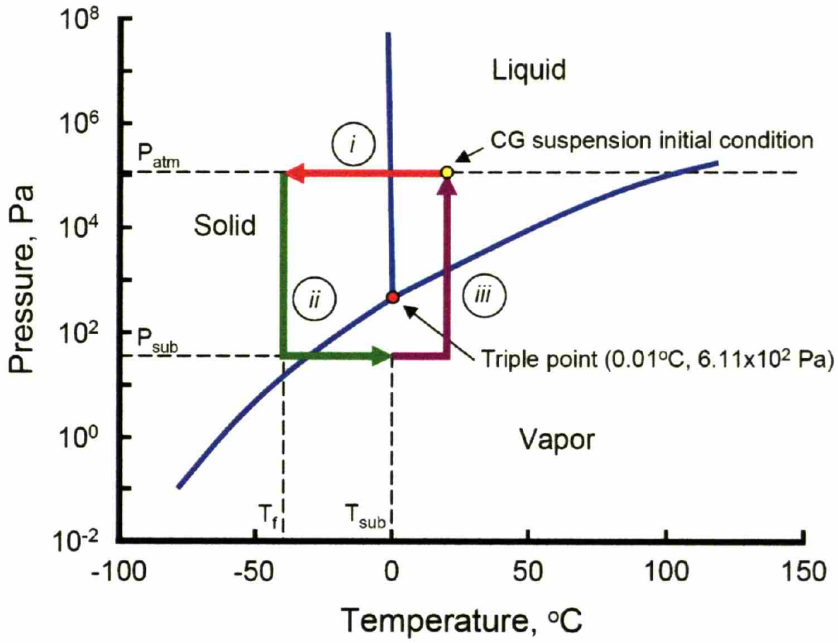

Figure 2.1. Phase diagram of freeze drying process to produce CG scaffolds.

As CG suspension solidification defines the final pore microstructure in the CG scaffold, improved scaffold microstructural uniformity extends from homogeneous heat transfer processes and growth of equiaxed ice crystals within the CG suspension. Heat transfer, and therefore solidification, is influenced by the level of contact between the mold and the freeze dryer chamber; regions of non-contact between the mold and the freeze dryer chamber typically result in regions of scaffold heterogeneity visible to the naked eye (Freyman, Yannas, et al., 2001; O'Brien, Harley, et al., 2004). The large (16.9 x 25.3 cm area) stainless steel molds used to

fabricate CG scaffolds have a tendency to warp slightly over time due to the extreme and rapid freeze-thaw cycles associated with scaffold fabrication. A change of mold dimensions from the standard large mold to a significantly smaller (12.5 x 12.5 cm area) mold, while maintaining a constant thickness (18 gauge stainless steel), was tested to determine whether an improvement in CG scaffold uniformity could be achieved. In addition to testing a change in the geometry of the molds, a variety of modifications to the solidification profile used to fabricate CG scaffolds were tested in an attempt to improve the uniformity of CG suspension solidification.

Fabrication of CG scaffold has typically utilized a rapid solidification (quenching) technique (**Figure 2.2**), where the CG suspension is placed into the freeze dryer chamber after it had been cooled to the final freezing temperature. This quenching process typically results in space- and time-variable heat transfer through the CG suspension where any heterogeneity in heat transfer will result in non-uniform solidification, leading to non-uniform nucleation and growth of ice crystals and, ultimately, scaffold heterogeneity. In localized regions of poor contact between the pan in which the suspension is frozen and the freeze dryer shelf, there is a lower rate of ice-crystal nucleation than in neighboring full contact regions, giving increased variation in pore size. Due to poor heat conduction and the increased temperature of the suspension at these points, these areas have been termed 'hot spots.' In previous studies using CG scaffolds (Freyman, Yannas, et al., 2001), areas which appeared by visual inspection to be heterogeneous were avoided in specimen selection. Selecting samples to avoid 'hot spots' introduces a subjective aspect to using CG scaffolds for tissue engineering, and does not allow for a standardized, fixed sample selection protocol. After solidification is complete, sublimation, typically at a pressure of 15 – 30 Pa for 17 hours, removes the solidified aqueous content, leaving the porous, CG scaffold

with a heterogeneous pore microstructure characterized by pores with a non-uniform pore size and shape (**Figure 2.2**).

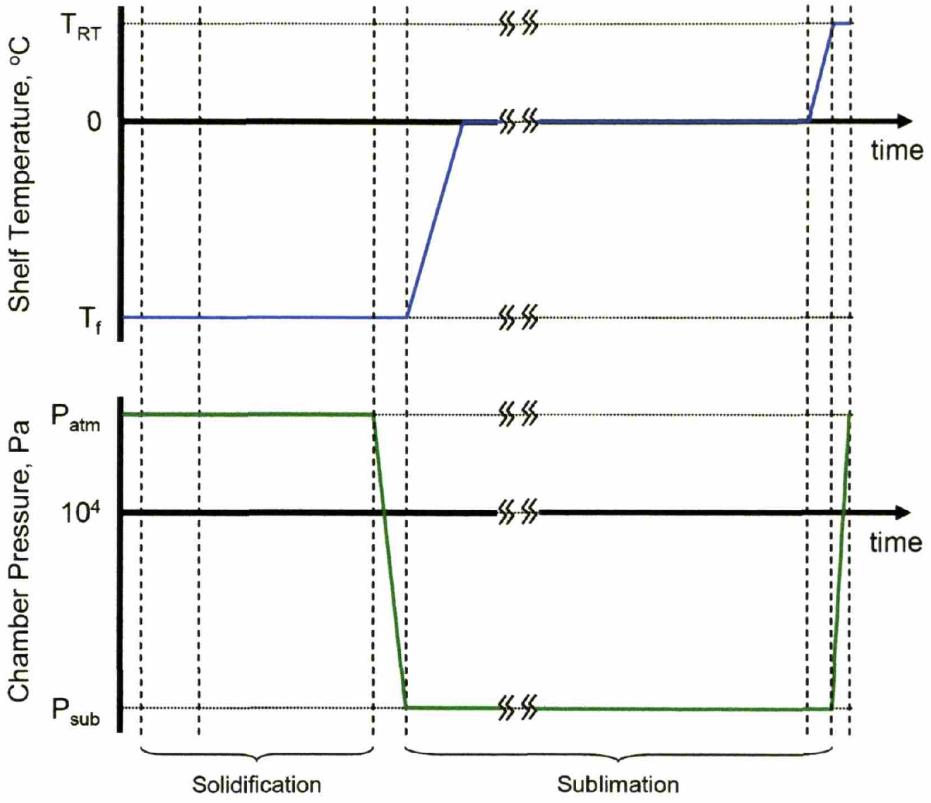

Figure 2.2. Freeze dryer temperature and pressure profiles during CG scaffold fabrication via quenching.

A constant cooling rate technique is the major focus of this chapter. Historically, a similar problem of modifying processing conditions to increase the homogeneity in solidified melts was addressed by the steel industry, providing valuable information for improving the homogeneity of our CG scaffold variants. Developing processing conditions to allow reproducible fabrication of steels with equiaxed grains of uniform size was of critical importance. Homogeneous heat transfer and careful control of the cooling rate of the molten metal was found to significantly

improve steel grain-size homogeneity (Flemings, 1974); these processing considerations provide the technological underpinnings for the improved fabrication protocols for producing structurally homogenous CG scaffolds.

A modified version of such steel processing conditions has been tested by this investigation (**Figure 2.3**). Instead of the rapid (quenched) solidification process typically utilized (**Figure 2.2**), the temperature of the freeze dryer and the CG suspension was cooled at a constant rate (R, **Figure 2.3**) from room temperature to the final freezing temperature (T_f) over an interval of critical duration, termed the solidification regime. The freeze dryer chamber was then held at T_f for a period of time to allow solidification of the entire suspension to complete, termed here the annealing regime in tribute to the metallurgical roots of this processing technique. A series of different solidification rates were tested in order to identify the appropriate solidification rate (R) to produce a CG scaffold with a homogeneous microstructure and equiaxed pores. It was hypothesized that appropriate modification of the solidification rate - slower and more spatially uniform than quenched cooling – will result in a scaffold with homogeneous microstructure. After solidification is complete, sublimation at a pressure of 15 – 30 Pa for 17 hours removes the solidified aqueous content, leaving the porous, CG scaffold with a heterogeneous pore microstructure characterized by pores with a non-uniform pore size and shape (**Figure 2.3**).

In order to quantitatively measure *in vitro* cell behavior (motility, contraction) within the CG scaffolds as a function of mean pore size it is important to be able to fabricate a standardized family of CG scaffolds with a homogeneous microstructure and distinct mean pore sizes. To produce scaffolds with different pore sizes, different final freezing temperatures were used with

the constant cooling rate technique. It was hypothesized that by using the constant cooling rate technique but decreasing the final freezing temperature will result in the fabrication of CG scaffolds with a uniform microstructure but with smaller pores.

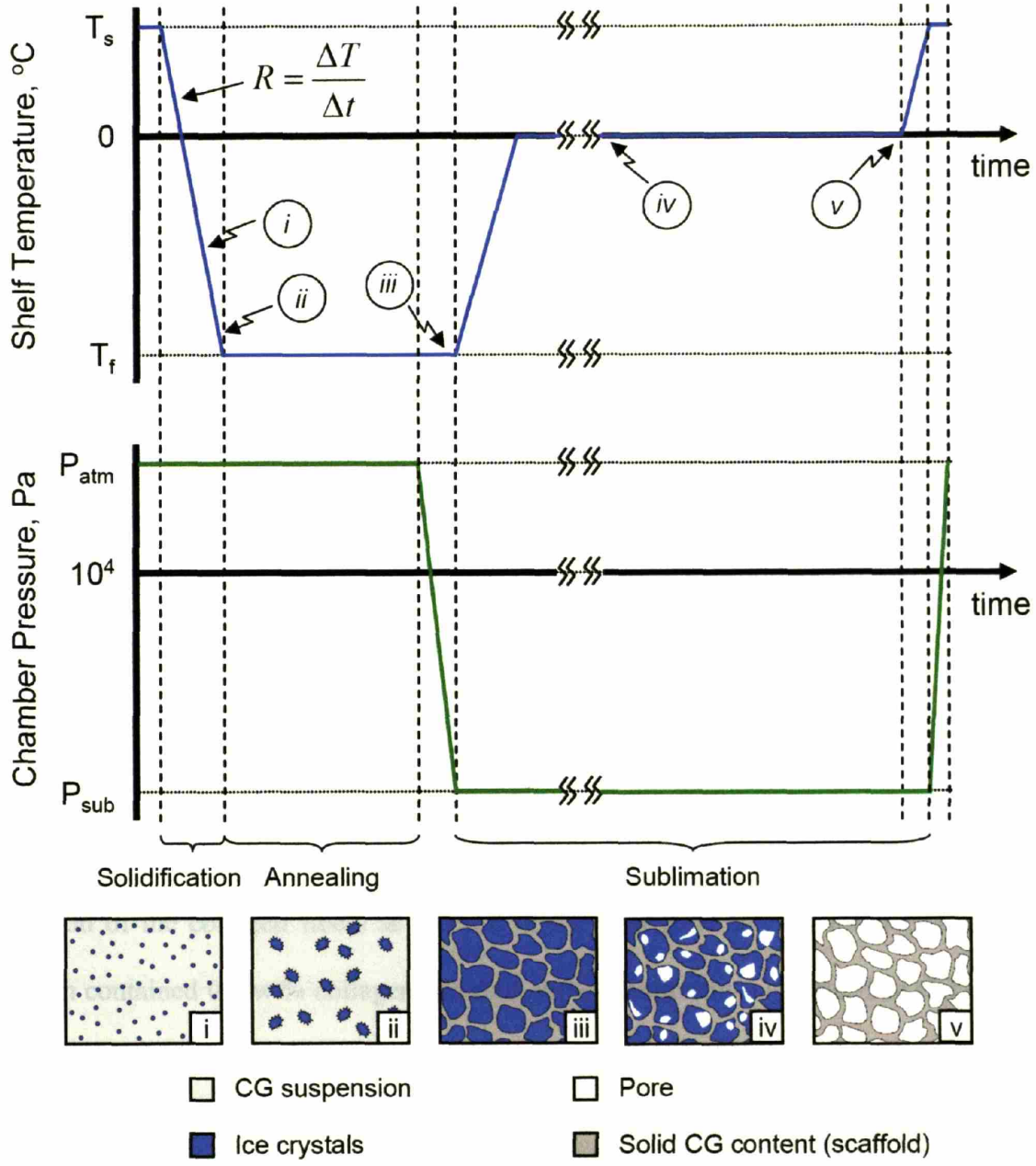

Figure 2.3. Freeze dryer temperature and pressure profiles and relevant period of ice crystal growth and sublimation during CG scaffold fabrication via constant cooling technique.

This constant cooling rate fabrication technique has significantly improved the structural uniformity of the CG scaffolds, and modulation of the final freezing temperature has resulting in the fabrication of a series of CG scaffolds with a uniform microstructure but with distinct mean pore sizes (O'Brien, Harley, et al., 2004; O'Brien, Harley, et al., 2005).

2.3. Materials and Methods

2.3.1. Preparation of collagen-glycosaminoglycan copolymer suspension

The CG scaffolds were fabricated from a collagen-glycosaminoglycan (CG) suspension via freeze drying (O'Brien, Harley, et al., 2004; O'Brien, Harley, et al., 2005). The CG suspension was produced by combining microfibrillar, type I collagen (0.5 wt%) isolated from bovine tendon (Integra LifeSciences, Plainsboro, NJ) and chondroitin-6-sulfate (0.05 wt%) isolated from shark cartilage (Sigma-Aldrich Chemical Co., St. Louis, MO) in a solution of 0.05M acetic acid (pH 3.2). The collagen, chondroitin-6-sulfate, and acetic acid were mixed at 15,000 rpm in an overhead blender (IKA Works, Inc., Wilmington, NC); the temperature of the suspension was maintained at 4°C throughout mixing by a cooling system (Brinkman, Westbury, CT) to prevent denaturation of the collagen fibers as a result of the heat generated by mixing. The final CG suspension contained 0.5 wt% collagen and 0.05 wt% chondroitin-6-sulfate. The CG suspension was then degassed under vacuum (15 Pa) at room temperature (20°C) for 60 minutes to remove air bubbles introduced by mixing and was stored at 4°C until use. Immediately prior to use, the volume of suspension was degassed for a second time, allowing the suspension to reach room temperature (O'Brien, Harley, et al., 2004; O'Brien, Harley, et al., 2005). CG scaffolds were

fabricated using either the traditional rapid-freeze (quenching) (**Figure 2.2**) (Yannas, Lee, et al., 1989; Chamberlain and Yannas, 1998) or the constant cooling rate (**Figure 2.3**) (O'Brien, Harley, et al., 2004; O'Brien, Harley, et al., 2005) technique using either a large surface area (16.9 x 25.3cm) or small surface area (12.5 x 12.5 cm) 18-gauge, 304 stainless steel pan.

2.3.2. Quenched solidification

For scaffolds fabricated using the rapid-freeze (quenching) freeze-drying technique, the CG suspension, originally at room temperature, is frozen in a 304 stainless steel pan (VirTis, Gardiner, NY) by placing it into a pre-cooled freeze dryer (VirTis Genesis) at –40°C for sixty minutes (Yannas, Lee, et al., 1989). The temperature of the freeze dryer shelf is maintained at a constant temperature of -40°C via computer control and the pan is constructed from the same alloy as the freeze dryer shelves to allow for more uniform heat transfer during freezing. The frozen suspension is then sublimated under a vacuum (15 – 30 Pa) for 17 hours at a temperature of 0°C (Yannas, Lee, et al., 1989; Chamberlain and Yannas, 1998).

2.3.3. Effect of mold dimensions and stiffness

To test the effects of the pan stiffness on the pore structure of CG scaffolds, two series of scaffolds were produced following the standard quench freezing protocol, but in pans with two distinct geometries. The first series of scaffolds were fabricated in the original large stainless steel pans (16.9 x 25.3 cm), while the second series of scaffolds were fabricated in smaller (12.5 x 12.5 cm) stainless steel pans. Both the pans were made of the same 18 gauge 304 stainless steel; geometrical differences resulted in a 2.78-fold reduction in pan area and an approximately 6-fold increase in pan stiffness for the smaller pan. The relative warping of the pans was

determined by mapping the surface topology of the bottom of each pan using a dial indicator (Starrett, Inc., Athol, MA). Two distinct sample selection protocols were utilized to select 5 pairs of samples from each scaffold sheet for pore size analysis. Samples were either selected from five fixed locations within the scaffold regardless of the apparent scaffold heterogeneity (*i.e.*, areas containing 'hotspots' were not excluded from analysis) in a process termed 'Fixed Selection' (**Figure. 2.4**), or samples were selected from five areas of the scaffold deemed by visual inspection to be the most homogeneous (*i.e.*, 'hot spots' were excluded) in a process termed 'Best Pick Selection.' Scaffolds produced in the smaller pans did not exhibit heterogeneities visible to the naked eye; consequently, samples were removed for analysis using only the 'Fixed Selection' technique.

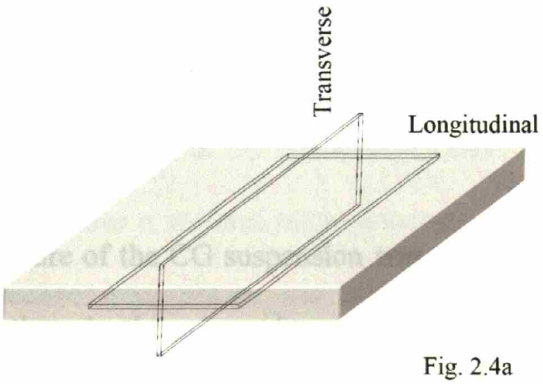

Fig. 2.4a

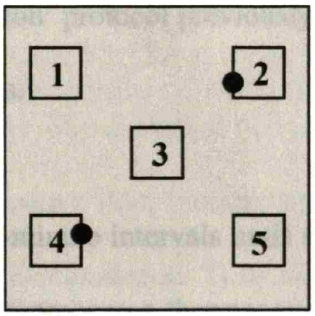

Fig. 2.4b

Figure 2.4. Schematic of CG scaffold sampling locations. Orientation of longitudinal and transverse planes used during pore size analysis (Fig. 2.4a) as well as the locations where samples were removed for analysis via the fixed selection protocol (1-5) and the location (•) of the thermocouples during measurement of the freezing kinetics of the CG suspension (Fig. 2.4b).

2.3.4. Constant cooling rate solidification: Effect of varying the solidification rate

The cooling rate of the freeze dryer shelf was varied in order to test the effects of variable freezing conditions on the final scaffold microstructure. With the constant cooling rate technique,

the CG suspension was placed into the chamber of the freeze dryer at room temperature (20°C) and the temperature of the chamber and shelf of the freeze dryer was then reduced (ramped) at a constant rate via computer control to the final freezing temperature (-40°C) (solidification regime, **Figure 2.3**); the temperature was then held constant at -40°C for 60 minutes (annealing regime, **Figure 2.3**). The ice phase was then sublimated under vacuum (15 – 30 Pa) at 0°C for a period of 17 hours as has previously been described (Yannas, Lee, et al., 1989). The term "constant cooling rate" refers to the constant cooling rate of the freeze dryer shelf and not to the cooling rate of the CG suspension, which will be characterized separately. The CG suspension was frozen at three distinct cooling rates, where the freeze dryer shelf temperature was ramped from 20°C to the final freezing temperature of -40°C in 65, 90 and 115 minutes. A fourth scaffold was produced using the quenching technique previously described. Samples were removed for pore analysis from all four types of scaffold using the 'Fixed Selection' protocol previously described. All samples were made using the smaller (12.5 x 12.5 cm) pans.

The temperature of the CG suspension was monitored at one-minute intervals until sublimation at two locations in the suspension using a two-channel microprocessor thermocouple (HH22, Omega Engineering, Stamford, CT). Two thermocouple elements (Type K Thermocouple, Omega Engineering, Stamford, CT) were placed approximately 10 cm apart along a diagonal between the opposite corners of the pan (**Figure 2.4**). The average freezing rate of the suspension (in °C/min) for all freezing protocols was computed between the starting temperature and -30°C. The lower limit of -35°C was used in this calculation because below that temperature, the temperature of the suspension and the freeze dryer shelf tended to asymptotically approach the final freezing temperature, and could not be modeled linearly. The liquid-solid transition time,

corresponding to the time where liquid and solid coexist, is a measure of how rapidly the suspension begins to solidify (Michel, 1978); it was measured as the time that the suspension temperature remained between 0°C and -1°C following the initial supercooling condition required to initiate ice crystal nucleation.

2.3.5. Fabrication of CG scaffold with different pore sizes

After identifying the appropriate solidification rate in order to produce CG scaffolds with a uniform pore microstructure with equiaxed pores, the degree of undercooling reached (mediated by the final freezing temperature) was varied in an attempt to produce uniform CG scaffolds with equiaxed pores with distinct mean pore sizes. The degassed CG slurry was poured into the smaller 18 gauge, 304 stainless steel mold (12.5 x 12.5 cm) (VirTis, Co., Gardiner, NY); the mold was then placed into the chamber of a freeze dryer (Genesis, VirTis) at room temperature (20°C). The temperature of the freeze dryer shelf and chamber was cooled at the constant rate identified to produce a uniform microstructure to a series of distinct final freezing temperatures; the shelf/chamber temperature was then held constant for 60 minutes at T_f to complete the freezing process. Final freezing temperatures of -10°C, -20°C, -30°C and -40°C were used to produce porous scaffolds of four different mean pore sizes. The ice phase was then sublimated under vacuum (15 – 30 Pa) at 0°C for a period of 17 hours to produce the porous CG scaffolds.

The temperature of the CG suspension and the freeze dryer shelf was monitored during the freezing process at one minute intervals at four locations in the suspension using a thermocouple (HH22, Omega Engineering, Stamford, CT) as was described in section 2.3.4 (O'Brien, Harley, et al., 2004). The average freezing rate of the suspension in °C/min was determined as the

average rate of freezing from the starting temperature of the suspension to a lower limit of 5°C greater than the final temperature of freezing.

2.3.6. CG scaffold crosslinking

All CG scaffolds manufactured in this study were crosslinked via a dehydrothermal process after freeze-drying to stiffen the collagen network by introducing covalent crosslinks between the polypeptide chains of the collagen fibers without denaturing the collagen into gelatin (Yannas and Tobolsky, 1967; Yannas, 1972). Crosslinking was carried out in a vacuum oven (Fisher IsoTemp 201, Fisher Scientific, Boston, MA) at a temperature of 105°C under a vacuum of 50 mTorr for 24 hours (Yannas, Lee, et al., 1989; Chamberlain, Yannas, et al., 1998).

2.3.7. Analysis of pore structure

To determine the average pore size of the scaffolds, pairs of samples were removed from five locations in each sheet of the CG scaffold using either the 'Fixed Selection' or 'Best Pick Selection' protocols (see Section 2.3.3); for all analysis utilizing the smaller (12.5 x 12.5 cm) molds, the 'Fixed Selection' technique was utilized. At each of the five locations, a sample was taken from the longitudinal plane (10 x 10 x 3 mm thick square section from the plane of the scaffold) and in an adjacent region from the transverse plane (10 x 5 x 3 mm thick rectangular section from the plane of the scaffold) (**Figure. 2.4**). Each of these samples was cut from the top surface through the entire depth of the scaffold (approximately 3.5 mm).

Each sample was embedded in glycolmethacrylate and serially sectioned longitudinally or transversely on a Leica RM2165 microtome (Mannheim, Germany) at a 5 μm thickness. The

sections were stained using aniline blue and observed on an optical microscope (Nikon Optiphot, Japan) at 4x magnification. Three digital images of each longitudinal section and two images of each of the smaller transverse sections were digitized using a CCD color video camera (Optronics Engineering, Inc., Goleta CA). A total of 125 digitized images (25 images from each of five locations per scaffold) were analyzed from each scaffold sheet.

The digitized images were analyzed using a linear intercept program in Scion Image™ software (Scion Corp., Frederick, MD) to determine the mean pore size for each cross-sectional image (Freyman, 2001). Briefly, the program calculated the number of times that a series of parallel lines drawn across the image intercepted a pore wall. This process was repeated with the series of lines rotated by 5° increments around the section. The linear intercept program utilized the distance and angle measurements to construct a best-fit ellipse representing an average pore cross-section for each analyzed region, and the mean intercept length was an average of the major and minor axes of this reconstructed best-fit shape (**Figure 2.5**).

The mean pore size at each position within the scaffold was calculated from the average of the results from the longitudinal and transverse planes at that location; the best-fit ellipses for adjoining transverse and longitudinal sections were used to construct a best-fit ellipsoid. To account for the effects of pores that were not sectioned through their maximal cross-section but rather at an arbitrary angle, the ellipse major and minor axes were corrected by multiplying by 1.5 (Gibson and Ashby, 1997). The mean pore size of each scaffold was determined by averaging the results from all analyzed regions.

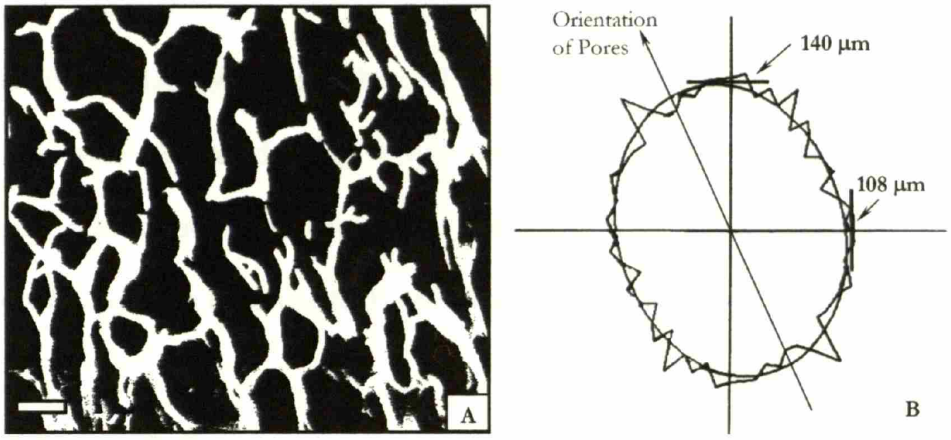

Figure 2.5. Linear intercept analysis of CG scaffold pore microstructure. Characteristic pore microstructure (scale bar: 100 μm) (A) and best-fit ellipse as reported by linear intercept analysis performed by Scion Imaging software (B) of a CG scaffold fabricated via quenching. The average mean pore size and pore aspect ratio was 124 μm and 1.3 (ellipsoidal pores) (Freyman, 2001).

2.3.8. Environmental scanning electron microscopy

Environmental scanning electron microscopy (ESEM) was used to qualitatively compare the pore structure of the scaffolds produced by the original quenching technique and the constant cooling rate technique. Cylindrical sections, 9 mm in diameter, were removed from the thickness of the scaffold and stored in phosphate buffered saline (PBS, Sigma-Aldrich Chemical Co., St. Louis, MO) prior to observation. The hydrated samples were removed from the PBS and placed directly onto the sample holder attached to the Peltier cooling stage in the ESEM without the need of prior sputter coating.

2.3.9. Micro computed-tomography

The three-dimensional structure of a CG scaffold manufactured using the original quenching technique was analyzed using micro computed-tomography (MicroPhotonics, PA), to obtain a separate quantitative measurement of mean pore size in order to confirm the scaffold pore

analysis by the linear intercept method. Scans were performed on a Skyscan 1072 Micro-CT system (Aartselaar, Belgium) with 100 keV x-ray source and a 12 bit cooled CCD camera. Cross-sections were generated using a full cone beam Feldkamp reconstruction algorithm. Morphological calculations were carried out on the reconstructed sections using the standard Skyscan software package to calculate the mean pore size of the scaffold.

2.3.10. Statistical analysis

All statistical calculations were performed using the StatView statistical software package (v. 5.0, SAS Institute, Inc., Cary, NC). Paired t-tests were performed to compare individual sets of data to determine statistical significance. One-way analysis of variance (ANOVA) and pair-wise multiple comparison procedures (Tukey Tests) were used to compare data groups. Error is reported in figures as the standard deviation (StDev), the standard error of the mean (SEM = $StDev/n^{1/2}$), or as the coefficient of variance (CV = StDev/Mean) in order to compare the relative variation in pore size between different scaffolds. A probability value of 95% ($p < 0.05$) was used to determine significance.

2.4. Results

2.4.1. Influence of pan size on pore size

Visual inspection revealed that the CG scaffolds produced in the smaller stainless steel pan were more homogeneous than those prepared in the larger stainless steel pan, with no apparent 'hot spots' due to variable nucleation of ice crystals. **Figure 2.6** shows the results of the pore size analysis of scaffolds produced using the large and small stainless steel pans. One-factor ANOVA indicated a significant effect of pan size and sample selection method on the pore structure ($p <$

0.05). The mean pore size of scaffolds produced using the smaller pan (Fixed Selection) was found to be significantly smaller ($p < 0.05$) than that of scaffolds produced in the larger, more compliant stainless steel pan (both 'Fixed Selection' and 'Best Pick Selection'). The coefficient of variance (CV) of the pore size of scaffolds produced in the smaller pans ('Fixed Selection') was found to be significantly smaller ($p < 0.05$) than that of scaffolds produced in the large pan ('Fixed Selection'). However, when heterogeneous regions were avoided when selecting samples from the large pan ('Best Pick Selection'), the CV of the mean pore size of scaffolds was not significantly different than that for scaffolds produced in the smaller pan ('Fixed Selection') ($p = 0.09$). Nevertheless, the use of the small pans removes a subjective element from the selection of samples from the scaffolds. There was an overall improvement of scaffold homogeneity by using the smaller pans.

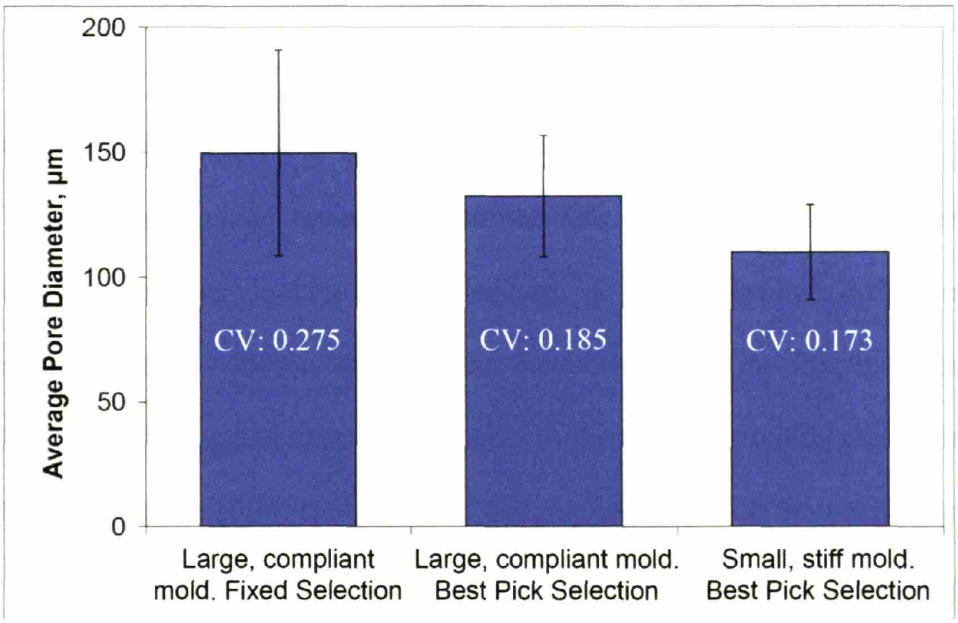

Figure 2.6. The effect of pan size and stiffness on scaffold mean pore size and homogeneity (proxy: CV). No 'hotspots' due to variable nucleation were found in scaffolds manufactured in the smaller stainless steel pan, and those scaffolds showed a smaller mean pore size with increased scaffold homogeneity.

Analysis of the surface topology of the pans was performed to determine whether there was a difference in the pan geometry that could account for the improvement in scaffold homogeneity observed in the scaffolds fabricated using the smaller pans. The average deflection at the center of the pan for the larger, more compliant pans (254μm) was considerably larger than for the smaller, stiffer pans (80μm). The relative pan warping of the larger and smaller pans was determined by comparing the average standard deviation of the deflection of the pan along the rows and columns of the grid used to measure the relative pan heights across the bottom. The average standard deviation of the deflection of the pan for the larger pans (144.6 ± 71.4 μm) was significantly larger ($p=0.002$) than that of the smaller pans (45.7 ± 18.0 μm). These results suggest that the smaller pans are significantly less warped and show a smaller overall deflection compared to the larger pans. The increased stiffness of the smaller pan is expected to reduce warping from repeated freeze-thaw cycles.

2.4.2. Control of the rate of freezing of the CG suspension

Figure 2.7 shows the average temperature of the CG suspension during freezing for the quenching and the constant cooling rate techniques. A larger absolute difference in slurry temperature was observed between measurement locations during the freezing process (larger error bars) for the quenching technique as compared to the constant cooling rate technique. One-factor ANOVA indicated a significant effect of freezing technique on the temperature variation throughout the pan ($p < 0.0001$). The constant cooling rate technique with a freezing time of 65 minutes displayed significantly improved freezing homogeneity compared to the quenching technique ($p < 0.0001$) and the constant cooling rate technique with a freezing time of 105 minutes ($p < 0.0001$), but not compared to the constant cooling rate technique with a freezing

time of 90 minutes (p = 0.52). **Table 2.1** shows the results of measurements of the average freezing rate of the slurry and the time required for the liquid-solid transition of the CG suspension at the point of freezing.

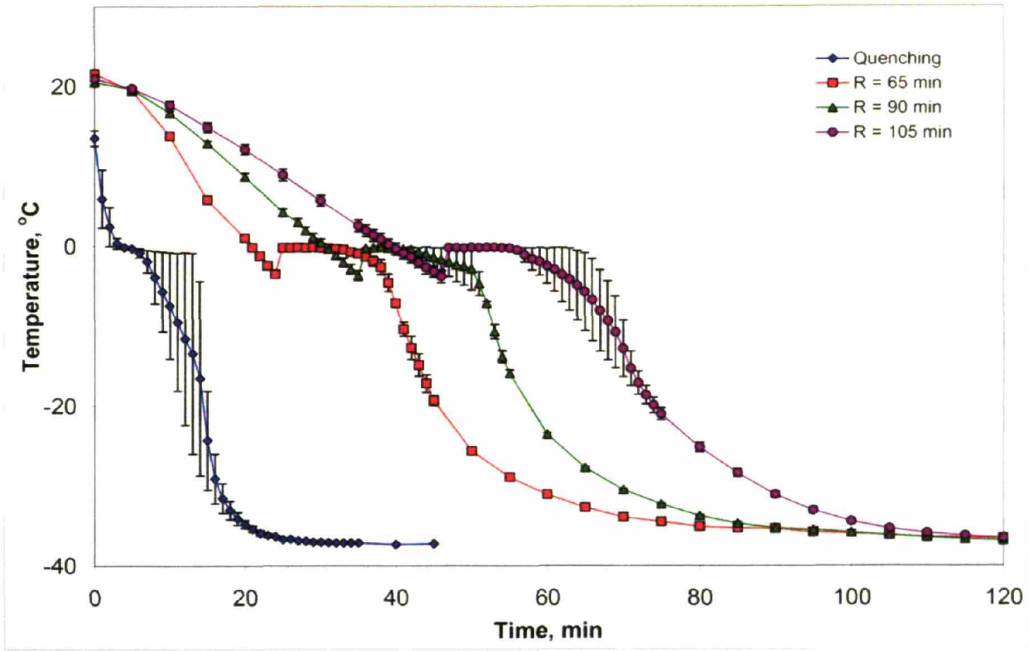

Figure 2.7. CG suspension thermal profiles during solidification. Average temperature of the CG suspension during freezing for the four freezing curves (R = length in minutes of the constant cooling period during the freezing process).

Freezing Time	Average Suspension Freezing Rate, °C/min	Liquid-Solid Transition Time, min
Quenching	4.1	2
65 min	0.9	10.5
90 min	0.7	11
105 min	0.6	14.5

Table 2.1. Freezing rate of CG suspension and the liquid-solid transition time during solidification.

The quenching technique showed the most rapid freezing rate (4.1°C/min) with the shortest duration at the liquid-solid transition (2min) while the constant cooling rate protocols had significantly slower rates of freezing (0.9°C/min, 0.7°C/min, 0.6°C/min) and longer liquid-solid transition times (10.5, 11, 14.5 minutes) for freezing times of 65, 90 and 105 minutes, respectively.

2.4.3. Constant cooling rate solidification: Influence of rate of freezing on pore microstructure

The cellular structure of scaffolds produced using the constant cooling rate technique (0.9°C/min) appears significantly more homogeneous throughout the entire scaffold than the scaffold structure produced using the original quenching technique (**Figure 2.8**).

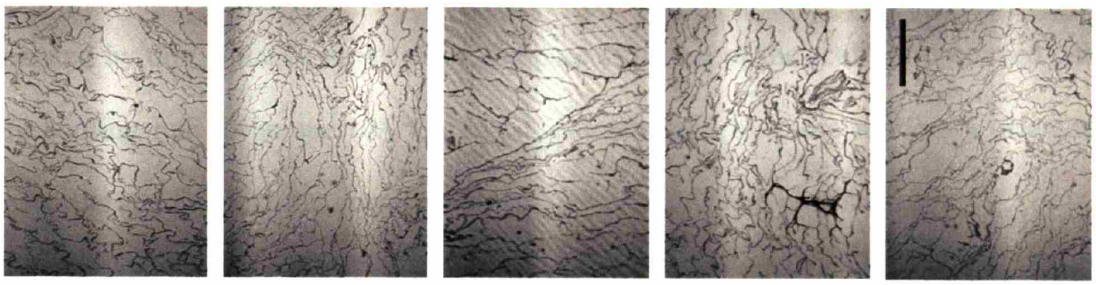

Fig. 2.8a

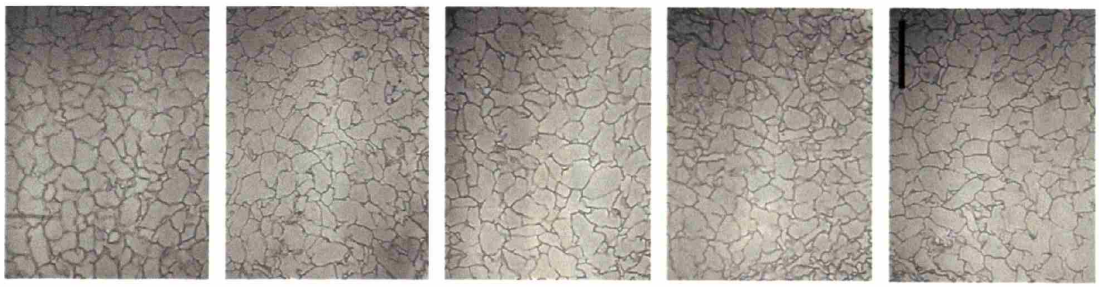

Fig. 2.8b

Figure 2.8. A series of longitudinal images selected via 'Fixed' selection protocol from a single CG scaffold sheet produced using the quenching (Fig. 2.8a) and the constant cooling rate technique that displayed the greatest freezing rate homogeneity (0.9°C/min) (Fig. 2.8b). The constant cooling rate technique produced pores with a more uniform size and structure at each sample point (locally), and also a more homogeneous nature throughout the scaffold (globally). Scale bar = 300μm.

Although locally, pores often tended to be aligned in a particular direction, no consistency of pore orientation was found between the five separate sampling locations in both the quenching and the constant cooling rate techniques. When the scaffolds are compared, it is apparent that using the new constant cooling rate technique, the pores are more uniform in size, have a consistent pore structure, and show no obvious variation in mean pore size, pore structure, or alignment throughout the scaffold, differing significantly from scaffolds fabricated using the quenching protocol. Similar results were found for analysis of both the transverse and longitudinal sections.

ESEM micrographs (**Figure 2.9**) indicate that the pore structure of the scaffold produced using the quenching technique (4.1°C/min) is characterized by roughly parallel planes of collagen that are separated by thin collagen struts while the pore structure of the scaffold produced using the constant cooling rate technique (0.9°C/min) is characterized by more randomly oriented solid collagen struts and membranes, corresponding to a more equiaxed pore structure.

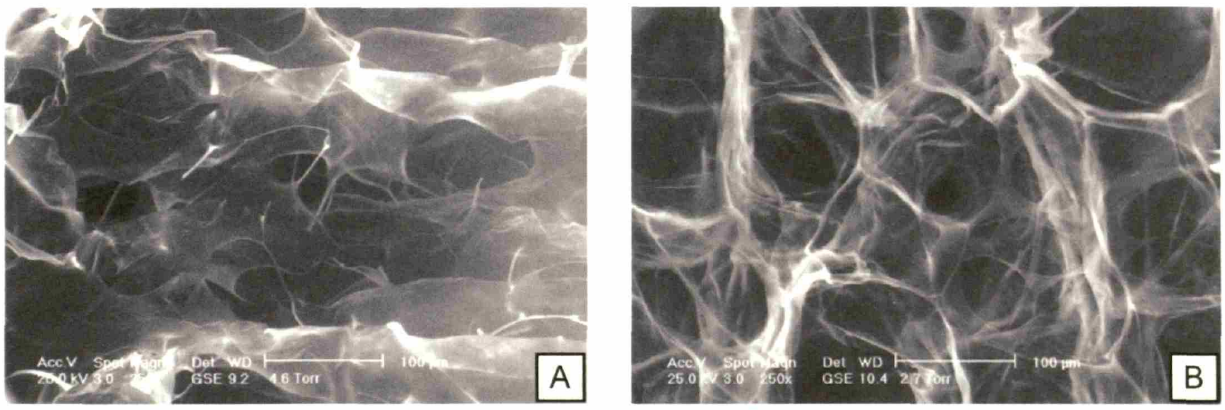

Figure 2.9. ESEM micrographs of CG scaffolds produced using the quenching technique in the large pans (Fig. 2.9a) and the constant cooling rate technique (0.9°C/min) in the small pans (Fig. 2.9b) (Pek, Spector, et al., 2004).

When examined with the naked eye, all scaffolds produced using the constant cooling rate techniques (0.9, 0.7, and 0.6 °C/min) appear to be homogeneous in nature throughout the entire scaffold with no evident 'hot spots.' The histomorphometric analysis of scaffolds produced using the quenching and the constant cooling rate techniques indicate that scaffolds fabricated with the constant cooling rate technique are more uniform than those produced with the quenching technique (**Figure 2.10**).

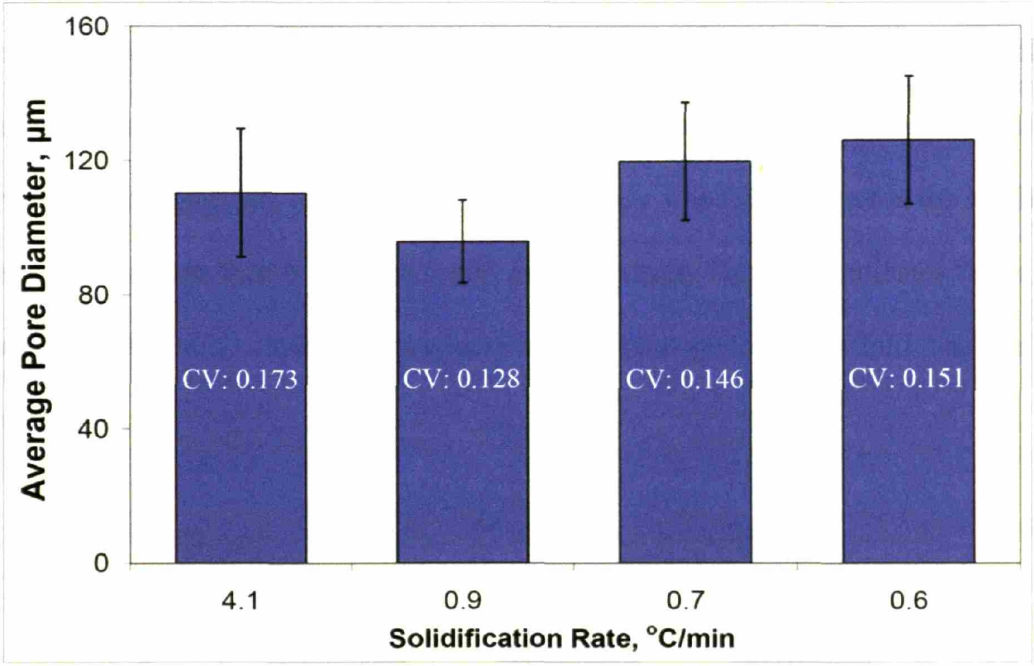

Figure 2.10. Average pore size for scaffolds fabricated with the quenching (4.1°C/min) and the constant cooling rate technique (0.9, 0.7, 0.6°C/min) in the small stainless steel pans.

A significantly higher coefficient of variance (0.173) was found for the scaffold produced using the original quenching technique ($p < 0.05$) compared to the three scaffolds formed using the constant cooling rate technique. The scaffold produced by freezing at a rate of 0.9°C/min was found to produce the most uniform scaffold, with a smaller coefficient of variance (0.128) compared to those observed for the other two rates of freezing (values of 0.146 and 0.151 for

freezing rates of 0.7 and 0.6°C/min respectively) ($p < 0.05$). In addition, scaffolds produced at a freezing rate of 0.9°C/min were also found to have a significantly smaller mean pore size ($p < 0.05$) compared to the more rapid (4.1°C/min) and slower rates of freezing (0.7 and 0.6°C/min).

This study demonstrated that a freezing rate of 0.9°C/min, corresponding to a more controlled freezing process than the original quenching protocol, produced a scaffold with a more homogeneous structure than the other techniques studied. Further analysis was conducted to determine whether uniform scaffolds could be produced consistently. Three scaffolds were produced in the smaller stainless steel pans using a freezing rate of 0.9°C/min, with results shown in **Figure 2.11**. No significant difference in mean pore size was found between the scaffolds ($p = 0.257$), and a CV of less than 0.167 was found for each sheet. This data indicates that a constant cooling rate of 0.9°C/min consistently produces a more homogeneous scaffold than the standard quenching technique.

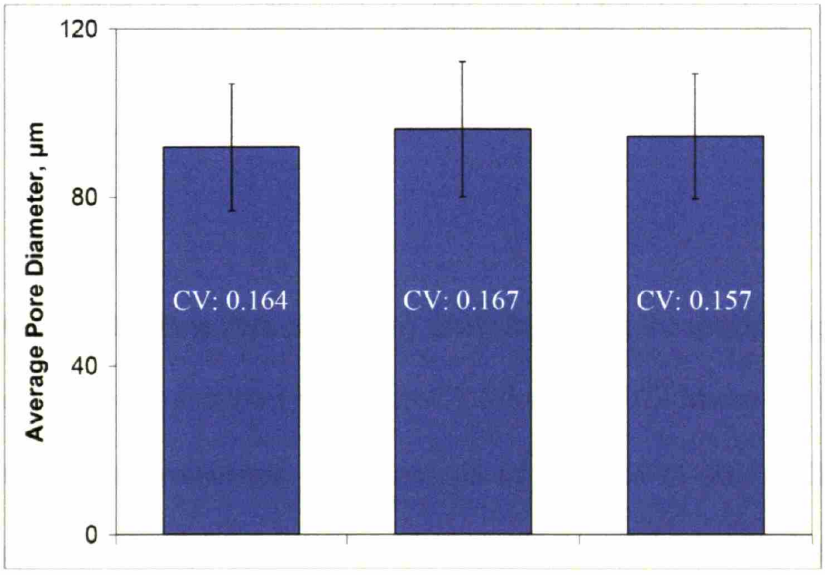

Figure 2.11. Sheet-to-sheet variability of the mean pore size of three CG scaffolds produced with an average shelf freezing rate of 0.9°C/min.

2.4.4. Pore structure and anisotropy

The mean pore size of scaffolds in the longitudinal and transverse planes, at five locations within the scaffold is shown in **Figure 2.12** for scaffolds made by the quenching (**Fig. 2.12a**) and the constant cooling rate technique (0.9°C/min) (**Fig. 2.12b**) in the small pans.

The quenching technique produces a significant variation in the mean pore size between locations throughout the scaffold ($p < 0.001$) and between the longitudinal ($114.9 \pm 17.7\mu m$) and transverse ($102.7 \pm 18.6\mu m$) planes ($p < 0.05$). For scaffolds produced by the constant cooling rate technique, no significant difference in mean pore size was found at the five sample points within each sheet ($p = 0.177$) or between the longitudinal ($96.8 \pm 11.1\mu m$) and the transverse planes ($94.2 \pm 13.9\ \mu m$) in the scaffold ($p = 0.313$). While scaffolds produced using the quenching technique show a significant spatial variation of mean pore size as well as oriented pores (significantly longer longitudinal than transverse mean intercept), scaffolds produced with the constant cooling rate technique show no significant spatial variation in pore size as well as equiaxed pores.

2.4.5. Micro CT Analysis

A section of a CG scaffold (Best Pick Selection) fabricated using the quenching technique in the large stainless steel pans was analyzed via micro-CT (Skyscan 1072 Micro-CT system). A mean pore size of 130 μm was calculated from analysis of a series of scans. The result of this calculation compares favorably with the mean pore size calculated from the linear intercept method (132.4 μm).

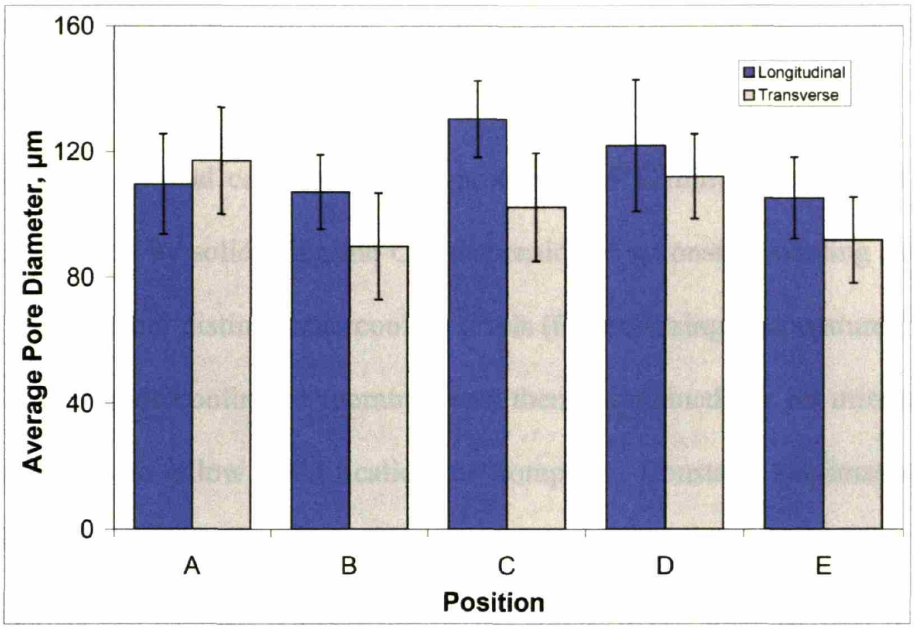

Fig. 2.12a

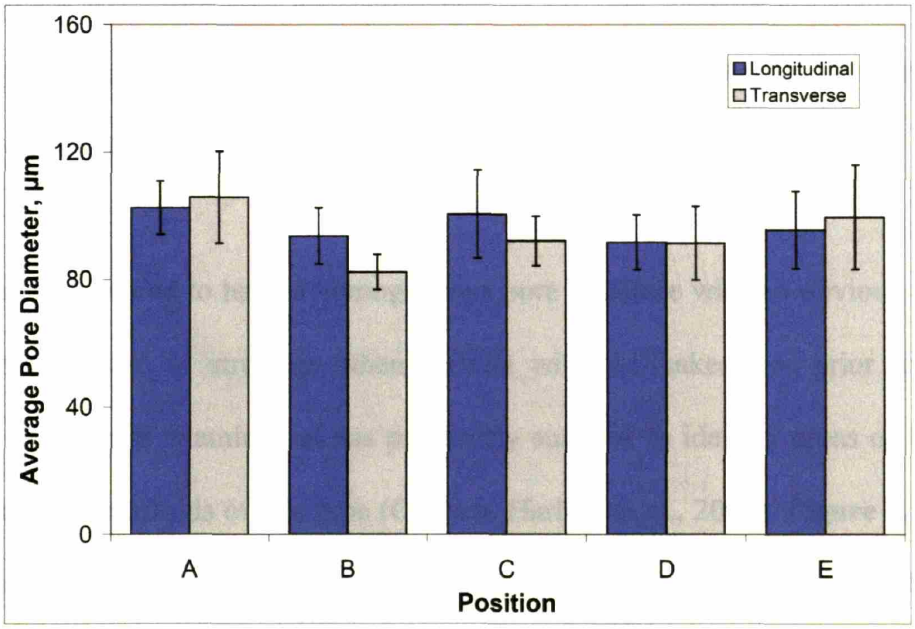

Fig. 2.12b

Figure 2.12. Analysis of the consistency of the pore microstructure at five locations (A – E) within a single CG scaffold sheet in the longitudinal and transverse planes for scaffolds produced using quenching (Fig. 2.12a) and the constant cooling rate technique (0.9°C/min) (Fig. 2.12b). Scaffolds manufactured via quenching have mean pore sizes of 114.9 ± 17.7 and 102.7 ± 18.6 µm, while scaffolds produced via constant cooling have mean pore sizes of 96.8 ± 11.1 and 94.5 ± 13.9 µm in the longitudinal and transverse planes, respectively.

2.4.6. Constant cooling rate solidification: Influence of final freezing temperature on pore microstructure

After identifying the optimal constant cooling protocol (0.9°C/min), four distinct CG scaffold variants were produced by solidifying the CG suspension at a constant cooling rate from room temperature (20°C) to four distinct undercooling levels (final freezing temperatures) of -10, -20, -30, and -40°C. The undercooling temperature was then maintained for 60 minutes (annealing regime, **Figure 2.3**) to allow solidification to complete. Constant sublimation processing conditions (0°C, 15 – 30 Pa, 17 hours) were then applied to produce the porous CG scaffolds. **Figure 2.13** shows the average temperature of the freeze dryer shelf as well as the average temperature of the CG suspension during freezing for the four freezing protocols. As expected, the CG suspension approached the final temperature of freezing more rapidly when exposed to greater undercooling (lower T_f) (**Fig. 2.13b**).

All CG scaffolds appeared to have a homogeneous pore structure with no obvious areas of non-uniformity in pore size or structure when viewed with the naked eye prior to histological examination. Such gross examination has previously sufficed to identify areas of heterogeneity and homogeneity in scaffolds of this type (O'Brien, Harley, et al., 2004). **Figure 2.14** shows the effect of freezing temperature on the scaffold mean pore size. Scaffolds fabricated at a final temperature of freezing of -40°C, -30°C, -20°C and -10°C were determined to have a mean pore size of 95.9 μm, 109.5 μm, 121.0 μm and 150.5 μm, respectively. One-way analysis of variance (ANOVA) showed the final temperature of freezing has a significant effect on the mean pore size ($p < 0.001$). Post-hoc testing between the four different scaffolds indicated that there was a significant difference in mean pore size between all groups ($p < 0.05$).

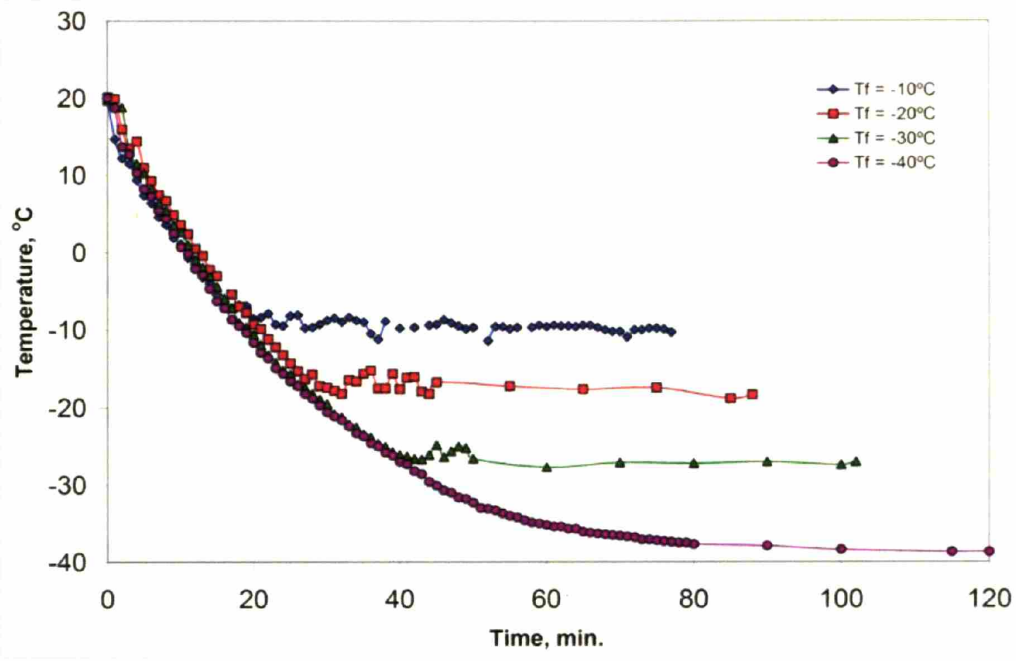

Fig. 2.13a

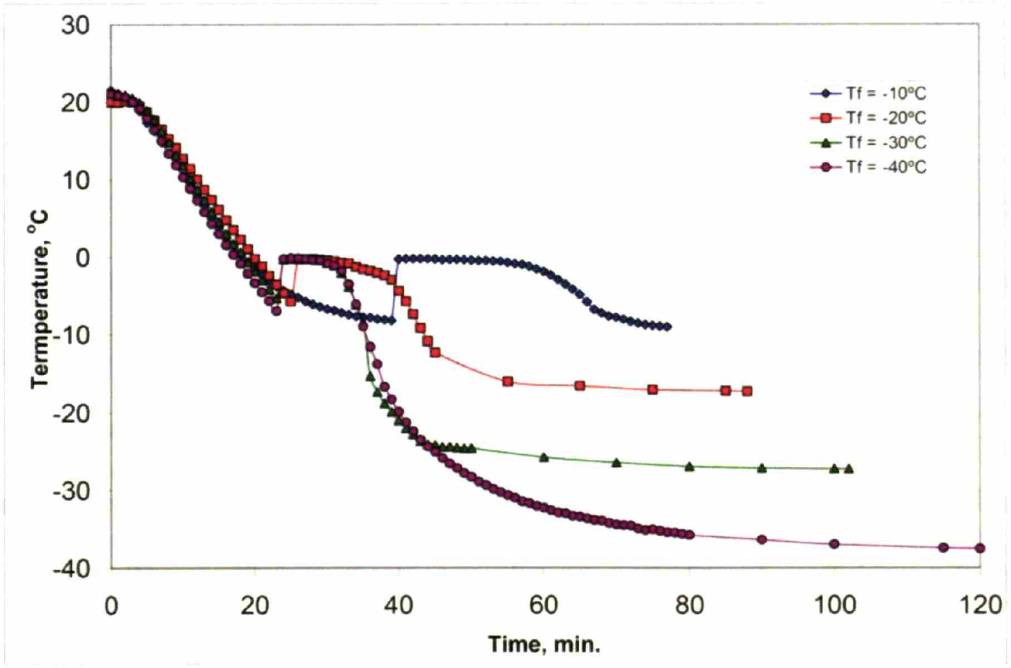

Fig. 2.13b

Figure 2.13. Average temperature of the freeze dryer shelf (Fig. 2.13a) and the CG suspension (Fig. 2.13b) during freezing for the four constant cooling rate freezing protocols.

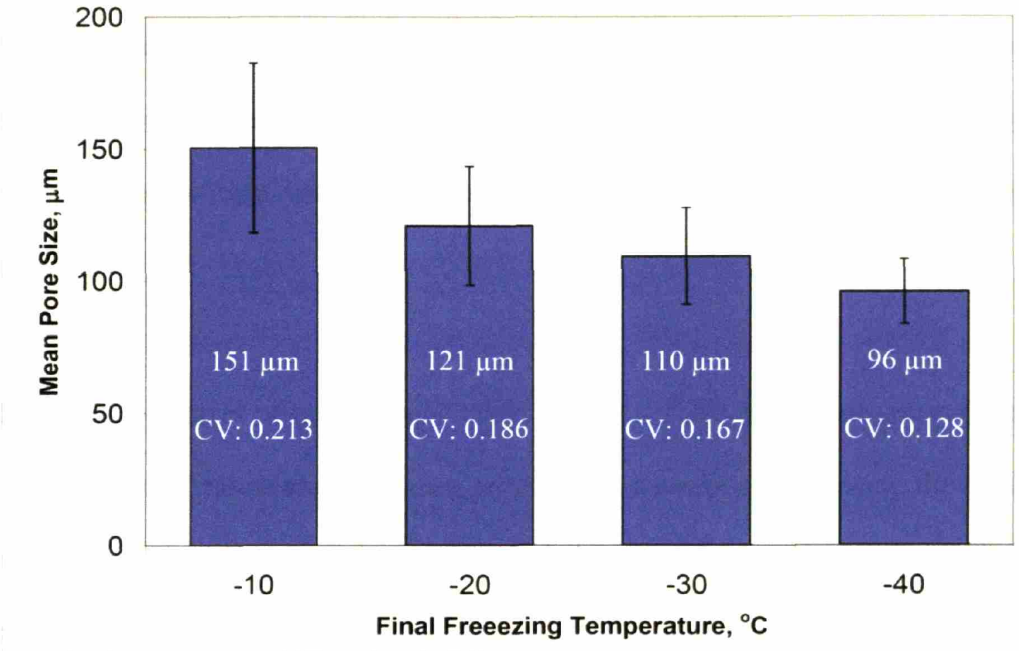

Figure 2.14. Effect of final freezing temperature on CG scaffold mean pore size. One-way analysis of variance (ANOVA) showed that final freezing temperature has a significant effect on the mean pore size ($p < 0.001$) of CG scaffolds produced using this freeze-drying technique.

Figure 2.14 also shows the results of a more detailed pore analysis of the four different CG scaffolds. The mean pore size of each scaffold was determined in both the longitudinal and transverse (cross-sectional) planes of the scaffold in order to estimate the three-dimensional geometry of the pores. In scaffolds produced at freezing temperatures of -40°C, -30°C, -20°C, no significant difference was found between the mean pore size in the transverse and longitudinal planes ($p > 0.05$). The coefficient of variance of mean pore size of scaffolds produced at final temperatures of freezing of -40°C, -30°C, and -20°C was 0.128, 0.167 and 0.186, respectively, indicating an equiaxed pore structure that has been previously reported for freezing to -40°C (O'Brien, Harley, et al., 2004). However, a significant difference in mean pore size of the longitudinal (163.9 ± 31.6 µm) and transverse (130.4 ± 20.6 µm) planes ($p < 0.05$) was observed

for CG scaffolds produced at a final temperature of freezing of -10°C. Consequently, scaffolds produced at this temperature, while having the largest mean pore size, were found to have the largest coefficient of variance (0.213). All four scaffold variants had a homogeneous pore structure, with no significant variation in mean pore size, shape, or alignment throughout the scaffold ($p > 0.05$).

Figure 2.15 shows a series of micrographs taken from scaffolds fabricated using different final freezing temperatures. The increase in mean pore size as a result of increasing the final freezing temperature is clearly evident. Pores were observed to be largely equiaxed with no obvious local alignment of pore channel axes.

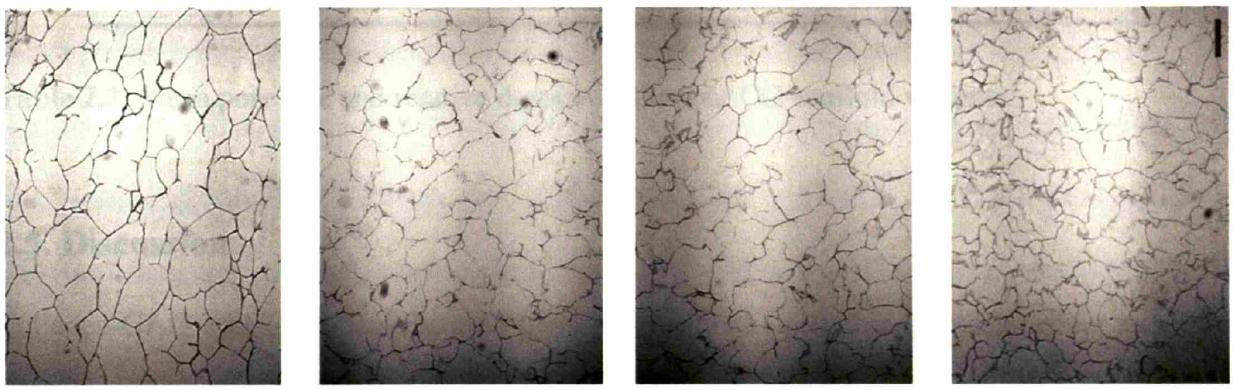

Figure 2.15. Light micrographs (transverse plane) of CG scaffolds fabricated at four distinct final freezing temperatures. Scaffolds fabricated at a lower final freezing temperature exhibit a smaller mean pore size. Scale bar = 100 μm.

The relative density (ρ^*/ρ_s) of the four CG scaffold variants was determined using the measured dry density (ρ^*) of the collagen scaffold sheets and the known dry density of solid collagen (ρ_s, 1.3 g/cm^3) (Yannas and Tobolsky, 1967; Yannas, Burke, et al., 1980). The dry density of the

collagen scaffolds was determined by measuring the dimensions of each sheet of scaffold using a micrometer (Mitutoyo, Japan) and the mass of the scaffold sheet using an analytical balance (Model CP124S, Sartorius, Germany). Results of microstructural analysis (mean pore size, relative density) of the four CG scaffold variants are presented in **Table 2.2.** No statistically significant difference in scaffold relative density was observed ($p > 0.05$), as would be expected since all scaffold variants were fabricated from a constant CG suspension.

T_f, °C	Mean Pore Size, μm Mean ± StDev	Relative Density, ρ^*/ρ_s Mean ± StDev
-10	151 ± 32	0.0062 ± 0.0005
-20	121 ± 23	0.0061 ± 0.0003
-30	110 ± 18	0.0059 ± 0.0003
-40	96 ± 12	0.0058 ± 0.0003

Table 2.2. Mean pore size and relative density of the four CG scaffold variants.

2.5. Discussion

Collagen-GAG scaffolds manufactured using the original (quenching) freeze-drying technique (Yannas, Lee, et al., 1989) show a characteristic heterogeneous pore structure with a large variation in average pore diameter at different locations and orientations (in and out of plane) in each sheet of scaffold. Control of the rate of cooling during fabrication and the use of smaller, less warped stainless steel pans significantly improved the structural characteristics of the scaffold: a more homogeneous microstructure with less variation in mean pore size throughout the scaffold and no difference in mean pore size between the transverse and longitudinal planes was observed.

The structure of the CG scaffold is controlled by the final freezing temperature and the heat transfer processes associated with freezing. Additionally, the direction of heat transfer and the speed of heat transfer influence the shape of ice crystals; the existence of a predominant direction of heat transfer leads to the formation of columnar ice crystals with the major axis aligned in the predominant direction of heat transfer (Loree, Yannas, et al., 1989; Chang, Yannas, et al., 1990; Chang and Yannas, 1992; Schoof, Apel, et al., 2001). Creation of a scaffold with an equiaxed pore structure requires removing predominant direction of heat transfer from the freezing process. Utilizing a solidification profile (constant cooling rate technique) that results in more homogeneous heat transfer (**Figure 2.7**) has allowed fabrication of a series of CG scaffolds with a homogeneous microstructure characterized by equiaxed pores.

When the quenching fabrication technique was used in conjunction with the larger, more warped, stainless steel molds to produce CG scaffolds, 'hot spots' were created throughout the scaffold due to areas of pan-shelf discontinuity. When these areas were included in the analysis of the pore structure, a significantly larger mean pore size with a significantly larger co-efficient of variance was found (Mean: 149.6 μm, CV: 0.275) than when the areas were avoided (Mean: 132.4 μm, CV: 0.185), validating previous studies where these areas were avoided (Freyman, Yannas, et al., 2001). Comparatively, CG scaffolds produced using the smaller molds (12.5 x 12.5 cm) showed no visual evidence of 'hot spots' to the naked eye. While a smaller mean pore size and lower coefficient of variance (CV: 0.173) was observed with the scaffolds produced in the smaller pans using the quenching technique, the improvements were not significantly improved ($p > 0.05$) compared to selection of the "best" areas from scaffolds produced in large pans with the quenching technique.

As a second component of this study, a comparison was made between the quenching process and a series of constant cooling rate freezing protocols. Three distinct constant cooling rates were tested by cooling the freeze dryer from 20°C to -40°C over 65, 90, or 115 minutes, corresponding to average slurry freezing rates of 0.9, 0.7, and 0.6°C/min, respectively. The scaffolds produced using the constant cooling rate technique were observed to have a more homogeneous pore structure than those produced using the quenching technique (**Figure 2.9**). This result parallels the finding that the quenching process gives rise to a wide variation in suspension temperature throughout the pan during freezing, while the constant cooling rate process produces virtually identical suspension temperatures throughout the pan during freezing.

Scaffolds produced using a constant cooling rate of 0.9°C/min were found to have the most homogeneous structure with the lowest coefficient of variance in pore size (0.128) and the smallest difference in pore size between the longitudinal and transverse planes in the scaffold. This freezing protocol also exhibited the greatest level of temperature uniformity during freezing (**Figure 2.7**). A series of scaffolds were manufactured at this constant cooling rate (0.9°C/min) in order to establish the reproducibility of this protocol. The scaffold pore size was found to be consistent from sheet to sheet, the coefficient of variance was found to be consistently smaller than under previous processing conditions, and no 'hotspots' were found in any of the scaffolds manufactured with a constant cooling rate of 0.9°C/min. These results suggest that the constant cooling rate technique establishes a more uniform temperature distribution throughout the suspension during freezing, resulting in consistent ice crystal nucleation and growth and a more uniform final scaffold structure.

Figure 2.11 shows an in-depth comparison of the pore size distribution in two scaffold types: a scaffold fabricated using the quenching technique and a scaffold fabricated using a constant cooling rate of 0.9°C/min. CG scaffolds produced using the constant cooling rate technique (0.9°C/min) showed significantly smaller variation in pore size throughout the scaffold and no variation in mean intercept length between the longitudinal and transverse planes while the scaffold manufactured using the quenching protocol had a considerably larger variation in pore size throughout the scaffold and in the longitudinal and transverse planes. These results suggest that there is reduced variation in pore size throughout the scaffold along with an equiaxed pore structure when the scaffold is manufactured using the constant cooling rate technique (0.9°C/min). ESEM micrographs of the scaffold pore structure (**Figure 2.8**) further support this conclusion; in the scaffold produced using the constant cooling rate technique, the collagen fibers (struts) are randomly arranged around approximately equiaxed pores while in the scaffold produced using the original quenching technique, there are roughly parallel planes of collagen membranes separated by thin collagen struts.

Overall, the pores produced using the new technique appear to be more equiaxed unlike the elongated pores in scaffolds produced using the quenching technique. Additionally, while pore orientation in scaffolds fabricated using the quenching technique in large pans (original technique) was observed to be grossly random, pore alignment was observed locally, indicating areas of directional heat transfer. However, the pore structure of the CG scaffolds produced using the constant cooling rate technique was observed to be equiaxed with no local or global alignment of pores, indicating the effects of local heat transfer phenomena were removed from the fabrication process (**Figures 2.8, 2.9, 2,12**).

The formation of individual ice crystals within a liquid medium is influenced by the nucleation of ice crystals and the rate of diffusion associated with the liquid, both of which are mediated by the final freezing temperature. Increasing the undercooling temperature while maintaining a constant cooling rate has been observed to decrease the mean pore size of the resultant CG scaffold without increasing scaffold microstructural heterogeneity (**Figure 2.14**). The four different final freezing temperatures (-40°C, -30°C, -20°C and -10°C) produced four distinct scaffolds with distinct mean pore sizes (96, 110, 121, 151 μm, respectively) and a constant relative density (0.006) (**Table 2.2**). Each scaffold exhibited a homogeneous pore microstructure and showed no obvious variation in mean pore size, structure, or alignment at distinct regions within the scaffold.

For scaffolds produced at freezing temperatures of -40°C, -30°C and -20°, no significant variation in mean intercept length was found between the longitudinal and transverse planes showing that the pores formed in these scaffolds were uniform in shape as well as in size, *i.e.* scaffolds with an equiaxed pore structure were produced. However scaffolds produced at a freezing temperature of -10°C were found to have a significant variation in mean pore size between the longitudinal and transverse planes ($p < 0.05$), suggesting that at this higher freezing temperature, columnar ice crystals are formed rather than the more equiaxed ice crystals that form at the lower temperatures of freezing. This result parallels previous studies that have shown that the direction and speed of heat transfer during freezing influence the shape of ice crystals, and suggests that the elongated ice crystals were formed due to a predominant direction of heat transfer during the freezing process (Hobbs, 1974; Kurz and Fisher, 1989; Loree, Yannas, et al., 1989; Chang and Yannas, 1992).

2.6. Conclusions

This investigation has shown that uniform CG scaffolds with an equiaxed pore structure can be produced via lyophilization with the use of a constant cooling rate technique rather than a quenching technique to freeze the CG suspension prior to sublimation. The constant cooling technique establishes a more uniform suspension temperature throughout the pan during the freezing process compared to the quenching technique, where the constant cooling rate that produced the most uniform temperature distribution also produced the most uniform scaffold structure. The most uniform scaffolds displayed approximately equiaxed pores, with no significant pore size variation throughout the scaffold. A standard series of CG scaffolds with constant relative density and a homogeneous pore microstructure has been fabricated using the constant cooling technique solidifying the CG suspension to four different final freezing temperatures, resulting in scaffolds with mean pore sizes ranging between 96 and 151 μm.

These microstructurally homogeneous CG scaffold variants can now be utilized for quantitative, *in vitro* studies of cell motility and contraction in ECM analogs where the extracellular environment is known. To further describe the fabrication of CG scaffold via lyophilization, a quantitative treatment of the mechanisms that influence CG suspension solidification, including development of predictive thermal models relating CG suspension processing conditions (cooling rate, T_f), will be discussed in Chapter 3. Further characterization of the specific surface area, permeability, and mechanical characteristics of these CG scaffolds, along with cellular solids modeling tools that can appropriately describe these scaffold variants will be discussed in Chapters 4 and 5. Finally, Chapter 6 will describe the results of a series of *in vitro* experiments

studying cell behavior (motility, contraction) in a series of these CG scaffold variants, where the independent effects of CG scaffold microstructural and mechanical properties were studied.

Chapter Reference

This chapter has been adapted from the following publications:

F.J. O'Brien, B.A. Harley, I.V. Yannas, and L.J. Gibson, "Influence of freezing-rate on pore structure in freeze-dried collagen-GAG scaffolds," *Biomaterials*, 25(6):1077-1086, 2004.

F.J. O'Brien, B.A. Harley, I.V. Yannas, and L.J. Gibson, "The effect of pore size and structure on cell adhesion in collagen-GAG scaffolds," *Biomaterials*, 26(4):433-441, 2005.

CHAPTER 3. *Coarsening-Mediated Solidification is Responsible for Defining the Pore Microstructure of Collagen-GAG Scaffolds: Experimental and Thermal Modeling Results*

3.1. Introduction

A number of critical microstructural criteria for the design of bioactive scaffolds have been previously introduced. In this chapter, we return to consideration of the scaffold mean pore size and structural homogeneity: the mean pore diameter must be large enough for cells (typically 5 – 30 μm in size) to migrate through the pores and small enough to retain a critical total surface area for appropriate cell binding. Typical pore sizes of biologically active scaffolds range from twenty to a few hundred micrometers, where scaffold mean pore size has been observed to significantly affect cell behavior within the scaffold and overall scaffold bioactivity (Yannas, Lee, et al., 1989; Yannas, 2001; O'Brien, Harley, et al., 2005). To allow for transport of cells and metabolites the scaffold must also have a high specific surface and large pore volume fraction (generally greater than 90%) as well as an interconnected pore network (Yannas, 2001). In the design and use of collagen-glycosaminoglycan (CG) scaffolds (**Figure 3.1**), the structural

features of the scaffold were required to be adjusted to provide the correct structural environment for the cells, tissues, and processes under investigation (Yannas, Lee, et al., 1989; Chang and Yannas, 1992; Harley, Spilker, et al., 2004; O'Brien, Harley, et al., 2005).

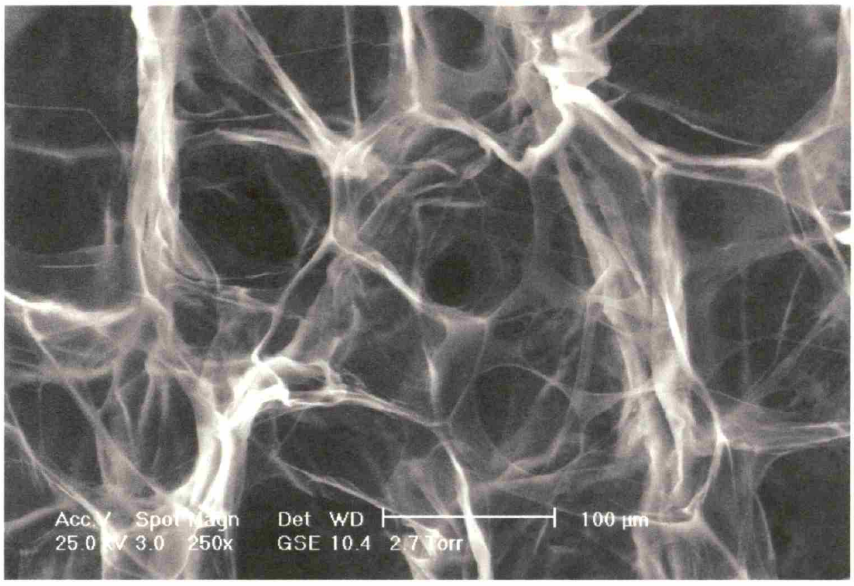

Figure 3.1. SEM image of collagen-GAG (CG) scaffold, mean pore size ~95 µm, 99.4% porosity (Pek, Spector, et al., 2004).

As previously described, CG scaffolds are primarily manufactured via freeze-drying, (Yannas, 2001), and the modeling the solidification kinetics during this process is the focus of this investigation. Briefly, an aqueous suspension of collagen and glycosaminoglycan fibers that are precipitated in acetic acid is solidified (frozen) in a freeze dryer, localizing the CG co-precipitate between the growing ice crystals that likely nucleate on the collagen-GAG fiber content within the suspension. Once complete, the solidification process produces a continuous, interpenetrating network of ice crystals surrounded by fibers of collagen and GAG (Hobbs, 1974; Kurz and Fisher, 1989). Sublimation removes the ice crystals, leaving a highly porous scaffold structure where the scaffold microstructure is defined by the ice crystals formed during solidification

(**Figure 2.1**). Suspension solidification is therefore responsible for the creation of a scaffold-ice preform, where the size and shape of the ice crystals within the scaffold-ice preform define the final pore microstructure of the sublimated scaffolds.

These CG scaffolds typically possess extremely high pore volume fractions (>95%) and exhibit an open-cell pore structure. The pore volume fraction and the size of the pores have been modified by altering the volume fraction of the precipitate in the suspension and by the underlying freezing processes (O'Brien, Harley, et al., 2004; O'Brien, Harley, et al., 2005; Harley, Hastings, et al., 2006). Scaffold heterogeneity has been previously implicated in the inferior performance of some scaffold materials (Zeltinger, Sherwood, et al., 2001; Hollister, Maddox, et al., 2002) so it is of critical importance to be able to fabricate homogeneous scaffolds with a defined and reproducible microstructure (*i.e.*, mean pore size, shape). Therefore, an improved understanding of the CG suspension solidification process and the effect of different thermal processing conditions on the final scaffold microstructure will be an important step for the design of future bioactive scaffolds. Mathematical models of the solidification process can guide the selection of processing variables and conditions (*i.e.*, solidification rate, undercooling temperature) to produce the desired CG scaffold microstructure.

The motivation for this study is the result of previous investigations focused on identifying improved processing conditions to produce a series of CG scaffolds characterized by a homogeneous microstructure and equiaxed pores with distinct mean pore sizes described in Chapter 2 (O'Brien, Harley, et al., 2004; O'Brien, Harley, et al., 2005). The traditional thermal processing conditions were modified to produce this series of uniform CG scaffolds (O'Brien,

Harley, et al., 2004) with pore sizes ranging from 96 – 151 μm (O'Brien, Harley, et al., 2005), and have provided information suitable for the development of thermal models of the solidification process responsible for defining the structural organization of the scaffold-ice preform.

The rapid cooling associated with the quenching thermal processing (**Figure 2.2**) produced spatially and temporally variable heat transfer, resulting in non-uniform solidification and significant scaffold heterogeneity. The processing change from the quenched to the constant cooling rate technique (**Figure 2.3**) was motivated by the observed solidification heterogeneities due to the quenching process and work in the literature describing the development of processing techniques to produce metals with equiaxed grains (Flemings, 1974). Equiaxed grains are produced during casting by controlled and homogeneous coarsening: increased coarsening time led to larger metal grains and uniform thermal conditions led to a more equiaxed grain structure throughout the casting (Flemings, 1974). Implementation of the constant cooling rate thermal processing conditions resulted in creation of equiaxed ice crystals within the scaffold-ice preform following suspension solidification and the resultant fabrication of an homogeneous CG scaffold microstructure with equiaxed pores following sublimation (O'Brien, Harley, et al., 2004).

By altering the degree of undercooling, uniform scaffolds with equiaxed pores of different mean pore size (96 – 151 μm) have been fabricated in a reproducible manner (**Table 3.1**) (O'Brien, Harley, et al., 2005). However, a wider range of pore sizes along with an improvement in scaffold uniformity is necessary for future experiments studying cell-scaffold interactions. A quantitative treatment of the solidification process can also guide the fabrication of future

scaffolds with novel microstructures in a predictive manner without the trial-and-error procedure traditionally employed (O'Brien, Harley, et al., 2004). Development of a quantitative treatment of the salient mechanisms of CG suspension solidification is the focus of this investigation. While the freeze-drying process for fabricating CG scaffolds is composed of two distinct processes, solidification and sublimation, suspension solidification is the focus of this investigation. Solidification is responsible for defining the size, shape and distribution of ice crystals in the scaffold-ice preform and hence the pore structure of the scaffold.

T_f, °C	Mean Pore Size, μm	Relative Density
-10	151 ± 32	0.0062 ± 0.0005
-20	121 ± 23	0.0061 ± 0.0003
-30	110 ±18	0.0059 ± 0.0003
-40	96 ± 12	0.0058 ± 0.0003

Table 3.1. Mean pore size and relative densities of CG scaffolds fabricated at different final freezing temperatures (Mean ± StDev).

3.2. Fabrication of collagen-glycosaminoglycan scaffolds via lyophilization

3.2.1. Preparation of the collagen-glycosaminoglycan (CG) co-polymer suspension

A complete description of CG suspension production is provided in Section 2.3.1 of this thesis. The CG suspension was produced by combining microfibrillar, type I collagen (0.5 wt%) isolated from bovine tendon (Integra LifeSciences, Plainsboro, NJ) and chondroitin-6-sulfate (0.044 wt%) isolated from shark cartilage (Sigma-Aldrich Chemical Co., St. Louis, MO) in a pH 3.2 solution of 0.05M acetic acid (0.3% v/v glacial acetic acid) in distilled water. The collagen, chondroitin 6-sulfate, and acetic acid were mixed in an overhead blender at a constant temperature of 4°C to prevent collagen denaturation. The CG suspension was then degassed

under vacuum (15 Pa) to remove air bubbles introduced by mixing (Yannas, Lee, et al., 1989; O'Brien, Harley, et al., 2004).

3.2.2. Fabrication of CG scaffold with different pore sizes

The CG suspension was frozen using the previously described constant cooling rate technique (Sections 2.3.4, 2.3.5) (O'Brien, Harley, et al., 2004; O'Brien, Harley, et al., 2005). The CG slurry was poured into a 304 stainless steel mold (12.5 x 12.5 cm) (VirTis, Co., Gardiner, NY) that was then placed into the chamber of a freeze dryer (Genesis, VirTis) at room temperature (20°C). The freeze dryer shelf was manufactured using the same 304 stainless steel and the temperature of the shelf is actively maintained by pumping cooled refrigerant (silicone oil) through the hollow shelf. The temperature of the chamber is cooled by cooling coils surrounding the chamber, but is not maintained as accurately as the shelf: the temperature of the shelf is maintained at the desired set-level during solidification while the chamber atmosphere is slightly warmer than the shelf. The temperature of the freeze dryer shelf was cooled at a constant rate (1.4°C/min) to the final freezing temperature (T_f); the shelf temperature was then held constant for 60 minutes at T_f to maintain a constant level of undercooling and ensure completion of the solidification process.

The ice phase was then sublimated under vacuum (15 – 30 Pa) at 0°C for a period of 17 hours to produce the porous CG scaffolds (O'Brien, Harley, et al., 2004; O'Brien, Harley, et al., 2005). Final freezing temperatures of -10°C, -20°C, -30°C and -40°C were used to produce porous scaffolds of four different measured mean pore sizes (151, 121, 110, 96 μm, respectively) (**Table 3.1**) (O'Brien, Harley, et al., 2004; O'Brien, Harley, et al., 2005).

3.2.3. Thermal conditions during CG scaffold fabrication

The temperature of the CG suspension and the freeze dryer shelf was monitored throughout the solidification process at one minute intervals at two locations in the suspension using a two-channel microprocessor thermocouple (HH22, Omega Engineering, Stamford, CT). Two thermocouple elements (Type K Thermocouple, Omega Engineering) were placed approximately 10 cm apart along a diagonal between the opposite corners of the mold. Thermal profiles of both the freeze dryer shelf and the CG suspension were recorded throughout solidification.

Regardless of final freezing temperature, the temperature of the freeze dryer shelf followed an identical thermal profile until the appropriate final freezing temperature was reached; once reaching T_f, the shelf temperature was then held constant until the suspension was completely solidified (**Figure 3.2a**). The temperature profiles of the CG suspension during solidification was found to be qualitatively similar for each of the four temperature ramping protocols (**Figure 3.2b**); CG suspension supercooling (~ -5°C) was observed prior to the onset of solidification, at which point the suspension temperature remained constant at ~0°C until the local solidification surrounding the thermocouple was completed. Once local solidification was complete, the scaffold-ice preform temperature cooled until it reached the final freezing temperature.

However the supercooling effect and overall temperature uniformity throughout the solidifying CG suspension that was observed with the constant cooling rate technique was not observed with the quenching technique (**Figure 3.3**).

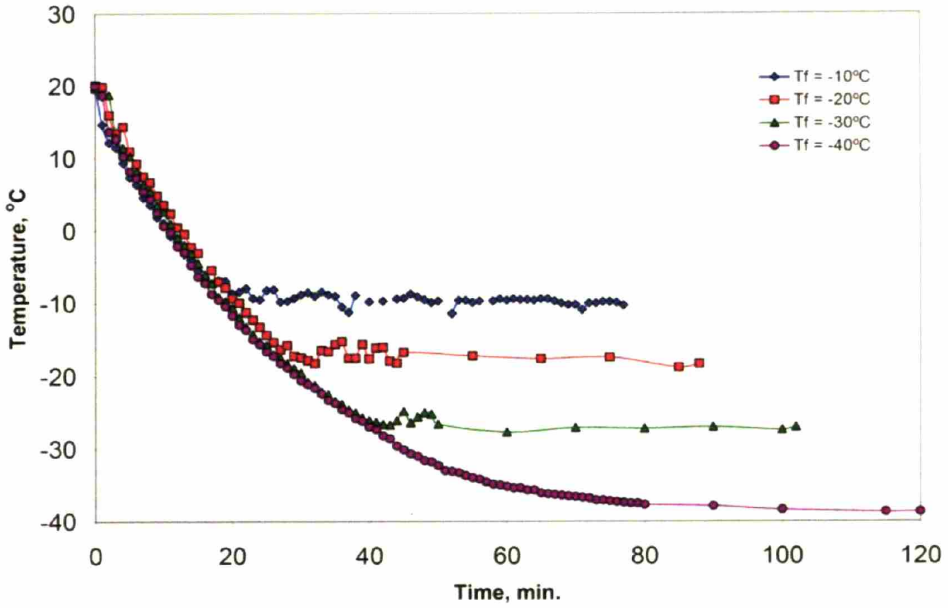

Fig. 3.2a

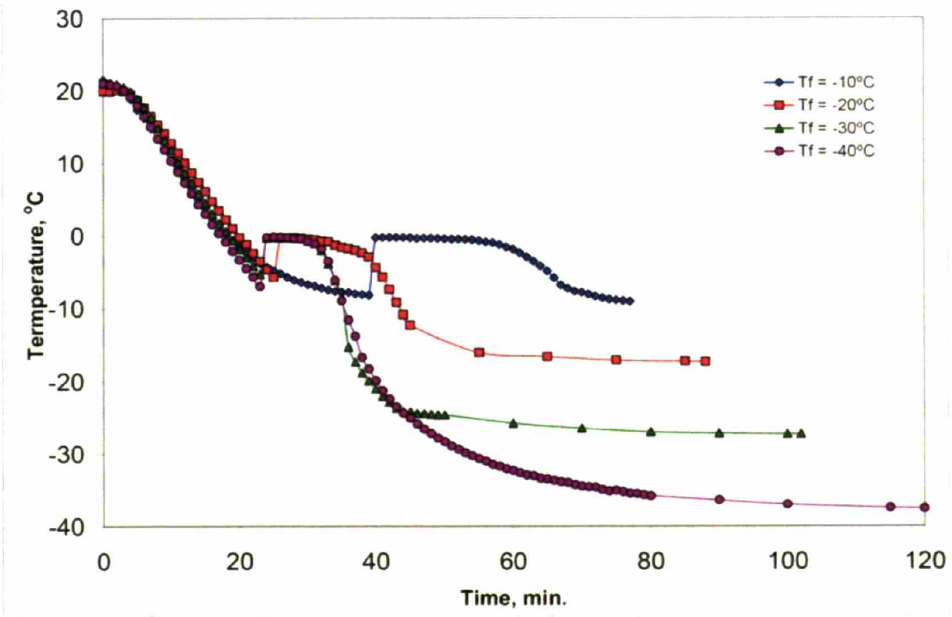

Fig. 3.2b

Figure 3.2. Average temperature of the freeze dryer shelf (Fig. 3.2a) and the CG suspension (Fig. 3.2b) during the four constant cooling rate freezing protocols.

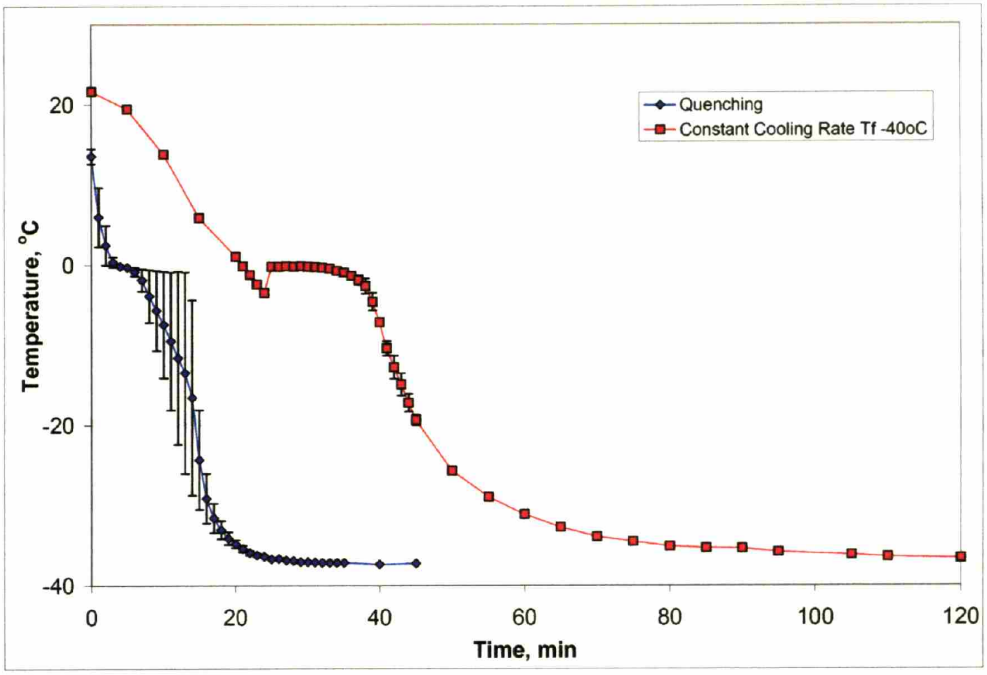

Figure 3.3. Average temperature of the CG suspension (Error bar: Half the difference between two temperature readings) during solidification for scaffolds fabricated using the quenching and constant cooling rate thermal processes.

The thermal conditions observed during the ramped solidification profiles (suspension supercooling followed by solidification at ~ 0°C) is characteristic of both a low Biot number system and a system where there aren't any significant thermal gradients in the solidifying suspension (Flemings, 1974). The low Biot Number and the homogeneous temperature profile observed throughout the CG suspension during solidification (O'Brien, Harley, et al., 2005), indicates that there is a high degree of nucleation taking place in an isothermal CG suspension, resulting in the formation of a homogeneous populations of equiaxed ice crystals of consistent size within the solidified scaffold-ice preform.

The observed homogeneous pore microstructure with equiaxed pores of the CG scaffolds created by the temperature ramping thermal processing conditions confirm the formation of equiaxed ice crystals within the scaffold ice preform. The spatially non-uniform temperature profiles and the lack of a supercooling effect in the solidifying CG suspension when the quenching thermal profile was utilized is indicative of the formation of columnar, dendritic ice crystal growth (Kurz and Fisher, 1989). Indeed, the pore microstructures of CG scaffold fabricated via quenching is heterogeneous, with widely variable mean pore sizes and areas of decidedly oriented pores (O'Brien, Harley, et al., 2005).

The average freezing rate (°C/min) of the suspension was determined between the starting temperature of the suspension and a pre-defined lower limit. A lower limit of 5°C greater than the final freezing temperature was established for this calculation; below this temperature the suspension and freeze dryer shelf temperatures tended to asymptotically approach the final freezing temperature and could not be modeled linearly. The local solidification time, the liquid-solid transition time for the local environment surrounding the thermocouple element, was measured as the time that the suspension temperature remained between 0°C and -2°C following the initial supercooling event required to initiate nucleation (**Figure 3.4**) (Michel, 1978).

As expected, the suspension cooled via quenching exhibited a significantly faster local solidification time when compared to those produced using the ramped freezing protocols. Additionally, the local solidification time was observed to increase for scaffolds fabricated using a warmer T_f, indicating that the suspension required a longer period of time to solidify when warmer processing conditions were used (**Table 3.2**) (O'Brien, Harley, et al., 2005).

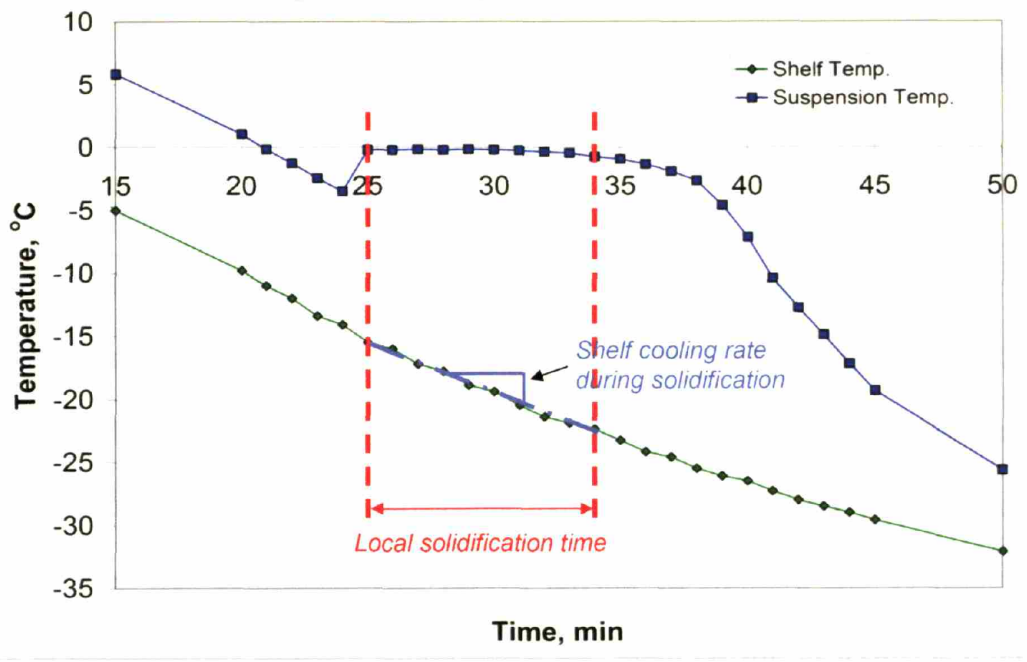

Figure 3.4. Local solidification time (t_s) and the shelf thermal profile ($T_O(t)$) during solidification. The region denoted "local solidification time" corresponds to time for solidification value given in **Table 3.2**. Regression of the shelf temperature over that region determined $T_O(t)$ (**Table 3.4**).

Freezing Condition	T_f, °C	Shelf Cooling Rate, °C/min	Average CG Suspension Freezing Rate, °C/min	Local Solidification Time, sec
Quenching	-40	n/a	4.1	120
Ramping	-40	1.4	0.9	480
Ramping	-30	1.4	0.9	510
Ramping	-20	1.4	0.9	660
Ramping	-10	1.4	0.9	1200

Table 3.2. Thermal processing conditions, average suspension freezing rate, and the solidification time for the CG suspension during processing.

3.3. Quantitative modeling of CG suspension solidification

A sequential series of models has been developed to quantitatively describe the solidification processes associated with CG scaffold fabrication. First, the dominant heat transfer processes responsible for suspension solidification were determined to guide selection of the most appropriate solidification model. A model of the bulk solidification process was then implemented to describe the local solidification time of the CG suspension based upon the predominant mode of heat transfer, processing conditions, and the physical parameters of the system. Finally, a coarsening model, predicting the final ice crystal size based upon the local solidification time was developed. This model, relying on ripening and coarsening models developed to quantitatively describe solidification and grain growth in metals and alloys, is a predictive model of CG scaffold mean pore size based upon freezing conditions.

A table of all the relevant constants and experimental parameters required for the remainder of the analysis has been compiled (**Table 3.3**). Parameters of the CG suspension are denoted with a prime (*i.e.*, k_t', C_p') while parameters of the mold are not (*i.e.*, k_t, C_p). For this analysis, the material properties of the mold were those of bulk 304 stainless steel while the CG suspension was approximated by water, an approximation made because the CG suspension is only 0.5% w/w solid (collagen and GAG) and only 0.3% v/v acetic acid in distilled water.

3.3.1. Predominant heat transfer process responsible for solidification

In order to properly model the freezing process associated with fabricating porous CG scaffolds, it is necessary to determine the predominant mode(s) of heat transfer during solidification. The three modes considered in this analysis were conduction through the bottom of the mold (18

gauge, 304 stainless steel pan) into the freeze dryer shelf (304 stainless steel), conduction through the sides of the mold (18 gauge, 304 stainless steel pan) into the freeze dryer chamber atmosphere, and convection from the CG suspension into the chamber atmosphere (**Figure 3.5**).

Parameter	Description	Value
T_{suspen}	Mean temperature of CG suspension during freezing	T_{suspen}, ^oC
T_f	Final freezing temperature of freeze dryer	^oC
T_{shelf}	Temperature of freeze dryer shelf during freezing	T_{shelf}, ^oC
T_{air}	Temperature of freeze dryer chamber during freezing	T_{air}, ^oC
l	Length of mold	0.127 m
w	Width of mold	0.127 m
Δx	Mold thickness (18 ga. Stainless steel)	0.00127m
M_S	Depth of CG suspension in mold	0.00335 m
A	Area of bottom face of mold (0.127 m x 0.127 m)	0.016129 m^2
V	Volume of CG suspension in mold ($V = M \times A$)	5.6 x 10-5 m^3
T_M	Temperature of CG suspension as solidification commences	0°C
T_O	Temperature of mold during solidification	-40°C
T_S	Temperature of suspension at mold-suspension interface	*variable*
ρ'	Density of ice (solidified water)	918 kgm^{-3}
ρ'_l	Density of water	1000 kgm^{-3}
C_p'	Specific heat of ice	2000 $Jkg^{-1}K^{-1}$
k'	Thermal conductivity of ice	2.4 $Wm^{-1}K^{-1}$
α'	Constant; $\alpha' = k'/(\rho' C_p')$	1 x 10^{-6}
H_f	Heat of fusion due to solidification	334,000 Jkg^{-1}
k	Thermal conductivity of 304 stainless steel	20.0 $Wm^{-1}K^{-1}$
ρ	Density of 304 stainless steel	8060 kgm^{-3}
C_p	Specific heat of 304 stainless steel	503 $Jkg^{-1}K^{-1}$
h	Heat transfer coefficient of CG suspension (water)	100 $Wm^{-2}K^{-1}$
h_{air}	Convective heat transfer coefficient into still air	2 – 100 $Wm^{-2}K^{-1}$
d	Mean pore size	*variable*
d_o	Initial nucleate size	*variable*
t	Time	*variable*
t_c	Local solidification time = local coarsening time	*variable*
M	Location of liquid-solid interface during solidification	*variable*
$C_{p,l}$	Specific heat of water	4230 $Jkg^{-1}K^{-1}$

Table 3.3. Relevant parameters for modeling CG suspension solidification time with quenching.

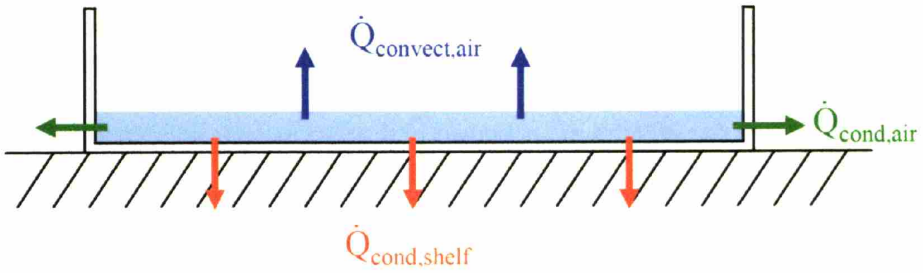

Figure 3.5. Schematic of the three modes of heat transfer during the freezing process: conduction through the pan into the freeze dryer shelf (orange), conduction through the pan into the chamber atmosphere (green), or convection into the chamber atmosphere (blue).

An order of magnitude description of the system was first constructed to identify the predominant modes of heat transfer. Heat transfer out the sides of the mold can be neglected compared to heat transfer out the mold bottom due to significant difference in scale between the thickness of the suspension (3.5 mm) and the surface area of the suspension in the mold (125 x 125 mm) and because there are no chill plates on the sides of the mold. The interface heat transfer coefficient at the top surface of the CG suspension/scaffold-ice preform is assumed small compared with that at the chilled bottom of the mold (Poirier and Geiger, 1994), and so heat transfer from the top surface should be neglected. The heat transfer during solidification through the mold bottom (conduction-mediated), through the mold sides (conduction-mediated), and from the top surface of the CG suspension/scaffold-ice preform (convection-mediated) was then calculated to confirm these conclusions.

Conduction through the mold bottom:

Equation 3.1. $$\dot{Q}_{cond,pan} = k \cdot A \cdot \frac{\Delta T}{\Delta x} = k \cdot l \cdot w \cdot \frac{T_{suspen} - T_{shelf}}{\Delta x}$$

Conduction through the mold side:

Equation 3.2. $$\dot{Q}_{cond,panside} = k \cdot A \cdot \frac{\Delta T}{\Delta x} = k \cdot 2 \cdot \left(l \cdot M_s + w \cdot M_s\right) \cdot \frac{T_{suspen} - T_{air}}{\Delta x}$$

Convection into the chamber atmosphere:

Equation 3.3. $$\dot{Q}_{convect} = h \cdot A \cdot \left(T_{suspen} - T_{shelf}\right) = h \cdot l \cdot w \cdot \left(T_{suspen} - T_{shelf}\right)$$

The temperature of the freeze dryer shelf is actively and accurately controlled while the temperature of the freeze dryer chamber atmosphere is always warmer than the shelf during the freezing process. As such (T_{suspen} - T_{shelf}) > (T_{suspen} – T_{air}) during processing. Keeping the temperature terms as variables in the equations describing heat transfer, the equations describing the rate of heat transfer (**Eq. 3.1 – 3.3**) have been simplified. Conduction though the mold bottom (254 $WK^{-1} \cdot \Delta T$) occurs at a rate an order of magnitude greater than conduction through the mold sides (28 $WK^{-1} \cdot \Delta T$) and at a rate of two orders of magnitude greater than convection into the chamber atmosphere (1.6 $WK^{-1} \cdot \Delta T$). Consideration of the difference between T_{shelf} and T_{air} would only magnify this discrepancy between conduction through the bottom of the pan and the remaining modes of heat transfer. For the remainder of the analysis presented in this report, convection and conduction through the sides of the mold was neglected, and unidirectional heat flow through the bottom of the mold was assumed to be the predominant mode of heat transfer during solidification.

3.3.2. Biot number and interface resistance

An appropriate thermal model to describe the mold characteristics and solidification conditions needs to be implemented to describe the CG suspension solidification. A model incorporating a conductive pan will be utilized in this analysis because the mold and freeze dryer shelf are made from stainless steel; however, whether or not interface resistance needs to be incorporated to appropriately model CG suspension solidification needs to be determined (Poirier and Geiger, 1994). The Biot number (*Bi*) of the CG suspension-mold system was used to determine whether interface resistance (between the solidified suspension and the mold surfaces) should be included in the analysis. The thermal profile observed within the solidifying scaffold-ice preform suggested a low *Bi* (Section 2.3). To confirm this observation, *Bi* was calculated:

Equation 3.4. $$Bi = \frac{h \cdot \Delta x}{k}$$

For the CG suspension-mold system, Bi = 6.4 x 10^{-3} << 1, confirming the conclusion made from the thermal profile of the CG suspension during solidification and additionally indicating that thermal resistance within the solidifying CG suspension is negligible and that significant interface resistance is present at the boundary between the solidifying suspension and the mold. This suggests that a model describing the solidification of the CG suspension must incorporate a conductive mold and interface resistance.

3.3.3. Model of CG suspension solidification in a conductive mold with interface resistance

Previous thermal models have been developed to describe solidification in a conductive mold with interface resistance using a constant temperature cooling source (Poirier and Geiger, 1994). However, in order to accurately describe the process of solidification exhibited during the

temperature ramping protocols, a conductive mold with interface resistance model that takes into account the variable temperature of the shelf and mold (Shelf, mold temperature = T_O = $T(t)$) during solidification has been implemented. The heat leaving the suspension through the mold and freeze dryer shelf is modulated via the heat transfer coefficient (h); the relative temperatures of the CG suspension (T_M), the scaffold-ice preform content forming within the suspension (T_S), and the mold ($T_O(t)$) are predicted by the low value for the Bi: $T_M > T_S >> T_O(t)$ (**Figure 3.6**).

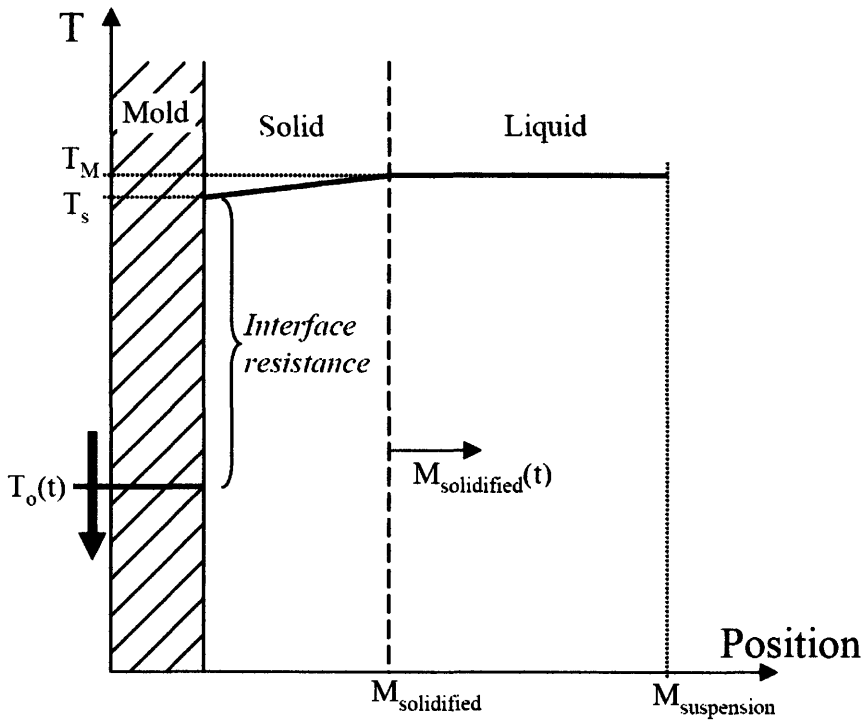

Figure 3.6. Temperature distribution in the mold (pan, freeze dryer shelf, $To(t)$) and the CG suspension during solidification via the temperature ramping protocol in a conductive mold with interface resistance.

To appropriately model solidification, a description of the temperature of the mold/freeze dryer shelf during the critical period of suspension solidification was determined ($T_O(t)$). To do this, a regression was performed on the experimentally measured temperature of the freeze dryer shelf

during the period where solidification is taking place (**Figure 3.4**) to determine $T_O(t)$ (**Table 3.4**). A first order polynomial regression was used to describe the temperature of the freeze dryer shelf for T_f = -30, -40°C; however, because solidification takes longer for the cases where a higher final freezing temperature was utilized, a second order polynomial regression was used to describe the temperature of the freeze dryer shelf for T_f = -10, -20°C.

T_f, °C	$T_O(t)$, °C
-10	$T_O(t) = 6x10^{-7}(°Csec^{-2})\cdot t^2 - 0.001(°Csec^{-1})\cdot t - 9.3344°C$
-20	$T_O(t) = 9x10^{-8}(°Csec^{-2})\cdot t^2 - 0.0002(°Csec^{-1})\cdot t - 16.605°C$
-30	$T_O(t) = -0.0128(°Csec^{-1})\cdot t - 15.15°C$
-40	$T_O(t) = -0.0125(°Csec^{-1})\cdot t - 15.804°C$

Table 3.4. Temperature of the freeze dryer shelf ($T_O(t)$, **Fig. 3.4**) during CG suspension solidification.

With a quantitative description of the freeze dryer shelf and mold temperature during solidification, the conductive mold model with interface resistance was implemented including $T_O(t)$. The heat flux at the suspension-mold interface can be determined in terms of the thermal conductivity and heat transfer coefficient of the suspension:

Equation 3.5. $$q\big|_{x=0} = k' \cdot \frac{T_M - T_S}{M}$$

Equation 3.6. $$q\big|_{x=0} = h \cdot \left(T_S - T_O(t)\right)$$

Combining these two terms (**Eq. 3.5, 3.6**) allows the total heat flux from the suspension to be described by equating the heat flux at the suspension-mold interface and the solid-liquid interface:

Equation 3.7. $$q\big|_{x=0} = q\big|_{x=M_S} = \frac{T_M - T_O(t)}{1/h + M/k'}$$

The latent heat evolved at the solid-liquid interface (x = M(t)) can be described as:

Equation 3.8. $$q\big|_{x=M_S} = \rho' \cdot H_f \cdot \frac{dM}{dT}$$

These two relations (**Eq. 3.7, 3.8**) were then equated because heat transfer through the liquid-solid interface must equal heat transfer through the solid-mold interface during solidification:

Equation 3.9. $$\rho' \cdot H_f \cdot \frac{\partial M}{\partial t} = \frac{T_M - T_O(t)}{1/h + M/k'}$$

Solving the differential equation (**Eq. 3.9**), a relationship between the depth of solidification (*M*), freeze dryer shelf and mold temperature ($T_O(t)$), and solidification time (t_c) can be determined:

Equation 3.10. $$\int_0^{t_c} \left(\frac{h}{\rho' \cdot H_f} \cdot [T_M - T_O(t)] \right) \partial t = \int_0^{M} \left(1 + \frac{h \cdot M}{k'} \right) \partial M$$

Assuming the boundary condition that M = 0 at t = 0 (the suspension is completely unsolidified at the start of the model simulation):

Equation 3.11.

$$\frac{h}{\rho' \cdot H_f} \cdot \int_0^{t_c} \left(T_M - T_O(t)\right) \partial t = M + \frac{h \cdot M^2}{2 \cdot k'}$$

Using the material property and shelf temperature information necessary for the CG suspension and each of the four distinct temperature ramping processes (**Tables 3.2, 3.4**), the local solidification time (t_c) for each of the thermal profiles was calculated using **Eq. 3.11**. The calculated solidification times correlated excellently with the experimental observations (**Figure 3.7**), suggesting that the implemented conductive mold with interface resistance model properly describes the macro-scale process of CG suspension solidification, and that this model (**Eq. 3.11**) can be utilized to predict the local solidification time for a new series of thermal profiles for fabrication of CG scaffolds.

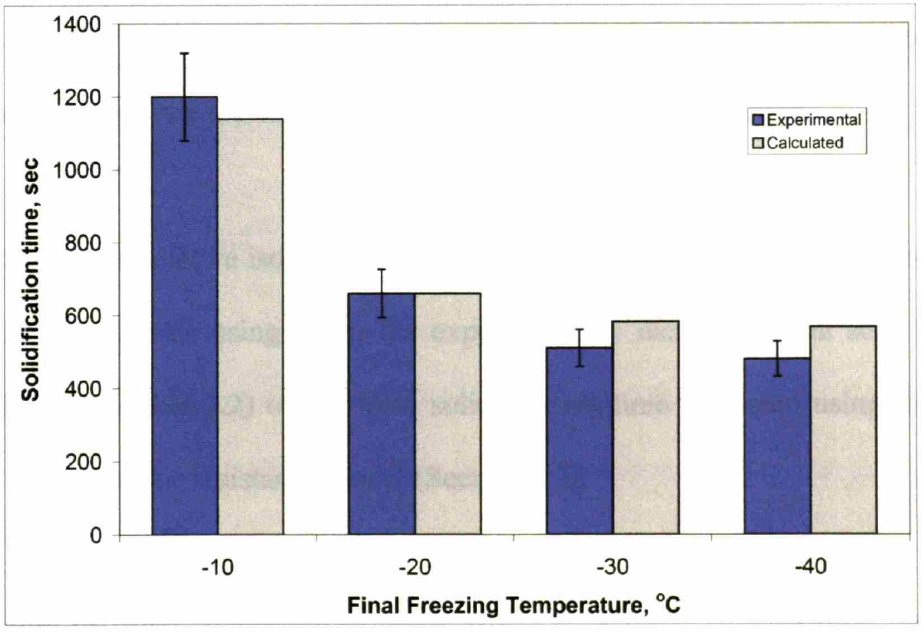

Figure 3.7. Experimentally observed vs. calculated (via conductive mold with interface resistance model) CG suspension solidification times.

3.3.4. Predictive isothermal coarsening model to describe scaffold mean pore size

Solidification of the bulk suspension relies on three major components: nucleation, crystallite growth, and coarsening. During solidification, nucleation commences at a degree of supercooling specific to each liquid suspension. Increasing the undercooling increases both the nucleation rate and growth rate of the crystallites. However, it is the effect of coarsening that most significantly influences the final crystallite size, as the final crystallite structure in the solidified bulk is much coarser than the initial structure of nucleation sites within the melt (Flemings, 1974). Due to coarsening, the initial spacing of nucleation points within the melt (liquid phase) has little influence on the structure of the final casting (scaffold-ice preform in this system); a description of ice crystal coarsening can therefore likely be used to describe the final size distribution of ice crystals within the scaffold-ice preform. The remainder of this work describes:

1. Determining whether isothermal coarsening effects are predominantly responsible for the difference in mean scaffold pore size created in CG scaffolds fabricated using the constant cooling rate technique to distinct final freezing temperatures.

2. Creation of a predictive isothermal coarsening model to describe the final mean pore size of the CG scaffolds using either the experimentally measured local solidification time (Section 2.3, **Table 3.2**) or the local solidification time predicted using the conductive mold with interface resistance model (Section 3.3).

The applicability of using coarsening to describe CG suspension solidification was first tested via a basic ripening model that relates the final ice crystal size to the local solidification (or coarsening) time. In this model, d is the final crystallite size after coarsening, d_o is the initial

crystallite size before coarsening, A is a system constant, and t_c is the local coarsening time (the local solidification time of the CG suspension, **Table 3.2**).

Equation 3.12. $$d^3 - d_o^{\,3} = A \cdot t_c$$

The initial ice crystal size (immediately after nucleation) was neglected for these calculations because the coarsened crystallite (d) is typically orders of magnitude larger than the initial crystallite size (d_o), a size difference only magnified by the cubic relationship, resulting in a simplified ripening equation:

Equation 3.13. $$d^3 \approx A \cdot t_c$$

The appropriateness of this ripening model was determined via regression between the experimentally measured scaffold mean pore size (d) and local solidification times (t_c) (**Table 3.1, 3.2**) to determine the exponent (n) and goodness of fit (R^2) for the ripening relation:

Equation 3.14. $$d^n \approx A \cdot t_c$$

Experimental results of this regression are shown in **Figure 3.8**. An exponent of 2.3 and a high degree of correlation (R^2 = 0.9354) was observed between scaffold pore size and the local solidification time. The good correlation between the experimentally measured and coarsening model predicted exponent, n, strongly suggests that ice crystal coarsening processes are responsible for determining CG scaffold pore microstructure (Flemings, 1974).

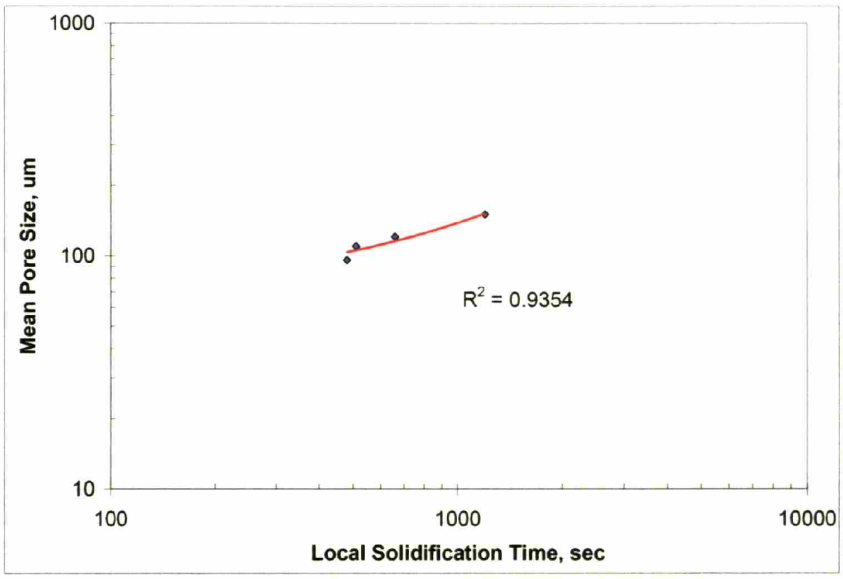

Figure 3.8. Relationship between the measured local solidification time and the scaffold mean pore size for CG scaffold system.

This simplified ripening relationship can be implemented to predict the scaffold mean pore size based on processing conditions once a series of experimental data points are determined. However, in order to develop an independent, predictive model to describe CG scaffold fabrication, we implemented an isothermal coarsening model to predict scaffold mean pore size based upon suspension solidification conditions. The same relation between solidification time and coarsened ice crystal size exists using the isothermal coarsening model, whereas the cooling rate increases, less time is available for coarsening, and the final solidified bulk displays smaller crystallites. In addition, however, the isothermal coarsening model describes the material constants that define the system constant (A) that was unknown in the ripening relationship. The isothermal coarsening model utilized here is based upon the work of Flemings (Flemings, 1974):

Equation 3.15.
$$t_c \approx \frac{\rho_s \cdot H_f \cdot C_L \cdot (1-k) \cdot m_L}{\sigma \cdot D_L \cdot T_L} \cdot d^3 = A' \cdot d^3$$

This model relates the crystallite arm spacing (CG scaffold mean pore size, d), and the coarsening time (local solidification time, t_c) via a system constant A'. Here, the constant A' is inversely proportional to the constant A utilized in the initial ripening model ($A' = 1/A$), but can be calculated based on system conditions. The system conditions required for calculating A' and the calculated A' are listed in **Table 3.5.**

Variable	Description	CG Suspension
ρ_s	Density of solid	918 $kg \cdot m^{-3}$
H_f	Heat of fusion for solidification	334,000 $J \cdot kg^{-1}$
C_L	Weight fraction of solute	0.6%
k	Assumed solidus slope	0.3
m_L	Assumed liquidus slope	3°C/%
σ	Liq.-solid surface energy	0.033 $J \cdot m^{-2}$
D_L	Diffusion coefficient	2.5×10^{-9} $m^2 \cdot s^{-1}$
T_L	Equilibrium liquidus temperature	273 K
A'	Constant of proportionality	1.715×10^{14} $s \cdot m^{-3}$

Table 3.5. CG suspension material properties and constant of proportionality (A') for the calculation of scaffold mean pore size (d) using the isothermal coarsening model (Flemings, 1974; Poirier and Geiger, 1994).

Using the value of A' calculated for the CG suspension (1.715×10^{14} $s \cdot m^{-3}$), the isothermal coarsening model was implemented to predict scaffold mean pore size. To do so, the isothermal coarsening model relationship for the CG suspension system was plotted against the observed local solidification time and mean pore size for each of the four ramped processing conditions (**Figure 3.9**). The observed relationship was strikingly similar to that observed for a classic example of isothermal coarsening: Al-Cu(4.5%) (**Figure 3.9**) (Flemings, 1974).

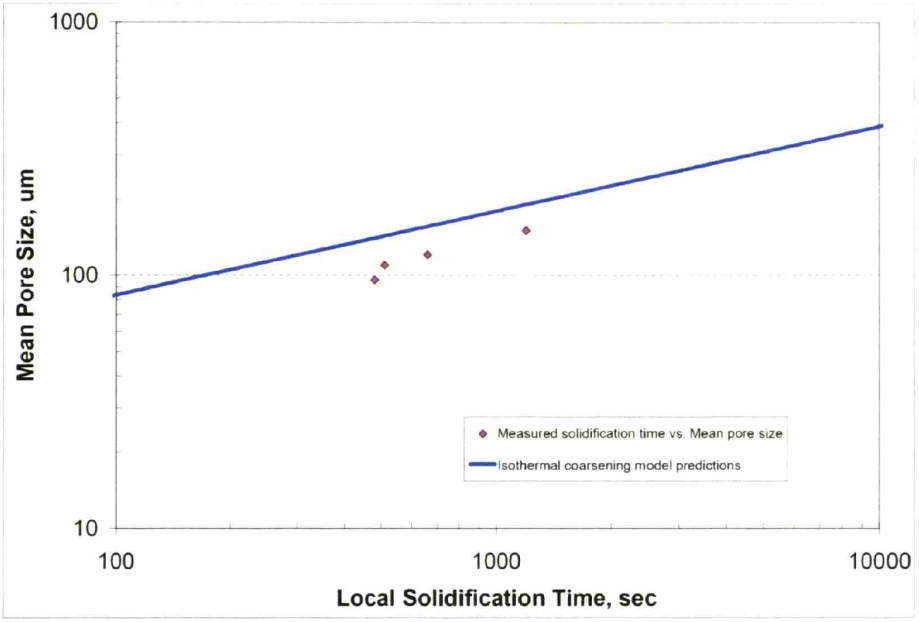

Fig. 3.9a

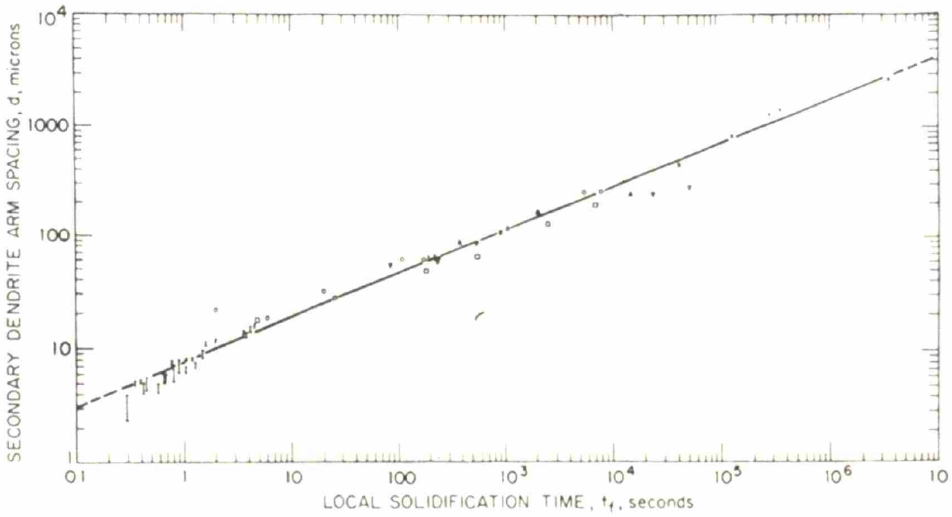

Fig. 3.9b

Figure 3.9. Comparison between measured local solidification time and scaffold mean pore size and prediction made using the isothermal coarsening model (**Eq. 3.15**, solid line) (Fig. 3.9a). Relationship between local solidification time and mean dendrite arm spacing (size) in Al-Cu(4.5%) (**Eq. 3.15**, solid line) (Fig. 3.9b).

Excellent agreement was observed between the isothermal coarsening model, calculated strictly from the properties of the CG suspension, and the observed CG scaffold variants. Good

agreement was also observed between the isothermal coarsening model predicted mean pore size regardless of whether the experimentally observed solidification time or the calculated solidification time (via the previously described conductive mold with interface resistance model) was used. These results indicate that the isothermal coarsening model provides an appropriate description of the CG suspension solidification during scaffold fabrication and when coupled with the conductive mold with interface resistance model provides a methodology to predict scaffold mean pore size based upon thermal processing conditions.

3.4. Discussion and Conclusions

In-depth analysis of the CG suspension solidification process has improved our understanding of the kinetics and relevant mechanisms responsible for defining the architecture of the scaffold-ice preform during solidification and the resultant CG scaffold microstructure following sublimation. The preliminary figure describing the relevant pressure and temperature profiles of the constant cooling rate technique (**Figure 2.3**) can now be more substantially described, including the temperature and pressure of the freeze dryer shelf, the corresponding thermal profile of the CG suspension, and the periods of ice crystal nucleation (*i*), coarsening (*ii – iii*), and sublimation (*iv – v*) during CG scaffold fabrication (**Figure 3.10**).

Two thermal models have been developed to describe the solidification process related to the fabrication of CG scaffolds via lyophilization. The predominant mode of heat transfer during scaffold fabrication was found to be conduction from the CG suspension into the freeze dryer shelf. The first model, describing CG scaffold processing as a conduction-mediated process in a conductive mold with interface resistance and a ramped mold temperature (**Eq. 3.11**), accurately predicts the CG suspension solidification time based upon processing conditions.

An isothermal coarsening model (**Eq. 3.15**) was then implemented that accurately predicts CG suspension ice crystal size (and hence scaffold mean pore size) based upon the local solidification time of the suspension (either experimentally measured or predicted using the first model).

These models correctly describe the observed phenomena that decreasing the final freezing temperature while maintaining a constant freezing rate leads to more rapid solidification, reduced coarsening time, and a smaller mean pore size (Harley and Flemings, In preparation, 2006). This thermal model has since been applied in the fabrication of a new series of collagen-based scaffolds for bone tissue engineering, where fabrication of a scaffold with significantly larger mean pore sizes (400 – 500 μm vs. 96 - 150 μm) were required; by significantly slowing the freezing rate of the system and lengthening the local solidification time, the desired scaffold microstructure was obtained (Harley, Lynn, et al., In preparation, 2006). These models provide valuable insight for manufacture of future scaffolds through predictive modeling of the effects of changes in the fabrication process such as the thickness of the suspension in the mold, the solid content of the suspension, the freezing rate and final freezing temperature, the mold material properties, and the use of nucleation agents.

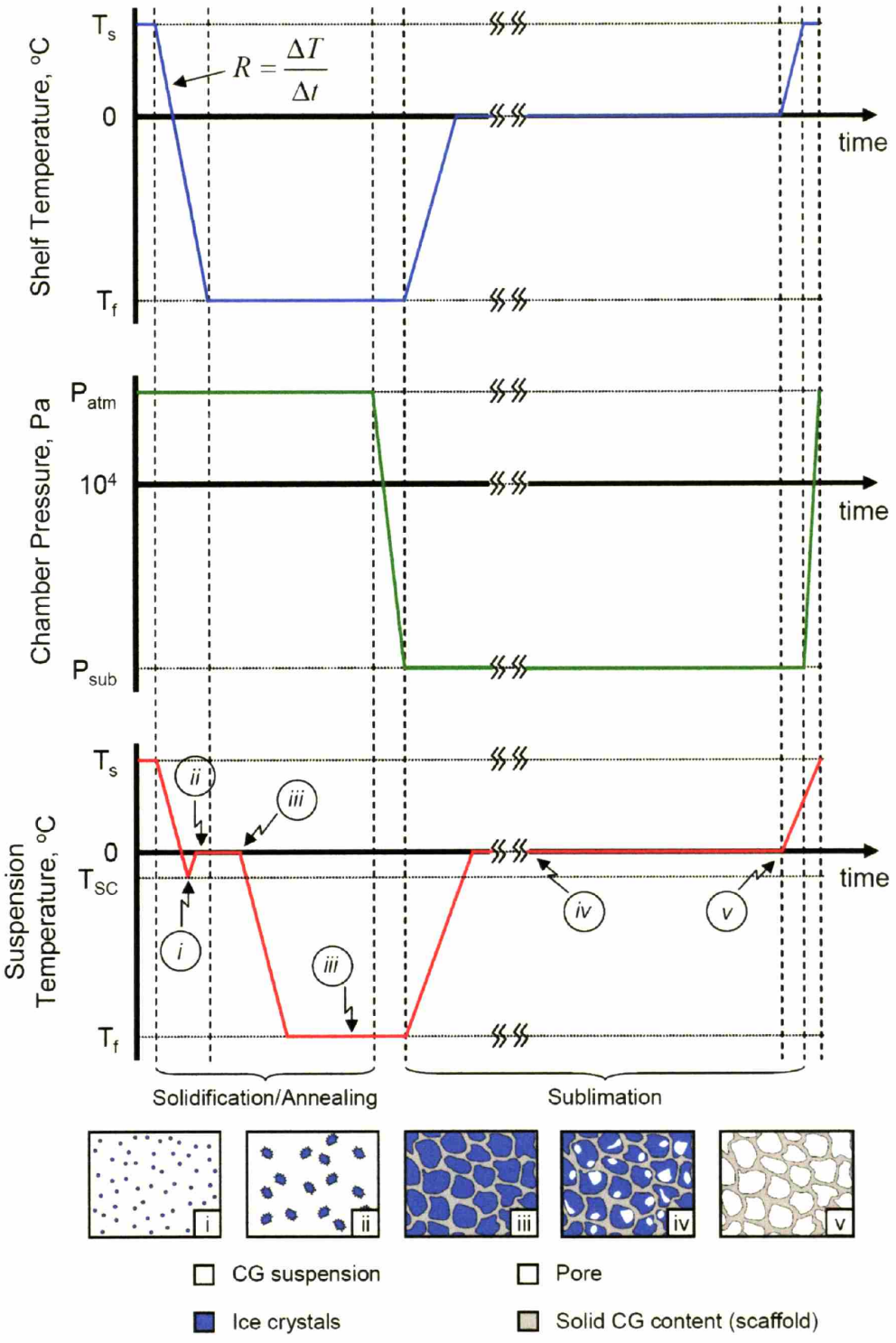

Figure 3.10. Thermal and pressure profiles of CG scaffold fabrication via constant cooling rate technique. Freeze dryer temperature and pressure profiles, CG suspension thermal profile, and relevant period of ice crystal nucleation (*i*), coarsening (*ii* – *iii*), and sublimation (*iv* – *v*).

Chapter Reference

This chapter has been adapted from the following publications:

F.J. O'Brien, B.A. Harley, I.V. Yannas, and L.J. Gibson, "Influence of freezing-rate on pore structure in freeze-dried collagen-GAG scaffolds," *Biomaterials*, 25(6):1077-1086, 2004.

F.J. O'Brien, B.A. Harley, I.V. Yannas, and L.J. Gibson, "The effect of pore size and structure on cell adhesion in collagen-GAG scaffolds," *Biomaterials*, 26(4):433-441, 2005.

B.A. Harley and M.C. Flemings, "Coarsening-mediated solidification is responsible for defining the pore microstructure of collagen-glycosaminoglycan scaffolds: Experimental and thermal modeling results," *In preparation*, 2006.

CHAPTER 4. *Cellular Solids Modeling of Collagen-GAG Scaffolds: Specific Surface Area, Permeability, and Mechanics*

4.1. Introduction

The goal of tissue engineering is to develop cell, construct, and living system technologies to restore the microstructure as well as functional mechanical properties of damaged or degenerated tissue. Tissue engineering relies extensively on the use of porous scaffolds to provide the appropriate microstructural, mechanical, and compositional environment to induce regeneration of injured tissues and organs. Scaffolds are typically seeded with cells and occasionally growth factors and are then either cultured *in vitro* to study cell behavior and tissue synthesis processes or are implanted in various anatomical sites to induce regeneration of damaged tissues or organs. The structurally isotropic CG scaffold variants with mean pore sizes ranging between 96 and 151 μm, whose fabrication and microstructural characterization were described in Chapter 3, provide a series of standardized, three-dimensional substrates for a variety of other tissue engineering assays. In this chapter, the specific surface area and permeability under differential levels of compressive stain of these substrates will be experimentally measured. Additionally, the structural homologies between these CG scaffolds and low-density, open-cell foams provide the

motivation for the development of cellular solids models to mathematically describe the mechanics, specific surface area, and permeability of these scaffolds. Successful development of such cellular solids models would significantly improve the fundamental understanding of the extracellular environment presented to cells within these scaffolds.

Of the four structural requirements for the development of bioactive collagen scaffolds previously described in Chapter 2 (abolishment of the collagen fiber periodic banding, chemical composition, mean pore size, degradation rate), the existence of upper and lower bounds of the mean pore size (Yannas, Lee, et al., 1989) was the initial motivation for the study of the specific surface area of CG scaffolds. It has been hypothesized that the pores need to be large enough to allow cells to migrate into the structure, where they eventually become bound to ligands expressed on the scaffold, but small enough to establish a sufficiently high specific surface for a minimal ligand density required for efficient binding of a critical number of cells to the scaffold (Yannas, 2001). A preliminary test of the hypothesis that the extent of cell binding is controlled by the mean pore size of the scaffold was attempted in this study. The density of bound cells was determined as a function of scaffold mean pore size and specific surface area where the scaffold structure was varied systematically.

While cell-scaffold attachment appears to play a critical role during *in vivo* synthesis of organs (induced regeneration), it has also been used as a measure of cell viability for *in vitro* studies (Assoian and Zhu, 1997; Howe, Aplin, et al., 1998; Luan and Diekwisch, 2002). Pore structure has been observed to significantly affect cell binding and migration *in vitro* and influence the rate and depth of cellular in-growth *in vitro* and *in vivo* (Wake, Patrick, et al., 1994; van Tienen,

Heijkants, et al., 2002). Cell adhesion and activity have been observed to vary considerably with cell type, scaffold composition, and pore size (Chvapil, 1977; Doillon, Whyne, et al., 1986; Tsuruga, Takita, et al., 1996); additionally, scaffold mean pore size significantly influences cell morphology and phenotypic expression (LiVecchi, Tombes, et al., 1994; Nehrer, Breinan, et al., 1997; Kuberka, von Heimburg, et al., 2002). In porous silicon nitride scaffolds, endothelial cells bind preferentially to scaffolds with pores smaller than 80 μm while fibroblasts preferentially bind to larger pores (>90 μm). In poly-L-lactic acid (PLLA) scaffolds, vascular smooth muscle cells preferentially bind to one range of pore sizes (63 - 150 μm) while fibroblasts bind to a wider range (38 - 150 μm) (Zeltinger, Sherwood, et al., 2001; Salem, Stevens, et al., 2002). A number of cell types exhibit a preference for binding to scaffolds with pore sizes significantly larger than the characteristic cell size, often utilizing a characteristic bridging mechanism where adjacent cells act as support structures to assist bridging large pores; examples include fibrovascular tissue in-growth into PLLA scaffolds, osteoblast adhesion to polylactide-co-glycolide (PLAGA) scaffolds, and rat marrow cells binding to poly(ethylene oxide terephthalate)/poly(butylene terephthalate) (PEOT/PBT) scaffolds (Wake, Patrick, et al., 1994; Borden, El-Amin, et al., 2003; Claase, Grijpma, et al., 2003). Based upon the scaffold design rules and a series of experiments, it is assumed that there is an optimal pore size for each specific tissue engineering application. While a multitude of variables may significantly affect overall scaffold bioactivity, it is hypothesized that the specific surface area influences the initial bioactivity of the scaffold by defining the total ligand density available for cells to bind to.

However, in order to maintain scaffold bioactivity, it is important to metabolically support the cells within the construct. The permeability of biological tissues and tissue-engineered scaffolds

plays a significant role in the nutrient and waste transport within the structure. There are two mechanisms available for transport of metabolites to and waste products from cells in a scaffold: diffusion, and with *in vivo* applications, transport through capillary networks formed in the scaffold via angiogenesis. While angiogenesis becomes the limiting factor *in vivo*, significant angiogenesis is not observed for the first few days after implantation, and is not present at all *in vitro*. Fluid flow, and therefore permeability, provides the means to transport nutrients to, and waste away from, cells. The permeability of, and fluid mobility through porous materials are two intrinsic properties describing the relative ease that fluids can flow through cellular materials such as most tissue engineering scaffolds, and the permeability of a scaffold plays a significant role in defining its bioactivity. In addition, as a result of the increasing complexity of *in vitro* bioreactors and the physiological loading conditions scaffolds typically experience *in vivo*, understanding scaffold permeability in the context of significant applied strains is also important.

Permeability (k, units of m^2) is the single-phase fluid conductivity of a porous material and is an intrinsic and quantitative parameter describing the scaffold structure independent of sample size and the fluid used. Scaffold permeability is defined by a combination of five important parameters: (1) porosity, (2) pore size and distribution, (3) pore interconnectivity (or tortuosity), (4) fenestration (pore interconnection) size and distribution, and (5) pore orientation. The fluid mobility (K, units of m^4/Ns) of a scaffold is another intrinsic property defining fluid flow through a porous material and is defined as the material permeability normalized by the viscosity of the fluid (μ, units of Pa·s):

Equation 4.1. $$K = \frac{k}{\mu}$$

In the tissue engineering literature describing characterization of a variety of biological materials and three-dimensional constructs such as gels and scaffolds, both the fluid mobility (K) through and permeability (k) of tissues and scaffolds are reported and are equally appropriate. While permeability and fluid mobility are often used interchangeably, the units of the reported values easily distinguish them (Permeability: m^2; Fluid mobility: m^4/Ns). In order to quickly compare the mobility and permeability of many tissue engineering constructs and biological tissues, the viscosity of water can be used (0.001 Pa·s).

The influence of fluid flow has been studied in a number of tissues including bone (Knothe-Tate and Knothe, 2000), tumor tissue (Netti, Berk, et al., 2000; Znati, Rosenstein, et al., 2003) and cartilage (Mansour and Mow, 1976). The permeability of articular cartilage is of interest because of the fluid mechanics of joint lubrication (Mansour and Mow, 1976) and nutrient transport (Maroudas and Bullough, 1968; Maroudas, Bullough, et al., 1968) of osteoarthritis. These studies have reported that the permeability of cartilage tissue ranges from 0.1 to 2 $x10^{-15}$ m^4/Ns (~0.1 to 2 $x10^{-18}$ m^2) and that cartilage permeability is dependent on the composition, organizational depth (Maroudas, 1968), and the mechanical loading of the sample (Mansour and Mow, 1976). It has been shown that cartilage permeability decreases with increasing tissue depth as far as the calcified layer. This decrease has been correlated with an increase in proteoglycans and to a lesser extent an increase in collagen content. Scaffold and tissue permeability also influences cyclical changes in biophysical stimuli due to fluid flow through the structure during mechanical loading. Specifically, permeability affects the magnitude of pressure and fluid shear stresses within the construct or tissue, both of which have been identified as potential stimuli for cellular differentiation or functional adaptation (Hillsley and Frangos, 1994; Owan, Burr, et al., 1997;

Prendergast, Huiskes, et al., 1997). Construct permeability has also been shown to influence the degradation rate of biodegradable scaffolds for tissue engineering (Agrawal, McKinney, et al., 2000).

The permeability of a scaffold is determined by a combination of microstructural factors including percent porosity, pore size, geometry, and distribution, as well as pore interconnectivity, fenestration size, and the orientation of pores with respect to flow direction (Li, De Wijn, et al., 2003). Additionally, construct chemical composition can influence permeability. Different biological compounds such as glycosaminoglycans (*i.e.*, hyaluronate or chondroitin sulfate) and collagen (Levick, 1987) have been shown to affect the permeability of many different tissues. The salt:polymer ratio of synthetic polymer scaffold systems significantly affects its permeability (Agrawal, McKinney, et al., 2000). **Table 4.1** shows experimentally measured values of permeability of a series of different tissue engineering scaffolds. Method 1 refers to direct measurement of construct permeability while method 2 refers to indirect measurement of construct permeability. The direct method applies a known pressure to the material, measures the flow rate, and calculates permeability according to Darcy's law. The indirect method applies mechanical load to the material, and curve-fits the reaction force vs. time curve to a theoretical model.

However, despite this previous research, very little data exists describing the permeability of natural polymer scaffolds. Ramanujan *et al.* (Ramanujan, Pluen, et al., 2002) determined the permeability of type I collagen gels in the context of transport within tumor tissue. These collagen gels were prepared from 1 - 4.5% weight/volume solutions and polymerized by

incubation; gel permeability ranged from 1 x 10^{-15} to 10^{-16} m^2 (~0.1 to 1 x 10^{-12} m^4/Ns). The permeability of a polyacrylamide (carbohydrate) gel (1.8 - 3% weight/volume) has also been reported, ranging from 0.004 to 0.013 x 10^{-12} m^2 (~0.4 to 1.3 x 10^{-11} m^4/Ns) (Grattoni, Al-Sharji, et al., 2001).

Ceramic and composite scaffolds

Material	Porosity	Method	Permeability
Ceramic and composite scaffolds			
Z-BCP; D-BCP; I-BCP (Li, De Wijn, et al., 2003)	75%; 74%; 54%	1	0.01 – 0.35 x 10^{-9} m^2
Coral; HA-CAM; HA-50 (Li, De Wijn, et al., 2003)	---	1	0.05 – 0.35 x 10^{-9} m^2
Corraline hydroxyapatite (Haddock, Debes, et al., 1999)	---	1	1.7 – 8.6 x 10^{-10} m^2
Synthetic polymer scaffolds			
PGA-PLLA (Beatty, Ojha, et al., 2002)	77%	2	1.77 ± 0.99 x 10^{-15} m^4/Ns
PLA/PGA (Spain, Agrawal, et al., 1998)	51 – 71%	1	1.82 ± 3.65 x 10^{-9} m^4/Ns
PLA/PGA (Agrawal, McKinney, et al., 2000) (salt:polymer 3.5-14:1)	80 – 92%	1	2 – 16.1 x 10^{-9} m^4/Ns
Natural polymer scaffolds			
Collagen gel (Ramanujan, Pluen, et al., 2002)	1 – 4.5% w/v	1	1 x 10^{-15} - 1 x 10^{-16} m^2
SIS (Beatty, Ojha, et al., 2002)	---	2	17.09 ± 8.95 x 10^{-15} m^4/Ns
Polyacrylamide gel (Grattoni, Al-Sharji, et al., 2001)	1.8 – 3% w/v	1	0.004 – 0.0013 x 10^{-12} m^2

Table 4.1. Permeability of a variety of tissue engineering scaffolds as reported in the literature.

Beatty *et al.* (Beatty, Ojha, et al., 2002) measured the permeability of small-intestinal submucosa (SIS), a decellularized, natural extracellular matrix derived from the intestinal lining of pigs that is used as a regeneration template for heart valves. SIS scaffold permeability, measured indirectly, was estimated to be 17 x 10^{-15} m^4/Ns (~17 x 10^{-18} m^2). Agrawal *et al.* (Agrawal,

McKinney, et al., 2000) measured the permeability of 50:50 PLGA scaffold systems and found that permeability ranged from 2 to 16 x 10^{-9} m^4/Ns (~2 to 16 x 10^{-12} m^2), and was dependent on the polymer:salt ratio. The permeability and porosity of these PLGA scaffolds was compared over time as the scaffold degraded; changes in permeability and porosity were not found to be similar suggesting a more substantial model of permeability is needed. Spain *et al.* (Spain, Agrawal, et al., 1998) also characterized the permeability of PLGA constructs and reported similar values. While there are studies characterizing the permeability characteristics of specific synthetic and natural three-dimensional constructs and biological tissues, there is little in the literature to suggest a systematic framework to describe construct permeability. Additionally, the effects of compressive strain on scaffold permeability is an important feature to characterize because many tissue engineering constructs are utilized in load-bearing applications that can significantly influence both construct permeability and the resulting metabolite diffusion.

The objective of this study was to experimentally characterize and mathematically model scaffold specific surface area as a function of pore size and scaffold permeability/fluid mobility as a function of pore size and compressive strain of the four CG scaffold variants with homogeneous pore microstructure and pore sizes ranging between 96 and 151 μm. The initial attachment of MC3T3 cells to the CG scaffolds was used as a proxy variable to measure the relative specific surface area of the CG scaffolds. The MC3T3 cell line was chosen to study the viability of an osteoblast-like cell in CG scaffolds for potential orthopedic applications (Kodama, Amagai, et al., 1981). The fluid mobility of saline solution through the CG scaffold variants under distinct levels of compressive strain was measured via Darcy's law. Scaffold permeability is hypothesized to be inversely proportional to its specific surface area due to the frictional

effects of fluid flow by the struts that define the scaffold microstructure. The resultant cellular solids models are capable of quantitatively describing the permeability and specific surface area characteristics of a variety of scaffold microstructures in terms of scaffold mean pore size, relative density, and applied strain. For the remainder of this study the permeability characteristics of the CG scaffold system will be described in terms of its fluid mobility (units m^4/Ns) for tests conducted with saline solution. In order to compare the mobility (K) results reported in this and many other studies with reported values of permeability (k) for many tissue engineering constructs and biological tissues, the viscosity of water can be used ($K = k/\mu$; μ = 0.001 Pa·s).

4.2. Cellular solids model of CG scaffolds

In nature, materials with a cellular (porous) structure are widespread, and extensive study and modeling of the microstructural and mechanical properties of these materials has been performed (Gibson and Ashby, 1997). Tissue engineering scaffolds often resemble low-density, open-cell foams, with an interconnected network of pores defined by struts; cellular solids theory provides a powerful tool to investigate and describe salient features of a scaffold.

The first critical component of ECM analog microstructure to consider is the open or closed-cell nature of the scaffold: foams may be either open (with solid only at the edges of the polyhedra-shaped pore) or closed (with solid membranes covering the faces of the pores). An open-cell pore microstructure exhibits pore interconnectivity while a closed-cell microstructure exhibits membrane-like faces between adjacent pores, effectively sealing the environment of one pore from its neighbors. Pore interconnectivity is critical for scaffold bioactivity because cells need to

be able to migrate through the construct and to interact with other cells in a manner similar to that observed *in vivo*.

The relative density (ρ^*/ρ_s) is a second critical microstructural feature of ECM analogs to consider. The relative density, also termed the solid volume fraction (*SVF*), of the scaffold is calculated as the ratio of the scaffold density (ρ^*) to the density of the solid from which the scaffold is made (ρ_s). Porosity, also termed the pore volume fraction (*PVF*) of a scaffold, is another variable often used in the literature to describe tissue engineering scaffolds. *PVF* is a measure of how porous the scaffold is, and is related to the relative density and *SVF*:

Equation 4.2. $$\frac{\rho^*}{\rho_s} = SVF = 1 - PVF$$

Together, relative density, the open- or closed-cell nature, and mean pore size define the amount and relative distribution of solid material in the scaffold. When the pores are closed, too small, or when the relative density is too large, cells are not able to migrate through the scaffold, a significant impediment for a tissue engineering scaffold. An active ECM analog must possess an open-cell pore structure with a relative density below a critical value that is characteristic of each application, but is typically significantly < 10% (bioactive porosity typically > 90%). These structural criteria, determined from the results of a number of experiments studying cell-scaffold interactions, suggest that a critical number of cells are required within a bioactive scaffold (Yannas, 2001).

Cellular solids modeling techniques can be utilized to describe both mechanical and microstructural (*i.e.*, specific surface area, permeability) properties of tissue engineering

scaffolds. The remainder of this section will introduce appropriate cellular solids modeling techniques to describe microstructural features while Chapter 5 will detail cellular solids modeling and experimental analysis of the mechanical properties of CG scaffolds.

While dimensional arguments that rely on modeling the mechanisms of deformation and failure in the foam, but not the exact cell geometry, can be used to describe many features of tissue engineering scaffolds, it is also appropriate to utilize some cellular solids modeling techniques that incorporate specific cell geometries in the form of particular cellular solids unit cells. There are a wide variety of potential unit cells that have been utilized in the literature, notably triangular, rectangular, and hexagonal (**Figure 4.1**) prisms, rhombic dodecahedra, and tetrakaidecahedral (**Figure 4.1**).

In particular, the tetrakaidecahedral unit cell (a fourteen-sided polyhedron that packs to fill space) offers a number of attractive features for describing structural parameters of the CG scaffold (**Figure 4.1**). The pore structure of a variety of low-density foams has been observed to have three distinct features (Williams, 1968): an average of approximately 14 faces per cell, an average of 5.1 edges per face, and vertices that are nearly tetrahedral. These morphological features are due to a minimization of the total surface area of the cells. The tetrakaidecahedron is a polyhedron that packs to fill space, approximates the structural features of low-density foams observed through experiment, nearly satisfies the minimum surface energy condition, and is often used for modeling low-density foams (Thompson, 1887; Gibson and Ashby, 1997).

Additionally, the value of the dimensionless measure of total edge length per (unit volume)$^{1/3}$ for the tetrakaidecahedral unit cell is nearly identical to that observed for many random cellular structures (Kraynik, Reinelt, et al., 2003), suggesting that the tetrakaidecahedral unit cell gives a good representation of the total edge length and can be used to model the specific surface area and permeability of random open-cell cellular structures such as the porous CG scaffold.

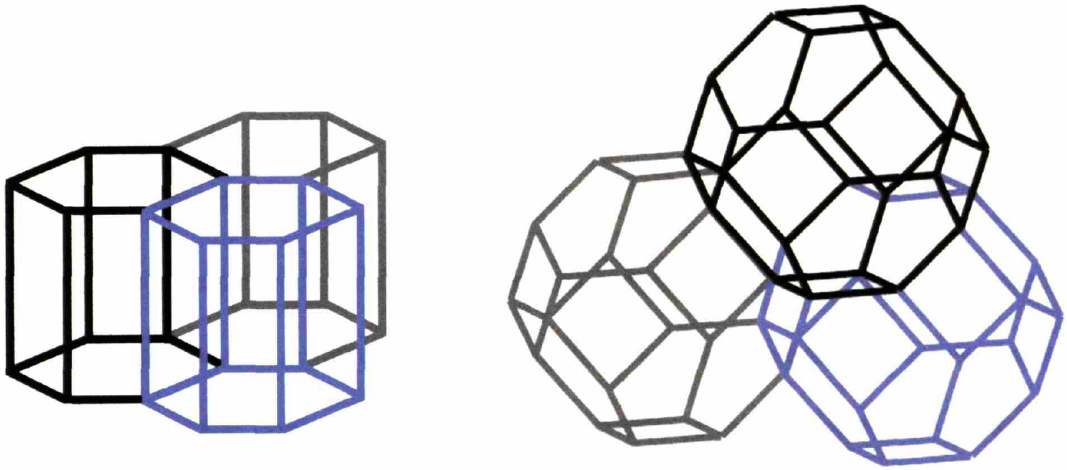

Figure 4.1. The geometry and packing of the hexagonal prism (left) and tetrakaidecahedral (right) unit cells. The tetrakaidecahedral unit cell has been used to model the CG scaffold microstructure.

4.3. Materials and Methods

4.3.1. Fabrication of collagen-GAG scaffolds

A complete description of the fabrication protocols of the four standard CG scaffolds used in this investigation (**Table 4.2**) have been previously described in this thesis in Section 2.3.1 (CG suspension), 2.3.4 (constant cooling rate solidification), and 2.3.5 (fabrication of uniform CG scaffolds with distinct mean pore sizes).

T_f, °C	Mean Pore Size, μm Mean ± StDev	Relative Density Mean ± StDev
-10	151 ± 32	0.0062 ± 0.0005
-20	121 ± 23	0.0061 ± 0.0003
-30	110 ±18	0.0059 ± 0.0003
-40	96 ± 12	0.0058 ± 0.0003

Table 4.2. CG scaffold variants utilized for permeability and specific surface area investigation.

4.3.2. CG scaffold crosslinking

All CG scaffolds manufactured in this study were crosslinked via a dehydrothermal process after freeze-drying to stiffen the collagen network by introducing covalent crosslinks between the polypeptide chains of the collagen fibers without denaturing the collagen into gelatin (Yannas and Tobolsky, 1967; Yannas, 1972). Crosslinking was carried out in a vacuum oven (Fisher IsoTemp 201, Fisher Scientific, Boston, MA) at a temperature of 105°C under a vacuum of 50 mTorr for 24 hours (Yannas, Lee, et al., 1989; O'Brien, Harley, et al., 2004). Dehydrothermal crosslinking also sterilized the CG scaffold variants due to the high heat and vacuum exposure, rending the scaffold suitable for cell culture.

4.3.3. CG scaffold specific surface area study

4.3.3.1. Cellular solids model of CG scaffold specific surface area

The surface area per unit volume (SA/V), or specific surface area, of each scaffold was estimated using a cellular solids model utilizing a polyhedral unit cell to determine the effect of mean pore

size on the specific surface area of the CG scaffolds. For an open-cell foam with an interconnected pore structure modeled using a polyhedral unit cell, the specific surface area can be related to the mean pore size and the relative density (the density of the porous foam relative to that of the solid it is made from) (Gibson and Ashby, 1997). We have used a tetrakaidecahedral unit cell (a fourteen-sided polyhedron that packs to fill space) to model the geometry of the CG scaffold (Section 4.2 provides further explanation of this choice). For an open-cell tetrakaidecahedron with edges of circular cross-section, the specific surface area can be described by the relation (Gibson and Ashby, 1997):

Equation 4.3. $$\frac{SA}{V} = \frac{3.65}{l}\left(\frac{\rho^*}{\rho_s}\right)^{1/2}$$

In this relation, l is the edge length of the tetrakaidecahedron, ρ^* is the density of the porous scaffold, and ρ_s is the density of the solid from which it is made. The relative density (ρ^*/ρ_s) of the CG scaffolds was determined by measuring the density of entire sheets of CG scaffold and comparing that density with the known density of collagen (1.3 mg/mm^3) (Yannas, 1972); the relative density was measured to be constant (0.6%) for all four scaffolds variants (**Table 4.1**). The specific surface area equation (*1*) can then be simplified:

Equation 4.4. $$\frac{SA}{V} = \frac{0.258}{l}$$

To calculate the mean spacing (equivalent to diameter) between opposite sides of this structure, we assume that the internal volume is similar to that of a sphere of diameter *d*. Using this assumption, the pore diameter can be calculated from the edge length by:

Equation 4.5. $$d = 2.78 \cdot l$$

From this calculation, we estimate that the specific surface area (*SA/V*) of the four CG scaffold variants used in this study is inversely related to the pore diameter (*d*) by:

Equation 4.6. $$\frac{SA}{V} = \frac{0.718}{d}$$

4.3.3.2. Experimental measurement of CG scaffold specific surface area via cell attachment

Full thickness (approximately 3 mm thick) samples, 30 mm x 22 mm in size, were cut from the four CG scaffold variants (T_f = -10°C, -20°C, -30°C, and -40°C) for the cell adhesion experiments described below.

MC3T3-E1 mouse clonal osteogenic cells were maintained in α-MEM supplemented with L-glutamine, 10% fetal bovine serum (FBS; Intergen, Purchase, NY, USA), penicillin (100 IU/ml; Sigma), and streptomycin (100 mg/ml; Sigma). Cells were removed from the culture flasks to seed the scaffolds using a trypsin-EDTA solution (Sigma, St. Louis, MO). Viable cell number was determined prior to seeding by live-cell staining using 0.4% Trypan Blue (Invitrogen Co., Chicago, IL) and counting viable cells with a standard hemacytometer (Bright-Line, Hausser Scientific, Horsham, PA) (Freyman, Yannas, et al., 2001).

Prior to seeding, the scaffolds were placed into wells of a 6-well tissue culture plate (Nalge Nunc International, Naperville, IL). Each well was pre-coated with agarose gel (J.T. Baker, Philipsburg, NJ) to prevent cells from migrating out of the scaffolds onto the tissue culture plate. The CG

scaffold was seeded on both sides with 3 x 10^6 cells in a manner that has previously been described (Freyman, Yannas, et al., 2001; Freyman, Yannas, et al., 2001). One milliliter of the MC3T3-E1 cell suspension (3 x 10^6 cells/ml) was pipetted onto the surface of the dry scaffold. The scaffold was then returned to the incubator for 10 minutes to allow for initial cell attachment; the seeded scaffold was then turned over and an additional 1 ml of the cell suspension was pipetted onto the reverse surface of the scaffold. The wells were then filled with 2 ml of the supplemented (L-glutamine, FBS, penicillin, streptomycin) α-MEM medium and placed into a cell culture incubator and maintained at 37°C with 5.0% CO_2 for either 24 or 48 hours.

While some work suggests that high cell densities can prevent cell migration into scaffolds, the cell density used in this experiment (9.1 x 10^5 cells/cm^2) was consistent with previous experiments in this laboratory using CG scaffolds for studies of cell-mediated contraction (Freyman, Yannas, et al., 2001). The pore volume fraction of these CG scaffolds is extremely high (99.5%) compared to many other scaffolds used for tissue engineering applications, allowing for easier cell migration into the scaffold even with higher cell densities. The relatively high cell density was chosen to provide a high density of integrins (cells) to allow a test of the hypothesis that the density of available ligands increases with decreased pore size and that the pore size affects cell attachment.

Following each adhesion experiment, the seeded scaffold was removed from the tissue culture plate. Each sample was rinsed with Dulbecco's phosphate buffered saline (Gibco, Grand Island, NY) at 37°C to remove unattached cells and was then placed in a 2.0 U/ml solution of dispase

(Gibco) for 30 minutes to digest the scaffold (Freyman, Yannas, et al., 2001; Freyman, Yannas, et al., 2001). The remaining cells were then stained with 0.4% Trypan Blue and the number of attached, viable cells was counted using a hemacytometer.

4.3.4. CG scaffold permeability study

4.3.4.1. Cellular solids model of CG scaffold permeability

A low-density, open-cell foam cellular solids model utilizing a tetrakaidecahedral unit was used to model the permeability of CG scaffolds with variable mean pore size under variable applied compressive strain. A quantitative, cellular solids model describing the permeability (k) of, or fluid mobility (K) through, CG scaffolds in terms of scaffold mean pore size (d), individual strut length (l), percent compression (ε), a dimensionless system constant (A'), and scaffold relative density (ρ^*/ρ_s) has been developed from a series of known cellular solids relationships. The permeability (k) of many open-cell foams has previously been reported in terms of mean pore size (d) and relative density (ρ^*/ρ_s) (Brace, 1977; Gibson and Ashby, 1997):

Equation 4.7. $$k = A' \cdot d^2 \cdot \left(1 - \frac{\rho^*}{\rho_s}\right)^{3/2}$$

This model can be modified to describe scaffold fluid mobility (K) using a single, system constant (A'', $A'' = A'/\mu$) with dimensions $(\text{Pa}\cdot\text{s})^{-1}$:

Equation 4.8. $$K = \frac{A'}{\mu} \cdot d^2 \cdot \left(1 - \frac{\rho^*}{\rho_s}\right)^{3/2} = A'' \cdot d^2 \cdot \left(1 - \frac{\rho^*}{\rho_s}\right)^{3/2}$$

The mean pore size of the compressed scaffold ($d_{compress}$) under a given applied compressive strain (ε_{app}) can be defined in terms of the initial edge length of the unit cell used to describe the scaffold microstructure (l) (Gent and Rusch, 1966). A relationship between applied compressive strain and compressed mean pore size, modified from that proposed by Gent and Rusch (Gent and Rusch, 1966) for this CG scaffold system with an observed Poisson's ratio of 0, is presented here:

Equation 4.9. $$d_{compress} \propto l \cdot (1 - \varepsilon_{app})$$

Additionally, for the tetrakaidecahedral unit cell, scaffold mean pore size (d) can be related to the average edge length of an individual strut (l) within the unit cell (**Eq. 4.5**) (Gibson and Ashby, 1997). Combining these relationships, a single model describing scaffold permeability (k) or fluid mobility (K) in terms of a system constant (A' *or* A''), scaffold mean pore size (d), applied compressive strain (ε_{app}), and relative density (ρ^*/ρ_s) that is valid for any low-density, open-cell foam is proposed. These models are identical with the exception of the single, system constant ($A'' = A'/\mu$):

Equation 4.10. $$k = A' \cdot \left(\frac{d}{2.785}\right)^2 \cdot (1-\varepsilon)^2 \cdot \left(1 - \frac{\rho^*}{\rho_s}\right)^{3/2}$$

Equation 4.11. $$K = A'' \cdot \left(\frac{d}{2.785}\right)^2 \cdot (1-\varepsilon)^2 \cdot \left(1 - \frac{\rho^*}{\rho_s}\right)^{3/2}$$

4.3.4.2. Experimental measurement of CG scaffold permeability

The permeability of the four uniform CG scaffold variants (**Table 4.1**) was experimentally measured in the laboratory of Prof. Fergal J. O'Brien (Trinity College and the Royal College of Surgeons in Ireland, Dublin, Ireland) by Ms. Mary Waller (Waller, McMahon, et al., 2004; O'Brien, Harley, et al., Submitted, 2005). A brief description of the experimental procedure utilized by these co-investigators (FJO, MW) is provided here to explain how the measurements were made.

A device (**Figure 4.2**) was constructed to measure the permeability of the scaffold variants under different levels of applied compressive strain. The device was constructed from two (top and bottom) brass plates, each with an attached 8mm inner diameter tube. A stainless steel mesh was secured over the tube openings in both brass plates. The mesh, a medical-grade stainless steel (Braun, Frankfurt, Germany) was adhered to the brass plates with a high-grade cyanoacrylate glue (LocTite 401, Herts, UK). The mesh served a two-fold purpose: to physically support the scaffold above the tube opening in the bottom plate, and to apply compressive strain to the scaffold via the height-adjustable top plate. Stainless steel spacers of varying thickness (2–5 mm) were placed between the two stainless steel meshes when the testing rig was assembled, regulating the degree of applied compressive strain. Importantly, the mesh did not inhibit or disrupt fluid flow through the rig. To secure the scaffold in place, the scaffold edges (away from the tube openings) were clamped to the bottom stainless steel mesh using a silicone spacer which also served as a leak-proof seal for the rig, preventing pressure loss. The inner diameter of the silicone spacer (10mm) was slightly larger than that of the brass plate (8mm). Cylindrical scaffold disks, 13 mm in diameter and 3.5 mm thick, were cut from each scaffold variant using a

dermal punch (Miltex, York PA USA) and then submerged in saline solution for 24 hours prior to testing in order to completely hydrate the scaffold.

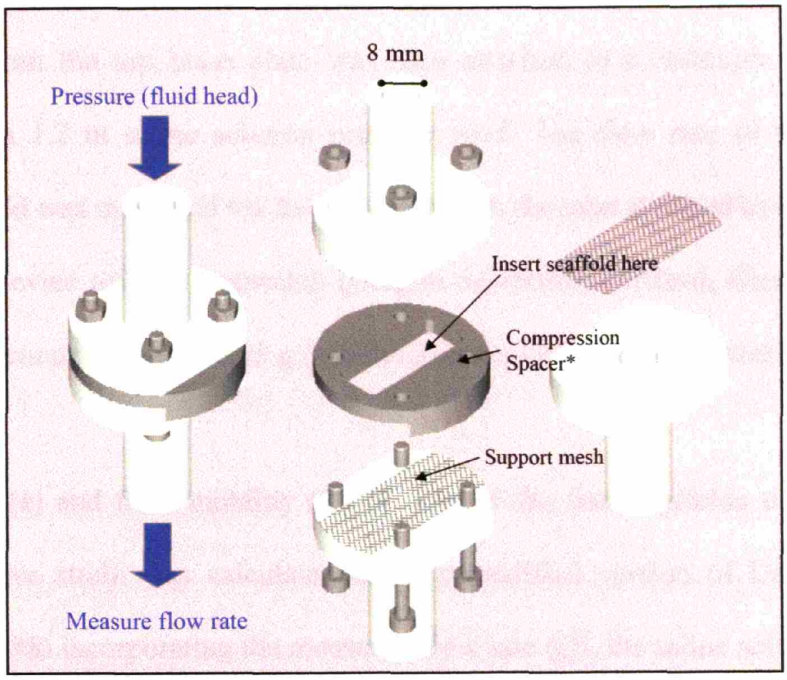

Figure 4.2. The device utilized in this study to measure the CG scaffold permeability (fluid mobility) (Waller, McMahon, et al., 2004).

Darcy's law was utilized to calculate CG scaffold permeability, k, in terms of the volumetric flow rate (Q, ml/s), the pressure difference across the sample (ΔP, N/m^2), the length of the specimen through which the fluid flows (l, m), the sample cross-sectional area in the direction of flow (A, m^2), and the viscosity (μ, Pa·s) of the fluid used for the test.

Equation 4.12. $$k = \frac{Q \cdot l \cdot \mu}{\Delta P \cdot A}$$

The degree of scaffold compression was controlled by the stainless steel spacers (2, 2.5, 3, or 5 mm thickness); these spacers maintained a constant separation distance between the top and

bottom stainless steel meshes, and hence a constant level of compressive strain on the CG scaffold, throughout the permeability test. The thickness of the scaffolds was 3.5mm, making these spacers correspond to compressive strains of 40%, 29%, 14%, and 0%, respectively. The tube extending from the top brass plate was then attached to a reservoir of saline solution pressurized with a 1.2 m saline solution pressure head. The flow rate of the saline solution through the scaffold was measured via the flow rate from the tube attached to the bottom plate of the permeability device using a stopwatch (Oregon Scientific, Portland, Oregon, USA) and an electronic scale accurate to within 0.05 g (Mettler Toledo, Greifensee, Switzerland) (**Figure 4.2**).

The permeability (k) and fluid mobility (K) of each of the four scaffolds under each level of applied compressive strain was calculated using a modified version of Darcy's law (Spain, Agrawal, et al., 1998) incorporating the measured flow rate (Q), the saline solution viscosity (μ), the radius of the scaffold sample (r, 4 mm), the thickness of the scaffold sample (l), and the height of the saline solution column (P, 1.2 m).

Equation 4.13. $$k = \frac{324.8(Q \cdot l \cdot \mu)}{r^2 P}$$

Equation 4.14. $$K = \frac{k}{\mu} = \frac{324.8(Q \cdot l)}{r^2 P}$$

4.3.5. Statistical analysis

All statistical calculations were performed using the StatView statistical software package (v. 5.0, SAS Institute, Inc., Cary, NC). One-way analysis of variance (ANOVA) and pairwise multiple comparison procedures (Dunn's Method) were used to compare groups of data. Paired t-tests

were performed to compare individual sets of data to determine statistical significance between 24 and 48 hour groups using the same scaffold. Error is reported in figures as the standard deviation (StDev), the standard error of the mean (SEM = StDev/$n^{1/2}$), or as the coefficient of variance (CV = StDev/Mean). A probability value of 95% ($p < 0.05$) was used to determine significance.

4.4. Results

4.4.1. Cell adhesion and cellular solids model calculated CG scaffold specific surface area

4.4.1.1. Effect of pore size on adhesion

Figure 4.3 shows the percentage of MC3T3-E1 cells seeded onto the matrix that were attached to the four different scaffolds at both 24 and 48 hours post-seeding. One-way analysis of variance (ANOVA) indicated that mean pore size of the scaffolds had a significant effect on cell attachment after both 24 ($p < 0.01$) and 48 hours ($p < 0.001$). In the scaffolds with the smallest mean pore size (T_f = -40°C) over 40% of cells seeded remained attached to the scaffolds and viable at both 24 and 48 hours compared to approximately 20% of cells that remained attached to the scaffolds and viable with the largest mean pore size (T_f = -10°C). No significant difference in cell attachment was found between the intermediate scaffolds (T_f = -20°C, T_f = -30°C) with approximately 30% of cells (31.1% and 27.5% respectively) remaining attached after both the 24 and 48 hour groups ($p = 0.99$, $p = 0.89$ respectively).

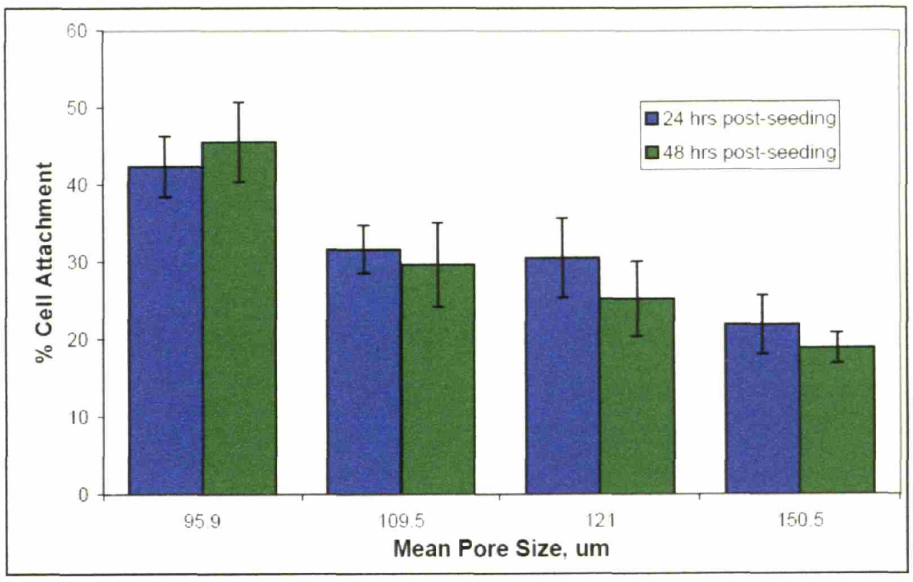

Figure 4.3. Percentage of MC3T3 cells attached to the CG scaffolds at 24 and 48 hours post seeding.

4.4.1.2. Effect of seeding time on adhesion

Paired t-tests indicated that there was no statistical difference between the percentage of cells attached and viable at 24 and 48 hours-post seeding for any of the four groups of scaffolds ($p > 0.05$).

4.4.1.3. Cellular solids specific surface area calculation vs. cell attachment

The specific surface area of the scaffold for each of the four different mean pore sizes was calculated using equation (4). **Figure 4.4** shows a graph of percentage of seeded cells that remained attached to the scaffold plotted against specific surface area showing strong linear relationships ($R^2 = 0.95, 0.91$) between specific surface area and the percentage of attached cells at 24 hours and 48 hours post seeding, respectively.

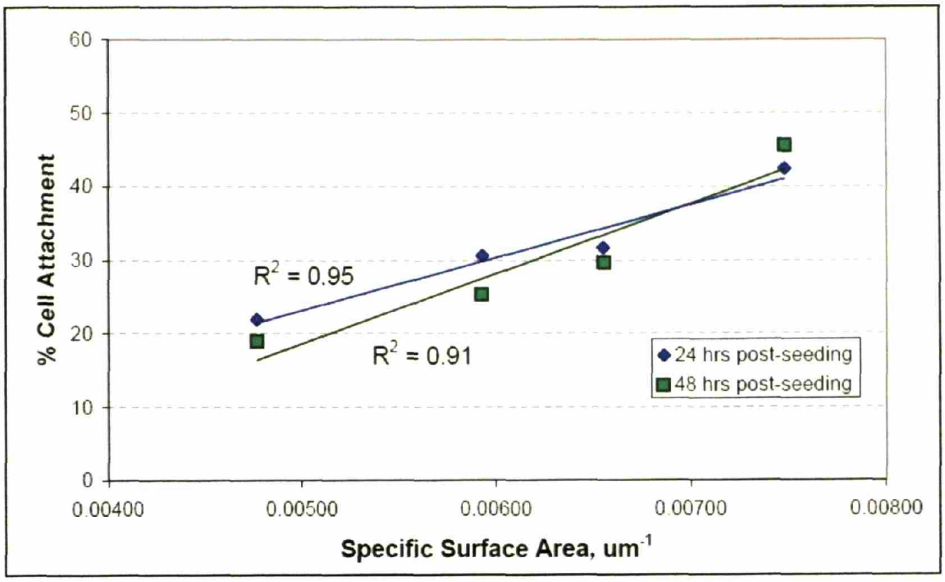

Figure 4.4. Attached cell number plotted against specific surface area showing a strong linear relationship at 24 (solid line) and 48 hours post seeding (dashed line).

4.4.2. CG scaffold permeability: Cellular solids model vs. experimental measurement

4.4.2.1. Experimental measurement of CG scaffold permeability

CG scaffold permeability (fluid mobility) was found to be on the order of 10^{-10} m^4/Ns. While expected since the scaffold in the dry state has a porosity of 99.5%, this is quite high when compared to tissues such as cartilage (10^{-15} m^4/Ns) but several orders lower than that of trabecular bone (10^{-6} m^4/Ns). **Figure 4.5** and **Table 4.3** show the experimentally measured scaffold permeability values (mean ± StDev) as a function of pore size and compressive strain. One-way ANOVA tests revealed that scaffold permeability increased significantly with pore size: $K = 0.660 \pm 0.256$ m^4/Ns to $K = 1.387 \pm 0.516 \times 10^{-10}$ m^4/Ns for the 96 and 151μm pore size scaffolds at 0% compression, respectively. Scaffold permeability was also observed to decrease with increasing compressive strain; $K = 0.660 \pm 0.256 \times 10^{-10}$ m^4/Ns and $0.231 \pm 0.180 \times 10^{-10}$ m^{4-}

/Ns for the 96μm pore size at 0 and 40% compressive strain, respectively. Similar trends were found for the other scaffold variants (**Figure 4.5**).

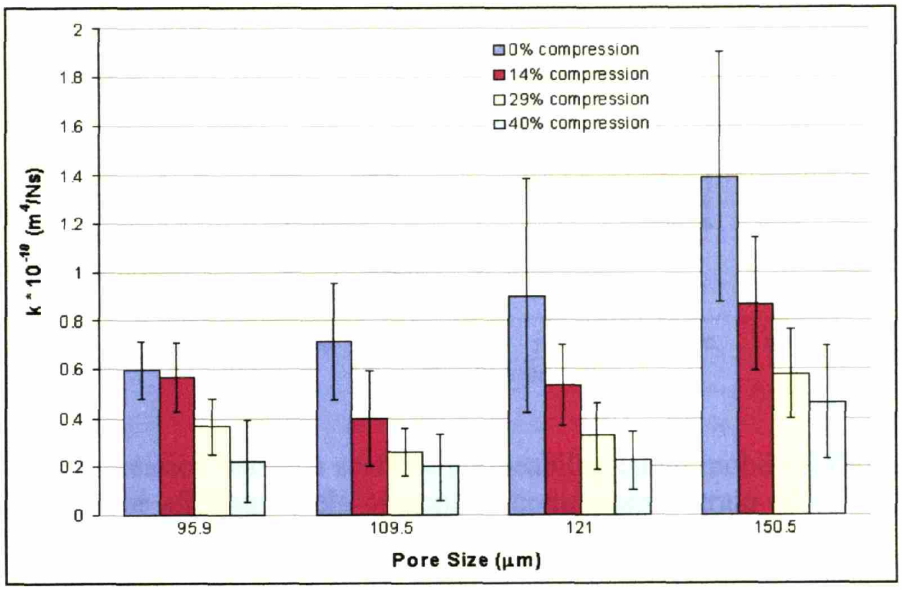

Figure 4.5. Experimentally measured scaffold permeability (fluid mobility) as a function of pore size and applied compressive strain.

4.4.2.2. Cellular solids model vs. experimental measurement of CG scaffold permeability

Power law regression analyses were performed between measured scaffold permeability (fluid mobility) (K) and both the mean pore size (d) and applied compressive strain (ε). The first regression (**Figure 4.6**) indicated a good correlation between K and d^2 for 0% ($R^2 = 0.9956$), 14% ($R^2 = 0.6811$), 29% ($R^2 = 0.6852$), and 40% ($R^2 = 0.8499$) compressive strain, in agreement with the relationship between K and d proposed by the cellular solids model.

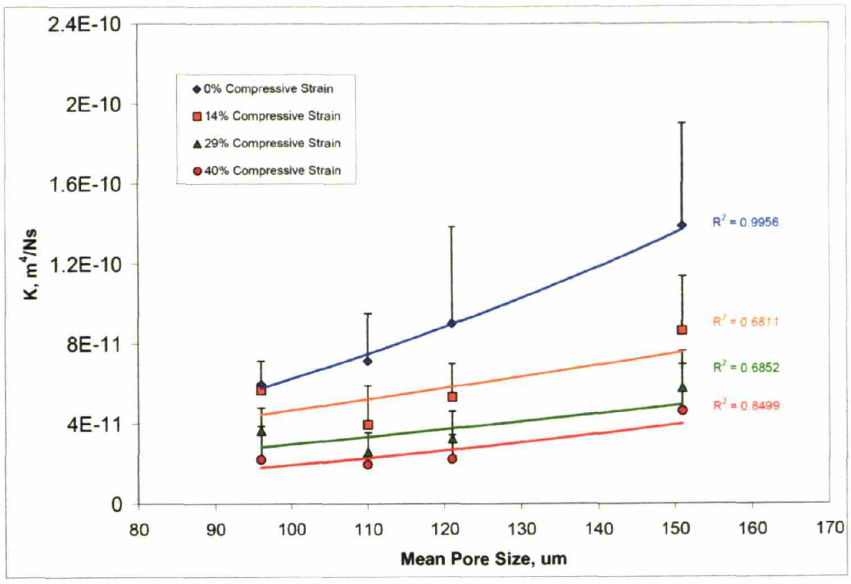

Figure 4.6. Power regression between scaffold permeability (fluid mobility) (K) and mean pore size (96 – 151 μm) for all four levels of applied compressive strain (0 – 40%), testing the relationship proposed by the cellular solids model: $K \alpha d^2$.

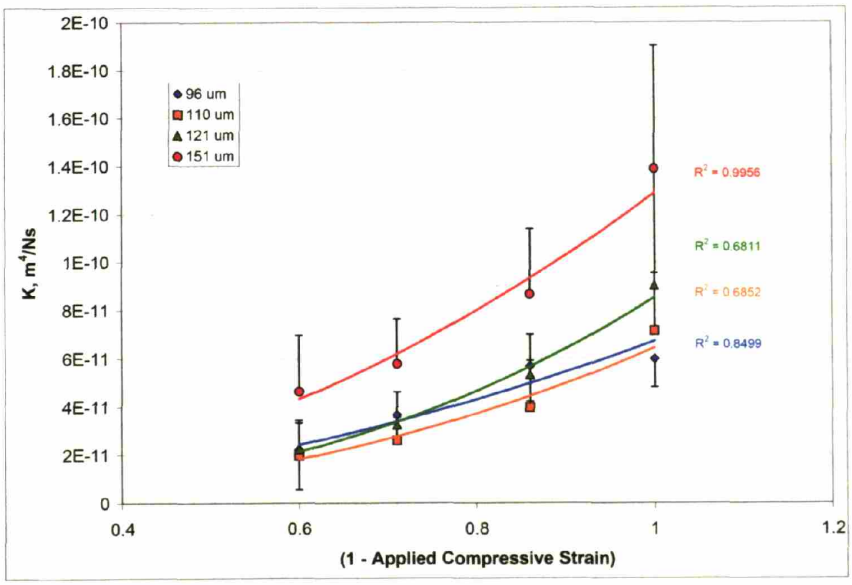

Figure 4.7. Power regression between scaffold permeability (fluid mobility) (K) and applied compressive strain (ε: 0 – 40%) for all four scaffold variants (Mean pore size: 96 – 151 μm), testing the relationship proposed by the cellular solids model: $K \alpha (1 - \varepsilon)^2$.

A power law regression was also performed between scaffold permeability (K) and ($1 - \varepsilon$), where ($1 - \varepsilon$) corresponds to the remaining relative thickness of the compressed sample (**Figure 4.7**). A good correlation was observed between K and $(1 - \varepsilon)^2$ for CG scaffolds with mean pore sizes of 96 μm ($R^2 = 0.8911$), 110 μm ($R^2 = 0.9498$), 121 μm ($R^2 = 0.9773$), and 151 μm ($R^2 = 0.9691$), again in agreement with the relationship proposed by the cellular solids model.

The mathematical modeling showed remarkable accuracy in predicting the permeability of the constructs for all pore sizes and at each level of compression in a single model. **Table 4.3** and **Figure 4.8** shows a comparison between the measured experimental results (K_{meas}) and the predicted values obtained from the mathematical model (K_{calc}) for the four distinct scaffold variants at the four levels of compressive strain. The cellular solids model predictions for all groups fit within the standard deviation of each experimentally measured value.

Mean Pore Size, μm	K_{meas}	K_{calc}	K_{meas}	K_{calc}	K_{meas}	K_{calc}	K_{meas}	K_{calc}
	ε = 0%		ε = 14%		ε = 29%		ε = 40%	
96	0.598 ± 0.117	0.564	0.568 ± 0.146	0.417	0.365 ± 0.114	0.284	0.222 ± 0.166	0.203
110	0.714 ± 0.240	0.735	0.396 ± 0.196	0.544	0.260 ± 0.097	0.371	0.197 ± 0.136	0.265
121	0.902 ± 0.483	0.898	0.532 ± 0.167	0.664	0.324 ± 0.137	0.453	0.223 ± 0.121	0.323
151	1.389 ± 0.513	1.389	0.866 ± 0.273	1.027	0.578 ± 0.186	0.700	0.463 ± 0.233	0.500

Table 4.3. Experimentally measured (K_{meas}, Mean ± StDev) and cellular solids model derived (K_{calc}) fluid mobility of the four CG scaffold variants under four levels of compressive strain (ε = 0, 14, 29, 40%). Units for K are 1 x 10^{-10} m^4/Ns.

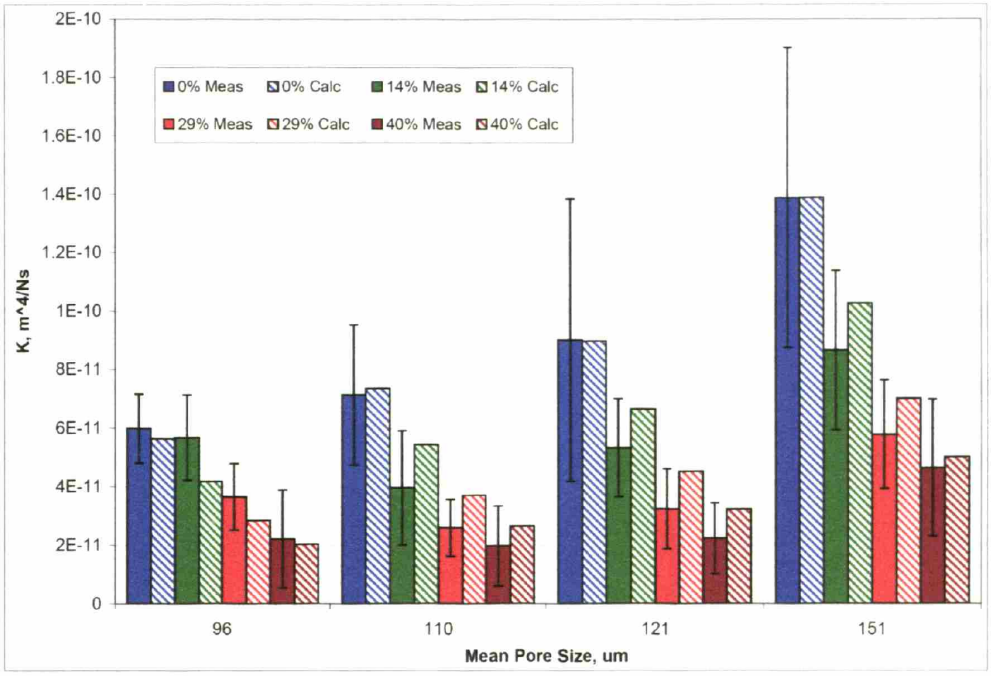

Figure 4.8. Comparison between the experimental results (K_{meas}) obtained and the predicted values obtained from the mathematical model (K_{calc}) for CG scaffold permeability (fluid mobility) under varying compressive strains.

4.5. Discussion

The specific surface area for each of the four CG scaffolds was determined using an open-cell foam cellular solids model utilizing a tetrakaidecahedral unit cell. As all scaffolds were fabricated from the same stock CG suspension, the density of ligands available for binding on each scaffold is assumed to be proportional to the scaffold specific surface; the specific surface area was calculated to be inversely proportional to the mean pore size (**Eq. 4.6**). The estimate of the specific surface area of the CG scaffolds is remarkably consistent with the results from the cell attachment study, showing a linear relationship between percent cell attachment and specific surface area (**Figure 4.4**). The attached cell number increases linearly with specific surface area for data taken both at 24 hours ($R^2 = 0.95$) and at 48 hours ($R^2 = 0.91$) post-seeding.

No significant difference was observed in the percentage of cell attachment after 24 and 48 hours (**Figures 4.3, 4.4**). This finding is consistent with the work of Freyman *et al.* (Freyman, Yannas, et al., 2001) who found that, although there was a significant effect of time on fibroblast attachment in CG scaffolds similar to those used in this study in the first hours post seeding, by 22 hours maximum attachment had been reached. The fraction of MC3T3-E1 cells attached to the CG scaffold over the range of pore sizes studied decreases with increasing mean pore size and increases linearly with specific surface area, consistent with the increase in ligand binding site density.

The permeability/fluid mobility of the CG scaffolds was found to be in the order of 10^{-10} m^4/Ns. The only previous permeability value found in the literature for a collagen material was for a collagen gel (Ramanujan, Pluen, et al., 2002) (**Table 4.1**). The values for permeability with these gels ranged from 1 x 10^{-15} to 1 x 10^{-16} m^2 (1 × 10^{-12} m^4/Ns to 1 × 10^{-13} m^4/Ns). The CG scaffold variants characterized in this study were 2 - 3 orders of magnitude more permeable than these collagen gels, a result that makes intuitive sense due to the gel's significantly lower porosity. From a tissue engineering perspective, such differences in construct permeability suggest significantly higher levels of metabolite diffusion will be observed in a scaffold structure as compared to a gel, allowing increased cell proliferation and facilitating cell migration further into the scaffold.

The results from both the experimental and the cellular solids modeling analysis reveal that scaffold permeability/fluid mobility increased with increasing pore size, where scaffold specific surface area was observed to decrease with increasing mean pore size (**Figure 4.5, Table 4.3**).

These permeability results are also consistent with previous mathematical models describing the permeability of low porosity (<90%) foams. The Carman-Kozeny mathematical model for foam permeability (Levick, 1987) described a number of geometric factors that influence the permeability of such foams: porosity, tortuosity (pore interconnectivity), pore size and orientation, fenestration size and shape, and specific surface area. In this model, the specific surface area influences permeability because it defines the total surface area within the scaffold; frictional effects that disturb and impede fluid flow resulting in reduced construct permeability are proportional to the scaffold surface area. While the Carman-Kozeny theoretical model has been successfully applied to a number of materials, the model is not applicable to highly porous materials (porosities greater than 90%), such as the constructs used in this study and most tissue engineering scaffolds. The results from this study however, demonstrate that even in materials with a high porosity, scaffold mean pore size defines the scaffold specific surface area which likely influences the ability of a fluid to pass through it. In addition, the particular relationship between scaffold permeability and mean pore size, $K \alpha d^2$, that is predicted using the cellular solids model is also observed experimentally, further validating the cellular solids model (**Eq. 4.10, 4.11; Figure 4.6**).

The results of the experimental and cellular solids modeling analysis also show that scaffold permeability decreases with increasing levels of compressive strain (**Figure 4.5, Table 4.3**). This result is similar to the relationship between compression and permeability described by Lai and Mow (Lai and Mow, 1980) for articular cartilage. Other biological materials have also been found to follow this relationship, including the human medial collateral ligament (Sander and Nauman, 2003). The reason for this relationship in the collagen-GAG scaffolds is intuitive: as

the material is compressed, the spacing between the collagen-GAG fibers decreases. Furthermore, the porosity of the constructs will also decrease under compression. Both of these factors would lead to the resultant increased resistance to fluid flow.

The particular relationship between scaffold permeability and compressive strain, $k \alpha (1 - \varepsilon)^2$, that is predicted using the cellular solids model is also observed experimentally, further validating the cellular solids model (**Eq. 4.10, 4.11; Figure 4.7**). The relationship between compressive strain and permeability in the collagen-GAG scaffolds will be useful in designing *in vitro* bioreactor-based culture protocols and for designing constructs for *in vivo* studies where significant loads may be applied to the scaffold. In a bioreactor we seek to apply the optimal biophysical stimuli to encourage cells to differentiate to specific phenotypes or to produce extracellular matrix formation. As the degree of compression to which a cell-seeded construct is exposed influences the permeability of fluid through the construct, the relationship between scaffold permeability with mean pore size, applied strain, and relative density will be used to determine the optimal bioreactor conditions required for specific tissue engineering applications. In addition, as constructs increase in size, it will be important to design appropriate microstructure in the scaffold to allow maximal nutrient influx to support scaffolds implanted into *in vivo* wound sites. Such utilizations of scaffold modeling tools and experimental measurements of scaffold permeability for designing the microstructure of future scaffolds is currently the subject of ongoing research in our laboratory.

4.6. Conclusions

Previous speculation regarding cell activity within porous scaffolds has indicated that there exists an optimal pore size, or range for each distinct cell type. A linear relationship was found between cell attachment and specific surface area, indicating that over the range of pore sizes studied (95.9 - 150.5 μm) short-term MC3T3 cell attachment is governed by the specific surface area available for binding. The increasing cell attachment with decreasing pore size would not be expected to continue as pore size would eventually drop to the point where cells could no longer fit into the pores; however the MC3T3 cell type was chosen for this experiment due to its small size so that cell size would not be a confounding factor. In order to properly identify an optimal pore size for maximal cell attachment, future experiments are necessary utilizing uniform scaffolds with a wider range of pore sizes. In addition, the use of a variety of cell types would allow the study of how different cell types respond to scaffold structure. The permeability characteristics of the uniform collagen-GAG scaffold variants, experimentally measured to decrease with decreasing pore size and with increasing compressive strain, have also been successfully modeled using cellular solids modeling techniques utilizing the same tetrakaidecahedral unit cell used to model CG scaffold specific surface area.

The excellent comparison between experimentally measured and cellular solids model predicted scaffold specific surface area and permeability validates the use of cellular solids modeling technique utilizing a tetrakaidecahedral unit cell to describe many physical properties of the CG scaffold cellular structure. These results also suggests that cellular solids modeling techniques can be used as a predictive model of scaffold specific surface area and permeability for many different scaffold architectures under a variety of physiologically-relevant loading conditions,

and as a predictive model to describe the specific surface area and permeability characteristics of future scaffold structures. Appropriate modeling tools that quantitatively describe scaffold characteristics (*i.e.*, permeability, specific surface area, mechanical properties) in terms of salient microstructural features are advantageous for further advancement in the field of tissue engineering, and it appears that cellular solids modeling techniques utilizing the tetrakaidecahedral unit cell can accurately model CG scaffolds and have the potential to quantitatively describe many other tissue engineering constructs. This information will be very important in understanding and modeling cell interactions with three-dimensional structures and in designing future bioactive scaffolds for use with specific cell types or in specific tissue systems.

Chapter Reference

This chapter has been adapted from the following publications:

F.J. O'Brien, B.A. Harley, I.V. Yannas, and L.J. Gibson, "The effect of pore size and structure on cell adhesion in collagen-GAG scaffolds," *Biomaterials*, 26(4):433-441, 2005.

F.J. O'Brien, B.A. Harley, M.A. Waller, I.V. Yannas, L.J. Gibson, and P.J. Prendergast, "The effect of pore size on permeability and cell attachment in collagen scaffolds for tissue engineering," Submitted, *Technol. Health Care*, 2005.

B.A. Harley, F.J. O'Brien, M.A. Waller, P.J. Prendergast, I.V. Yannas, and L.J. Gibson, "Mean pore size and compressive strain effects on the permeability of collagen-GAG scaffolds: cellular solids modeling and experimental results," *Trans. Soc. Biomater.*, 32, 2006, Pittsburg, PA.

CHAPTER 5. *Mechanical Characterization of Collagen-GAG Scaffolds*

5.1. Introduction

Tissue engineering scaffolds act as a physical support structure and as an insoluble regulator of cell biological activity. Many scaffold parameters have been shown to significantly influence cell behaviors such as adhesion, growth and differentiation, notably scaffold microstructure (porosity, mean pore size, pore shape, interconnectivity, specific surface area) (Yannas, Lee, et al., 1989; Wake, Patrick, et al., 1994; Nehrer, Breinan, et al., 1997; Yannas, 2001; Zeltinger, Sherwood, et al., 2001; O'Brien, Harley, et al., 2005) and mechanical properties (Young's modulus) (Pelham and Wang, 1997; Grinnell, Ho, et al., 1999; Schulz-Torres, Freyman, et al., 2000; Freyman, Yannas, et al., 2001; Grinnell, 2003; Engler, Bacakova, et al., 2004; Jiang and Grinnell, 2005; Peyton and Putnam, 2005; Yeung, Georges, et al., 2005; Zaman, Trapani, et al., In preparation, 2006). However, the influence of specific mechanical features is unknown. Despite the large body of evidence suggesting that the mechanical properties of a scaffold are a significant factor affecting its bioactivity, comprehensive mechanical characterization of most biomaterials is not typically performed. In many tissue engineering studies, characterization of scaffold mechanical

properties is only done in a cursory manner or not at all. The rapidly increasing use of scaffolds has led to the need to better understand the role scaffold mechanical properties play in influencing cell behavior and overall scaffold bioactivity.

Uniform collagen-glycosaminoglycan (CG) scaffolds with well-characterized and controllable chemical, mechanical, and microstructural properties are an ideal platform for *in vitro* studies of the effect of the extracellular matrix environment, particularly mechanical stiffness, on cell behavior. The development of improved fabrication methods for CG scaffolds with a uniform, equiaxed pore structure (O'Brien, Harley, et al., 2004; O'Brien, Harley, et al., 2005) has been described in Chapter 2 and Chapter 3. These scaffolds have been engineered such that well-defined microstructural environments can be presented to individual cells within the scaffold. However, characterization of the mechanical properties of these scaffolds has not yet been performed.

Tissue engineering scaffolds often resemble low-density, open-cell foams, with an interconnected network of struts. Both can be modeled as cellular solids. In Chapter 4 cellular solids modeling was utilized to describe the specific surface area (O'Brien, Harley, et al., 2005) and permeability (O'Brien, Harley, et al., Submitted, 2005) of the CG scaffold variants under study in this investigation. The relationship between the microstructure and mechanical properties of cellular materials such as engineering foams has been studied extensively (Gibson and Ashby, 1997) and provides a model of the mechanical behavior of the CG scaffold variants. Since the microstructure of our CG scaffolds is similar to that of open-cell foams, we expect similar deformation mechanisms and stress-strain behavior.

The objective of this study is to characterize the mechanical properties of the series of uniform CG scaffolds with homogeneous microstructural characteristics that have been previously described in Chapters 2 - 4 (O'Brien, Harley, et al., 2004; O'Brien, Harley, et al., 2005). Here, we report the results of extensive tensile and compressive mechanical tests of the macroscopic scaffold as well as bending tests of the individual struts making up the scaffold network. The independent effects of hydration, pore size, crosslink density, and relative density on the compressive mechanical properties of the CG scaffolds are also reported. The macroscopic scaffold compression modulus and compressive strength are related to the individual strut modulus using models for low-density, open-cell foams. Coupled with previous microstructural characterization (O'Brien, Harley, et al., 2005), detailed mechanical characterization of these scaffolds represents a pathway for standardizing and quantifying the extracellular environment of the cells within these constructs. This characterization also allows quantitative *in vitro* experiments of cell behavior (contraction, migration) in defined microstructural and mechanical environments.

5.2. Cellular solids description of CG scaffold mechanical properties

Models describing the mechanical behavior of cellular solids such as open-cell foams are well developed (Gibson and Ashby, 1997). Of greatest interest in the study of cell-mediated contraction of CG scaffolds are the Young's modulus and the compressive strength, as fibroblasts have been shown to bend and buckle individual struts within the scaffold during contraction (Freyman, Yannas, et al., 2001). Both the Young's modulus and compressive strength of elastomeric open-cell foams depend on the relative density (ρ^*/ρ_s) of the foam (the

density of the foam, ρ^*, relative to that of the solid from which it is made, ρ_s), the Young's modulus of the solid from which the foam is made, E_s, and a constant related to the cell geometry. The complex geometry of foams (and of scaffolds) is difficult to model exactly; instead, dimensional arguments that rely on modeling the mechanisms of deformation and failure in the foam, but not the exact cell geometry, are used. Consider, for instance, the relative density of an open-cell foam of similar geometry (on average), with an edge length characterized by a distance l, and a thickness, t. The relative density is given by:

Equation 5.1.
$$\frac{\rho^*}{\rho_s} = \frac{M_s}{V^*} \cdot \frac{V_s}{M_s} \propto \frac{t^2 l}{l^3} = C \cdot \left(\frac{t}{l}\right)^2$$

where M_s is the mass of the solid, V^* is the volume of the foam and V_s is the volume of the solid. The relative density is proportional to $(t/l)^2$, independent of the choice of cell geometry; C is a constant of proportionality related to the cell geometry.

The stress–strain curve for a low-density, open-cell foam in compression is characterized by three distinct regimes (**Figure 5.1**) (Gibson and Ashby, 1997). At low levels of strain the struts bend, giving rise to a *linear elastic regime*. Additional strain results in elastic buckling, plastic yielding or brittle crushing of the struts depending on the material characteristics of the struts; all three mechanisms of strut failure continue at roughly constant load up to large strains, giving rise to a stress plateau (termed *collapse plateau*). For CG scaffolds, elastic buckling of the struts is expected to be the primary mechanism for this phenomenon. Finally, under increased strain, the pores collapse completely throughout the material and the struts are loaded against one another, leading to the final regime of *densification*.

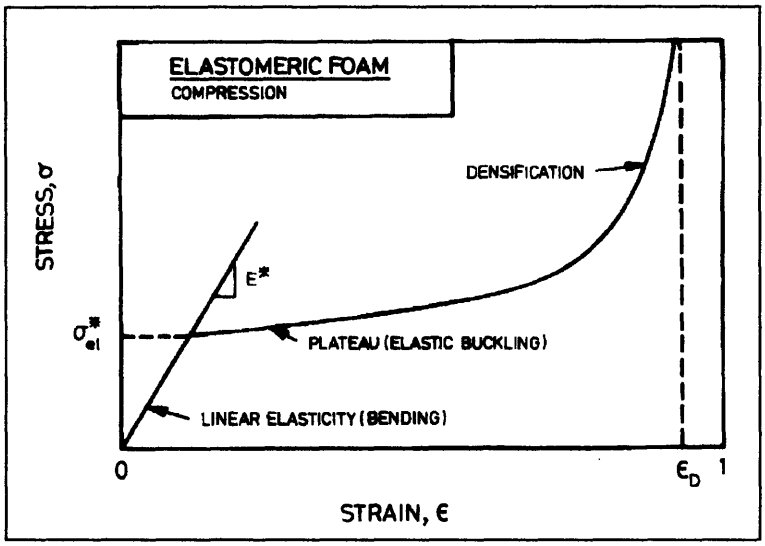

Figure 5.1. Schematic uniaxial stress–strain curve for an elastomeric cellular solid in compression showing linear elastic, collapse plateau, and densification regimes as well as the linear elastic modulus (E^*) and plateau stress (σ_{el}^*) (Gibson and Ashby, 1997).

For cellular materials with low relative densities (< 30%), the linear elastic-collapse plateau transition is typically observed at approximately 5% strain, while densification is not observed until very large strains (> 80%). In tension, for small strains, the initial linear elastic response is typically the same as is observed in compression. However, as the strain increases, the struts become increasingly oriented in the direction of applied tension, resulting in an increased material stiffness until tensile failure occurs. Extensive quantitative models have been developed to describe the mechanical behavior of foams, encompassing the linear elastic, collapse plateau, and densification regions (Gibson and Ashby, 1997). The linear elastic and collapse plateau regimes of the scaffold under compressive testing are of greatest interest for studies of cell-mediated contraction within CG-scaffolds.

Scanning electron microscopy, as well as micro-computed tomography observations, on open-cell foams indicate that at small strains within the linear elastic regime, the struts deform by bending (Gibson and Ashby, 1997; Gioux, McCormack, et al., 2000; Nazarian and Muller, 2004). The Young's modulus of open-cell foams, E^*, can be calculated using dimensional arguments (Gibson and Ashby, 1997):

Equation 5.2. $$E^* = C_1 \cdot \left(\frac{\rho^*}{\rho_s}\right)^2 \cdot E_s$$

where C_1 is a constant of proportionality related to the cell geometry and E_s is the Young's modulus of the solid from which the foam is made. Data for a wide variety of open-cell foams indicates that $C_1 \sim 1$ (Gibson and Ashby, 1997).

At sufficiently high strains, the struts of an elastomeric open-cell foam buckle (Gibson and Ashby, 1997). The compressive strength (also called the compressive plateau stress), σ_{el}^*, can be estimated using dimensional arguments involving the critical load for buckling of a strut (Gibson and Ashby, 1997):

Equation 5.3. $$\sigma_{el}^* = C_2 \cdot \left(\frac{\rho^*}{\rho_s}\right)^2 \cdot E_s$$

where C_2 is another constant of proportionality. Data for a wide variety of open-cell foams indicate that $C_2 \sim 0.05$, implying that the strain at which the cells start to collapse by elastic buckling is 0.05. It is also important to note that both the Young's modulus (E^*) and the

compressive strength (σ_{el}^*) of elastomeric open-cell foams vary with the square of the relative density and are independent of the cell or pore size.

While the pore size does not influence the mechanical properties of cellular solids, pore shape can significantly influence the isotropy/anisotropy of the scaffold. A more in depth description of this phenomena has previously been published (Gibson and Ashby, 1997). For illustrative purposes, a rectangular-prism unit cell with edge lengths of e_1, e_2, and e_3 (and *shape-anisotropy ratio* $R_{ij} = e_i/e_j$) will be utilized to explore its isotropic/anisotropic nature (**Figure 5.2**).

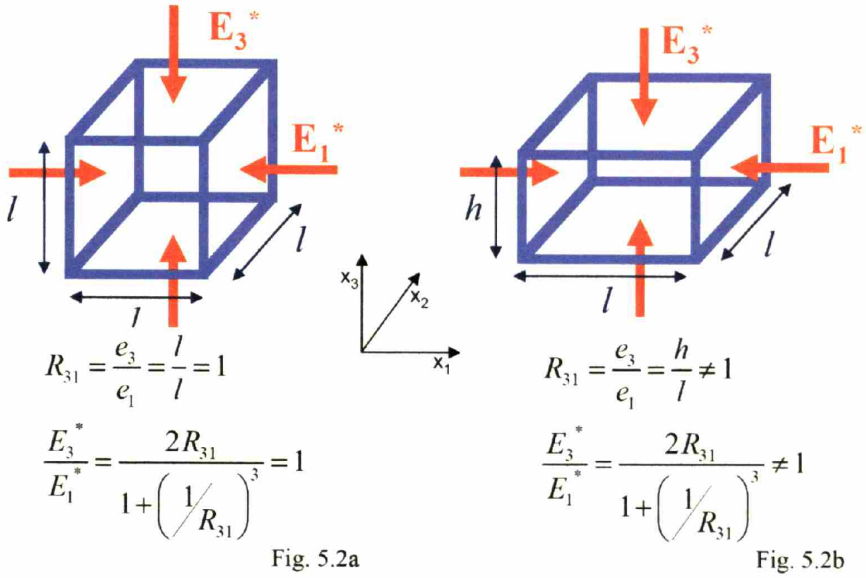

Figure 5.2. An axisymmetric unit cell with $R = 1$ ($e_1 = e_2 = e_3 = l$) (Fig. 5.2a); an axisymmetric unit cell with $R = 1.5$ ($e_1 = e_2 = l$; $e_3 = h$) (Fig. 5.2b).

The relative stiffness in two orthogonal directions can be defined by the *Young's modulus anisotropy number* (E_{rel}) (Gibson and Ashby, 1997):

Equation 5.4. $$E_{rel} = \frac{E_j^*}{E_i^*} = \frac{2 \cdot R_{ji}^{\,2}}{1 + \left(1/R_{ji} \right)^3}$$

For structurally isotropic cellular solids, $R = 1$, the cellular solid will be mechanically isotropic ($E_{rel} = 1$). However, for even small discrepancies in edge length ($R \neq 1$), E_{rel} rapidly diverges from 1, suggesting that even small levels of structural anisotropy result in significant mechanical anisotropy for the cellular solid.

5.3. Materials and Methods

5.3.1. Fabrication of CG scaffolds with different pore sizes

A complete description of the fabrication protocols of the four standard CG scaffolds with distinct mean pore sizes used in this investigation (**Table 5.1**) have been previously described in this thesis in Sections 2.3.1 (CG suspension), 2.3.4 (constant cooling rate solidification), and 2.3.5 (fabrication of uniform CG scaffolds with distinct mean pore sizes).

T_f, °C	**Mean Pore Size, μm Mean ± StDev**	**Relative Density Mean ± StDev**
-10	151 ± 32	0.0062 ± 0.0005
-20	121 ± 23	0.0061 ± 0.0003
-30	110 ±18	0.0059 ± 0.0003
-40	96 ± 12	0.0058 ± 0.0003

Table 5.1. CG scaffold variants utilized for permeability and specific surface area investigation.

Scaffolds fabricated at -20, -30, and -40°C display a uniform pore structure with equiaxed pores with no statistically significant difference in mean pore size between longitudinal (x-y plane) and transverse (x-z, y-z planes) planes. Scaffolds fabricated at -10°C display a uniform pore structure with slightly non-equiaxed pores: ellipsoidal pores with larger characteristic dimension in the longitudinal plane (x-y plane).

The relative density (ρ^*/ρ_s) of the CG scaffold variants was determined using the measured dry density of the collagen scaffold sheets (ρ^*) and the known dry density of solid collagen (ρ_s: 1.3 g/cm^3) (Yannas and Tobolsky, 1967; Yannas, Burke, et al., 1980). No significant difference in scaffold relative density (scaffold density divided by the density of the solid from which it is made) was found between the four scaffold variants, an expected result because all scaffolds were fabricated from an identical CG suspension recipe which established the amount of solid in the freeze-dried scaffold (**Table 5.1**) (O'Brien, Harley, et al., 2005).

5.3.2. Fabrication of CG scaffolds with different degrees of crosslinking

Two distinct crosslinking techniques were utilized following freeze-drying to modify scaffold stiffness independent of pore structure: a physical, dehydrothermal-based (DHT) process and a chemical, carbodiimide-based (1-ethyl-3-(3-dimethylaminopropyl)carbodiimide – EDAC) process (**Figure 5.3**). The DHT crosslinking treatment is carried out at a defined temperature (typically 90°C < T < 160°C) in a vacuum oven (Fisher IsoTemp 201, Fisher Scientific, Boston, MA) under a 50 mTorr vacuum for a defined length of time (Yannas, Lee, et al., 1989; Harley, Spilker, et al., 2004; O'Brien, Harley, et al., 2004; O'Brien, Harley, et al., 2005); this treatment induces the formation of covalent bonds between the polypeptide chains of the collagen fibers

without denaturing the collagen into gelatin (Yannas, 1972). The degree of crosslinking can be modulated by the length (time) and intensity (temperature) of the thermal treatment (Yannas, Lee, et al., 1989; Harley, Spilker, et al., 2004). The standard crosslinking treatment for all CG scaffolds in this study was DHT crosslinking at a temperature of 105°C for 24 hours. This standard treatment was used on all the scaffolds for this study with the exception of those used in the component that studied the effect of crosslink density on scaffold stiffness and should be considered the default crosslinking treatment for all scaffolds unless otherwise noted.

The carbodiimide-based (EDAC) crosslinking agent acts as a catalyst for formation of collagen-collagen and collagen-GAG crosslinks; as such, the cytotoxic EDAC chemicals are not incorporated into the amide crosslinks and can be rinsed from the scaffold following crosslinking (Osborne, Barbenel, et al., 1998; Pieper, Oosterhof, et al., 1999; Lee, Grodzinsky, et al., 2001). Scaffolds are immersed in a solution of 1-ethyl-3-(3-dimethylaminopropyl)carbodiimide (EDAC, Sigma Aldrich Chemical Co.) and N-hydroxysuccinimide (NHS, Sigma Aldrich Chemical Co.) for 30 minutes at room temperature; after crosslinking, the scaffolds are then washed in fresh phosphate buffered saline (PBS, Sigma Aldrich Chemical Co.) to remove any remaining chemical. The degree of crosslinking is modulated by altering the molar ratio of EDAC:NHS:COOH. The relative amounts of EDAC and NHS are proportioned relative to the density of carboxylic acid groups (COOH) per gram of collagen (1.2 mmol/gm) within the scaffold and the weight of each scaffold sample being crosslinked (Olde Damink, Dijkstra, et al., 1996). Greater crosslinking is achieved with higher ratios of EDAC and NHS to COOH (Olde Damink, Dijkstra, et al., 1996).

To study the effect of crosslink density on scaffold mechanical properties, a series of DHT and EDAC crosslinking treatments of varying intensity were used to differentially crosslink portions of the same scaffold sheet (mean pore size = 96 μm; relative density = 0.0058). Five distinct crosslinking treatments of increasing crosslink density were created: non-crosslinked (NX), DHT 105°C for 24 hours (DHT105/24), DHT 120°C for 48 hours (DHT120/48), 1:1:5 EDAC:NHS:COOH ratio (EDAC1:1:5), 5:2:1 EDAC:NHS:COOH ratio (EDAC5:2:1).

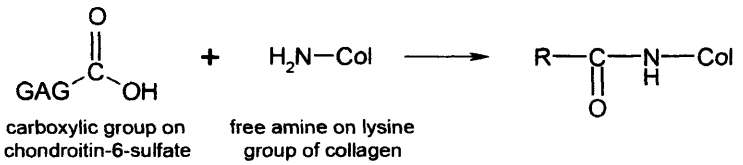

Fig.5.3a

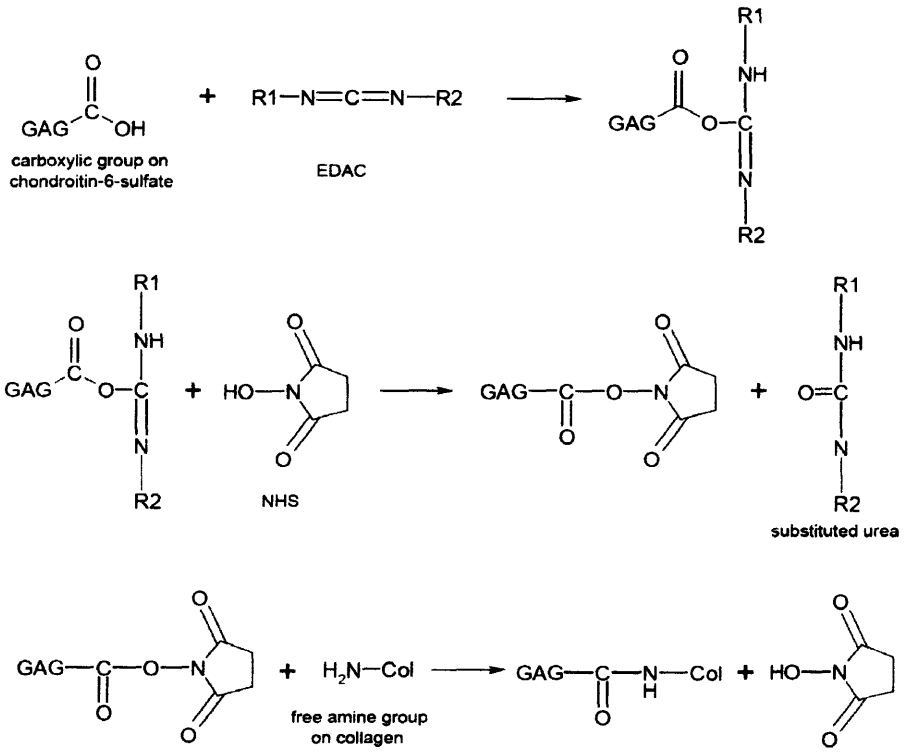

Fig. 5.3b

Figure 5.3. Crosslinking mechanism between collagen and GAG induced by dehydrothermal treatment (Fig. 5.3a) and by carbodiimide treatment (Fig. 5.3b) (Yannas and Tobolsky, 1967; Lee, Grodzinsky, et al., 2001; Lynn, 2005).

5.3.3. Fabrication of CG scaffolds with different relative densities

Four distinct scaffold variants with different relative densities were fabricated using a constant thermal profile (T_f = -40°C) to test the effect of scaffold relative density on mechanical properties. Increasing amounts of collagen and GAG were mixed together in 0.05M acetic acid using the standard mixing process defined in section 2.1 while maintaining a constant collagen:GAG weight ratio. A series of CG scaffolds were produced with relative densities of 0.006 (standard formulation, 1.0x), 0.009 (1.5x density), 0.012 (2.0x density), and 0.018 (3.0x density). All scaffolds were then crosslinked via the standard dehydrothermal crosslinking treatment (DHT105/24). SEM analysis confirmed that all scaffold variants maintained a consistent pore microstructure.

5.3.4. Mechanical characterization of CG scaffolds

Unidirectional, unconfined compression and tension tests, both at a constant strain rate of 0.1% strain/sec, were performed on dry and hydrated samples of the CG scaffold. Hydrated scaffold samples were prepared by placing each sample in phosphate buffered saline (PBS, Sigma Aldrich Chemical Co.) for 12 hours prior to testing to allow the scaffolds to become fully hydrated (Harley, Spilker, et al., 2004). A series of scaffolds with different mean pore sizes (96, 110, 121, 151 μm), constant relative density (0.006), and constant crosslinking treatment (DHT105/24) were tested in compression in both the dry and hydrated state to measure the independent effect of scaffold microstructure on mechanical properties. The remainder of the mechanical tests were then performed on either dry or hydrated scaffolds where at least one of the initial series of scaffolds described above was tested in order to determine the relative effect of the variable under testing (*i.e.*, relative density, crosslinking density, isotropy) and where the

hydration state was determined based upon the variable being tested. For example, EDAC crosslinked scaffolds are hydrated during the crosslinking process so the mechanical tests on scaffolds with variable crosslinking density were all performed on hydrated scaffold sample.

Scaffold samples from one of the uniform scaffold variants with equiaxed pores (mean pore size: 96 μm), constant relative density (0.006), and constant crosslinking treatment (DHT105/24) was then tested in compression in the dry state in three orthogonal axes to determine scaffold mechanical isotropy. A second series of scaffolds with constant mean pore size (96 μm), constant relative density (0.006), and variable crosslinking treatment (NX, DHT105/24, DHT120/48, EDAC1:1:5, EDAC5:2:1) were then tested in compression in the hydrated state to measure the independent effect of scaffold crosslinking on mechanical properties. A third series of scaffolds with constant mean pore size (96 μm), constant crosslinking treatment (DHT105/24), and variable relative density (0.006, 0.009, 0.012, 0.018) were then tested in compression in the dry state to measure the independent effect of scaffold relative density on mechanical properties. Finally, scaffold samples with a constant mean pore size (96 μm), constant relative density (0.006), and constant crosslinking treatment (DHT105/24) were tested in the hydrated state in tension to measure the difference in the compressive and tensile behavior of these scaffolds.

Two distinct sample geometries were cut from CG scaffold sheets (125 mm x 125 mm x 3.4 mm) and used during this experiment: disks and rectangular prisms. Arbitrary orthogonal axes were assigned to the system for the course of this investigation: the x- and y-axes were defined to be in the plane of the scaffold sheet while the z-axis was defined to be perpendicular to the plane of the scaffold sheet. Cylindrical disk samples were cut from sheets of CG scaffold using dermal

biopsy punches for mechanical tests on dry scaffold samples (5, 6, 8 mm diameter circular biopsy punches, Miltex, Inc., York, PA) or using larger, sharpened circular punches for mechanical tests on hydrated samples (16, 18, 20 mm diameter punches, Hollow Punch Set, Boehm, France). All compression tests were performed on cylindrical scaffold disks in the z-direction (perpendicular to the plane of the scaffold sheet). To test scaffold mechanical isotropy in compression, a series of rectangular samples were cut from the sample scaffold sheet (3.4 mm x 3.4 mm x 16.5 mm) and tested in the appropriate axis (x, y, z). For tensile tests, rectangular samples (3.4mm thick x 21 mm wide x 42 mm gauge length) were also utilized.

Compression tests were performed using two distinct mechanical testing devices. Initial mechanical tests and high resolution compression tests on dry and hydrated CG scaffolds were performed using a custom fabricated mechanical testing device. A 0.25 N precision tension-compression load cell (GSO-25, Error: ± 0.125 mN, Transducer Techniques, Temecula, CA) was attached via a custom bracket to the high-precision motor platform of the NanoTest600 Micro/Nanoindenter (MicroMaterials LLC, Wrexham, UK). The motor platform was moved at a defined strain rate (0.1% strain/sec) to perform unconfined compression tests to a maximum strain of 95%. Load cell data was acquired using a customized VI built in LabVIEW (National Instruments, Austin, TX) sampling at a frequency of 5 Hz; both load-hold and load-unload cycles were tested (**Figure 5.4**). The custom mechanical testing device was used to perform mechanical tests on dry and hydrated scaffolds with variable mean pore size (96 – 151 μm) and constant relative density and crosslinking (0.006, DHT105/24); on dry scaffolds with variable relative density (0.006 – 0.018) and constant pore size and crosslinking (96 μm, DHT105/24); and on a single dry scaffold variant (96 μm, 0.006 relative density, DHT105/24) in three orthogonal axes.

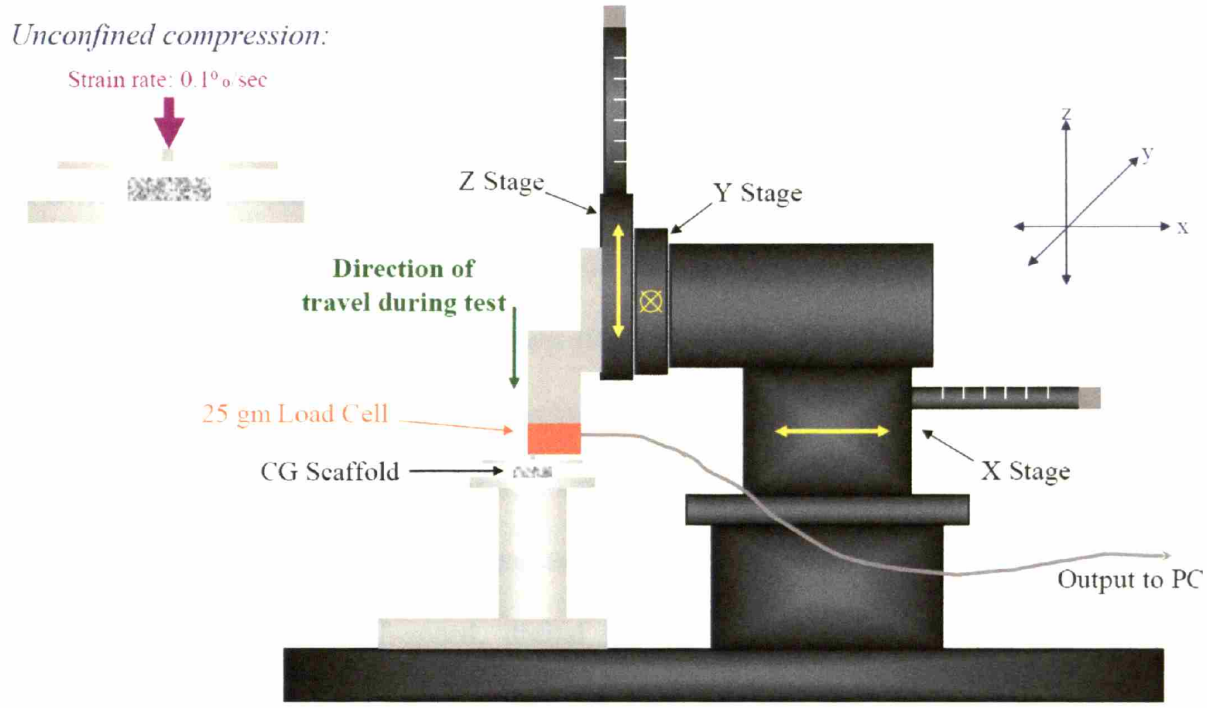

Figure 5.4. Custom mechanical testing device built on the NanoTest600 Micro/Nanoindenter motor platform using a precision load cell; all tests were performed at a strain rate of $\partial\varepsilon/\partial t$ = 0.001/sec to a maximum strain: $\varepsilon_{max} = 0.95$.

During the course of this investigation, access to Zwick/Roell Z2.5 static materials tester (Zwick GmbH & Co., Ulm, Germany) with integrated testing software was obtained. Mechanical tests on dry and hydrated scaffolds (mean pore sizes: 96, 110, 121, 151 μm; relative density: 0.006; crosslinking: DHT105/24) were performed at a constant compression rate of 0.1% strain/sec to a maximum strain of 85% with a 20 N load cell (Part No. BTC-LC0020N.P01, Zwick) sampling at a frequency of 2 Hz. Control of the testing profile (*i.e.*, strain rate, ultimate strain, sampling rate, data collection and storage) was controlled on a PC using the testXpert software package (Zwick). Comparisons were made of the results obtained from the two different mechanical

testing devices, and no difference was observed between mechanical tests using either testing apparatus.

The Zwick/Roell mechanical tester was used to perform mechanical tests on hydrated scaffolds with variable crosslinking density (NX, DHT105/24, DHT120/48, EDAC1:1:5, EDAC5:2:1) and constant mean pore size and relative density (96 μm, 0.006). The Poisson's ratio (ν) of the dry (mean pore sizes: 96, 110, 121, 151 μm; relative density: 0.006; crosslinking: DHT105/24) and hydrated (mean pore sizes: 110, 121 μm; relative density: 0.006; crosslinking: DHT105/24) CG scaffolds was also calculated from compression tests performed using the Zwick/Roell Z2.5 static materials tester. A high-speed, digital CCD Camera (Retiga 1300, QImaging Corp., Canada) with a 200 mm lens (Nikon, Japan) was used to observe the lateral expansion of the CG scaffold sample disk during unconfined compression up to 80% applied strain at a sample rate of 2 Hz. A software analysis package (Vic2D, Correlated Solutions, West Columbia, SC) was used to correlate the applied vertical strain with the observed lateral strain to determine the Poisson's ratio of the CG scaffolds for the linear elastic and collapse plateau regimes.

Hydrated CG scaffolds (96 μm mean pore size, 0.006 relative density, DHT105/24) were tested in tension in the plane of the scaffold (x, y) at a constant strain rate of 0.01%/sec using the Zwick/Roell Z2.5 static materials testing machine with a 20 N load cell (Zwick) sampling at a rate of 10 Hz. A rectangular sample (width: 21mm, thickness: 3.4mm, gauge length: 42 mm) of the scaffold cut from the plane of the sheet of scaffold was hydrated for 12 hours in PBS (Sigma Aldrich) and then held vertically in the Zwick mechanical tester using custom designed clamps for testing. The sample and the clamps remained submerged in PBS throughout the mechanical

test, and the actual gauge length for each experimental run was determined automatically by the Zwick data acquisition software.

5.3.5. Mechanical characterization of individual struts of CG scaffold

The bending stiffness of the individual scaffold struts cut from a non-hydrated CG scaffold (121 μm pore size, 0.006 relative density, DHT105/24) was measured via atomic force microscopy (MFP3D AFM, WaveMetrics, Inc., Portland, OR) using the supplied control and analysis software (IgorPro, WaveMetrics). Individual struts of the CG scaffold were removed from the scaffold using microsurgical forceps and a scalpel under a dissecting microscope. The individual struts were attached to a standard glass slide using superglue with the strut cantilevered over the edge of the glass slide. Bending tests were performed on the cantilevered CG scaffold strut using an AC240TS AFM cantilever (Asylum Research, Santa Barbara, CA) (**Figure 5.5a**). Frequency analysis of the AFM cantilever calculated the AFM cantilever stiffness ($K_{cantilever}$ = 1.1 N/m). A variety of loading rates (1 – 96.72 μm/sec) and loading distances (2 – 5.42 μm) were utilized for tests on the CG scaffold struts. Experimental results were expressed in terms of the displacement of the AFM cantilever base (d_t) and the displacement of the AFM cantilever tip (d_2).

To calculate the CG scaffold strut modulus (E_s), the strut-AFM cantilever system was simplified to a conventional beam bending system by calculating the vertical displacement of the CG scaffold strut at the point of contact with the cantilever (d_1) (**Figure 5.5b**):

Equation 5.5. $$d_1 = d_t - d_2$$

Experimental arrangement:

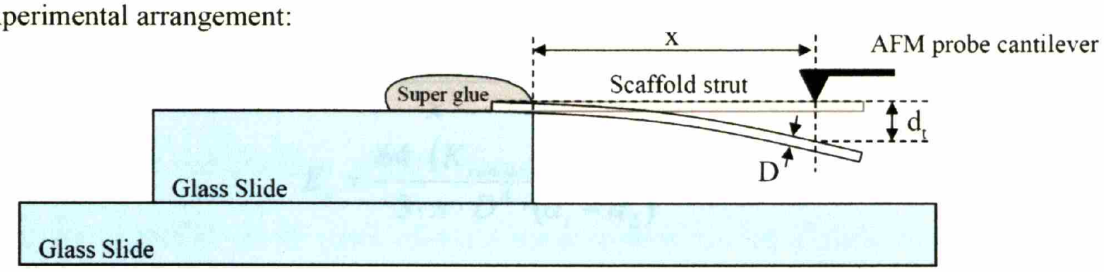

Fig. 5.5a

Equivalent beam bending model:

Experimental condition: *Simplified system for analysis:*

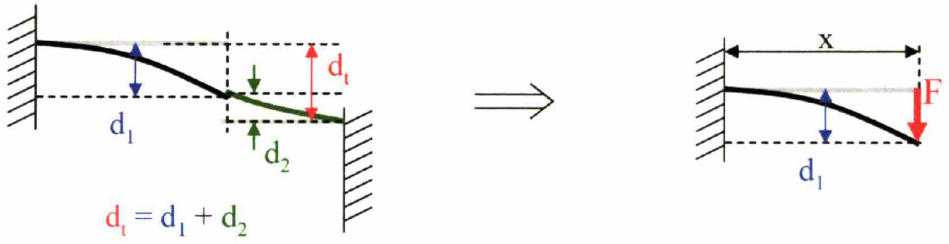

Fig. 5.5b

Figure 5.5. Experimental arrangement to perform bending tests on individual CG scaffold struts (Fig. 5.5a). Simplified beam bending system utilized to calculate CG scaffold strut modulus (E_s) in terms of experimentally measured parameters (d_t, d_2, $K_{cantilever}$) (Fig. 5.5b).

Using conventional beam theory, the force of the AFM cantilever on the scaffold strut (F) was calculated from the measured stiffness of the AFM cantilever ($K_{cantilever}$) and the deflection of the AFM cantilever (d_2) (**Eq. 5.6a**). Using beam theory (**Eq. 5.6b**) and the assumption of a cylindrical scaffold strut for the calculation of the moment of inertia ($I = \pi \cdot D^4/64$), the scaffold strut modulus (E_s) was calculated using the AFM cantilever stiffness ($K_{cantilever}$), the AFM cantilever base displacement (d_t), the AFM cantilever tip displacement (d_2), the average CG scaffold strut diameter for each sample (D), and the distance from the glass slide support where the test was performed (x) (**Figure 5.5b**) (**Eq. 5.6c**):

Equation 5.6.

$$F = K_{cantilever} \cdot d_2 \quad \text{(5.6a)}$$

$$F = \frac{3 \cdot E_s \cdot I \cdot d_1}{x^3} \quad \text{(5.6b)}$$

$$E_s = \frac{64 \cdot \left(K_{cantilever} \cdot d_2\right) \cdot x^3}{3 \cdot \pi \cdot D^4 \cdot \left(d_t - d_2\right)} \quad \text{(5.6c)}$$

Using the cellular solids relationship introduced in **Eq. 5.2** (Section 5.2), the measured strut modulus, E_s, and measured scaffold relative density (**Table 5.1**) were used to estimate the Young's modulus, E^*, of the scaffold. This calculated modulus was then compared to the experimentally measured scaffold modulus (as described in section 5.3.4) to provide improved understanding of the relationship between the macroscopic and microscopic mechanical properties of the CG scaffolds.

5.3.6. Statistical analysis

One-way analysis of variance (ANOVA) and pair wise multiple comparison procedures (Dunn's Method) were used to compare groups of data. Paired t-tests were performed to compare individual sets of data to determine statistical significance between 24 and 48 hour groups using the same scaffold. Error is reported in figures as the standard deviation (StDev), the standard error of the mean (SEM = StDev/$n^{1/2}$), or as the coefficient of variance (CV = StDev/Mean). A probability value of 95% ($p < 0.05$) was used to determine significance. A minimum of 6 distinct scaffold samples were tested for each data point reported in this investigation.

5.4. Results

5.4.1. Unconfined compression tests on CG scaffolds

Figure 5.6 shows compressive stress-strain curves observed for the dry and hydrated CG scaffolds. As expected, in all cases, distinct linear elastic, collapse plateau, and densification regimes were observed for both dry and hydrated CG scaffolds. The linear elastic modulus (E^*), the elastic collapse stress and strain (σ_{el}^*, ε_{el}^*), and the collapse plateau modulus ($\Delta\sigma/\Delta\varepsilon$) were calculated for each compression test.

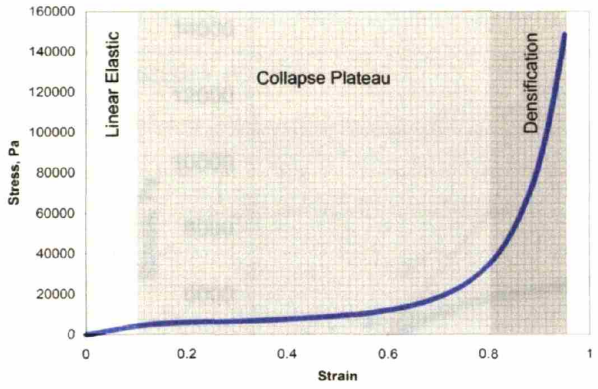

Fig. 5.6a

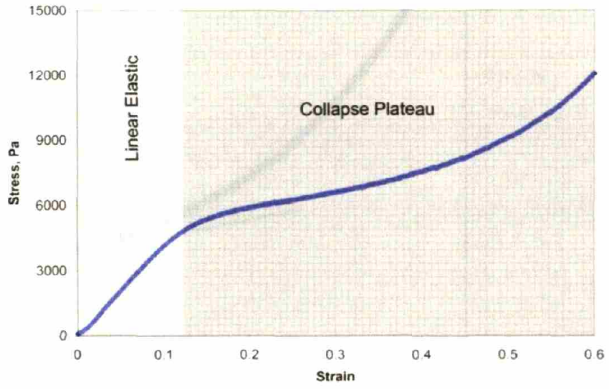

Fig. 5.6b

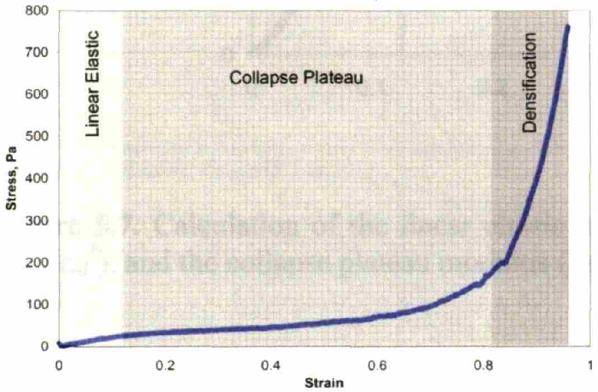

Fig. 5.6c

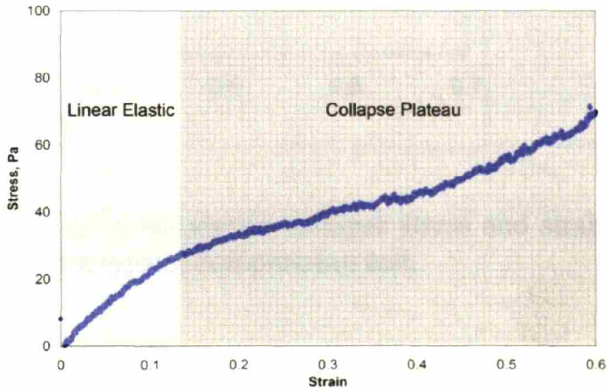

Fig. 5.6d

Figure 5.6. Characteristic stress-strain curves observed for the dry (Fig. 5.6a, b) and hydrated CG scaffold variants (Fig. 5.6c, d) showing the full stress-strain curves for the entire compression test (ε: 0 – 0.95, Fig. 5.6a, c) and increased detail of the linear elastic region (ε: 0 – 0.60, Fig. 5.6b, d). Distinct linear elastic, collapse plateau, and densification regimes were observed for the CG scaffolds (regimes approximately demarked by individually shaded regions) regardless of scaffold mean pore size, relative density, crosslinking density, loading direction, or level of hydration.

The linear elastic modulus was determined by linear regression of the initial linear regime of the compressive stress-strain curve. The collapse plateau modulus was determined by linear regression of the linear region in the stress-strain curve following the "knee" corresponding to the strut bending-buckling transition. The elastic collapse stress and strain was determined from the intersection of the linear elastic and collapse plateau linear regression curves (**Figure 5.7**).

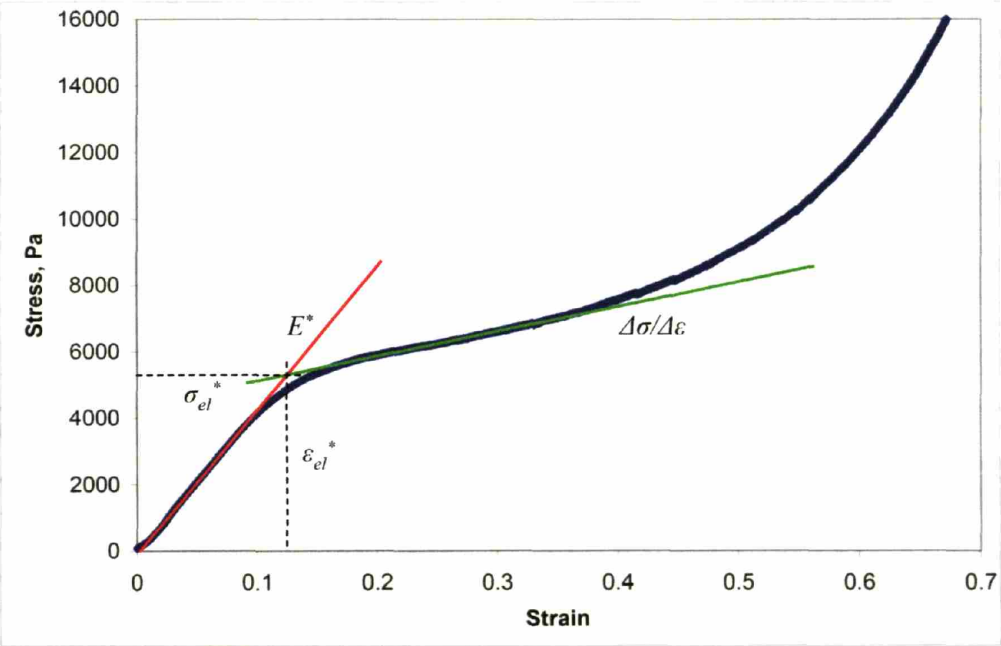

Figure 5.7. Calculation of the linear elastic modulus (E^*), the elastic collapse stress and strain (σ_{el}^*, ε_{el}^*), and the collapse plateau modulus ($\Delta\sigma/\Delta\varepsilon$) for a typical compression test.

The linear elastic modulus (E^*), elastic collapse stress and strain (σ_{el}^*, ε_{el}^*), and the collapse plateau modulus ($\Delta\sigma/\Delta\varepsilon$) for each experimental system was then calculated. Results describing the effect of mean pore size, hydration, crosslink density, relative density, and direction of compression on each of these variables are reported in **Table 5.2.**

Test	Scaffold Variant	E^*	σ_{el}^*	ε_{el}^*	$\Delta\sigma/\Delta\varepsilon$
Effect of mean pore size (dry)		**E^*, kPa**	**σ_{el}^*, Pa**	**ε_{el}^***	**$\Delta\sigma/\Delta\varepsilon$, kPa**
	96 μm	31.7 ± 3.9	5350 ± 630	0.184 ± 0.017	7.0 ± 0.9
	110 μm	28.5 ± 3.4	4810 ± 520	0.196 ± 0.024	9.2 ± 1.5
	121 μm	29.8 ± 3.9	5290 ± 280	0.202 ± 0.021	10.6 ± 1.9 *
	151 μm	39.4 ± 4.5 *	6250 ± 280 *	0.182 ± 0.027	13.9 ± 3.8 **
Effect of mean pore size (hydrated)		**E^*, Pa**	**σ_{el}^*, Pa**	**ε_{el}^***	**$\Delta\sigma/\Delta\varepsilon$, Pa**
	96 μm	206 ± 36	18 ± 4	0.079 ± 0.017	98 ± 15
	110 μm	176 ± 41	14 ± 8	0.076 ± 0.031	83 ± 11
	121 μm	221 ± 47	31 ± 5 *	0.151 ± 0.055 *	93 ± 11
	151 μm	229 ± 22	22 ± 4	0.107 ± 0.022	94 ± 18
Effect of crosslink density (hydrated)		**E^*, normalized**	**σ_{el}^*, normalized**	**ε_{el}^*, normalized**	**$\Delta\sigma/\Delta\varepsilon$, normalized**
	Standard	***208 ± 41 Pa***	***21 ± 8 Pa***	***0.10 ± 0.04***	***92 ± 14 Pa***
	NX	0.74 ± 0.13	0.73 ± 0.096	0.94 ± 0.073	0.85 ± 0.23 *
	DHT105/24	***1.00 ± 0.051*** *	***1.00 ± 0.057***	***1.00 ± 0.093***	***1.00 ± 0.087***
	DHT120/48	1.08 ± 0.063 *	1.03 ± 0.076	1.02 ± 0.091	1.03 ± 0.11
	EDAC1:1:5	2.0 ± 0.11 **	1.06 ± 0.65	0.72 ± 0.42	1.25 ± 0.14 **
	EDAC5:2:1	7.20 ± 0.14 ***	3.59 ± 0.87 *	0.83 ± 0.35	3.06 ± 0.18 ***
Scaffold isotropy (dry)		**E^*, normalized**	**σ_{el}^*, normalized**	**ε_{el}^*, normalized**	**$\Delta\sigma/\Delta\varepsilon$, normalized**
	Standard	***30.0 ± 3.9 kPa***	***5.2 ± 0.53 kPa***	***0.20 ± 0.02***	***10.2 ± 3.3 kPa***
	x-axis	0.81 ± 0.27	0.64 ± 0.21 *	1.00 ± 0.18	0.58 ± 0.071
	y-axis	1.01 ± 0.15	0.94 ± 0.11	1.00 ± 0.11	0.66 ± 0.25
	z-axis	***1.00 ± 0.13***	***1.00 ± 0.17***	***1.00 ± 0.095***	***1.00 ± 0.23*** *
Effect of relative density (dry)		**E^*, normalized**	**σ_{el}^*, normalized**	**ε_{el}^*, normalized**	**$\Delta\sigma/\Delta\varepsilon$, normalized**
	Standard	***30.0 ± 3.9 kPa***	***5.2 ± 0.53 kPa***	***0.20 ± 0.02***	***10.2 ± 3.3 kPa***
	0.006 (1.0x)	***1.00 ± 0.11***	***1.00 ± 0.10***	***1.00 ± 0.019***	***1.0 ± 0.082***
	0.009 (1.5x)	1.28 ± 0.11 *	1.21 ± 0.063 *	1.05 ± 0.042	2.16 ± 0.065 *
	0.012 (2.0x)	2.24 ± 0.058 **	2.06 ± 0.025 **	1.00 ± 0.065	3.32 ± 0.049 **
	0.018 (3.0x)	2.76 ± 0.10 ***	2.77 ± 0.62 ***	1.25 ± 0.064 *	8.66 ± 0.062 ***

Table 5.2. Results of mechanical characterization of CG scaffold variants. Except for the specific parameter being tested in each section, all scaffold characteristics were kept constant (96 μm mean pore size; 0.006 relative density; DHT105/24 crosslinking; dry; z-axis compression). Results are reported as Mean ± StDev for the tests of the effect of mean pore size (dry and hydrated). All other results are reported as normalized Mean ± CV; the standard values reported in the top row of each test results (shaded, italicized) correspond to other italicized data series (*i.e.*, DHT105/24 for the test of the effect of crosslink density). *, **, and *** denote distinct, statistically significant results.

5.4.2. CG scaffold linear elastic modulus: Effect of mean pore size

Complete results of the mechanical characterization (E^*, σ_{el}^*, ε_{el}^*, $\Delta\sigma/\Delta\varepsilon$) of the CG scaffold variants are reported in **Table 5.2**. **Figure 5.8** shows the linear elastic modulus for the dry and hydrated CG scaffold variants with variable mean pore sizes (96, 110, 121, 151 μm), constant relative density (0.006), and constant crosslinking (DHT105/24).

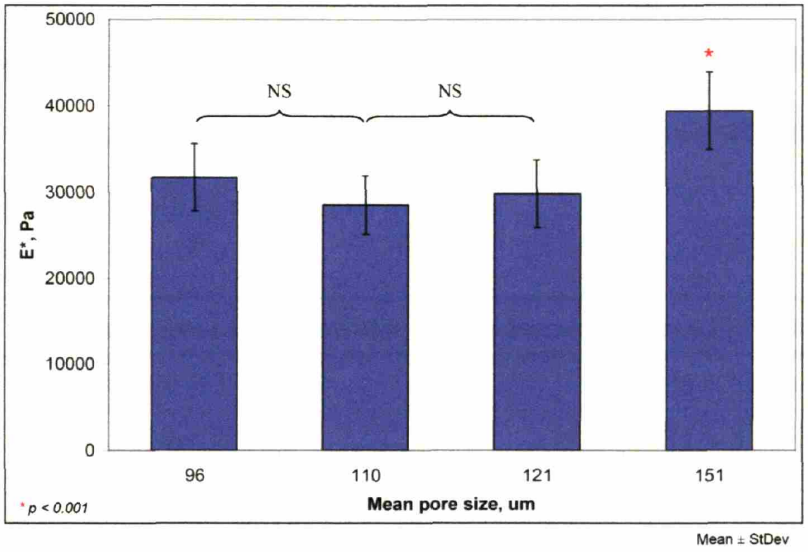

Fig. 5.8a

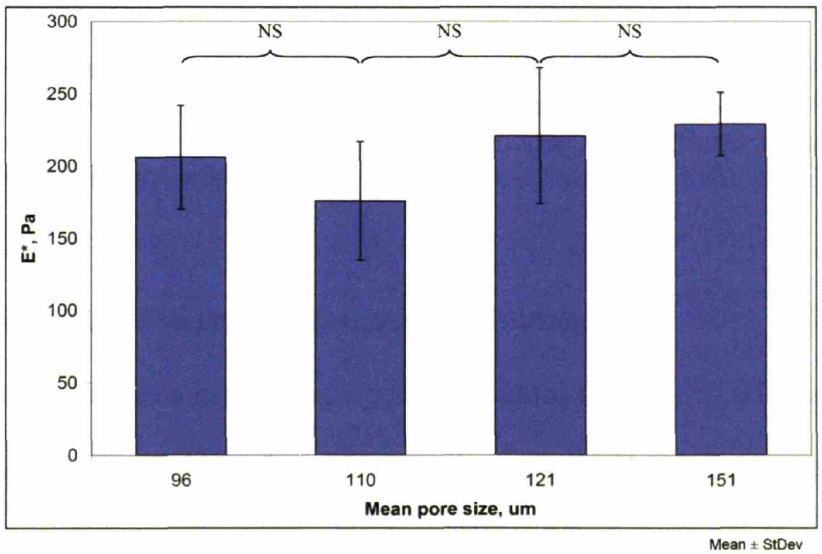

Fig. 5.8b

Figure 5.8. Linear elastic modulus (E^*) of the dry (Fig. 5.8a) and hydrated (Fig. 5.8b) CG scaffold variants (96 – 151 μm mean pore size; DHT crosslinking; 0.006 relative density).

No significant difference in E^* was found for any of the scaffolds with a uniform, isotropic pore structure and equiaxed pores (Mean pore size: 96 – 121 μm). However, the scaffold with slightly anisotropic microstructure (Mean pore size: 151 μm) displayed a statistically significant stiffer E^* in the dry state ($p < 0.001$). This effect was not observed in the hydrated state.

The average mechanical properties of the CG scaffolds (E^*, σ_{el}^*, ε_{el}^*, $\Delta\sigma/\Delta\varepsilon$) are listed in **Table 5.3**. As the scaffold with slightly anisotropic microstructure (Mean pore size: 151 μm) displayed a statistically significant greater E^* and σ_{el}^* in the dry state, these values were not included in the calculation of the average scaffold properties.

Criteria	Non-hydrated CG Scaffold	Hydrated CG Scaffold (12 hours PBS)
E^*	30,000 ± 3900 Pa $^{\zeta}$	208 ± 41 Pa
σ_{el}^*	5150 ± 530 Pa $^{\zeta}$	21 ± 8 Pa
ε_{el}^*	0.20 ± 0.02	0.10 ± 0.04
$\Delta\sigma/\Delta\varepsilon$	10,200 ± 3300 Pa	92 ± 14 Pa

Table 5.3. Average (Mean ± St. Dev.) mechanical properties of the CG scaffold variants (results independent of mean pore size). $^{\zeta}$ The 151 μm mean pore size scaffold showed a statistically significant increase in linear elastic modulus and collapse stress; these values, likely due to scaffold structural anisotropy, were not used to calculate average mechanical values.

5.4.3. CG Scaffold Linear Elastic Modulus: Scaffold isotropy

The results of mechanical tests in three orthogonal directions (X-axis, Y-axis, Z-axis) on samples from a single sheet of a scaffold variant with a uniform pore microstructure and equiaxed pores (96 μm mean pore size, 0.006 relative density, DHT105/24 crosslinking, dry) are shown in **Table 5.2** and **Figure 5.9**. The linear elastic modulus results from each of the three axes (E_x^*, E_y^*, E_z^*) were normalized by the modulus from the standard test direction (E_z^* = 208 ± 41 Pa) for

ease of comparison. No significant difference ($p > 0.05$) in modulus was found for any of the loading directions, indicating that the scaffolds are mechanically as well as microstructurally isotropic.

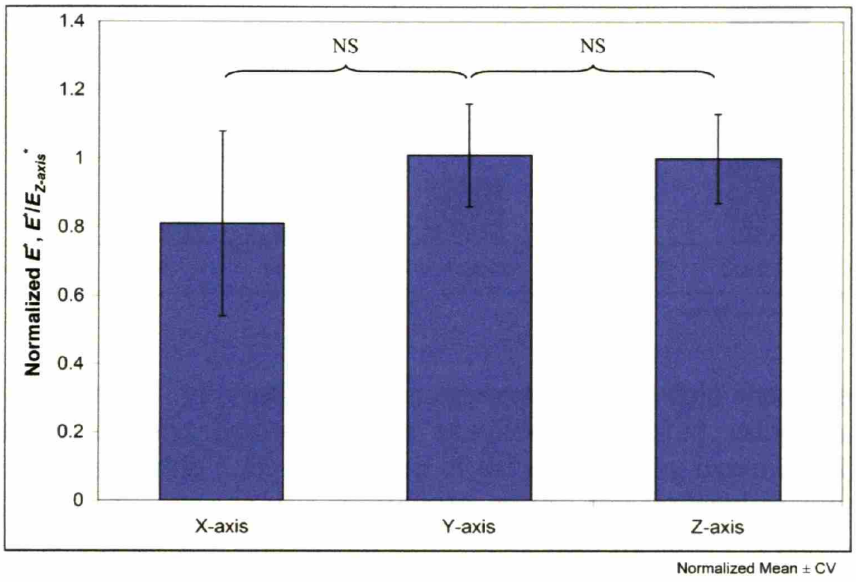

Figure 5.9. Normalized E^* of structurally homogeneous CG scaffold (96 μm mean pore size; DHT crosslinking; 0.006 relative density; dry) from tests in three orthogonal directions. E^* for each of the three axes (E_x^*, E_y^*, E_z^*) was normalized by the modulus from the standard test direction ($E_z^* = 208 \pm 41$ Pa).

5.4.4. CG scaffold linear elastic modulus: Effect of crosslinking density

Figure 5.10 and **Table 5.2** show the results of mechanical tests (E^*) on hydrated scaffold samples with constant mean pore size (96 μm) and relative density (0.006), but variable crosslinking density (NX, DHT105/24, DHT120/48, EDAC1:1:5, EDAC5:2:1). All results were normalized by the modulus of the scaffold treated with the standard crosslinking density ($E_{DHT105/24}^* = 208 \pm 41$ Pa) for ease of determining the independent effect of crosslinking density on the stiffness of the CG scaffold and on the stiffness of the individual scaffold struts.

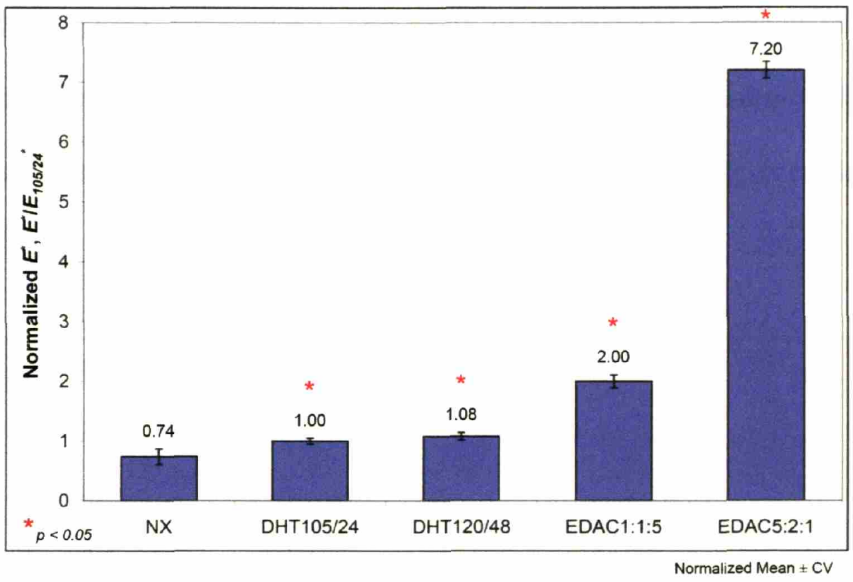

Figure 5.10. Normalized E^* of structurally homogeneous CG scaffold sheet (96 μm mean pore size; 0.006 relative density; hydrated) with samples crosslinked using each of the five crosslinking treatments (**Table 5.2**). E^* for each of the crosslinking treatment (E_{NX}^*, $E_{DHT105/24}^*$, $E_{DHT120/48}^*$, $E_{EDAC1:1:5}^*$, $E_{EDAC5:2:1}^*$) was normalized by the standardized crosslinking treatment ($E_{DHT105/24}^* = 208 \pm 41$ Pa). The normalized stiffness of each treatment is displayed above each data bar.

Relative stiffnesses of 0.74, 1.0, 1.08, 2.0, and 7.2 were found for NX, DHT105/24, DHT120/48, EDAC1:1:5, and EDAC5:2:1 crosslinking treatments, respectively. A significant effect of crosslink treatment ($p < 0.0001$) was observed between all crosslinking treatments except between DHT105/24 and DHT120/48; in this case, a significant effect was suggested ($p = 0.10$), but the result was not statistically significant.

5.4.5. CG scaffold linear elastic modulus: Effect of relative density

CG suspensions with increasing solid content were used to fabricate a series of higher density CG scaffolds. 1.0x, 1.5x, 2.0x, and 3.0x dense suspensions were produced, resulting in scaffolds with relative densities of 0.006, 0.009, 0.012, and 0.018 (Actual normalized relative densities:

1.0x, 1.53x, 2.10x, 3.13x), respectively. The result of mechanical characterization on dry CG scaffold variants with constant freezing conditions (T_f = -40°C), constant crosslinking treatment (DHT105/24) and variable relative density (0.006, 0.009, 0.012, 0.018) is presented in **Figure 5.11** and **Table 5.2**.

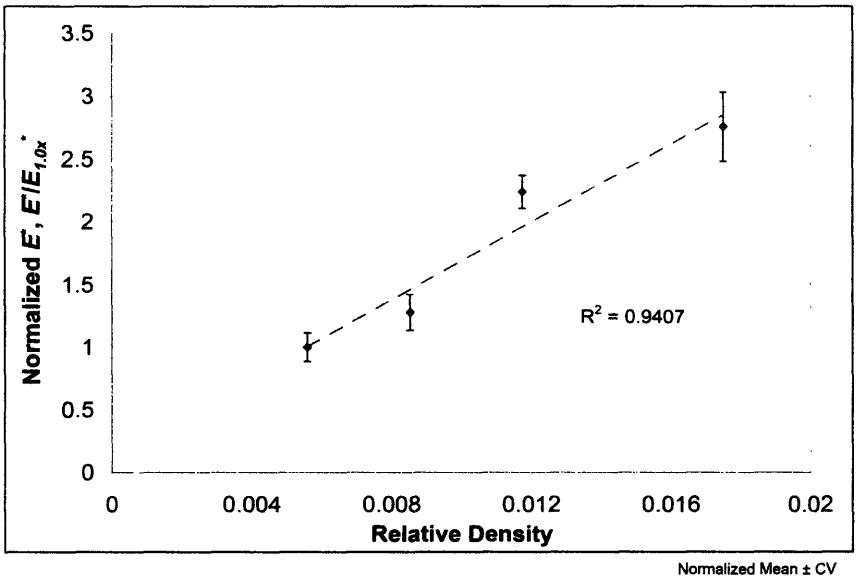

Figure 5.11. Normalized E^* of CG scaffolds (T_f = -40°C; DHT crosslinking; dry) fabricated with distinct relative densities (0.006, 0.009, 0.012, 0.018). E^* for each of the relative densities ($E_{0.006}^*$, $E_{0.009}^*$, $E_{0.012}^*$, $E_{0.018}^*$) was normalized by the standard relative density ($E_{0.006}^*$, 1.0x = 208 ± 41 Pa). Normalized regression curve from **Eq. 5.8** is also plotted.

A significant effect of relative density was found ($p < 0.05$), where scaffolds with increased relative densities had significantly greater E^*, $\Delta\sigma/\Delta\varepsilon$, and σ_{el}^* but a consistent ε_{el}^* with the exception of a significantly greater ε_{el}^* for the scaffold with the highest relative density. To determine the relationship between E^* and scaffold relative density, a regression was performed between $\ln(E^*)$ and $\ln(\rho^*/\rho_s)$:

Equation 5.7. $$\ln(E^*) = 0.9518 \cdot \ln\left(\frac{\rho^*}{\rho_s}\right) + 15.215$$

The results of the regression suggest that at these extremely low relative densities (0.006 – 0.0175) a nearly linear relationship exists between scaffold modulus and relative density:

Equation 5.8. $$E^* = 4.05 \times 10^6 Pa \cdot \left(\frac{\rho^*}{\rho_s} \right)^{0.9518}$$

5.4.6. CG scaffold compressive buckling stress, strain, and collapse modulus

Complete results of the analysis of the effect of mean pore size (dry, hydrated), crosslinking density, relative density, and scaffold isotropy on the buckling stress (σ_{el}^*), buckling strain (ε_{el}^*), and collapse modulus ($\Delta\sigma/\Delta\varepsilon$) are shown in **Table 5.2**. The trends observed for the buckling stress (σ_{el}^*) closely mirror those seen for the linear elastic modulus (E^*): no significant effect of mean pore size; increasing σ_{el}^* with crosslinking density; isotropy; and increasing σ_{el}^* with relative density. As with E^*, a linear relationship between σ_{el}^* and (ρ^*/ρ_s) was observed:

Equation 5.9. $$\sigma_{el}^* = 6.65 \times 10^5 Pa \cdot \left(\frac{\rho^*}{\rho_s} \right)^{0.9473}$$

The trends observed with the buckling strain (ε_{el}^*) appear to be largely independent of mean pore size, crosslink density, direction of testing, and relative density. The trends observed with the collapse modulus ($\Delta\sigma/\Delta\varepsilon$) closely mirror those seen for the linear elastic modulus (E^*): no significant effect of mean pore size, increasing $\Delta\sigma/\Delta\varepsilon$ with crosslinking density, isotropy, and increasing $\Delta\sigma/\Delta\varepsilon$ with relative density. The increase in $\Delta\sigma/\Delta\varepsilon$ with crosslink density was not as significant as was observed with E^* and was similar to that seen with σ_{el}^*. A power relationship was observed between $\Delta\sigma/\Delta\varepsilon$ and (ρ^*/ρ_s) for dry scaffolds:

Equation 5.10. $$\Delta\sigma / \Delta\varepsilon = 1.58 \times 10^{8} Pa \cdot \left(\frac{\rho^{*}}{\rho_{s}} \right)^{1.867}$$

5.4.7. CG scaffold linear Poisson's ratio: Effect of mean pore size

The Poisson's ratio of a series of CG scaffolds (96, 110, 121, 151 μm mean pore sizes, 0.006 relative density, DHT105/24 crosslinking, dry and hydrated) was calculated continuously over applied strains between 0 and 40% from the optically observed lateral strain. **Figure 5.12** shows example side-view images of a CG scaffold disk (121 μm mean pore size, 0.006 relative density, DHT105/24 crosslinking, dry) at applied strains of ε = 0.00, 0.20, and 0.40.

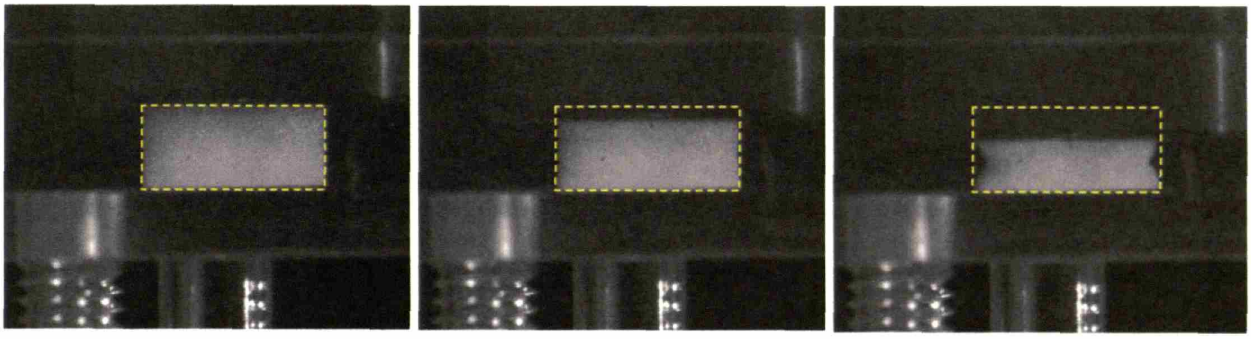

Figure 5.12. Side-view of CG scaffold (121 μm mean pore size; DHT crosslinking; 0.006 relative density; hydrated) under uniaxial compressive strain at ε: 0.00 (left), 0.20 (Linear-elastic, collapse plateau regime transition, middle), and 0.40 (collapse plateau regime, right). The yellow dashed line corresponds to the initial scaffold dimensions.

Identical behavior of both dry and hydrated scaffolds was observed over the entire range of tested strains (0 – 40%). Both dry and hydrated CG scaffolds exhibited a Poisson's ratio (□) of approximately 0 over the entire linear elastic regime, with no significant effect of mean pore size on Poisson's ratio ($p > 0.05$) (**Table 5.4**). After the transition from the linear elastic to the collapse plateau regime, the scaffold appeared to be constrained at the boundaries with the

platens and to contract inward at the mid-plane, suggesting □ < 0, for both the dry and hydrated scaffolds.

Mean Pore Size, μm	Poisson's ratio
96	0.01 ± 0.02
110	0.00 ± 0.01
121	0.01 ± 0.01
151	0.01 ± 0.01

Table 5.4. Poisson's ratio (Mean ± StDev) over the linear elastic regime for the dry CG scaffold variants (96 - 151 μm mean pore sizes; DHT crosslinking; 0.006 relative density) with four distinct mean pore sizes.

5.4.8. CG scaffold tensile modulus

CG scaffolds (96 μm mean pore size, 0.006 relative density, wet, DHT105/24) exhibited uniaxial tension stress-strain curves characteristic of cellular solids (**Figure 5.13**).

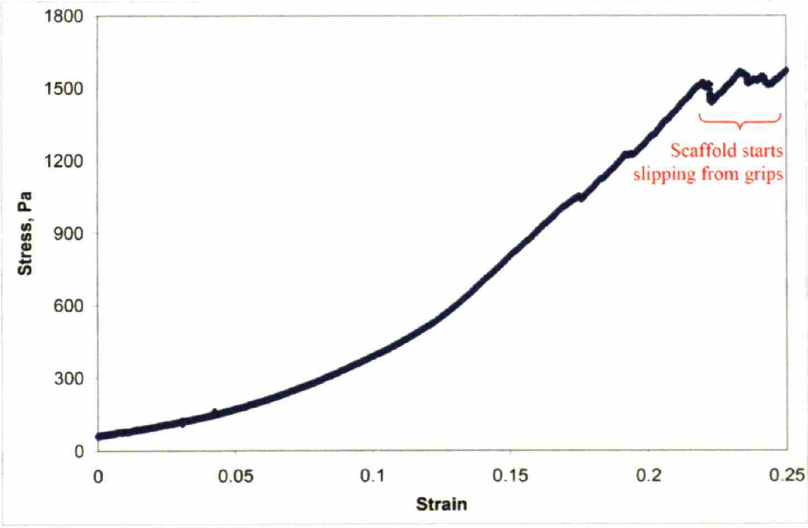

Figure 5.13. Characteristic stress-strain curve observed for the hydrated CG scaffold variants (96 μm mean pore size; 0.006 relative density; DHT crosslinking; hydrated; x-y plane loading) under tensile testing showing initial elastic regime followed by stiffening characteristic of cellular solids under tensile loading.

The initial elastic modulus, measured for the initial loading regime (strain: 0 to 5%), was calculated to be approximately 2000 Pa for the hydrated scaffolds, an order of magnitude stiffer than the E^* of the same scaffolds under uniaxial compression. Above 20% strain, the CG scaffold typically slipped from the grips, preventing measurement of CG scaffold mechanical properties under tension at higher levels of strain.

5.4.9. CG scaffold strut modulus

Bending tests were successfully performed on individual CG scaffold struts (121 μm mean pore size; DHT crosslinking; 0.006 relative density; dry) via AFM (**Figure 5.14**).

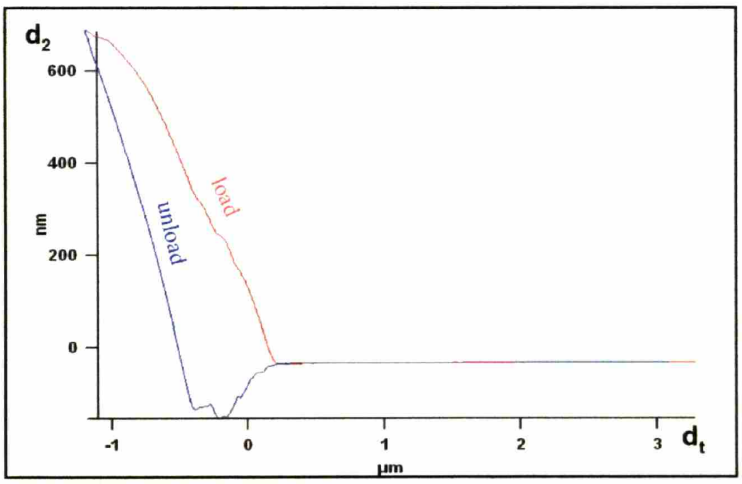

Figure 5.14. Characteristic load-unload curve for bending tests performed via AFM on individual CG scaffold struts.

Analysis of the linear unloading regime of each bending test was performed using **Eq. 5.6c** described in Section 5.3.5 to calculate the individual strut modulus (E_s). The unloading regime was used instead of the loading regime to remove the effects of plasticity from the calculations; the strut modulus of the dry CG scaffold ($E_{s,\,dry}$) was calculated to be 762 ± 35.4 MPa. The strut

modulus of the hydrated CG scaffold ($E_{s,\,hyd}$) was calculated to be 5.28 ± 0.25 MPa from the dry strut modulus (E_s = 762 ± 35.4 MPa) and the relative difference in the dry and hydrated CG scaffold elastic modulus (E_{dry}^* = 30.0 ± 3.9 kPa; $E_{hydrated}^*$ = 208 ± 41 Pa; $E_{hydrated}^*/E_{dry}^*$ = 0.00693).

5.5. Discussion

All CG scaffold variants (Mean pore size: 96 – 151 μm) exhibited stress-strain curves with distinct linear elastic, collapse plateau, and densification regimes, characteristic of low-density, open-cell foams. For the sub-series of structurally isotropic scaffolds (Mean pore size: 96 – 121 μm), scaffold mechanical properties (E^*, σ_{el}^*, ε_{el}^*, $\Delta\sigma/\Delta\varepsilon$) were found to be independent of scaffold pore size, as predicted by cellular solids theory. Additionally, the structurally isotropic scaffolds were also found to be mechanically isotropic, as expected.

In addition to the ability to modify CG scaffold mean pore size independent of scaffold stiffness, scaffold stiffness can be modulated independently of scaffold microstructure via variable crosslinking. Using dehydrothermal and carbodiimide-based crosslinking techniques, scaffold stiffness was varied by nearly an order of magnitude independent of scaffold microstructure. As predicted, increasing the crosslinking density was found to result in a significantly greater E^*, σ_{el}^*, and $\Delta\sigma/\Delta\varepsilon$.

As would be predicted by the similarity of **Eq. 5.2** and **Eq. 5.3**, the trends observed with the buckling stress (σ_{el}^*) closely mirror those seen for the linear elastic modulus (E^*). As with E^*, a linear relationship between σ_{el}^* and (ρ^*/ρ_s) was observed while σ_{el}^* was found to be independent

of mean pore size. The trends observed with the buckling strain (ε_{el}^*) appear to be largely independent of mean pore size, crosslink density, direction of testing, and relative density and are characteristic of buckling strains for many low-density, open-cell foams, although the buckling strain (ε_{el}^*) is higher than previously observed for open-cell foams. The trends observed with the collapse modulus ($\Delta\sigma/\Delta\varepsilon$) closely mirror those seen for the linear elastic modulus (E^*): increasing $\Delta\sigma/\Delta\varepsilon$ with crosslinking density and relative density. The increase in collapse modulus is likely due to the increased stiffness in the scaffold struts obtained by the increased crosslink density.

The measured scaffold modulus, E^*, and collapse stress, σ_{el}^*, were found to vary nearly linearly with relative density (ρ^*/ρ_s), in contrast to **Eq. 5.2** and **Eq. 5.3**, which predict a squared dependence. The measured relative moduli (E^*/E_s) for the collagen-GAG scaffolds are compared with the predictions of the open-cell foam cellular solids model in **Table 5.5**.

ρ^*/ρ_s	E^*, kPa (*meas*)	E^*/E_s (*meas*)	E^*/E_s (*model*)	E^*/E_s Ratio (*meas/model*)
0.006 (*1.0x*)	30.0 ± 3.9	3.94×10^{-5}	3.60×10^{-5}	1.09
0.009 (*1.5x*)	38.4 ± 4.2	5.04×10^{-5}	8.10×10^{-5}	0.62
0.012 (*2.0x*)	67.2 ± 3.9	8.82×10^{-5}	1.44×10^{-4}	0.61
0.018 (*3.0x*)	82.8 ± 8.3	1.09×10^{-4}	3.24×10^{-4}	0.34

Table 5.5. Comparison of normalized scaffold density (ρ^*/ρ_s) and modulus (E^*/E_s, E_s = 762 ± 35.4 MPa) for CG scaffold variants. A comparison between the experimental results (*meas*) and those predicted using a low-density, open-cell model (*model*).

The experimental data for the relative modulus (E^*/E_s) for scaffolds with distinct relative densities are compared to the predictions of models for open- and closed-cell foams in **Figure**

5.15. The open-cell model predicts the measured modulus for the standardized scaffold density (0.006, 1.0x). However, the open-cell foam model overestimates the experimental results for the higher density scaffolds (0.009, 0.012, 0.018; 1.5x, 2.0x, 3.0x).

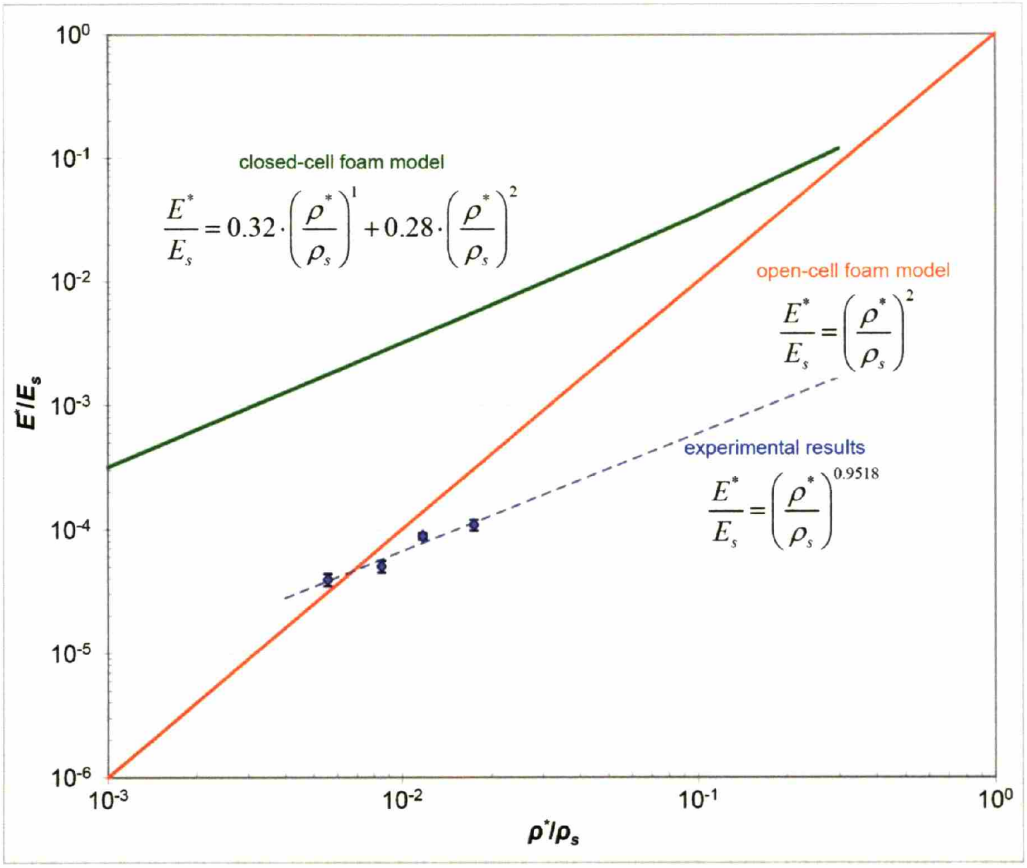

Figure 5.15. Open-cell and closed-cell model predications and experimental results for a comparison of the normalized scaffold density (ρ^*/ρ_s) and modulus (E^*/E_s). The open-cell model predicts the relationship $(E^*/E_s) \sim (\rho^*/\rho_s)^2$; the closed-cell model predicts the relationship $(E^*/E_s) \sim 0.32 \cdot (\rho^*/\rho_s)^1$ for low relative densities (Gibson and Ashby, 1997; Simone and Gibson, 1998). The relationship $(E^*/E_s) \sim (\rho^*/\rho_s)^{0.9518}$ was found for the experimental results.

The experimental data for the relative collapse stress (σ_{el}^*/E_s) for scaffolds with distinct relative densities are compared to the predictions of models for open- and closed-cell foams in **Figure 5.16**. Again, a nearly linear relationship was observed. In this case, the model for open-cell foams underestimates the data; this is related to the higher buckling strain observed in the

scaffolds (20% for dry CG scaffolds, 10% for hydrated CG scaffolds) than in open-cell foams (5%).

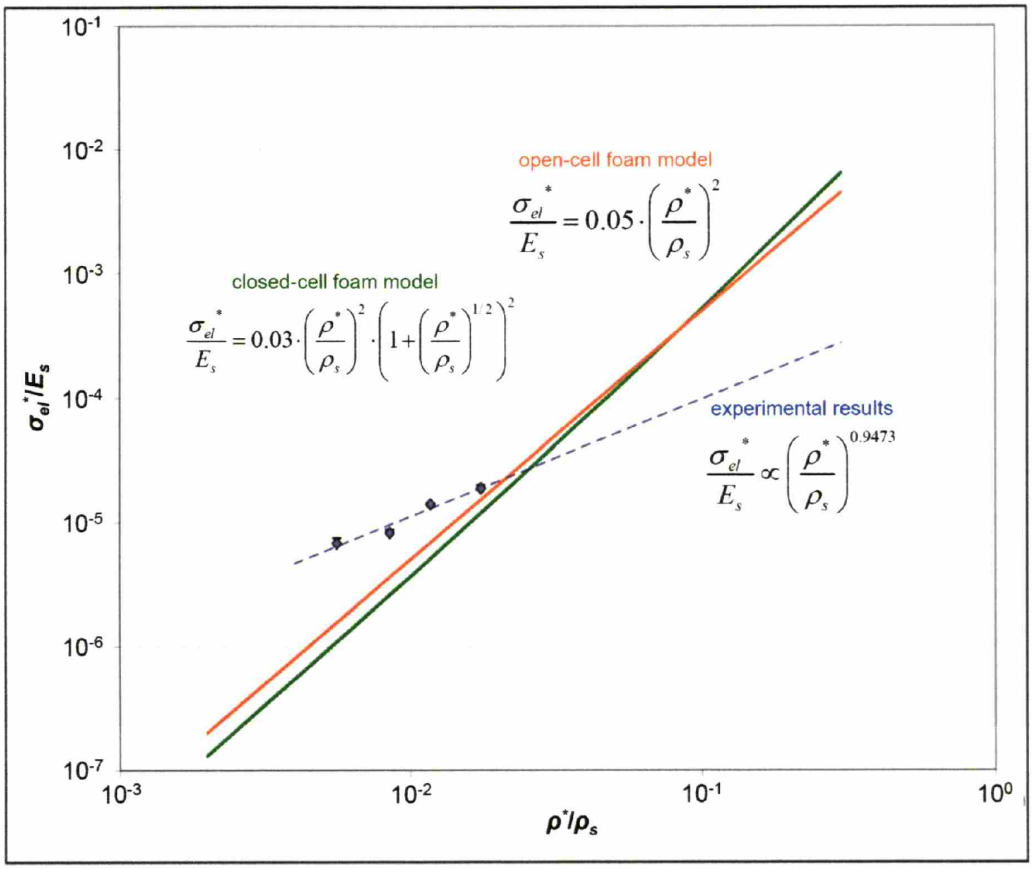

Figure 5.16. Open-cell and closed-cell model predications and experimental results for a comparison of the normalized scaffold density (ρ^*/ρ_s) and collapse stress (σ_{el}^*/E_s). Cellular solids relationships from Gibson and Ashby, 1997.

The standard density ($\rho^*/\rho_s = 0.006$) scaffold has been previously observed to display a uniform pore microstructure with equiaxed pores (**Figure 5.17a, 5.17b**). SEM analysis of the higher density scaffolds (**Figure 5.17c – 5.17f**) revealed scaffolds with microstructural heterogeneities: large pores or "holes," with diameters on the order of over 500 μm, as well as local regions, on the order of 100 – 200 μm, of higher density.

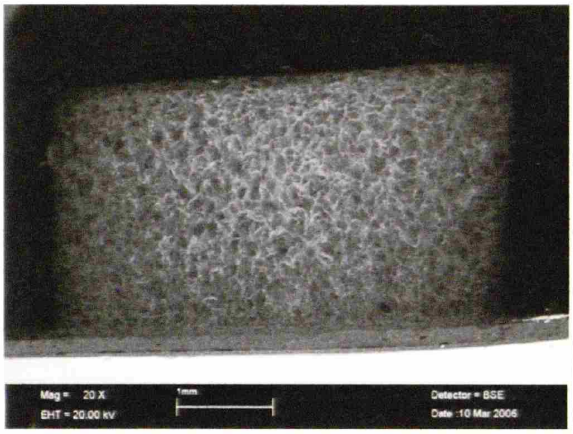

Fig. 5.17a

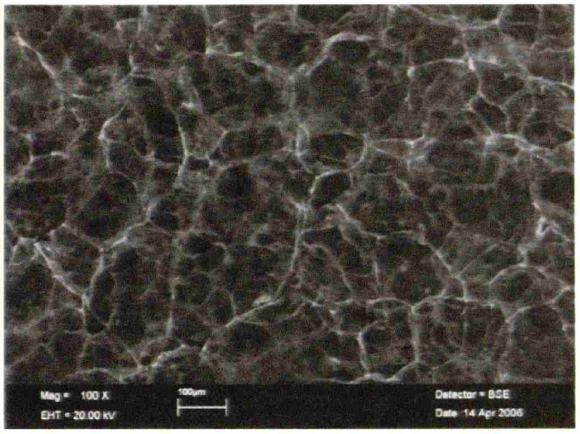

Fig. 5.17b

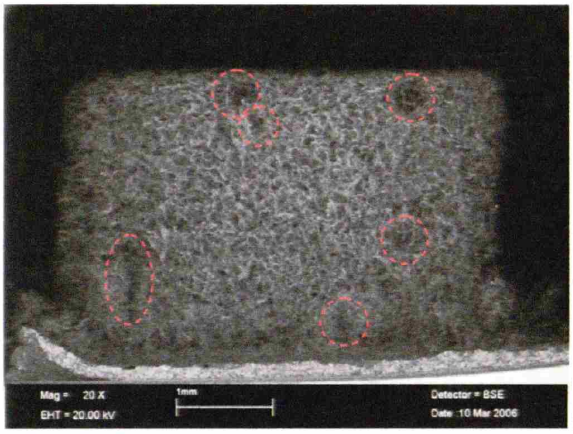

Fig. 5.17c

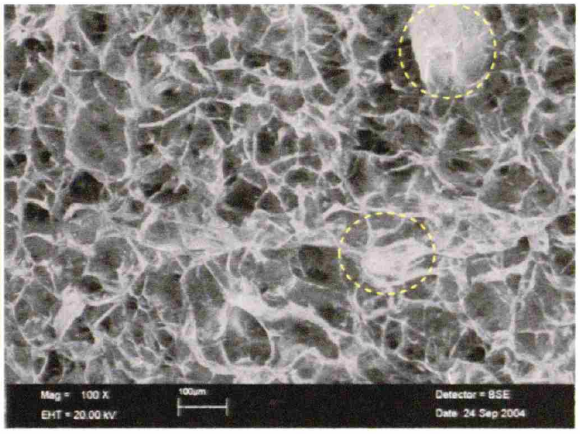

Fig. 5.17d

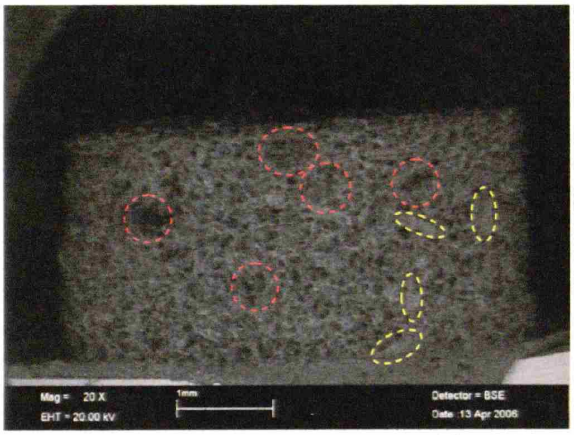

Fig. 5.17e

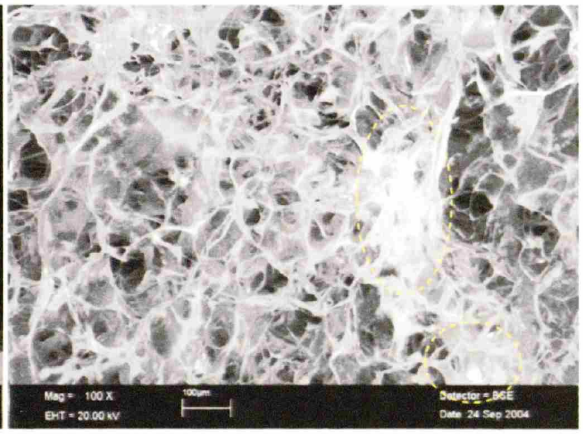

Fig. 5.17f

Figure 5.17. SEM images of CG scaffolds with three distinct relative densities (ρ^*/ρ_s: 0.006, 0.012, 0.018) at low (20x: Fig. 5.17a/c/e) and high (100x: Fig. 5.17b/d/f) magnification. Non-uniform solid content distribution, regions of reduced density denoted by red ellipses and regions of increased density denoted by yellow ellipses, is observed in the higher density (ρ^*/ρ_s: 0.012, 0.018) CG scaffolds. Some SEM images (Fig. 15a/c/e) courtesy of Janet Leung (MIT).

A mechanistic explanation of this phenomena has been developed based upon CG suspension mixing. Note that increasing the density of solid in the CG suspension increases the CG suspension viscosity, making it increasingly difficult to achieve a uniform dispersion of solid throughout the mixture. In this study, the attempt to produce a 4.0x dense CG suspension resulted in a suspension with distinct regions of clumped CG content within a significantly less viscous liquid. We were unable to produce a homogeneous 4.0x dense CG suspension or CG scaffold.

The effect of regions of reduced CG content on the relative modulus (E^*/E_s) of the scaffold will now be addressed; while these regions have CG content they will be referred to as "holes" for the remainder of this analyses in order to simplify the vocabulary. A significant effect of structural non-uniformities within the microstructure of a cellular solid has been previously reported using both theoretical analyses and experimental results (Guo and Gibson, 1999; Andrews, Gioux, et al., 2001; Onck, Andrews, et al., 2001). Regions of increased density have the effect of reducing the open-cell nature of the scaffold in that region, and reducing the overall density of the remainder of the scaffold. A significantly reduced modulus is expected for an appropriately sized region surrounding, and including, each "hole" in the scaffold microstructure. Results in the literature suggest that a 42% reduction in modulus is observed for a region of a 2-D honeycomb with a central void region comprising just 12.5% of the local foam area (Guo and Gibson, 1999). The literature also suggests that a critical number of unit cells (6 – 10) are required in all dimensions of the foam for it to behave mechanically as an infinite cellular solid (Andrews, Gioux, et al., 2001; Onck, Andrews, et al., 2001); smaller specimens have reduced moduli.

The question considered here is whether small regions of holes within the CG scaffold microstructure can result in the 38%, 39%, and 66% reduction of E^*/E_s compared to the predictions of the open-cell foam model that were observed for the scaffolds with relative densities of 0.009, 0.012, and 0.018, respectively (**Table 5.5**). Using the mechanics of composites, the composite modulus (E_c) can be calculated in terms of the moduli (E_1, E_2) and volume fraction (V_1, V_2) of the macroscopic scaffold and "hole" regions:

Equation 5.11.
$$E_c = \frac{E_{scaffold} \cdot E_{hole}}{E_{scaffold} \cdot V_{hole} + E_{hole} \cdot V_{scaffold}}$$

For this preliminary analysis, "hole" regions were modeled as having an 80% reduced modulus, and the required volume fraction of "holes" (V_{hole}) to induce the observed reduction in scaffold relative modulus (E^*/E_s) was calculated:

Equation 5.12.
$$E_{scaffold} = E_s \cdot \left(\frac{\rho^*}{\rho_s}\right)^2$$
$$E_{hole} = 0.2 \cdot E_{scaffold}$$
$$V_{scaffold} = x$$
$$V_{hole} = 1 - x$$

"Hole" volume fractions between 15% and 49% can explain the reduced relative modulus (E^*/E_s) of the high density CG scaffolds (ρ^*/ρ_s: 0.009, 0.012, 0.018) compared to the open-cell foam model. Small volume fractions of "hole" regions in CG scaffolds with increased relative density (1.5x, 2.0x, 3.0x) could account for the reduction of the measured scaffold modulus below the theoretical predictions made by the open-cell foam model. However, open-cell foam model predictions accurately predict the mechanical properties of the CG scaffold variants with the

standard relative density (0.006, 1.0x) which has a uniform microstructure, further validating the use of cellular solids theory to describe the CG scaffolds used in this thesis.

The Poisson's ratios of the CG scaffold variants were found to be 0 for the linear elastic regime, inconsistent with many low-density, open-cell foams ($\nu \sim 0.30$) (Gibson and Ashby, 1997). The Poisson's ratio < 0 observed after the transition from the linear elastic to the collapse plateau regime for the central region of the scaffold, but not at the top or bottom scaffold surface near the platens, suggests that the result of this analysis are likely affected by an edge constraint (between the scaffold and platens) artifact. Further testing is required in order to gain a more definitive description of the scaffold Poisson's ratio over a wide range of applied strains.

The results of the CG scaffold tensile tests are consistent with previous preliminary mechanical characterization performed on a number of CG scaffolds fabricated without the uniform pore structure and equiaxed pores (Schulz-Torres, Freyman, et al., 2000; Freyman, Yannas, et al., 2001; Freyman, Yannas, et al., 2001; Freyman, Yannas, et al., 2002). In these previous investigations, the scaffolds were found to be significantly stiffer in tension than compression in the plane of the scaffold sheet (Schulz-Torres, Freyman, et al., 2000; Freyman, Yannas, et al., 2001). In this investigation, the structurally isotropic CG scaffolds were found to be mechanically isotropic under compression; however, the structurally and mechanically (under compression tests) isotropic CG scaffolds in this study were still found to be significantly stiffer ($E_{compression}^{*}$ = 208 Pa, $E_{tension}^{*}$ = 2000 Pa) under tension than compression. A mechanistic explanation of this phenomenon has been developed, based upon the observation of a very thin

layer of higher density scaffold at the top surface of the scaffold sheets (**Figure 5.18**, representative illustration **Figure 5.19**).

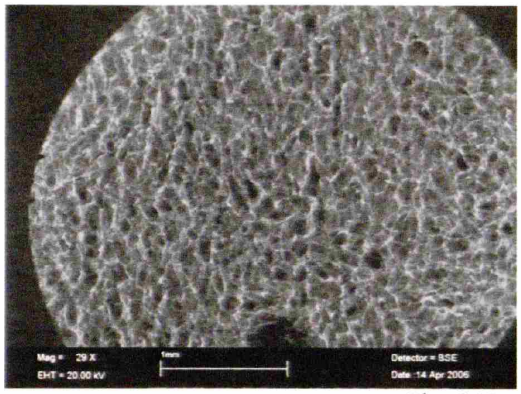
Fig. 5.18a

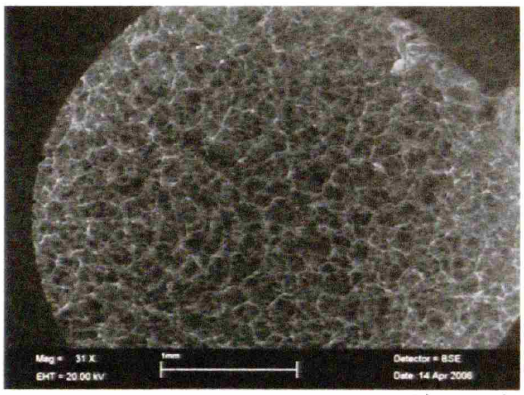
Fig. 5.18b

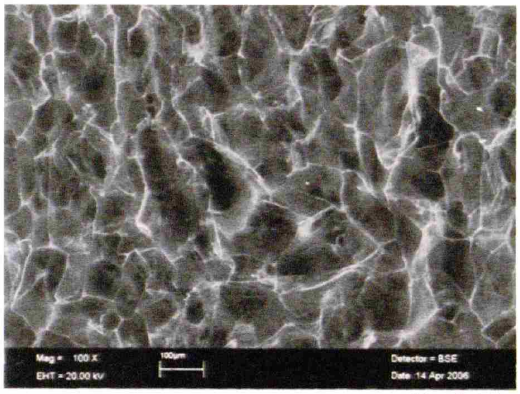
Fig. 5.18c

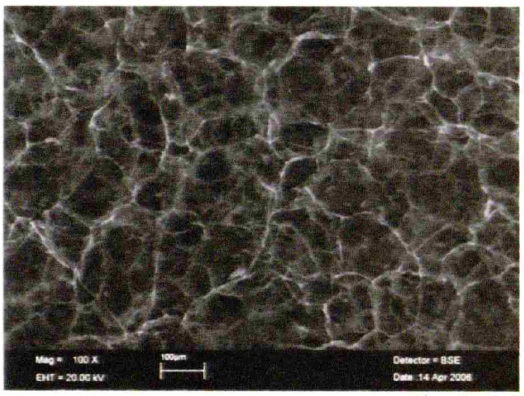
Fig. 5.18d

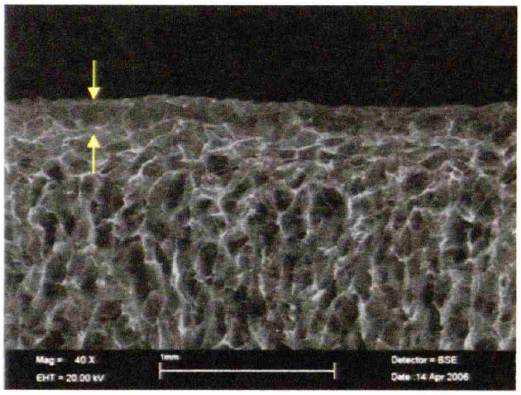
Fig. 5.18e

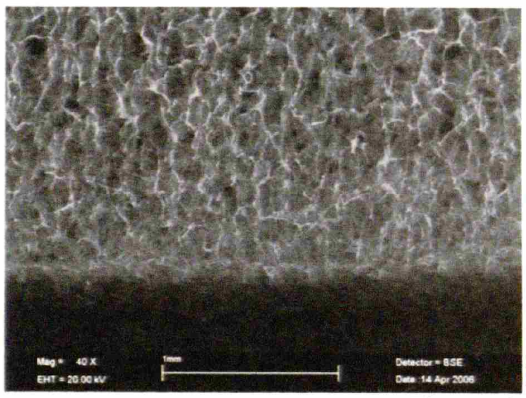
Fig. 5.18f

Figure 5.18. CG scaffold "air side" vs. "pan side." SEM images taken normal to the "air side" (Fig. 5.18a, 5.18c) and "pan side" (Fig. 5.18b, 5.18d) surface showing higher density scaffold (brighter image under backscatter detector) and the presence of some closed cells on the "air side." Cross sectional SEM images of CG scaffold showing "aid side" (Fig. 5.18e, region defined by yellow arrows) and "pan side" scaffold surface (Fig. 5.18f). Scale bars: 1 mm (Fig. 5.18a, 5.18b, 5.18e, 5.18f), 100 μm (Fig. 5.18c, 5.18d).

This layer is an artifact of the freeze-drying process where convective cooling (opposed to the conductive cooling prevalent throughout the rest of the suspension) dominates the solidification process at the surface of the CG suspension exposed to the freeze-dryer atmosphere. The effects of such a higher density (and therefore stiffer) scaffold were analyzed using the mechanics of layered composites.

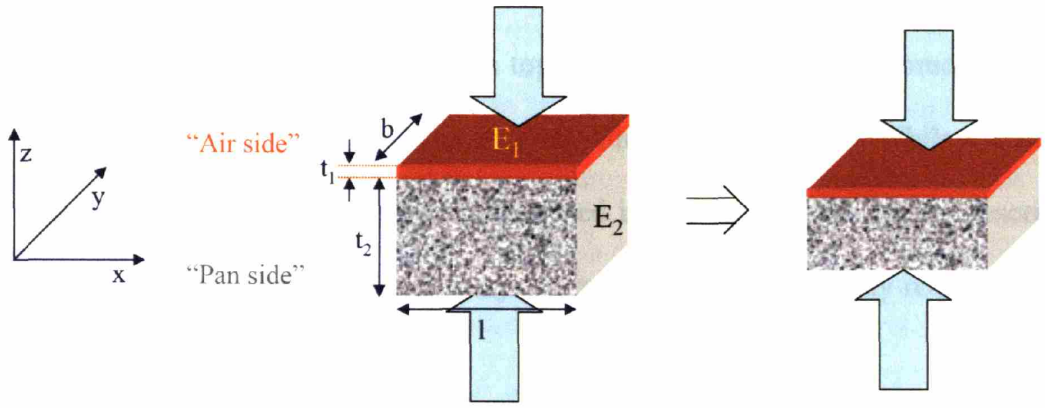

Fig. 5.19a

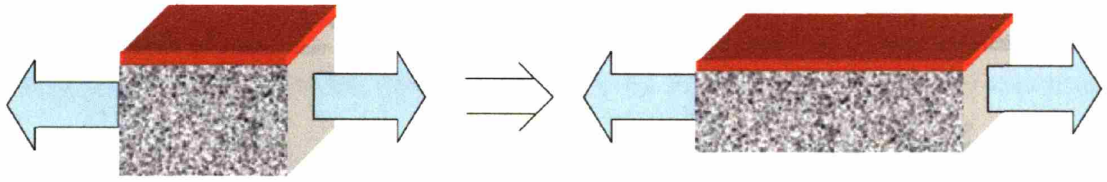

Fig. 5.19b

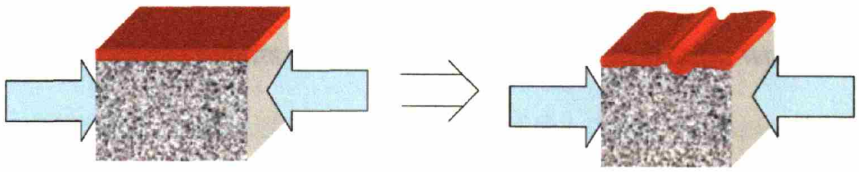

Fig. 5.19c.

Figure 5.19. Mechanistic explanation for the observed discrepancy between the elastic modulus of the CG scaffolds under compressive loading normal to the plane of the scaffold sheet (Fig. 5.19a), tensile loading in the plane of the scaffold (Fig. 5.19b), and compressive loading in the plane of the scaffold sheet (Fig. 5.19c).

For this analysis, the thickness of the higher density layer on the "air side" of the scaffold surface was taken to be 200 μm based upon visual inspection of SEM images (**Figure 5.18**); this is approximately twice the mean pore size of the scaffolds. The total cross-sectional thickness of the scaffold sheet, incorporating the thin "air side" region, is 3.4 mm. The separate regions of the scaffold were incorporated as a thin, high density "pan side" layer (thickness t_1 = 0.200 mm; modulus E_1; total volume $V_1 = t_1 \cdot b \cdot l$) on top of the remainder of the homogeneous scaffold structure (thickness t_2 = 3.2 mm; modulus E_2; total volume $V_2 = t_2 \cdot b \cdot l$). While a layer thickness of 200 μm was utilized for the calculation described in this section, the results described below can also be achieved using dimensional analysis arguments where the only requirement is that $t_1 << t_2$.

Under compression tests in the z direction (normal to the "air side" layer, **Fig. 5.19a**), the composite modulus ($E^*_{compression}$) can be modeled using the mechanics of composites:

Equation 5.13.
$$E^*_{compression} = \frac{E_1 \cdot E_2}{E_1 \cdot V_2 + E_2 \cdot V_1} = \frac{E_1 \cdot E_2}{E_1 \cdot \frac{3.2 \cdot b \cdot l}{3.4 \cdot b \cdot l} + E_2 \cdot \frac{0.2 \cdot b \cdot l}{3.4 \cdot b \cdot l}}$$

Simplifying and including the results of the mechanical characterization work from this study:

Equation 5.14.
$$E^*_{compression} = 208Pa = E_2$$

In compression, for loading normal to the plane of the scaffold sheet, the measured modulus of the composite is that of the bulk scaffold (not that of the top "skin" layer). Applying similar

modeling techniques to describe uniaxial tensile loading in the plane of the scaffold sheet (**Fig. 5.19b**):

Equation 5.15.

$$E^*_{tension} = 2000Pa = E_1 \cdot V_1 + E_2 \cdot V_2$$

$$E^*_{tension} = E_1 \cdot \frac{0.2 \cdot b \cdot l}{3.4 \cdot b \cdot l} + 208 \cdot \frac{3.2 \cdot b \cdot l}{3.4 \cdot b \cdot l}$$

Simplifying this relationship to solve for the modulus of the higher density membrane, $E_1 = 30.7$ kPa, suggesting that a thin, denser layer at the "air side" of the scaffold can significantly increase the stiffness of the scaffold under tension. The relative density of this higher density region was calculated to be approximately 7% using the relation described in **Eq. 5.2**; while this represents a significant increase over the relative density of the bulk scaffold (0.6%), it is not so large as to preclude cell migration into the scaffold. Cell migration into the scaffold through the "air side" has been previously observed (O'Brien, Harley, et al., 2005).

With all of the required variables now known (t_1, t_2, E_1, E_2), the case of uniaxial compression in the plane of the scaffold can be analyzed. Experimentally, the scaffolds were found to be mechanically isotropic, suggesting that the thin higher density (air side) layer should not affect the compressive modulus in the directions perpendicular and parallel to the scaffold sheet ($E_{compression}^*$ = 208 Pa). Examining the effects of compressive loading on the layered composite (**Fig. 5.19c**), the buckling stress and strain (σ_{cr}, ε_{cr}) of the thin membrane observed on the "air side" of the scaffold sheet was calculated using the result for buckling of a stiff sheet on an elastic foundation (Allen, 1969):

Equation 5.16.

$$\sigma_{cr} = 0.57 \cdot (E_1)^{1/3} \cdot (E_2)^{2/3}$$
$$\sigma_{cr} = 0.57 \cdot (30.7kPa)^{1/3} \cdot (208Pa)^{2/3}$$
$$\sigma_{cr} = 630Pa$$
$$\varepsilon_{cr} = \frac{\sigma_{cr}}{E_1} = \frac{630Pa}{30.7kPa} = 0.02$$

This model suggests that the thin layer of higher density, stiffer material is responsible for the increased tensile modulus of the scaffold in the x-y plane. Under compression, the thin, stiffer layer buckles at a strain of 2% and has a negligible effect on the scaffold modulus. These results confirm experimentally observed phenomena: the CG scaffolds were mechanically isotropic under compression but exhibited a significantly stiffer modulus under tensile tests in the plane of the scaffold, likely due to the thin layer of higher density scaffold (thickness ~100 - 200 μm) found along the top surface of the scaffold structure.

5.6. Conclusions

Extensive, quantitative microstructural and mechanical analysis of a series of CG scaffolds has been performed. These scaffolds, previously found to be structurally isotropic with a uniform pore microstructure and equiaxed pores (Mean pore size: 96 – 121 μm) (O'Brien, Harley, et al., 2004; O'Brien, Harley, et al., 2005), have now been mechanically characterized.

The CG scaffold variants exhibited stress-strain behavior characteristic of low-density, open-cell foams with distinct linear elastic, collapse plateau, and densification regimes. The structurally isotropic scaffolds were also found to be mechanically isotropic. Further independent control

over scaffold stiffness (via post-fabrication crosslinking independent of scaffold microstructure) and microstructure (scaffold pore size independent of stiffness) was observed.

In addition to mechanically characterizing the macroscopic scaffold, the Young's modulus (E_s) of the individual struts that define the scaffold microstructure was measured. Good agreement was observed between open cell foam model prediction of E^*/E_s vs. ρ^*/ρ_s for the standard CG scaffold variants ($\rho^*/\rho_s = 0.006$). The predictions of the open-cell foam model overpredicted the measured moduli at higher relative densities (0.009, 0.012, 0.018), probably due to large diameter "holes" observed in the denser scaffolds. The effect on scaffold modulus of the "hole" regions in the scaffold was described using the mechanics of composites; a small volume fraction of "hole" regions throughout the scaffold is sufficient to reduce the model predictions of moduli to those measured. Besides further validating the use of cellular solids theory to describe the materials and mechanical properties of this CG scaffold system, the most significant aspect of this investigation is that an experimental substrate has been fabricated, structurally characterized, and mechanically characterized.

Based upon the results of this investigation, the local microstructural and mechanical properties of the extracellular environment surrounding individual cells within the scaffold can be defined and controlled. These characterized scaffold variants provide a standardized framework for a series of *in vitro* and *in vivo* tissue engineering studies, notably a quantitative investigation of the effect of the extracellular environment (mechanics, microstructure) on cell behaviors such as migration and contraction that will be described in the following chapter.

CHAPTER 6. *Quantifying Cell Migration and Contraction Behavior in a Series of Characterized Collagen-GAG Scaffolds*

6.1. Introduction

The standardized series of CG scaffolds with independently variable microstructural and mechanical properties developed (Chapters 2 and 3) and characterized (Chapters 4 and 5) in this thesis present a platform to facilitate rigorous study of cell behavior and cell-scaffold interactions. Here cell migration and contraction processes will be investigated. Cell motility and cell-mediated contraction play critical roles in a number of physiological and pathological processes, notably organized wound contraction and fibroblast and vascular endothelial cell migration during wound healing, metastatic tumor cell migration, and migratory processes as a critical element of embryonic development and tissue remodeling. Quantitative study of individual cell behavior within a three-dimensional construct requires understanding the local extracellular environment of the individual cells through accurate compositional, microstructural, and mechanical characterization, as has been performed on the CG scaffold variants developed during this work.

Studies of cell behavior on flat, two-dimensional substrates have shown that substrate stiffness significantly modifies cell behaviors such as DNA biosynthesis, migration speed, directional persistence, and applied traction forces (Wang, Butler, et al., 1993; Fishkind, Silverman, et al., 1996; Pelham and Wang, 1997; Chen and Ingber, 1999; Dembo and Wang, 1999; Pelham and Wang, 1999; Lo, Wang, et al., 2000; Wang, Dembo, et al., 2000; Beningo, Dembo, et al., 2001; Munevar, Wang, et al., 2001; Wang, Dembo, et al., 2001; Beningo and Wang, 2002; Tan, Tien, et al., 2003). Such experiments have provided valuable information concerning cell-ECM interactions with, and cell behavior on, two-dimensional surfaces. Experiments utilizing three-dimensional constructs such as gels and scaffolds have made significant recent progress in studying cell migration and contraction. The average cell contraction force generated by dermal fibroblasts within CG scaffolds, calculated by measuring gross changes in scaffold size when seeded with millions of cells, has been reported to be 1 nN (Freyman, Yannas, et al., 2001). Experimental (Zaman, Trapani, et al., In preparation, 2006) and computational studies (Zaman, Kamm, et al., 2005) of prostate cancer cell migratory behavior within gel constructs have recently reported the significant effect of a number of extracellular parameters such as gel density and stiffness on cell migration speed and persistence length.

The lack of standardized three-dimensional constructs with well characterized mechanical, compositional, and microstructural properties have made it difficult to draw quantitative conclusions concerning the independent effect of the specific extracellular features on cell behavior. In order to appropriately investigate the critical biochemical and biophysical parameters that affect cell behavior in three-dimensions, an appropriate ECM analog that provides a standardized extracellular environment (composition, microstructure, mechanical

properties) conducive to long-term cell culture (*i.e.*, an interconnected pore structure to support cell migration, cell-cell interactions, and metabolite diffusion) and investigational technique (*i.e.*, light or confocal microscopy) is required. The collagen-GAG scaffolds described in this thesis (Chapters 2 – 5) provides such a platform. These low-density, open-cell foams are biodegradable and are characterized by an interconnected pore network defined by struts, providing an ideal environment for *in vitro* cell behavior studies.

The objective of this study was to use two series of CG scaffolds with independently varying mean pore size (Chapter 2) and stiffness (Chapter 5) to study the effect of the extracellular matrix environment on the contractile and migratory behavior of NR6 fibroblasts and DU-145 prostate cancer cells. The independent effects of cell type, cell seeding density, mean pore size, and scaffold stiffness on the average migration speed of NR6 fibroblasts and DU-145 prostate cancer cells will be reported. Additionally, two distinct methodologies to calculate the average cell-mediated contractile force generated by individual cells within the CG scaffold will be described. These two new methodologies calculate the cell-generated contractile force (F_c) using fewer experimental assumptions than have been previously utilized, theoretically producing a more accurate calculation of F_c.

6.2. Materials and Methods

6.2.1. CG scaffolds with independently variable mean pore size, linear elastic modulus

A complete description of the fabrication protocols for the four standard CG scaffolds with distinct mean pore sizes and a uniform pore microstructure used in this investigation (**Table 6.1**)

have been previously provided in this thesis in Section 2.3.1 (CG suspension), 2.3.4 (constant cooling rate solidification), and 2.3.5 (fabrication of uniform CG scaffolds with distinct mean pore sizes). All four scaffold variants were utilized in this investigation (**Table 6.1**).

T_f, °C	**Mean Pore Size, μm Mean ± StDev**	**Relative Density Mean ± StDev**
-10	151 ± 32	0.0062 ± 0.0005
-20	121 ± 23	0.0061 ± 0.0003
-30	110 ±18	0.0059 ± 0.0003
-40	96 ± 12	0.0058 ± 0.0003

Table 6.1. CG scaffold variants utilized for permeability and specific surface area investigation.

6.2.2. CG scaffold crosslinking

Two distinct crosslinking techniques were utilized following freeze-drying to modify scaffold stiffness independent of pore structure: a physical, dehydrothermal-based (DHT) process and a chemical, carbodiimide-based (1-ethyl-3-(3-dimethylaminopropyl)carbodiimide – EDAC) process. The standard crosslinking treatment for all CG scaffolds in this investigation, except for the portion of investigating the effect of scaffold stiffness, was DHT at a temperature of 105°C for 24 hours.

To study the independent effect of scaffold stiffness on cell behavior, a series of three DHT and EDAC crosslinking treatments were used: DHT 105°C for 24 hours (DHT105/24), 1:1:5 EDAC:NHS:COOH ratio (EDAC1:1:5), and 5:2:1 EDAC:NHS:COOH ratio (EDAC5:2:1). A

complete description of the crosslinking procedure and mechanical characterization of these constructs has been provided in Chapter 5.

6.2.3. NR6 fibroblast and DU145 prostate cancer cell culture techniques

NR6 mouse fibroblasts (NR6 FBs), a cell line derived from a Swiss 3T3 fibroblast line isolated from 17-19 day mouse embryos that lack endogenous receptors (Pruss, 1977; Chen, Gupta, et al., 1994; Chen, Xie, et al., 1994) were the predominant cell type used in this study. NR6 FBs (parental) were maintained in MEM-α (Cat. No. 11900, Invitrogen, Carlsbad, CA) supplemented with 2 mM L-glutamine (Cat. No. 25030, Invitrogen), 7.5% fetal bovine serum (FBS; Cat. No. 16140-071, Invitrogen), 100 U/ml penicillin and 100 μg/ml streptomycin (Cat. No. 15140, Invitrogen), 0.1 mM non-essential amino acids (Cat. No. 11140-050, Invitrogen), and 1 mM sodium pyruvate (Cat. No. 11360-070, Invitrogen) (Chen, Gupta, et al., 1994; Ware, Wells, et al., 1998; Koo, Irvine, et al., 2002).

Parental DU145 cells (DU145), an invasive prostate cancer cell line, were utilized for the portion of this investigation that studied how different cell types behave in identical extracellular environments. DU145 cells were grown in DMEM containing 10% fetal bovine serum (Invitrogen), and 1% supplement of each of the following: MEM non-essential amino acids, sodium pyruvate, penicillin/streptomycin and L-glutamine (all from GIBCO, Gaithersburg, MD) (Kharait, Dhir, et al., 2006).

Cells were maintained in culture flasks until ready for use and were passaged when the flask became confluent; passaging and removing a cell population to seed into the scaffolds for the

cell tracking studies was performed using a trypsin-EDTA solution (Sigma, St. Louis, MO). Viable cell number was then determined prior to seeding or passaging by live-cell staining using 0.4% Trypan Blue (Invitrogen Co., Chicago, IL) and counting viable cells with a standard hemacytometer (Bright-Line, Hausser Scientific, Horsham, PA) (Freyman, Yannas, et al., 2001).

6.2.4. Confocal imaging of CG scaffold and cell population

NR6 mouse fibroblasts and DU145 prostate cancer cells were fluorescently labeled for 20 minutes with a 10 μM solution of CellTracker Green (CMFDA, Cat. No. C2925, Molecular Probes, Carlsbad, CA) in the complete MEM-α medium while still in the tissue culture flask. The cells were then washed twice with Phosphate Buffered Saline (PBS, GIBCO) to remove any excess fluorescent stain before the cells were removed via trypsin-EDTA for seeding into the CG scaffolds. The CellTracker Green CMFDA reagent is a fluorescent chloromethyl derivative (5-chloromethylfluorescein diacetate, $C_{25}{\cdot}H_{17}{\cdot}Cl{\cdot}O_7$, M.W. 464.86 gm/mol) (**Figure 6.1**) that freely diffuses through the membranes of live cells. CMFDA remains colorless and nonfluorescent until the acetate groups are cleaved by intracellular esterases: the CellTracker Green CMFDA dye contain a mildly thiol-reactive chloromethyl group that, once inside the cell, reacts with intracellular thiols (**Figure 6.1**), likely via a glutathione *S*-transferase mediated reaction (Zhang, Olson, et al., 1992). Glutathione levels are typically high (up to 10 mM) in most cells, so glutathione transferase activity is ubiquitous. Upon acetate cleavage, CMFDA is transformed into a cell-impermeable fluorescent dyethioether adduct; cells remain both fluorescent (Abs: 492nm, Em: 517 nm) and viable for at least 24 hours after loading. CellTracker Green CMFDA has a relatively low pKa, which ensures that it will exhibit bright, green fluorescence in the cytoplasm at all physiological pH levels.

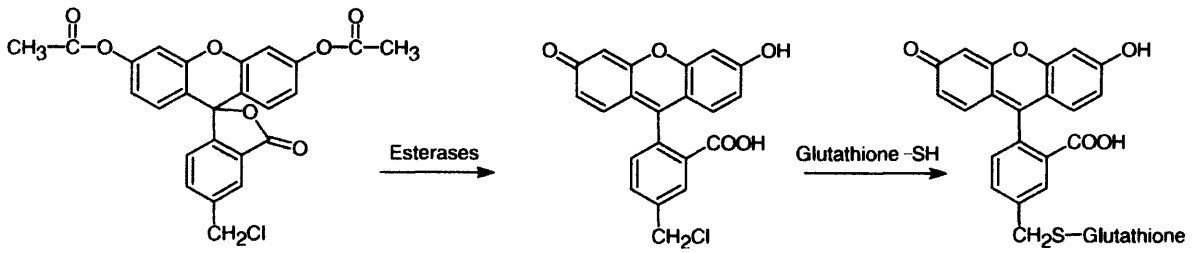

Figure 6.1. The two intracellular reactions of the CellTracker Green CMFDA reagent (the non-reacted form of CMFDA is shown in the left-most image). Although the dye may react with intracellular glutathione first, the product is nonfluorescent until acted upon by intracellular esterases, shown here as the first reaction (Zhang, Olson, et al., 1992).

The CG scaffold was fluorescently labeled for 20 minutes with a 2 μM solution of Alexa Fluor 633 (Cat. No. A20005, Molecular Probes) in Phosphate Buffered Saline, (PBS, GIBCO). The scaffold was then washed twice with PBS to remove any excess fluorescent stain before cells were seeded into the scaffold. The Alexa Fluor 633 dye is bright and photostable, with Abs./Em. maxima of ~632/647 nm. Most importantly, the Alexa Fluor 633 succinimidyl esters provide an efficient and convenient way to selectively link the fluorescent Alexa Fluor 633 dye to primary amines ($R\text{-}NH_2$) located on peptides, proteins or amine-modified nucleic acids. In the case of CG scaffolds, the target amines are those that are part of the collagen and GAG chemical composition (Yannas and Tobolsky, 1967; Yannas, 1972; Gordon, Huang, et al., 1974; Yannas, Burke, et al., 1975; Bansil, Yannas, et al., 1978).

Unlike other reactive moieties, succinimidyl esters demonstrate very low reactivity with aromatic amines, phenols, and alcohols, making them highly attractive for attaching a fluorophore to the amine-containing CG scaffold because the amide bonds formed in the reaction are as stable as peptide bonds (Banks and Paquette, 1995).

For studies examining cell distribution within the CG scaffolds, both the cells and scaffolds were fluorescently labeled. For the portion of the investigation focusing on cell migratory processes, only the scaffolds were fluorescently labeled in order to remove any potential complicating factors due to adverse effects on cell-scaffold interactions as a result of the Alexa Fluor fluorophore bonded to the scaffold surface.

Cells stained with CMFDA have been observed to be brightly fluorescent for at least 72 hours and through at least four cell divisions with incubation in fresh medium at 37°C (Cumberledge and Krasnow, 1993). However, recent studies have suggested that long term exposure to CMFDA may significantly and deleteriously affect cell motility (Timp, Hopp, et al., 2005). Careful attention was paid therefore to standardize the exposure time to CMFDA and to standardize the amount of light (due to fluorescent imaging) the cells were exposed to. The cells (NR6 or DU-145) were stained with a constant dilution of CMFDA (10 μM) for a standardized length of time (20 minutes). CG scaffold disks (6 mm diameter) that had been previously hydrated first in PBS and then in complete MEM-α medium were placed into individual wells of an ultra low attachment 6-well plate (Cat. No. 07-200-601, Corning, Inc., Corning, NY); the low attachment wells prevent preferential migration of the cells out of the scaffold and onto the tissue culture plastic substrate following seeding. 1×10^5 or 5×10^5 fluorescently labeled cells were then seeded into each scaffold disk. Half of the cell population was pipetted in a 10 μl volume onto one surface of the CG scaffold disk and allowed to diffuse into the scaffold for 10 minutes while in the incubator (37°C, 5% CO_2 content, >95% Relative Humidity). The scaffold was then flipped over and the remainder of the cell population was then pipetted onto the other side of the scaffold. The scaffold was then returned to the incubator for two hours to allow the cells to begin

to integrate into the scaffold. After the two hour period, additional medium was added and the scaffold was then placed back into the incubator for an additional ten hours (12 hours total post-seeding) to allow the cells to diffuse and migrate into the scaffold and reach a quasi-steady state level.

At the end of the twelve hour period following seeding, the cells-scaffold construct was then placed into a glass bottom culture dish (Cat. No. P35G-1.5-14-C, MatTek, Corp., Ashland, MA) with 1.5 ml of complete MEM-α medium; the glass bottom culture dish provides superior high resolution microscopic imaging via confocal microscopy. The CG scaffold-cell construct was imaged at 25x magnification with a heated (37°C), oil-immersion objective (Carl Zeiss, Inc., Germany) using the Ultraview Live Cell Imager (PerkinElmer, Wellesley, MA) built on an Axiovert 200M bio-inverted fluorescent microscope (Carl Zeiss). Combining the 25x objective with a 100 μm z-travel piezo, a 364 x 246 x 100 μm three-dimensional field of view was imaged. Cell motion was tracked at 15 minute intervals for 10 hours. At each 15 minute time point, a z-stack of images from the x-y plane (246 μm x 364 μm) was captured. 101 images were captured with 75 – 100 ms temporal and 1 μm z-axis spacing, for a total image volume of 246 x 364 x 100 μm (**Figure 6.2**).

A precision x-y translational stage (OptiScan Stage System, Prior Scientific, Cambridge, UK) was used to capture a series of volumes for each experiment. After capturing the first 246 x 364 x 100 μm volume, the stage moved to a series of other precisely defined locations to capture an additional 8 volumes. After capturing the final volume (#9) in the series, the stage returned to the starting point to capture the first volume again after the 15 minute interval; this experimental

arrangement allowed rapid capture of large volumes of data (**Figure 6.2**). The MetaMorph Imaging System (Molecular Devices Corp., Sunnyvale, CA) was used to control both image capture and the movement of the translational stage throughout the experiment.

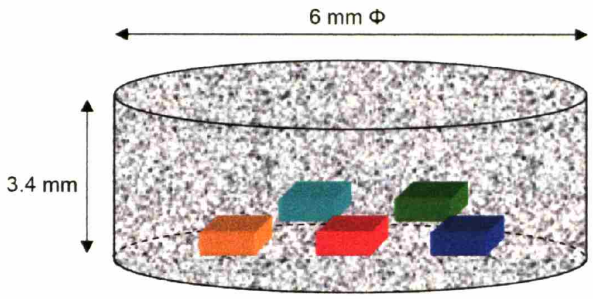

Fig. 6.2a

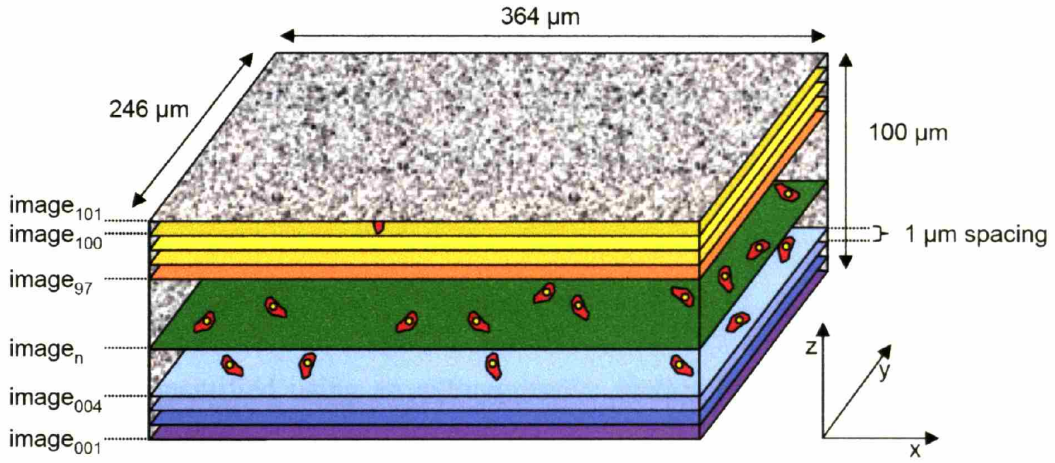

Fig. 6.2b

Figure 6.2. Multiple experimental volumes, each 246 x 364 x 100 µm, were imaged at 15 minute intervals during cell tracking experiments (Fig. 6.2a). Within each volume, 101 images were taken at 1 µm spacing (colored planes) to assemble a three-dimensional description of cell motility (Fig. 6.2b).

6.2.5. Three-dimensional image analysis

A three-dimensional image rendering software package (Imaris XT, Bitplane AG, Switzerland) was used to quantify cell motility within the CG scaffolds and to generate three-dimensional

images of cell-scaffold interactions. Three-dimensional renderings of cell motility and cell-scaffold interactions were created using the Surpass functionality within Imaris. The overall average speed and displacement of cell migration was computed by tracking cell position vs. time using the built-in spot tracking routine (Veenman, Reinders, et al., 2001). Using this automated routine, a 10 μm sphere was placed at the centroid of each cell for every time point. Cell motility was defined by the movement of the sphere at the cell centroid from time point to time point, with migration speeds calculated from the centroid displacement and interval time (15 minutes). An optimization experiment identified the 10 μm sphere (~50% cell diameter) as most appropriate for this experiment: experimental results for smaller spheres (<10 μm, less selective) exhibited significantly larger Standard Deviations. Because the cells within the scaffold exhibited an elongated, spindly morphology, larger spheres (>10 μm, more selective) frequently tracked very few of the cells within the experimental volume (Harley, unpublished data).

Cell motility was quantified using an autoregressive motion tracking algorithm. A Brownian algorithm, which assumes random walk behavior, while appropriate for studying cell migration within a gel construct was deemed inappropriate for tracking cell motility within a scaffold structure with an ordered strut network. An autoregressive motion algorithm, which assumes point-to-point correlated motion but overall random motion, was used to track three-dimensional cell movement (Veenman, Reinders, et al., 2001; Mueth, 2003). Only motile cells were included in the analyses of average cell migration speed; a motile cell was defined as one whose centroid moved further than 10 μm (~50% of the cell diameter) from its initial position during the imaging period. Because the experimental volume was only a small fraction of the entire CG

scaffold volume (246 x 364 x 100 μm vs. 6 mm diameter, 3.4 mm thick disk), cells frequently crossed in and out through the edges of the experimental volume. In order to improve the accuracy of the results, only cells that remained within the experimental volume for 7 or more data points (a minimum of 1 hour 45 minutes) were analyzed. Such data parsing removes significant error from the calculations due to fluorescent bodies that appear briefly in the experimental volume. The Imaris XT software was used to determine the centroid displacement of each cell within the volume from time point to time point and to calculate cell displacement from time point to time point, total cell displacement over the 10 hour imaging period, and average cell speed.

Directional persistence in cell migration describes significant correlation in the direction of motion of a cell over time and is an important variable in describing features of cell migration and invasion. Most experimental studies of, and the appropriate mathematical formulations to describe, cell persistence are based on cells moving on two-dimensional substrates (Dunn, 1983; Dickinson and Tranquillo, 1993; Harms, Bassi, et al., 2005; Zaman, Kamm, et al., 2005). Initial calculation of cell persistence in the three-dimensional CG scaffold system was performed from this dataset by a collaborator, Hyung-Do Kim (Biological Engineering Department, MIT). Using a custom designed Matlab script, the initial cell position and displacement information was combined to produce Wind-Rose plots to better illustrate the effect of scaffold mean pore size on cell persistence (96 – 151 μm mean pore size; 5 x 10^5 cells/scaffold; 0.006 relative density; DHT105/24 crosslinking; hydrated). Historically, Wind-Rose plots have been a convenient method to depict the predominant wind speeds and directions at measurement sites (typically frequency distributions of wind gust speed and wind direction). Common Wind-Rose plots show

the conditions for a particular location or group of locations (**Figure 6.3**). A location's annual Wind-Rose forms a distinctive pattern that is often reflective of large-scale weather systems and large or smaller-scale terrain effects (analogous to the extracellular environment and scaffold microstructural features for studies of cell motility).

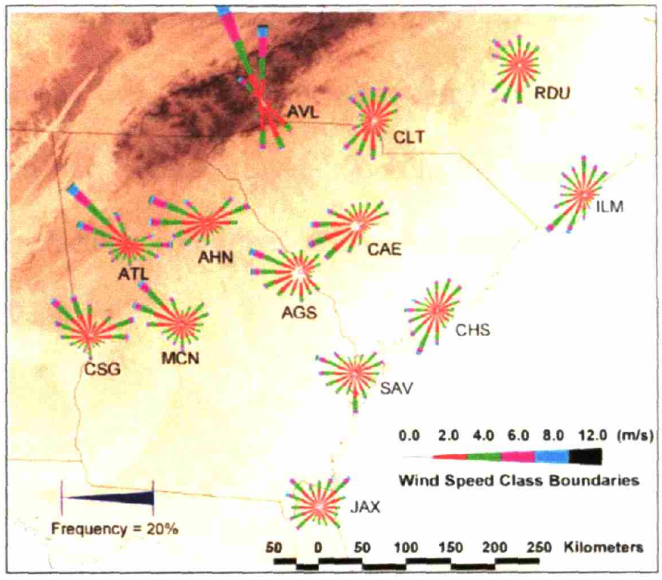

Figure 6.3. Conventional Wind-Rose plot for meteorological applications of wind conditions at airports in the southeastern United States (Westinghouse_Savannah_River_Company, 2002).

The Wind-Rose plot has significant use as a graphical tool to qualitatively describe three-dimensional cell motility, particularly cell persistence length and overall cell displacement. The Wind-Rose plot in this investigation was constructed by translocating the starting position of all cells within the experimental volume to the origin ([x,y,z] = [0,0,0]) of a single three-dimensional graph and then plotting their three-dimensional movement tracks from the origin. Overall persistence and total cell displacement can be qualitatively assessed from the Wind-Rose plot for each of the four scaffold (96 – 151 μm mean pore size) variants by observing the density of cell tracks at a particular distance from the origin and by noting the furthest distance the tracks

reached from the origin. The Wind-Rose plots (generated by H-D Kim) are reported in the results section of this thesis in order to provide a more complete summary of the three-dimensional cell tracking experiments and analyses performed to date.

6.2.6. Calculation of cell-mediated contraction force generated within a CG scaffold

Two distinct methodologies were utilized to make calculations of cell-mediated contraction forces generated within the CG scaffolds: free-floating contraction and individual cell contraction assays. Both calculations utilized the detailed mechanical characterization of the CG scaffolds described in Chapter 5.

6.2.6.1. Free-floating contraction assay

Previous investigations of cell-mediated contraction have measured the gross contraction of cylindrical disks of CG scaffold when seeded with NR6 fibroblasts (Soller, 2005), cells from peripheral nerve explants (Spilker, Asano, et al., 2001), and synovial cells (Vickers, Johnson, et al., 2004). Comparisons of the gross dimensional changes of the scaffold disks seeded with cells versus unseeded controls and between disks seeded with different cell populations or treated with different insoluble regulators have previously been used to compare the contractile capacity of different cell types. A quantitative free-floating contraction assay has now been developed where the contraction of the CG scaffold was modeled as an elastic solid under hydrostatic pressure (**Figure 6.4**) and the detailed mechanical characterization described in Chapter 5 was used to calculate the average applied force per cell (F_c).

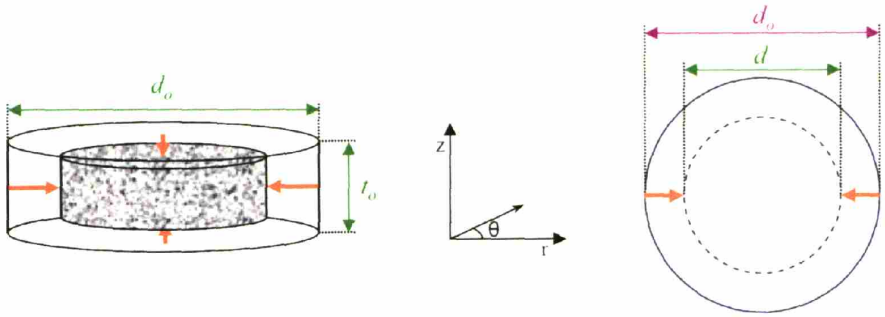

Fig. 6.4a

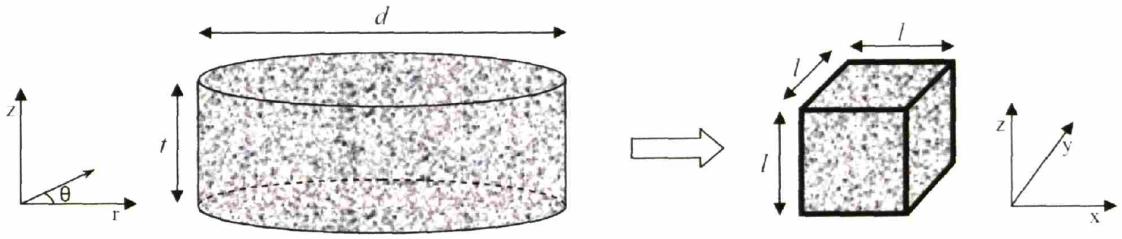

Fig. 6.4b

Figure 6.4. Experimentally observed free-floating contraction of CG scaffolds (Fig. 6.4a, left); cylindrical coordinate representation of scaffold contraction (Fig. 6.4a, right). Representative scaffold volume described by Cartesian coordinates (Fig. 6.4b).

The applied strains can be calculated from the observed dimensional changes in the CG scaffold disk diameter (d) and thickness (t):

Equation 6.1.

$$\varepsilon_{rr} = \frac{\Delta d}{\cdot d_o} = \frac{d_o - d}{d_o}$$

$$\varepsilon_{\theta\theta} = \frac{\pi \cdot d_o - \pi \cdot d}{\pi \cdot d_o} = \frac{d_o - d}{d_o} = \varepsilon_{rr}$$

$$\varepsilon_{zz} = \frac{\Delta t}{t_o} = \frac{t_o - t}{t_o}$$

In past experiments, scaffold thickness has often not been measured. A dimensional argument, based upon the observed mechanical and microstructural isotropy of the CG scaffolds, the spatially uniform distribution of cells within the scaffold (Harley, Unpublished data), and an

assumption that individual cells within a population will generate similar levels of applied force, have been here utilized to estimate ε_{zz}:

Equation 6.2.
$$\varepsilon_{zz} = \varepsilon_{rr} = \frac{d_o - d}{d_o}$$
$$\varepsilon_{rr} = \varepsilon_{zz} = \varepsilon_{\theta\theta}$$

The average force per cell required to produce the observed strain is calculated using the material dilation (e) and a continuum mechanics description of the effect of hydrostatic pressure (p) on a scaffold volume. During free-floating contraction of the isotropic CG scaffold where the cells are randomly distributed through the strut network and the cells contract the scaffold uniformly in all three directions, so the scaffold is effectively under hydrostatic compression. The material dilation (e) can be described in terms of the applied strain (ε), in terms of the material volume (V) and change of the material volume (ΔV), or in terms of the construct modulus (E), applied hydrostatic pressure and Poisson's ratio (ν):

Equation 6.3.
$$e = 1 - (1 - \varepsilon)^3 = \frac{\Delta V}{V} = \frac{3 \cdot (1 - 2 \cdot \nu)}{E} \cdot p$$

In order to simplify the mathematics of the cylindrical disk sample, an equivalent square prism volume element (edge length, l) is defined from the cylindrical scaffold disk (**Figure 6.4b**). This sample undergoes the same material dilation as the scaffold disk, and the force applied to the square prism scaffold sample (F) due to a hydrostatic pressure (p) can be calculated from the scaffold material dilation:

Equation 6.4.
$$F = p \cdot l^2 = \frac{E \cdot e}{3 \cdot (1 - 2 \cdot \nu)} \cdot l^2$$

However, the CG scaffold does not display a simple linear elastic relationship suggested in **Eq. 6.4**. For the range of strains observed with the free-floating scaffold disks reported in the literature (Vickers, Johnson, et al., 2004; Soller, 2005), both the linear elastic and collapse plateau regimes must be considered. The moduli of these two regimes was experimentally characterized in Chapter 5 and the Poisson's ratio for generic open-cell foams has been experimentally measured and reported in the literature (Gibson and Ashby, 1997). The material constants utilized for this analyses are $E^* = 208$ Pa and $v^* = 0.33$ for the linear elastic regime ($0 < \varepsilon \leq 0.1$), $E_c = 92$ Pa and $v_c = 0$ for the collapse plateau regime ($\varepsilon > 0.1$) (**Figure 6.5**).

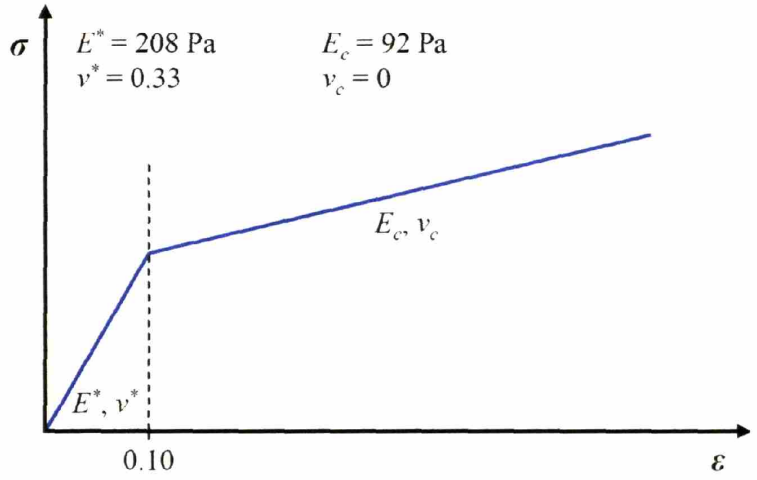

Figure 6.5. Material constants associated with the linear elastic and collapse plateau regimes of the CG scaffolds considered for the free-floating contraction assay.

However this calculation is further complicated because the buckling load at the transition between the linear elastic and collapse plateau regimes changes with different applied stress states. The scaffold modulus (E^*, E_c) was determined under uniaxial compression while the free-floating contraction treated here is best represented as hydrostatic compression. The hydrostatic

buckling stress (σ^*) is reduced compared to that measured for uniaxial compression (σ_{el}^*) by a factor of 0.83 (Triantafillou, Zhang, et al., 1989). This pre-factor was applied to **Eq. 6.4** to more accurately calculate the force (F) required to be applied to the scaffold in order to generate the observed material dilation. The effect of the transition between the linear elastic and collapse plateau regime, which takes place at e_{el}^* can then be calculated by summing the influence of the two regimes:

Equation 6.5.

$$0 < \varepsilon \leq 0.1 : \_F = \frac{0.83 \cdot E^* \cdot e}{3 \cdot (1 - 2 \cdot \nu^*)} \cdot l^2 \quad \text{(6.5a)}$$

$$\varepsilon > 0.1 : \_F = \frac{0.83 \cdot E^* \cdot e_{el}^*}{3 \cdot (1 - 2 \cdot \nu^*)} \cdot l^2 + \frac{0.83 \cdot E_c \cdot (e - e_{el}^*)}{3 \cdot (1 - 2 \cdot \nu_c)} \cdot l^2 \quad \text{(6.5b)}$$

The average force per cell (F_c) was then calculated from the force required to produce the observed deformation (F, **Eq. 6.5**) and the viable cell population (n) acting in each of the three orthogonal axes of the system. Only a portion of the total number of cells within the scaffold (N) are oriented such that they apply force in one of the three orthogonal directions of the Cartesian coordinate system. For free-floating contraction of an isotropic CG scaffold where the struts are randomly oriented in space and the cells are randomly distributed through the strut network, approximately one-third of cells are oriented in each of the three orthogonal axes. Additionally, the effect of the use of a square prism scaffold volume to represent the free-floating scaffold disk must also be accounted for. An edge length (l) was chosen such that the volume of the square prism matched that of the free-floating scaffold disk in order to simplify the mathematics. The force per cell was calculated from **Eq. 6.5** and the relation:

Equation 6.6.

$$F_c = \frac{F}{\frac{1}{3} \cdot N}$$

6.2.6.2. Individual cell contraction assay

Combining strut mechanical characterization data obtained in Chapter 5 with strut deformation data observed during cell-mediated contraction (via confocal or light microscopy) allows calculation of individual cell-mediated contractile forces generated within the scaffold. The buckling load applied to an individual strut within the scaffold network was calculated using cellular solids theory in order to most appropriately model the boundary conditions of the buckled strut, incorporating the effect of the surrounding strut network. When an elastomeric cellular solid is loaded such that the cell edges (CG scaffold struts) are under compression, the edges first bend and then buckle; this buckling has been observed for many different classes of cellular solids such as open-cell foams and hexagonal honeycombs (**Figure 6.6**) (Gibson and Ashby, 1997).

The effect of individual fibroblasts buckling the CG scaffold struts can be similarly described using previously developed isotropic open-cell foam models; for this analysis an idealized CG scaffold structure described by a tetrakaidecahedron was used. In the tetrakaidecahedral unit cell, four cell edges meet symmetrically at each vertex in a tetrahedral arrangement. When a cell-generated contractile force is applied to the local strut network, the single strut – of the four – most nearly aligned with the axis of compression buckles. This strut is restrained at its ends by the other three struts; this strut network tends to reduce rotation of the buckling strut ends. This restoring moment per unit rotation is most closely modeled by a rotational stiffness applied at the ends of the buckling strut by the three restraining struts (**Figure 6.7**) (Gibson and Ashby, 1997).

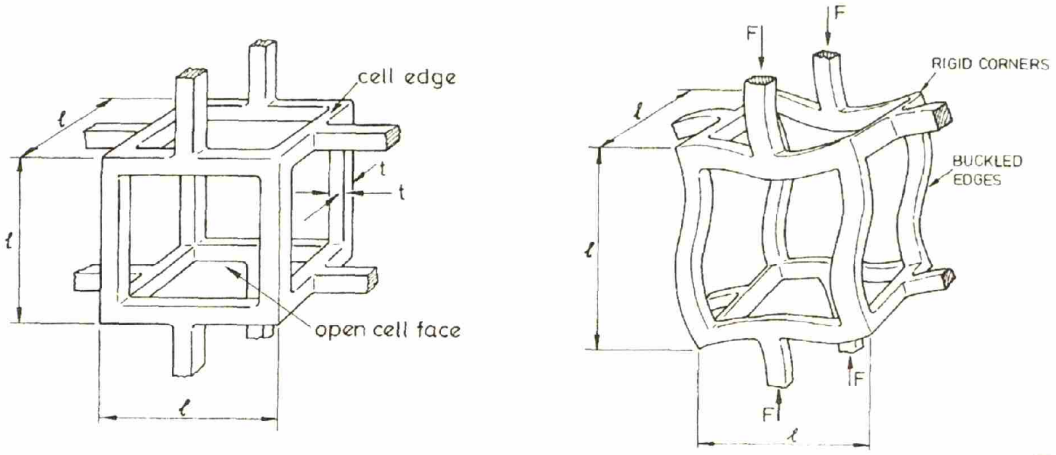

Fig. 6.6a

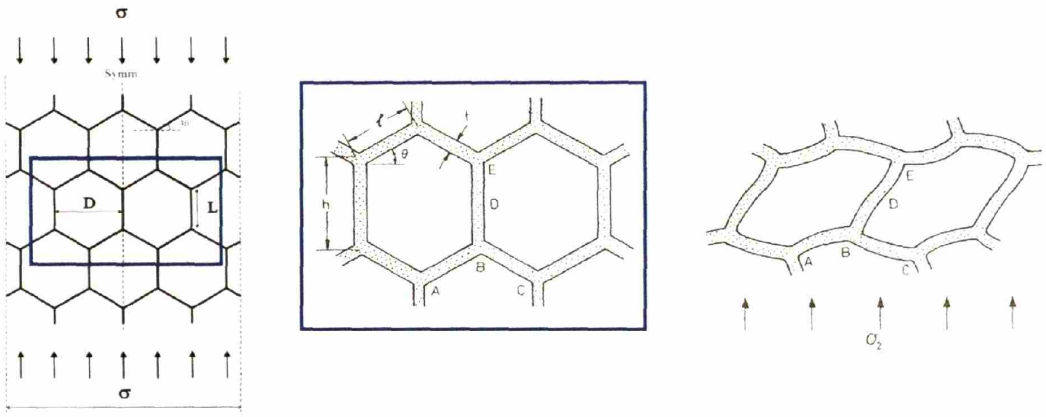

Fig. 6.6b

Figure 6.6. Elastic buckling in the cell edges of an open-cell foam (Fig. 6.6a) (Gibson and Ashby, 1997) and for a hexagonal honeycomb (Fig. 6.6b) (Gibson and Ashby, 1997; Onck, Andrews, et al., 2001).

Using this description, the force per cell was calculated using a column buckling model where critical care must be taken to appropriately describe the system boundary constraints (end restrains of the buckling scaffold strut and the eccentricity of loading). While an eccentrically loaded column would most precisely describe the idealized case of a cell buckling a CG scaffold strut, there are a number of confounding issues to make the implementation of an eccentrically loaded column difficult. The nature of cell interactions with a scaffold strut involves many cell

processes, making determination of the eccentricity difficult. More significantly, calculation of the applied load using an eccentrically loaded column model requires measurement of the strut deflection at each time point during cell-mediated contraction. A centrically-loaded column buckling model was instead utilized in order to simplify the calculation.

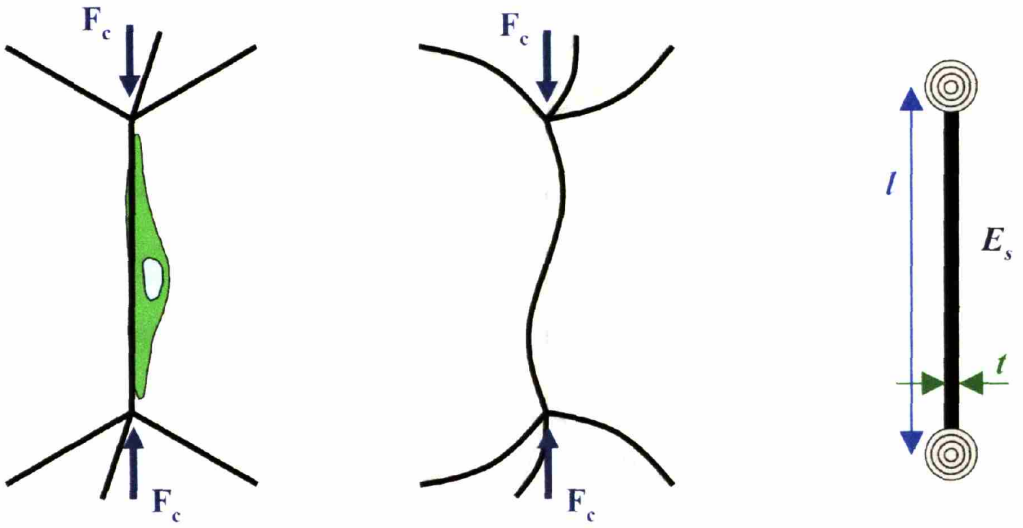

Figure 6.7. Application of a critical buckling load (F_c) to a scaffold strut within an idealized CG scaffold network (left). Deformed configuration of the idealized CG scaffold strut; the three attached struts prevent rotation of the buckling strut edges (middle). Simplified model of CG scaffold strut buckling where the scaffold strut is retrained at its ends with a rotational spring (right).

The critical load (F_c) at which a scaffold strut of length l, Young's Modulus E_s, and second moment of area I, buckles can be calculated by Euler's formula:

Equation 6.7. $$F_c = \frac{n^2 \cdot \pi^2 \cdot E_s \cdot I}{l^2}$$

For this analysis, strut geometry was approximated as a cylindrical fiber ($I = \pi \cdot d^4/64$). The factor n^2 describes the end constraint of the CG scaffold strut and depends on the surrounding

mechanical environment. The effect of multiaxial loads applied to the scaffold network is to change the rotational stiffness of the vertices. Applied loads to the surrounding strut network bend the surrounding (restraining) struts, thereby reducing their rotational stiffness (Gibson and Ashby, 1997). The effect of such applied stress states on the degree of constraint has been previously described for many different cellular materials. For isotropic honeycombs under uniaxial compression, $n_{uni} = 0.686$. Under biaxial compression, the elastic buckling load ($\sigma_{el,\,bi}^{*}$) and hence critical buckling load ($F_{c,\,bi}$) is approximately 80% of that of the same honeycomb structure under uniaxial compression ($\sigma_{el,\,uni}^{*}$, $F_{c,\,uni}$), and isotropic honeycombs under biaxial compression display $n_{bi} = 0.61$ (Gibson and Ashby, 1997). Similar calculations have been performed for isotropic open-cell foams, with values of the degree of constraint (n^2) for uniaxial, biaxial and hydrostatic compression reported: $n_{uni}^2 = 0.41$, $n_{bi}^2 = 0.36$, $n_{hydro}^2 = 0.34$ (Triantafillou, Zhang, et al., 1989).

During free-floating contraction of the isotropic CG scaffold where the cells are randomly distributed through the strut network, the cells contract the scaffold uniformly in all three directions and the scaffold is effectively under hydrostatic compression. This boundary condition most closely approximates the edge restraint applied to any particular strut within the scaffold network due to the random nature of the applied compressive loads in the surrounding strut network. The cell-mediated contractile force (F_c) was calculated from Euler's buckling relation and the hydrostatic compression end restraint:

Equation 6.8.

$$F_c = \frac{n_{hydro}^2 \cdot \pi^2 \cdot E_s \cdot I}{l^2}$$

$$F_c = \frac{0.34 \cdot \pi^3 \cdot E_s \cdot d^4}{64 \cdot l^2}$$

This calculated cell-mediated contractile force is an upper bound for the applied force due to the likely eccentricity of the actual system. However, this calculation represents a new methodology for estimating the contractile force applied by an individual cell within a three-dimensional construct. Previous methods in the literature (Delvoye, Wiliquet, et al., 1991; Kolodney and Wysolmerski, 1992; Eastwood, McGrouther, et al., 1994; Brown, Talas, et al., 1996; Chapuis, Lucarz-Bietry, et al., 1996; Eastwood, Porter, et al., 1996; Brown, Prajapati, et al., 1998; Eastwood, Mudera, et al., 1998; Jenkins, Redwood, et al., 1999; Freyman, Yannas, et al., 2001; Freyman, Yannas, et al., 2001; Freyman, Yannas, et al., 2001; Freyman, Yannas, et al., 2002; Sethi, Yannas, et al., 2002) have relied on calculating an average individual cell contractile forces from the observed macroscopic deformation of a construct and assumptions of the fraction of the cells that were contracting as well as their orientation within the construct.

6.2.7. Statistical analysis

All statistical calculations were performed using the StatView statistical software package (SAS Institute, Inc., Cary, NC). One-way analysis of variance (ANOVA) and pair wise multiple comparison procedures (Dunn's Method) were used to compare groups of data. Error is reported in figures and tables as the standard deviation (StDev), the standard error of the mean (SEM = $StDev/n^{1/2}$), or as the coefficient of variance (CV = StDev/Mean). A probability value of 95% ($p < 0.05$) was used to determine significance.

6.3. Results

6.3.1. CG scaffold microstructural and mechanical properties

The results of extensive mechanical characterization (E^*, σ_{el}^*, ε_{el}^*, $\Delta\sigma/\Delta\varepsilon$) of the CG scaffold variants used in this study have been reported in Chapter 5 (**Table 5.2**). Two homologous series of CG scaffolds described in Chapter 5 were utilized for this investigation. The first is a series of scaffolds with variable pore microstructure and constant stiffness (96 – 151 μm mean pore size; 0.006 relative density; DHT105/24 crosslinking; hydrated) (**Figure 6.8**). The average mechanical properties (E^*, σ_{el}^*, ε_{el}^*, $\Delta\sigma/\Delta\varepsilon$, E_s) of these CG scaffold variants (DHT 105/24 crosslinking) are reported in **Table 6.2**.

The second series of CG scaffolds used in this investigations are scaffolds with variable stiffness and constant microstructure (96 μm mean pore size; 0.006 relative density; DHT105/24, EDAC1:1:5, or EDAC5:2:1 crosslinking; hydrated) (**Figure 6.9**).

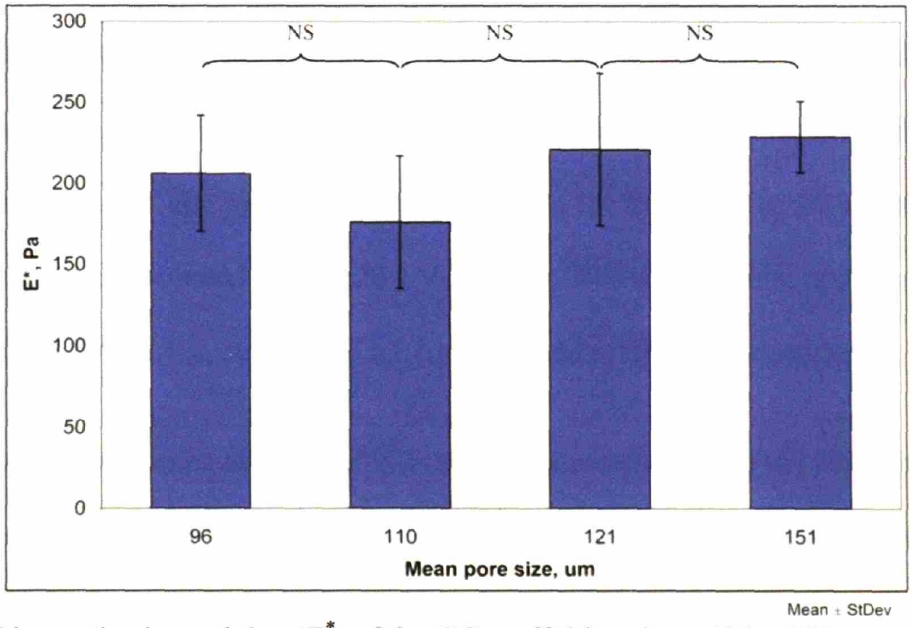

Figure 6.8. Linear elastic modulus (E^*) of the CG scaffold variants (96 – 151 μm mean pore size; DHT105/24 crosslinking; 0.006 relative density; hydrated).

Criteria	Hydrated CG Scaffold
E^*	208 ± 41 Pa
σ_{el}^*	21 ± 8 Pa
ε_{el}^*	0.10 ± 0.04
$\Delta\sigma/\Delta\varepsilon$	92 ± 14 Pa
E_s	5.28 ± 0.25 MPa

Table 6.2. Average (Mean ± St. Dev.) mechanical properties of the CG scaffold variants (96 – 151 μm; 0.006 relative density; DHT105/24 crosslinking; hydrated).

The strut stiffness (E_s) of the hydrated DHT105/24 scaffold variant (E_s = 5.28 ± 0.25 MPa) was calculated from the measured strut stiffness of the dry DHT105/24 scaffold strut (E_s = 762 ± 35.4 MPa) and the relative softening of the overall scaffold modulus (E^*) induced by hydration of the DHT105/24 CG scaffold variant (E_{dry}^* = 30.0 ± 3.9 kPa; $E_{hydrated}^*$ = 208 ± 41 Pa; $E_{hydrated}^*/E_{dry}^*$ = 6.93 x 10^{-3}) as measured in Chapter 5. The hydrated strut stiffness of the two more highly crosslinked scaffolds (EDAC1:1:5, EDAC5:2:1) were calculated from the hydrated strut stiffness of the DHT105/24 CG scaffold and the relative increase in stiffness (2.0x and 7.2x for the EDAC1:1:5 and EDAC5:2:1 scaffolds, respectively) observed in the overall scaffold modulus (E*) due to crosslinking. The local strut stiffness (E_s) of the three CG scaffold variants used for this investigation was estimated to be 5.28 ± 0.25 MPa, 10.6 ± 0.50 MPa, and 38 ± 1.8 MPa for the DHT105/24, EDAC1:1:5, and EDAC5:2:1 crosslinked scaffolds, respectively.

These two homologous series of CG scaffolds allow characterization of the independent effect of the mechanical and microstructural extracellular environment as well as cell type and seeding density on cell behavior, allowing development of multi-dimensional plots of quantifiable cell behaviors such as migration or contraction (**Figure 6.10**).

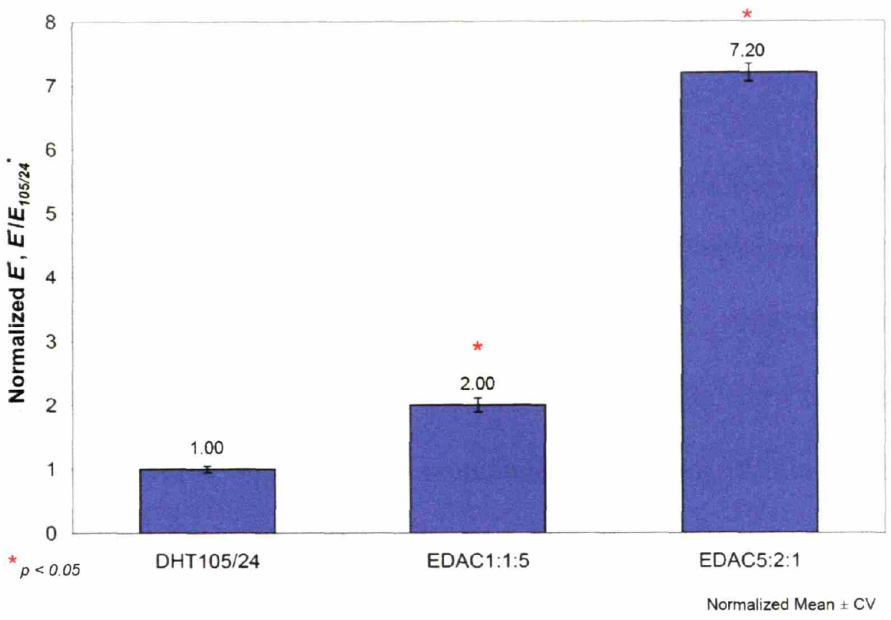

Figure 6.9. Normalized E^* of structurally homogeneous CG scaffold sheet (96 μm mean pore size; 0.006 relative density; DHT105/24, EDAC1:1:5, EDAC5:2:1 crosslinking; hydrated).

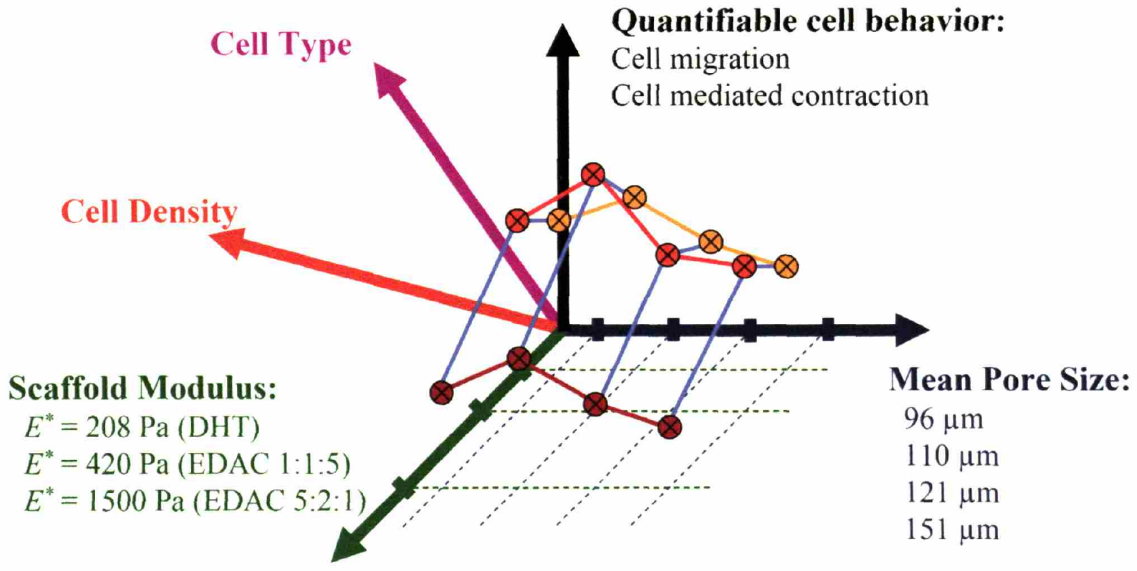

Figure 6.10. Multi-dimensional studies of cell behavior using the CG scaffold variants.

6.3.2. Confocal imaging of cell-scaffold interactions

In an effort to further standardize the experiment, NR6 FBs between p33 and p39 were utilized for all cell tracking experiments; while NR6 FBs exhibit a stable phenotype for long periods of passaging (Pruss, 1977; Chen, Gupta, et al., 1994; Chen, Xie, et al., 1994), the passage number was limited here for sake of reducing experimental error. No significant cell death or photo-bleaching affect was observed during the 10 hour imaging interval. While CMFDA has been previously noted to have a deleterious effect on cell motility for some cell types, likely due to the creation of free radicals as a result of exposure of the CMFDA molecule to the mercury lamp light source, this effect is usually seen in extremely sensitive cell lines (*i.e.*, IC-21 mouse macrophage cell line) and is typically seen almost instantaneously following exposure of the cells to light (Timp, Hopp, et al., 2005). No phototoxic effect was observed, likely due to the robust nature of the NR6 FB and DU-145 cell lines.

Figure 6.11 depicts three-dimensional reconstructions of NR6 FBs within the CG scaffold from confocal imaging analysis at a single time-point. The open-cell pore structure of the CG scaffold (red) is evident and the NR6 FBs (green) exhibit an elongated (not rounded) phenotype similar to what has been previously observed via light microscopy for dermal fibroblasts within CG scaffolds (Freyman, Yannas, et al., 2001; Freyman, Yannas, et al., 2001).

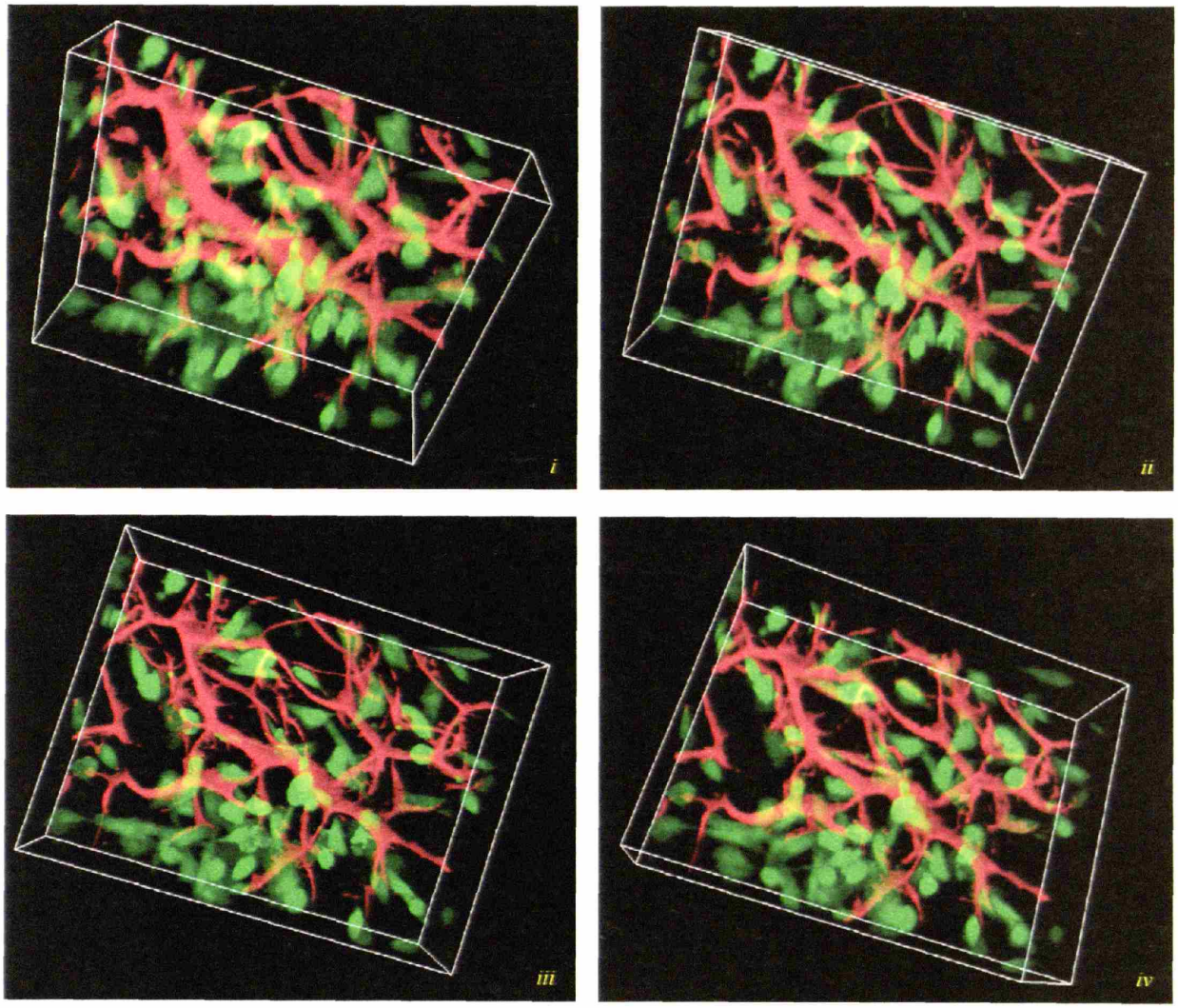

Figure 6.11. Three-dimensional reconstruction of NR6 FBs within a CG scaffold (121 μm mean pore size; 0.006 relative density; DHT crosslinking) at four distinct angles of rotation (*i* – *iv*). Field of view: 246 x 364 x 100 μm.

The majority of FBs appear to be actively bound to the CG scaffold strut network, with only a minority of cells observed floating in the open pore space. Increasingly higher magnification reconstructions allow interrogation of cell behavior from the population to the individual cell level. The representation shown in **Figure 6.12** highlights the experimental power of the CG

scaffold system combined with fluorescent microscopy for quantitatively studying individual cell behavior and specific cell-scaffold interactions.

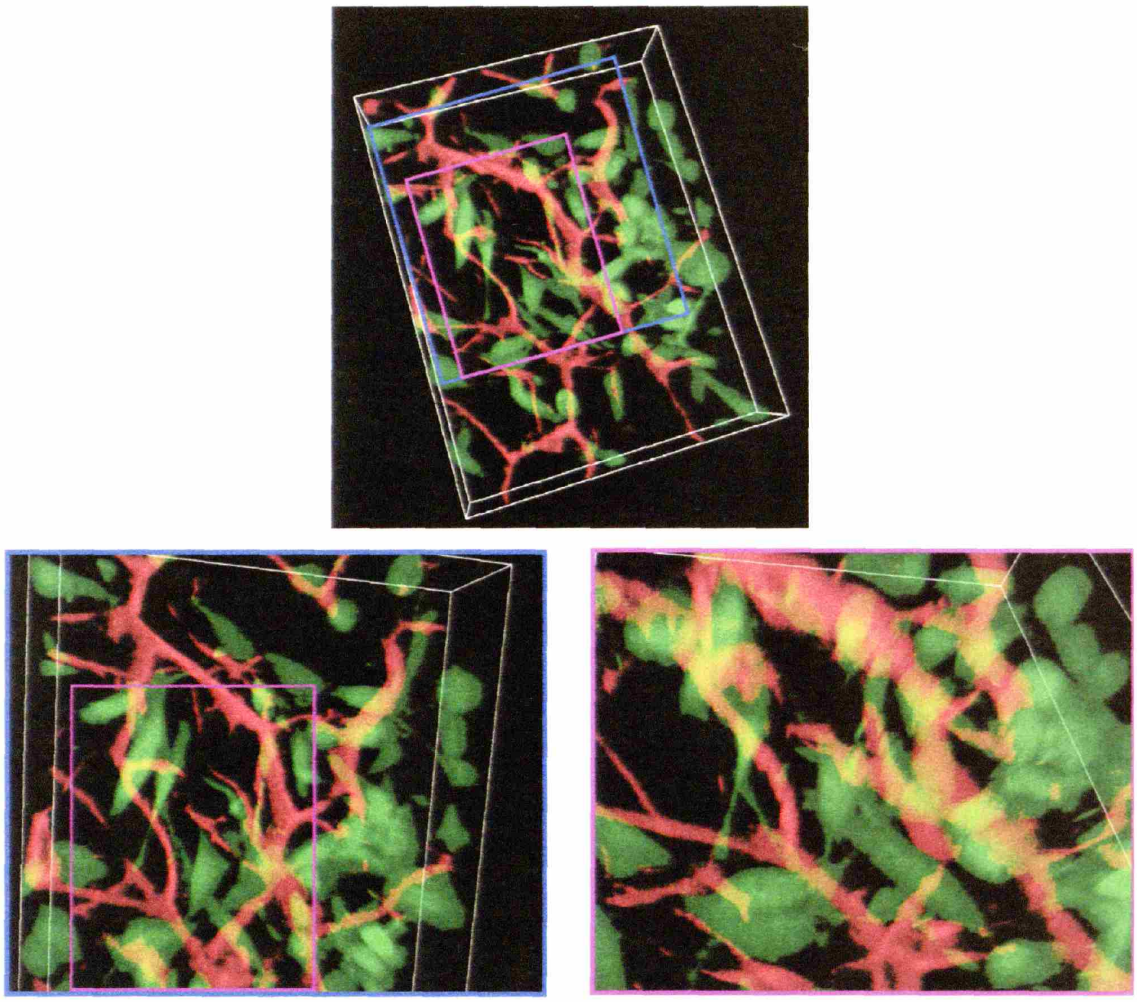

Figure 6.12. Three-dimensional reconstruction of NR6 FBs within a CG scaffold (121 μm mean pore size; 0.006 relative density; DHT105/24 crosslinking). Increasingly selective regions (bottom left, right, respectively) from the full imaged volume (246 x 364 x 100 μm field of view, top) are shown.

6.3.3. Time-lapse cell tracking within CG scaffolds

The time-lapse confocal images of fluorescently labeled NR6 FBs and DU-145 prostate cancer cells migrating in the CG scaffold were analyzed to first identify cell location at each time point.

The most basic representation of cell motility are two-dimensional projections of cell position created by merging the 100 μm image stack at each time point (**Figure 6.13**). Significant cell movement and pore shape modification is evident from these time lapse images.

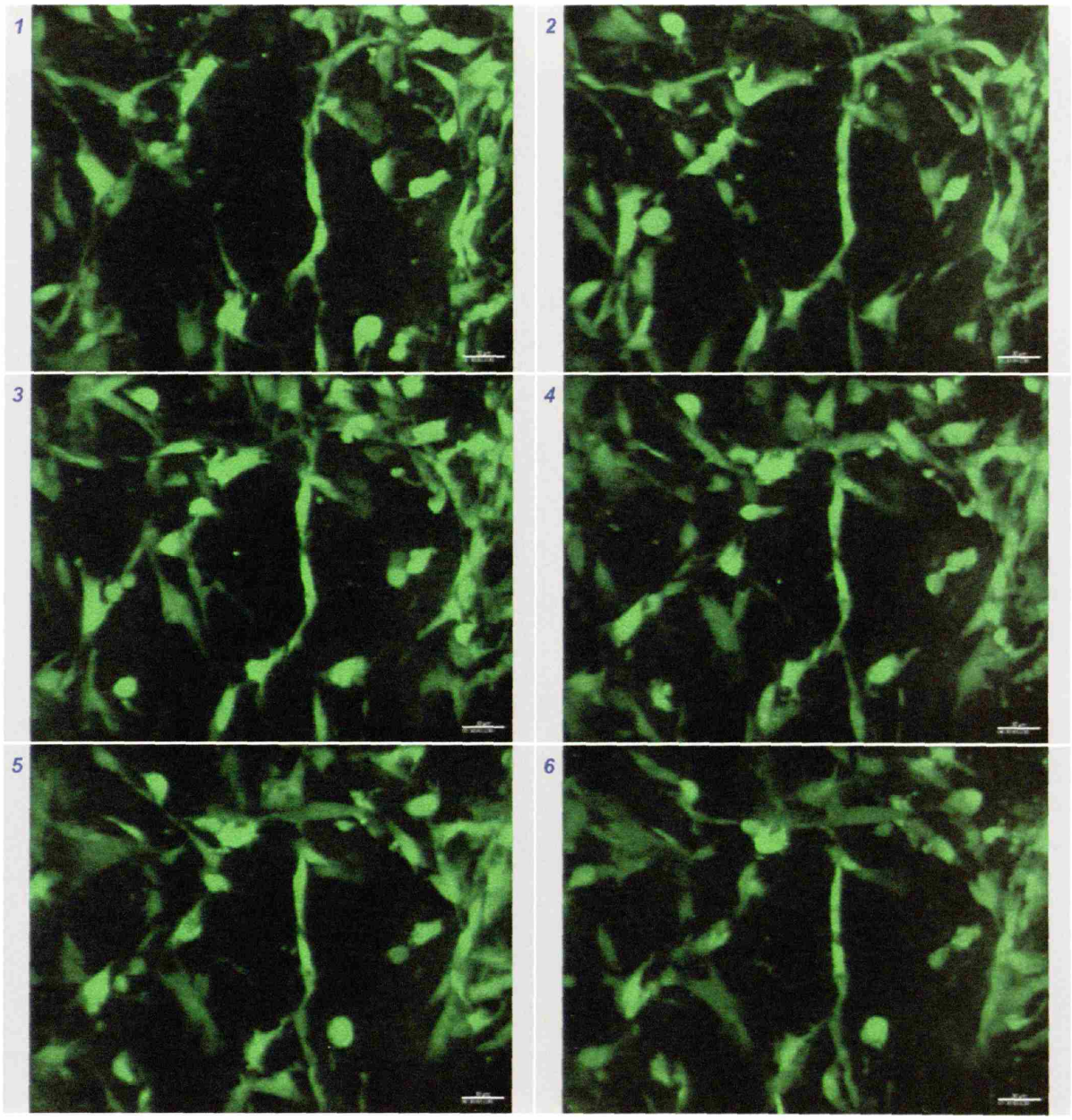

Figure 6.13. Time lapse fluorescent images (0, 1.5, 3, 4.5, 6, 7.5 hours: 1 – 6) of NR6 FB distribution in CG scaffold (96 μm mean pore size; 0.006 relative density; DHT105/24 crosslinking). Scale bar: 30 μm.

Two-dimensional projections (**Figure 6.13**) lack information about cell motion in the Z-direction. To better represent the motile behavior of the cell population within the experimental volume, the confocal microscopy derived image stacks were converted into three-dimensional representations of cell position (**Figure 6.14**).

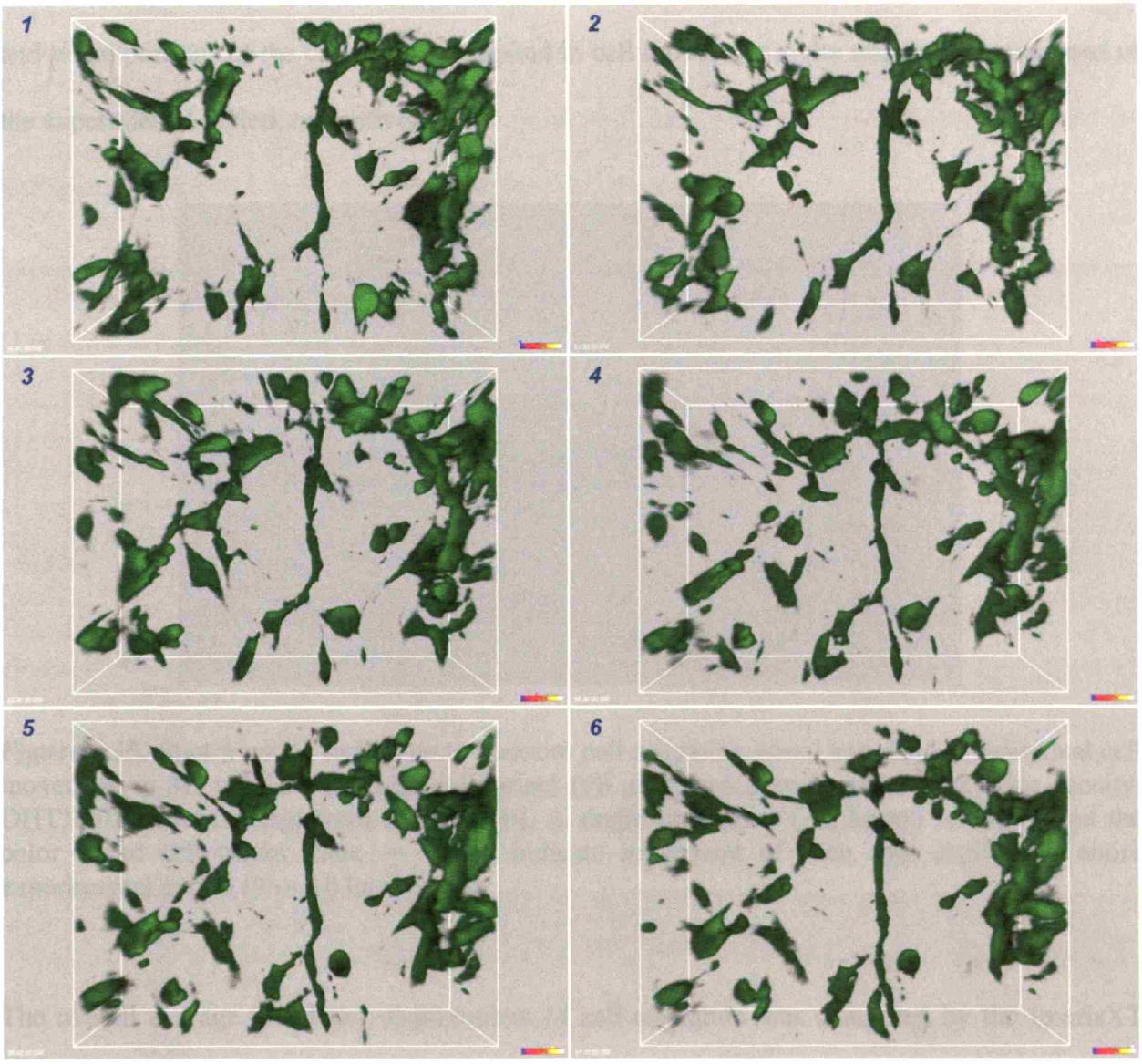

Figure 6.14. Time lapse three-dimensional reconstructions (0, 1.5, 3, 4.5, 6, 7.5 hours: 1 – 6) from **Figure 6.13** of NR6 FBs distribution in CG scaffold (96 μm mean pore size; 0.006 relative density; DHT105/24 crosslinking).

An autoregressive motion algorithm was utilized to calculate cell motility by tracking the movement of each cell centroid using ImarisXT's integrated spot tracking capability (10 μm diameter spot). The autoregression motion algorithm calculated the displacement and average migration speed for every cell within the volume during the experimental period (**Figure 6.15**). Individual cell tracks are color coded to represent temporal information: the dark blue, orange, and white portions of the cell track correspond to cell movement at the start, middle, and end of the experimental period, respectively.

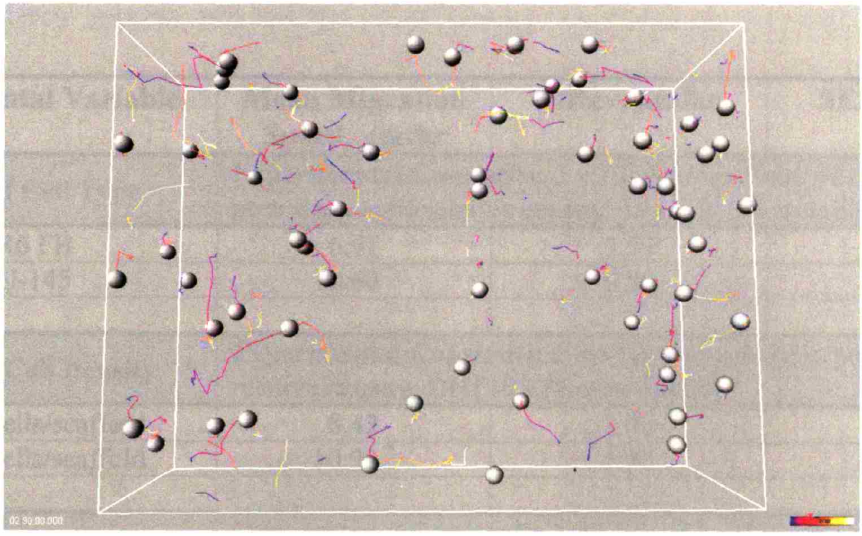

Figure 6.15. Spot tracking technique to measure cell migration speed and display individual cell movement in 3D within a CG scaffold variant (96 μm mean pore size; 0.006 relative density; DHT105/24 crosslinking) from **Figure 6.14**. A single time point (2.5 hours) is shown, but the color coded cell tracks (blue → white) indicate movement of each spot during the entire experimental period (0 → 10 hours).

The overall average speed and displacement of cell migration was computed by the ImarisXT three-dimensional image analysis program by tracking cell position vs. time using the built-in spot tracking routine (Veenman, Reinders, et al., 2001). Cell motility was defined by the movement of the sphere at the cell centroid from time point to time point, with migration speeds

calculated from the centroid displacement and interval time (15 minutes). An autoregressive motion algorithm, which assumes point-to-point correlated motion but overall random motion, was used to track three-dimensional cell movement (Veenman, Reinders, et al., 2001). Only motile cells were included in the analyses of average cell migration speed; a motile cell was defined as one whose centroid moved further than 10 μm (~50% of the cell diameter) from its initial position during the imaging period. Full results of analysis of cell migration speed through the CG scaffold variants are presented in **Table 6.3**; individual analyses of each experimental variable are presented in the following sections (6.3.4 – 6.3.7).

Experimental Variable	Mean Migration Speed, μm/hr	StDev, μm/hr	SEM, μm/hr
Effect of Cell Type	**Experimental Constants:** 5 x 10^5 cells/scaffold; 121 μm mean pore size; 0.006 relative density; DHT105/24 crosslinking		
NR6 FB	6.91	3.59	0.27
DU-145	12.60 *	6.50	0.23
Effect of Cell Density	**Experimental Constants:** NR6 FBs; 96 μm mean pore size; 0.006 relative density; DHT105/24 crosslinking		
1 x 10^5 cells/scaffold	8.42	3.95	0.25
5 x 10^5 cells/scaffold	10.92 *	5.92	0.44
Effect of Mean Pore Size	**Experimental Constants:** NR6 FBs; 5 x 10^5 cells/scaffold; 0.006 relative density; DHT105/24 crosslinking		
96 μm	10.92	5.92	0.44
110 μm	8.58 *	3.59	0.34
121 μm	6.91 **	3.60	0.27
151 μm	4.90 ***	1.75	0.29
Effect of Scaffold Strut Stiffness	**Experimental Constants:** NR6 FBs; 96 μm mean pore size; 1 x 10^5 cells/scaffold; 0.006 relative density		
DHT105/24 (E_s = 5.28 MPa)	8.42	3.95	0.25
EDAC1:1:5 (E_s = 10.6 MPa)	12.32 *	6.42	0.53
EDAC5:2:1 (E_s = 38.0 MPa)	12.66 *	8.49	0.59

Table 6.3. Average cell migration speeds within the CG scaffold variants. Except for the specific parameter being tested in each section, all scaffold characteristics were kept constant and are

specified in the header of each experiment. Results are reported as Mean, StDev, and SEM for each migration speed. *, **, and *** denote distinct, statistically significant results compared to the first value in each experimental group.

6.3.4. Cell motility in CG scaffolds: Effect of cell type (NR6 vs. DU-145)

Figure 6.16 shows the result of cell tracking experiments probing the effect of cell type (NR6 FBs vs. DU-145 prostate cancer cells) on the average cell migration speed (mean track speed) under otherwise identical experimental conditions (5 x 10^5 cells/scaffold; 121 μm mean pore size; 0.006 relative density; DHT105/24 crosslinking). As expected, DU-145 prostate cancer cells migrated at a significantly faster speed than NR6 FBs ($p < 0.05$).

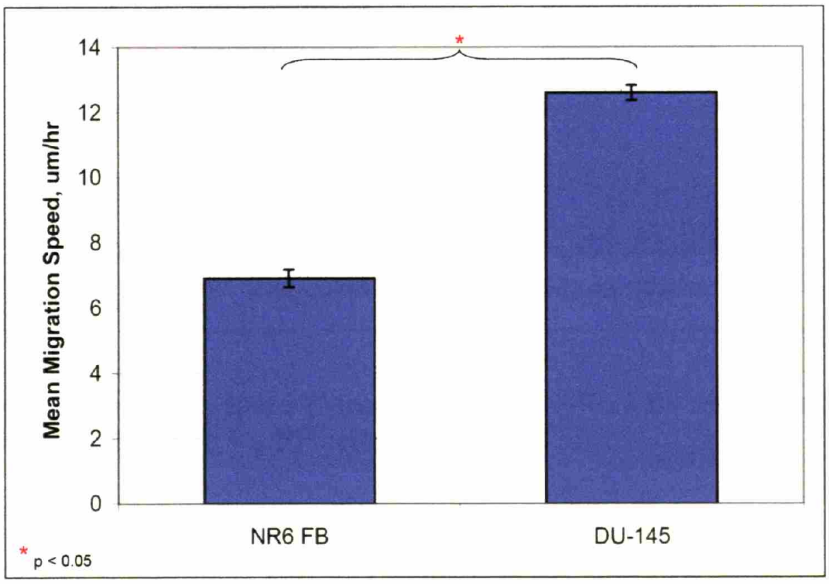

Figure 6.16. Average migration speed (Mean ± SEM) of NR6 FBs vs. DU-145 prostate cancer cells.

6.3.5. Cell motility in CG scaffolds: Effect of seeding density

Figure 6.17 shows the result of cell tracking experiments probing the effect of cell seeding density (1 x 10^5 cells/scaffold vs. 5 x 10^5 cells/scaffold) on the average cell migration speed of NR6 FBs under otherwise identical experimental conditions (96 μm mean pore size; 0.006 relative density; DHT105/24 crosslinking). NR6 FBs seeded at a higher density were observed to migrate at a significantly faster speed ($p < 0.05$).

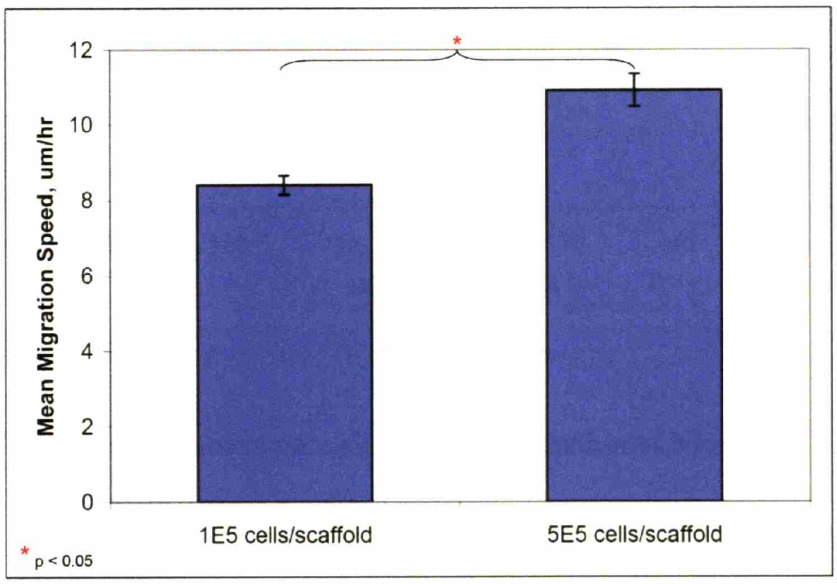

Figure 6.17. Average migration speed (Mean ± SEM) of NR6 FBs seeded at distinct densities (1E5: 1 x 10^5 cells/scaffold, 5E5: 5 x 10^5 cells/scaffold).

6.3.6. Cell motility in CG scaffolds: Effect of scaffold mean pore size

6.3.6.1. Motile fraction

Figure 6.18 shows the result of cell tracking experiments probing the effect of scaffold mean pore size (96 – 151 μm) on the fraction of NR6 FBs within the scaffold measured to be motile under otherwise identical experimental conditions (5 x 10^5 cells/scaffold; 0.006 relative density; DHT105/24 crosslinking). Linear regression identified a significant effect ($p = 0.002$) of mean

pore size on the motile fraction of NR6 FBs, with a greater fraction of cells migrating in scaffolds with increasingly smaller mean pore size.

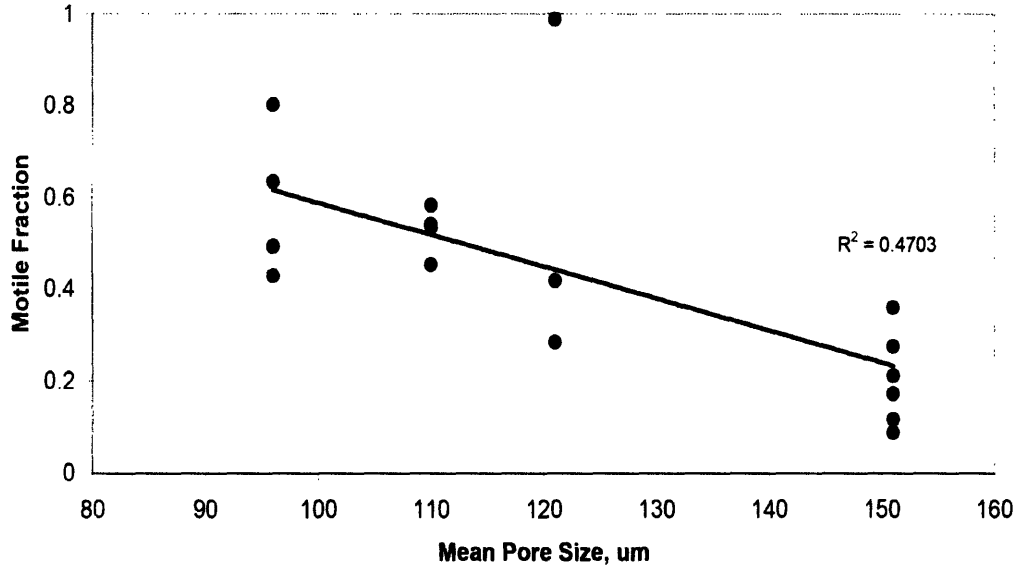

Figure 6.18. Effect of scaffold mean pore size on motile fraction of NR6 FBs.

6.3.6.2. Wind-Rose plot

The directional persistence of cell migration within the CG scaffold variants is reported qualitatively in terms of overall centroid displacement from the starting points using a Wind-Rose plot; cell tracks extending further from the starting point are taken to be showing increased correlation of directional movement, and hence increased directional persistence. **Figure 6.19** shows Wind-Rose plots illustrating the effect of scaffold mean pore size (96 – 151 μm) on overall cell motility, specifically a qualitative representation of directional persistence, of NR6 FBs under otherwise identical experimental conditions (5 x 10^5 cells/scaffold; 0.006 relative

density; DHT105/24 crosslinking). Increased directional persistence is observed with decreasing mean pore size.

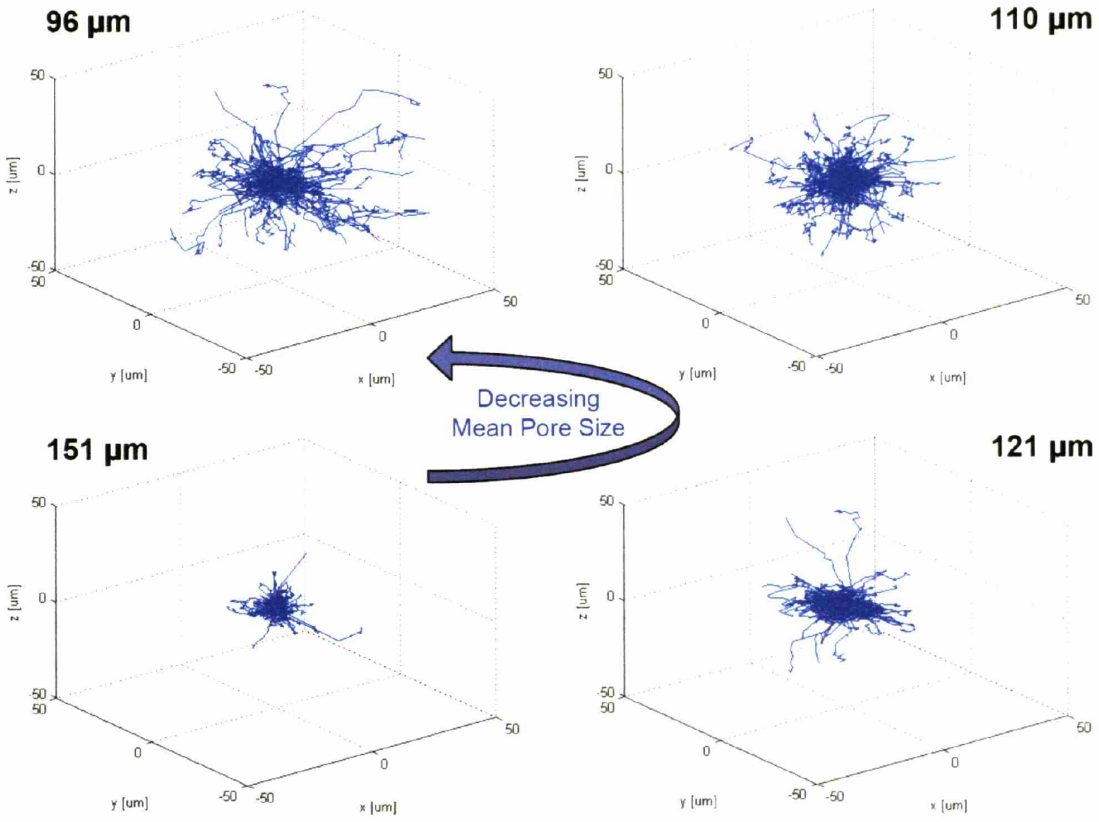

Figure 6.19. Effect of scaffold mean pore size on distribution of NR6 FBs motility, as depicted via a Wind-Rose plot (x, y, z axes: ± 50 µm). Image and analysis courtesy of Hyung-Do Kim, MIT.

6.3.6.3. Mean cell migration speed

Figure 6.20 shows the result of cell tracking experiments probing the effect of scaffold mean pore size (96 – 151 µm) on the average cell migration speed of NR6 FBs under otherwise identical experimental conditions (5 x 10^5 cells/scaffold; 0.006 relative density; DHT105/24

crosslinking). A significant effect ($p < 0.05$) of mean pore size on NR6 FBs migration speed was observed.

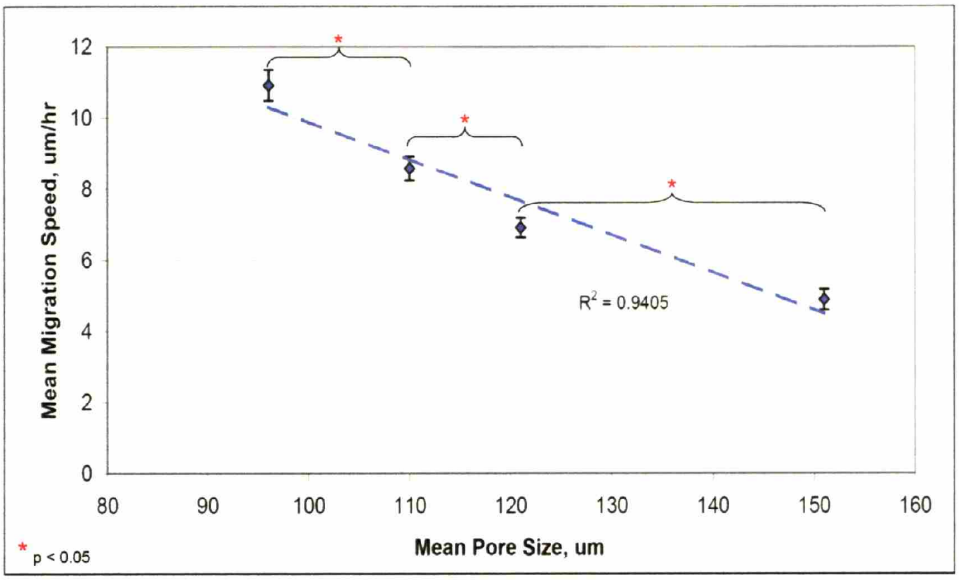

Figure 6.20. Effect of scaffold mean pore size on the average migration speed (Mean ± SEM) of NR6 FBs.

6.3.7. Cell motility in CG scaffolds: Effect of scaffold stiffness

Figure 6.21 shows the result of cell tracking experiments probing the effect of scaffold stiffness on the average cell migration speed of NR6 FBs under otherwise identical experimental conditions (1×10^5 cells/scaffold; 96 μm mean pore size; 0.006 relative density).

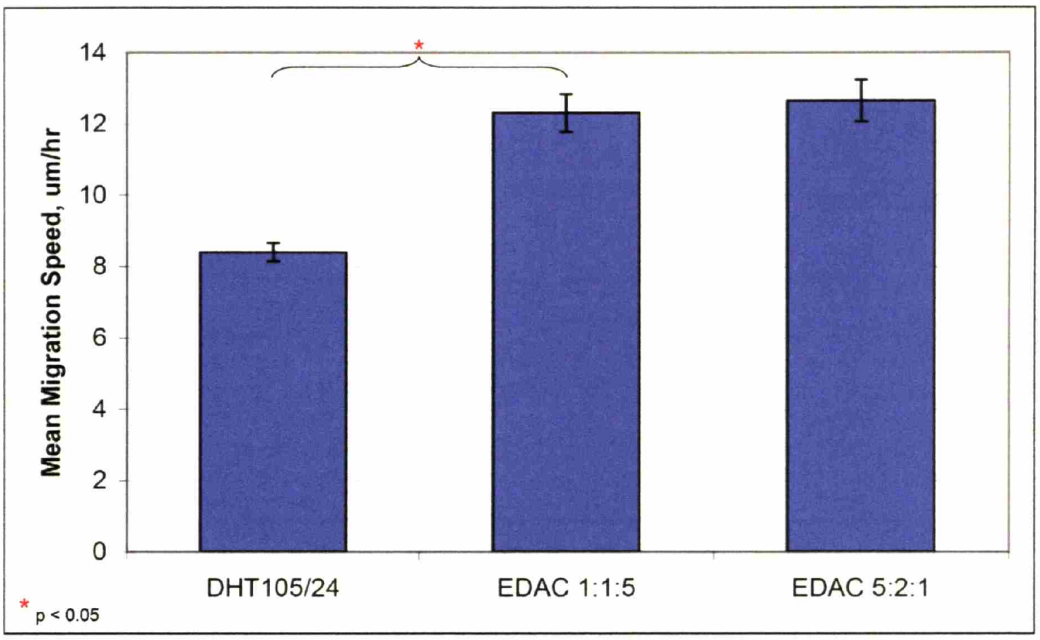

Figure 6.21. Independent effect of scaffold crosslinking treatment on the average migration speed (Mean ± SEM) of NR6 FBs.

Results of mechanical characterization of CG scaffold strut stiffness (E_s, Chapter 5) allow reinterpretation of the results in **Figure 6.21** to determine the direct effect of scaffold strut stiffness (E_s) on migration speed. The strut stiffness for the three CG scaffold variants (DHT105/24, EDAC1:1:5, EDAC5:2:1) was calculated from the hydrated strut modulus for the DHT105/24 scaffold ($E_{s,\,hyd}$ = 5.28 ± 0.25 MPa) and the relative elastic moduli (E*) of the EDAC1:1:5 and EDAC5:2:1 groups compared to the DHT105/24 group (2.0x, 7.2x, respectively).

A significant effect ($p < 0.05$) of scaffold stiffness from 5.28 to 10.6 MPa was observed on NR6 FB migration speed, where cell migration speed increases asymptotically with strut stiffness (**Figure 6.22**).

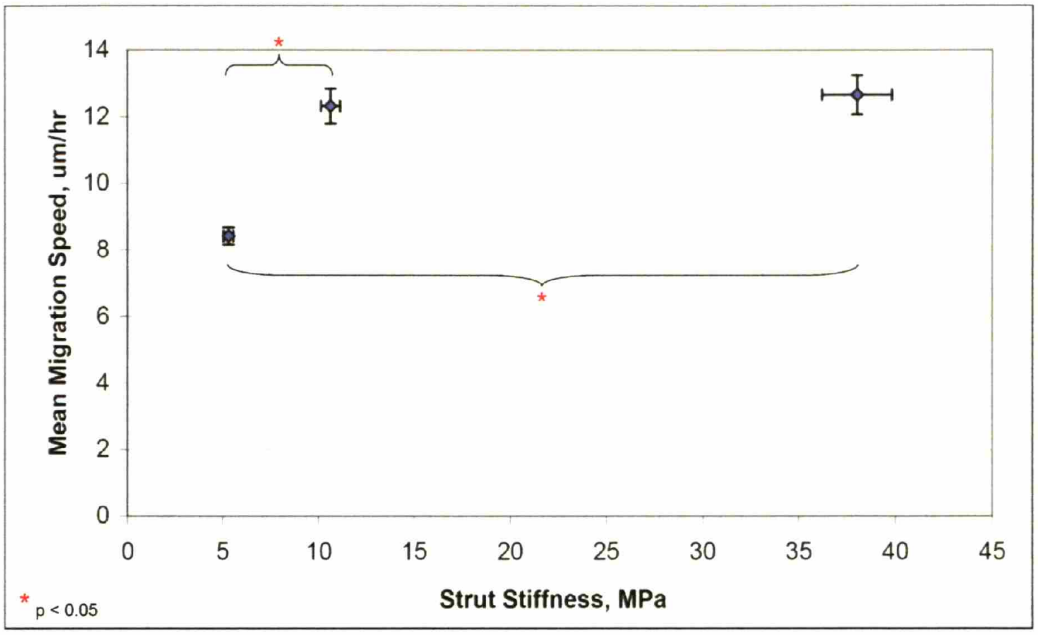

Figure 6.22. Effect of scaffold strut stiffness on the average migration speed (Mean ± SEM) of NR6 FBs.

6.3.8. Cell contraction in CG scaffolds: Measurement of cell-mediated contraction force

6.3.8.1. Free-floating contraction assay

Two datasets from distinct cell experiments were analyzed using the free-floating contraction assay: synovial cells (Vickers, Johnson, et al., 2004) and NR6 FBs (Soller, 2005). In the first experiment, 2 x 10^6 synovial cells were seeded into 9 mm diameter CG scaffold disks (96 μm mean pore size; 0.006 relative density; DHT crosslinking). Approximately 50% of the cells initially attached to the scaffolds and remained viable; overall cell viability after 30 days in culture was found to be 25%. The synovial cells were observed to substantially contract the CG scaffolds over the 30 day experimental period (**Figure 6.23**); maximal cell-mediated contraction (contraction of the seeded scaffold minus contraction of the unseeded scaffold) was observed to occur within the first two weeks of the experiment.

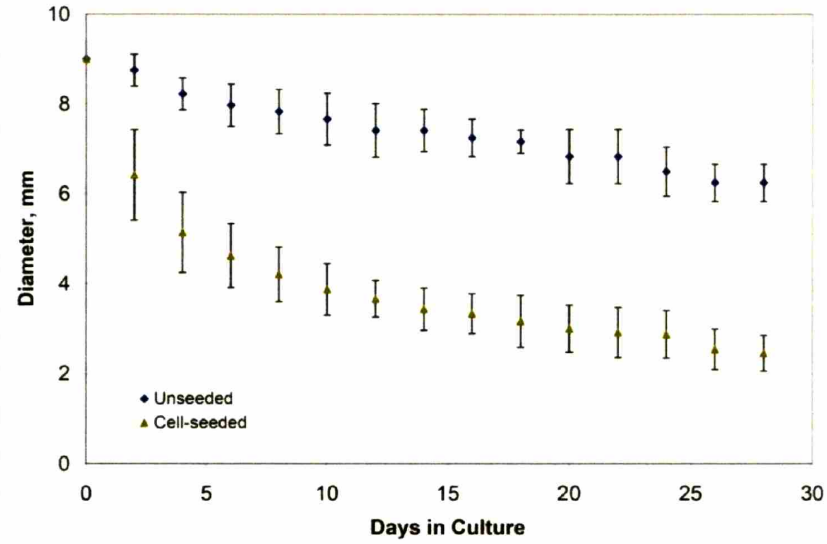

Fig. 6.23a

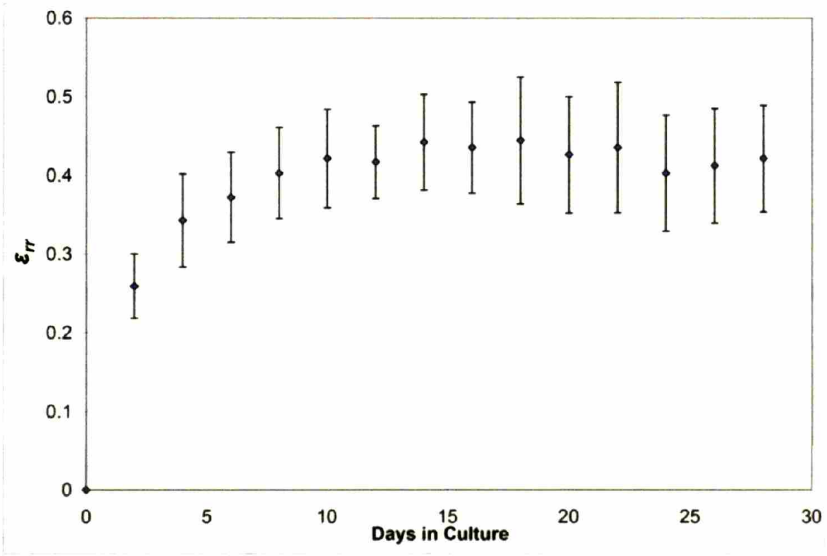

Fig. 6.23b

Figure 6.23. Measurement of synovial cell contraction of CG scaffolds. Temporal change in CG scaffold diameter (d) for unseeded and synovial cell seeded scaffolds (Fig. 6.23a). Calculated radial strain (ε_{rr}) applied to CG scaffold by synovial cells ($d_{seeded} - d_{unseeded}$) using free-floating contraction assay (Fig. 6.23b).

In the second experiment, 1.2 x 10^6 NR6 FBs were seeded into CG 8 mm diameter scaffold disks (96 μm mean pore size; 0.006 relative density; DHT crosslinking); as maximal cell mediated contraction was achieved within 14 days post-seeding in the first experiment, contraction was

only measured for the first 12 days in culture for this experiment. Approximately 50% of the cells initially attached to the scaffolds and remained viable; overall cell viability after 12 days in culture was found to be 13% (Soller, 2005). As expected, NR6 cells were also observed to contract the CG scaffolds (**Figure 6.24**).

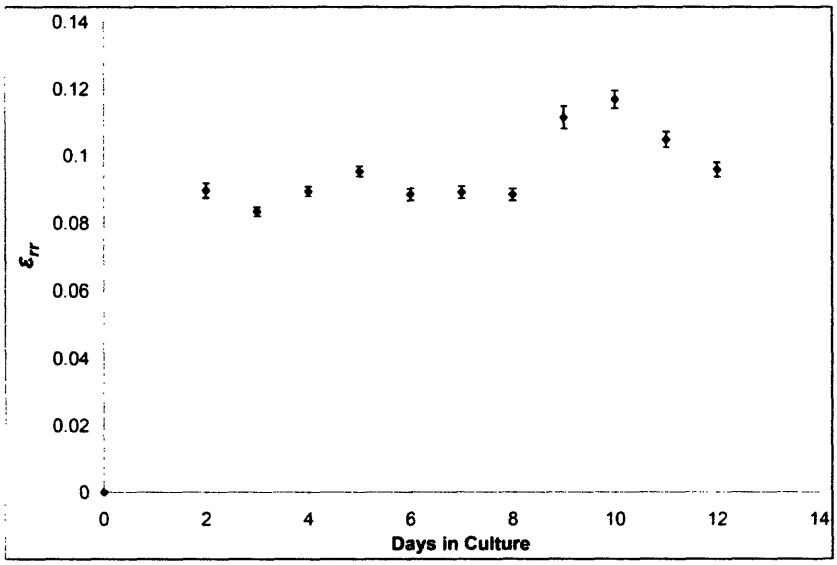

Figure 6.24. Calculated radial strain (ε_{rr}) applied to CG scaffold by NR6 FBs using free-floating contraction assay.

The average contractile force generated per cell (F_c) within the CG scaffold was calculated using the methodology described by **Eq. 6.5** and **Eq. 6.6** and the scaffold mechanical properties described in **Table 5.2**. The average F_c was calculated to be 6.5 ± 0.1 nN and 8.9 ± 0.9 nN for the synovial cells and NR6 FBs, respectively.

6.3.8.2. Individual cell contraction assay

The contractile force generated (F_c) by individual cells within the CG scaffold was calculated using the methodology described by **Eq. 6.8** from light microscopy images of dermal fibroblasts

within CG scaffolds. These images that were analyzed were taken from datasets generated during previous investigations of cell-mediated contraction of CG scaffolds (Freyman, 2001; Freyman, Yannas, et al., 2001; Freyman, Yannas, et al., 2001) (**Figure 6.25**).

The CG scaffold used in this previous investigation exhibited a more heterogeneous pore structure: the scaffold was fabricated via the "quenching" technique and scaffold samples were selected from the scaffold sheet using the 'Best Pick' methodology described in Chapter 2 (132 ± 24 μm mean pore size; 0.006 relative density; DHT105/24 crosslinking). While this scaffold did not exhibit a homogenous microstructure, the mechanical characterization performed on the uniform, homogeneous scaffold variants in Chapter 5 provide sufficient detail to describe the mechanical environment of the dermal FBs within this heterogeneous scaffold. Both the heterogeneous scaffold used here and the homogeneous versions were fabricated with an identical relative density (0.006), crosslinking density (DHT105/24), and chemical composition (identical ratio of type I collagen:chondroitin 6-sulfate).

Due to the non-uniform, non-equiaxed pore microstructure, the heterogeneous scaffold will not exhibit the same mechanical isotropy and macroscopic mechanical characteristics (E^*, σ_{el}^*, ε_{el}^*, $\Delta\sigma/\Delta\varepsilon$) observed with the homogeneous scaffold variants, making it inappropriate to use the heterogeneous scaffold for the free-floating contraction assay. However, the mechanical characterization performed on the individual struts of the homogeneous scaffold (E_s) determined the CG scaffold strut modulus for the DHT105/24 crosslinked scaffold ($E_{s,\,hyd}$ = 5.28 ± 0.25 MPa); this result is an inherent characteristic of the CG scaffold strut that is independent of strut geometry and pore shape. The measured strut modulus ($E_{s,\,hyd}$) for the homogeneous CG scaffold

variants was used to describe the strut modulus of the heterogeneous CG scaffold variants. Measurement of the individual strut length (l) and diameter (d) from each light micrograph allowed calculation of the contractile force exerted by the individual cell on the strut.

Image analysis was performed on CG scaffolds seeded with a suspension of 5^{th} to 7^{th} passage dermal FBs isolated from New Zealand white rabbit skin explants (Freyman, Yannas, et al., 2001). The contractile force generated by individual dermal FBs within the CG scaffold, determined using the column buckling relationships derived earlier (**Eq. 6.8**). Previous analysis of the CG scaffold strut system had identified an average strut thickness of 3.9 μm (Harley and Wong, Unpublished data); this result correlates well with predictions of strut thickness using an open-cell foam model. Confocal analysis has also confirmed the open-cell nature of the scaffold and the use of a cylindrical strut as a first order approximation of strut shape. As such, while strut length was measured for each sample, determination of an average strut diameter was much more complicated due to the small length scale, so a strut diameter of 3.9 μm was used for all calculations of individual cell contraction force. This diameter correlated well with the observed strut thickness in the individual images. Results of analysis of a series of images of contractile cells are reported in **Table 6.4**.

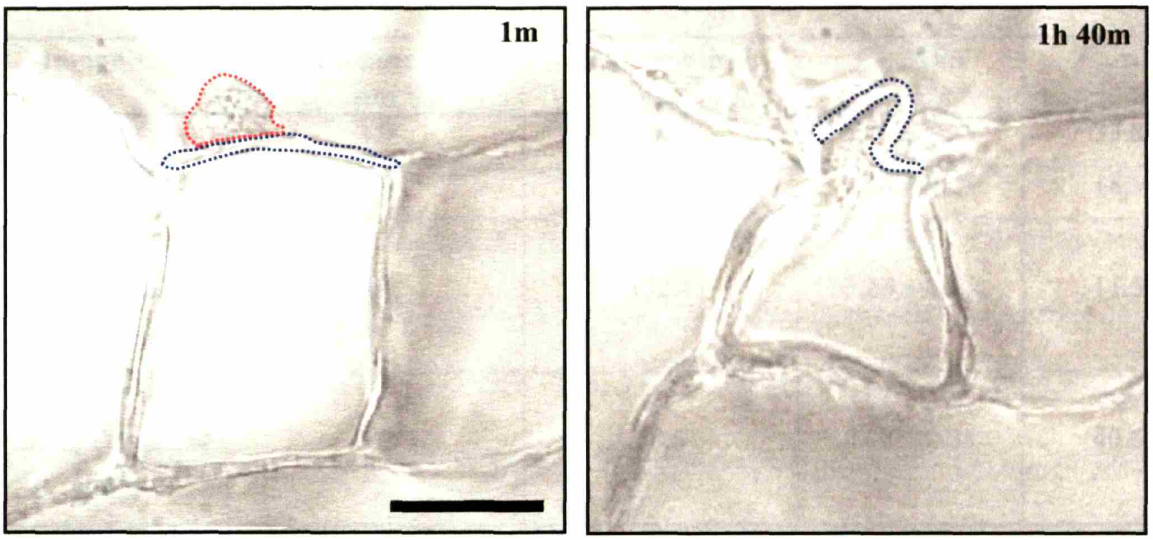

Fig. 6.25a

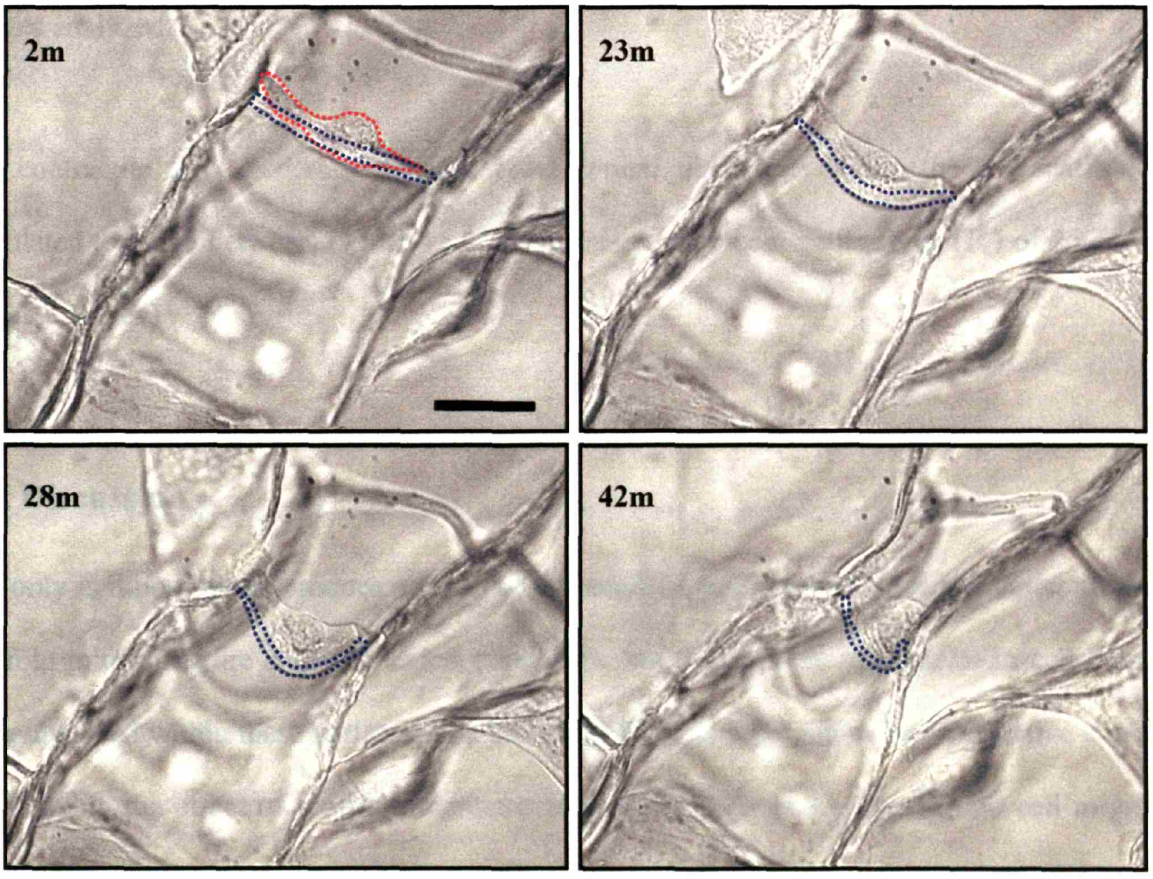

Fig. 6.25b

Figure 6.25. Time lapse light microscopy images of individual dermal fibroblasts (Fig. 6.25a, 6.25b) buckling a CG scaffold strut. Red dotted line highlights the FB while the blue dotted line identifies the strut the FB is buckling. Scale bars: 50 μm.

Image	Strut diameter, d, μm	Strut length, l, μm	E_s, MPa	F_c, nN
Fig. 6.25a	3.9	77.2	5.28 ± 0.25	33.8
Fig. 6.25b	3.9	104.3	5.28 ± 0.25	18.5
Fig. 3d (Freyman, Yannas, et al., 2001)	3.9	132.4	5.28 ± 0.25	11.5
Fig. 6b (Freyman, Yannas, et al., 2001)	3.9	68.5	5.28 ± 0.25	40.6

Table 6.4. Calculations of F_c from light micrograph images. References are provided for all images analyzed.

The contractile force generated by individual dermal fibroblasts within the CG scaffold was calculated to range between 11 and 41 nN, with an average contractile force (F_c) of 26 ± 13 nN (Mean ± StDev) .

6.4. Discussion

Not only is it possible to produce a series of CG scaffold variants with independent control over scaffold microstructure and mechanical properties, but quantifiable differences in cell behavior were observed within these variants. The CG scaffold system proved to be an effective construct for studying the effect of scaffold microstructural and mechanical properties on cell migratory processes using confocal microscopy. NR6 FBs appeared to be primarily attached to the scaffold struts and remained in an elongated phenotype for the entirety of the experimental period (**Figure 6.10 – 6.13**). The few NR6 FBs that were observed not attached to a scaffold strut

appeared primarily in a rounded morphology and many were undergoing apoptotic behavior characterized by membrane blebbing (Harley, Unpublished data). Any cell observed to be undergoing apoptotic behavior or proliferation was not considered in calculation of migratory behavior. No significant photo-bleaching effect was observed during the 10 hour imaging interval, suggesting that relevant data was gathered throughout the investigational period.

NR6 FBs and DU-145 prostate cancer cells were found to migrate at different speeds within the same CG scaffold environment, with the DU-145 cells migrating at a significantly faster speed (12.6 vs. 6.9 μm/hr; **Figure 6.16**). This effect was expected, as the DU-145 cells are significantly smaller and have been previously observed to migrate at high speeds on flat membranes (Zaman, Trapani, et al., In preparation, 2006) while the NR6 FB is more often characterized by a contractile and only slightly motile phenotype (Pruss, 1977; Chen, Gupta, et al., 1994; Chen, Xie, et al., 1994; Ware, Wells, et al., 1998; Koo, Irvine, et al., 2002).

Turning to the migratory behavior of NR6 FBs within a variety of extracellular environments, a significant effect of scaffold stiffness and seeding density on FB migration speed was found (**Figure 6.17, 6.21, 6.22**). A significant effect of mean pore size was also found on the motile fraction of the FB cells and on the average migration speed (**Figure 6.18, 6.20**), and a qualitative difference in FB migratory persistence in scaffold with different mean pore sizes was observed via Wind-Rose plots (**Figure 6.19**).

The asymptotic increase in cell migration speed with increasing scaffold strut stiffness (8.4, 12.3, and 12.7 μm/hr for substrate stiffnesses of 5.28, 10.6, and 38 MPa, respectively; **Figure 6.22**)

correlates well with theoretical predictions of cell migration speed in the literature. Asymptotic behavior would be expected when the underlying substrate stiffness reaches a saturation value where the substrate is significantly stiffer than that which can be resolved by the cell; above such a saturation value, an increase in substrate stiffness would not be expected to influence cell behavior. Two distinct computational models, one using lattice Monte Carlo methods (Zaman, Matsudaira, et al., In preparation, 2006) and a second calculating cell velocity vectors from internally generated forces that were modeled to produce external traction forces (Zaman, Kamm, et al., 2005), and others in the literature (DiMilla, Barbee, et al., 1991) have suggested a saturation value for the underlying substrate modulus (thought to be $E_{sat} \geq 1$ MPa) above which an increase in modulus stiffness will not result in an increase in cell migration speed. A saturation stiffness (E_{sat}) between 5 and 10 MPa was observed for this CG scaffold system, correlating well with current computations studies of three-dimensional cell motility. This experimental finding also correlates well with previous investigations of cell-substrate interactions that found a significant influence in substrate stiffness on cell migration speed on flat surfaces (Lo, Wang, et al., 2000); a substrate saturation stiffness was not observed in this experiment, likely because substrate stiffnesses of 14 and 20 kPa – a full two orders of magnitude lower than those used in this experiment – were utilized.

The observed increase in NR6 FB migration speed with increasing seeding density (8.4 and 10.9 μm/hr for cell densities of 1 x 10^5 and 5 x 10^5 cells/scaffold, respectively; **Figure 6.17**) suggests two potential influences that will require future experimental investigation. The five-fold increase in cell density, while still far below the typical cell density in the ECM of tissues, increases the probability of cell-cell interactions. These interactions and any group behaviors that

may result could potentially have significant effects on cell behavior; future investigations would require consideration of the frequency of cell-cell contact and the presence of large groups of cells congregating together. However, the increase in cell density also plays a significant role in altering the composite mechanical environment of the cells within the scaffold, and the mechanical environment has been observed to influence cell migration speed. Increasing the cell density would increase both the composite (global) scaffold modulus (E^*) but could also play a role in modifying the effective local strut modulus (E_s). These effects have not been addressed in this investigation, but these results suggest a new series of experiments to measure the change in global and local mechanical properties of CG scaffolds as cell seeding density and technique (*i.e.*, static vs. active seeding) are modified.

The significant effect of mean pore size on the motile fraction (increasing motile fraction with decreasing mean pore size; **Figure 6.18**), migration speed (4.9, 6.9, 8.6, and 10.9 μm/hr for mean pore sizes of 151, 121, 110, and 96 μm, respectively; **Figure 6.20**), and persistence (qualitatively greater persistence with decreasing mean pore size; **Figure 6.19**) presents a slightly more difficult effect to explain. It is unlikely that the NR6 FB (critical dimension 20 – 30 μm) is able to probe the entire pore in which it is sitting with its cell processes (mean pore sizes 96 – 151 μm) (**Figure 6.26**) and be able to discern a difference in the microstructure (*i.e.*, sense a difference in a 121 μm and a 151 μm pore). Instead it is much more likely that the observed effect of mean pore size on cell behavior is due to a structural or mechanical cue that the FB is able to detect from the local strut network. Cellular solids modeling provides an ideal tool to investigate potential local mechanical and structural differences that could influence cell behavior. For this analysis a tetrakaidecahedral unit cell, with characteristic mean pore size (d),

strut thickness (t), edge (strut) length (l), and relative density ($\rho^*/\rho_s \alpha (t/l)^2$) (**Eq. 5.1**) (Gibson and Ashby, 1997), was utilized.

Differences in the bending rigidity of the struts in the different scaffold variants was first considered as the local cue that influences cell migration speed. The CG scaffold variants with different mean pore sizes have a constant relative density (**Table 6.1**), allowing the modulation of scaffold mean pore size independent of the elastic modulus (E^*). Additionally, because all scaffolds were fabricated from a constant chemical composition, the local strut modulus (E_s) for all the scaffold variants would remain unchanged. However, maintaining a constant relative density while changing the mean pore size results in differential distribution of the CG content throughout the scaffold that manifests itself as differences in the thickness and length of the scaffold struts. For scaffolds with a constant relative density, as the mean pore size decreases, the strut length ($l = d/2.78$, **Eq. 4.5**) and strut thickness decrease (t, $\rho^*/\rho_s \alpha (t/l)^2$, **Eq. 5.1**) (Gibson and Ashby, 1997) (**Figure 6.26**).

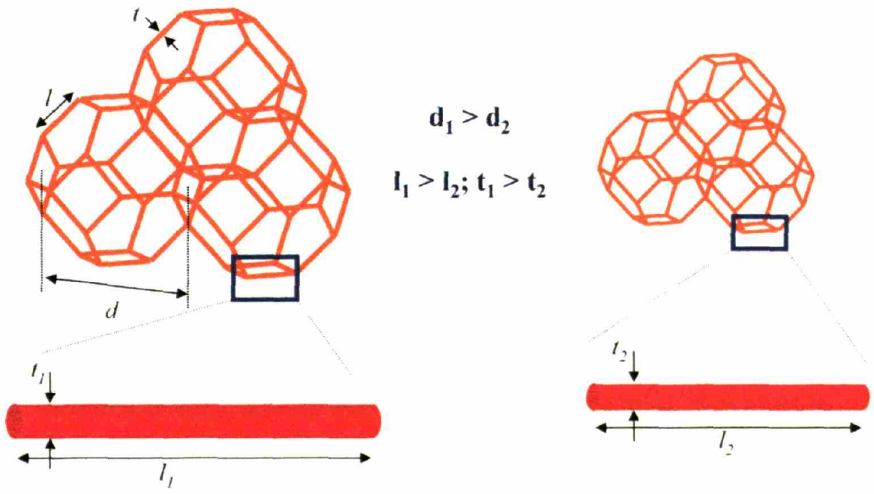

Figure 6.26. Cellular solids description of changes in scaffold strut thickness and length with changes in mean pore size.

Increasing the mean pore size at constant relative density results in scaffold struts that are relatively longer and thicker. Scaffold struts that are thicker and longer have a resultant larger moment of inertia (I) and larger bending rigidity ($E_s \cdot I$). Therefore as mean pore size increases, the effective bending stiffness of the strut ($E_s \cdot I$) increases even though the modulus remains unchanged (E_s): the struts of the scaffold with a larger mean pore size would feel relatively "stiffer" than struts from a scaffold with a smaller mean pore size. The decrease in migration speed as mean pore size increases suggests that cell migration speed would decrease as scaffold stiffness increases. However, experimentally cell migration speed was observed to increase asymptotically as scaffold stiffness increases (**Figure 6.22**), making it less likely that local differences in strut stiffness are responsible for the effect of mean pore size on NR6 FB migration speed. If the effects of the change in strut stiffness with mean pore size (as observed in Section 6.3.7) is incorporated into the experimental finding of cell migration speed vs. scaffold mean pore size, the overall effect of pore size would be even more significant. In actuality, the scaffold struts are not nearly as perfectly defined as those in cellular solids theory, so future investigation of this potential complicating factor needs to be considered.

Differences in local microstructural features were then examined as the local cue that influences cell migration speed in scaffolds with different mean pore sizes. Many microstructural features, such as strut curvature, strut surface area, strut junction spacing, and strut junction density, can also be considered to explain the effect of mean pore size on NR6 FB migration speed; all of these strut characteristics would also be affected by the differential distribution of CG content in scaffolds with distinct mean pore sizes. Here, the effect of strut junction spacing and density will be discussed. Strut junctions are regions in the scaffold where more than 1 strut meet (**Figure**

6.27). These regions are significant because cells reaching strut junctions likely have the ability to change their phenotype; cells on a single scaffold strut typically exhibited an elongated morphology while those reaching a strut junction have the ability to spread across multiple struts. The presence of strut junctions within the series of CG scaffolds with distinct mean pore sizes is now described using open-cell foam model to determine whether a correlation is observed between strut junctions and the cell migration speed.

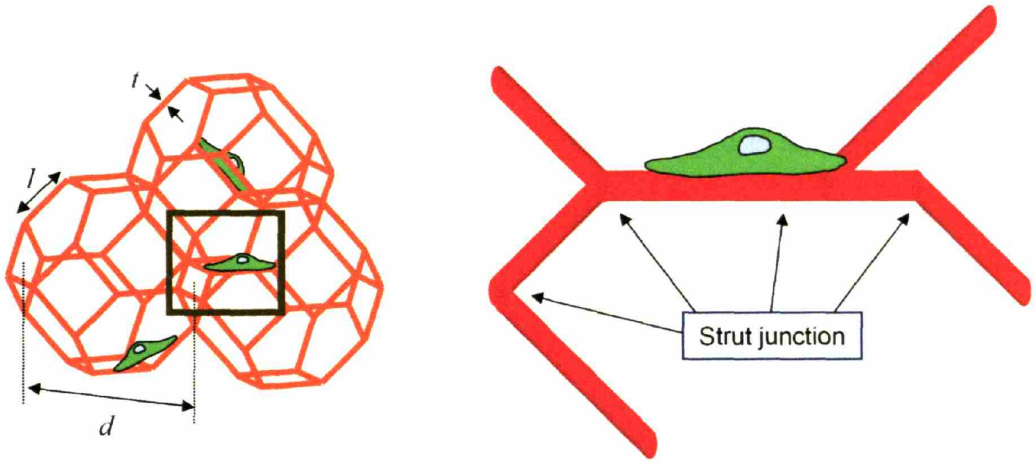

Figure 6.27. Tetraikaidecahedral unit cell (left). Comparative length scale of NR6 FBs vs. mean pore size.

For a series of open-cell foams with distinct mean pore sizes, the distance between (D_{jxn}) and density (ρ_{jxn}) of strut junctions (**Figure 6.27**) can be modeled simply. The distance between the strut junctions (D_{jxn}) is the mean scaffold edge length (l). The density (ρ_{jxn}) of strut junctions can be calculated from the number of strut junctions per unit cell (jxn/UC) divided by the volume of the unit cell (vol/UC). Calculations of D_{jxn} and ρ_{jxn} are made using the tetrakaidecahedral unit cell and are also reported for a generic unit cell:

Equation 6.9.

$$D_{jxn} = l = \frac{d}{2.785} = \frac{d}{C_1}$$

$$\rho_{jxn} = \frac{6(jxn/UC)}{11.31 \cdot \left(\frac{d}{2.785}\right)^3 (vol/UC)} = \frac{11.459}{d^3} = \frac{C_2}{d^3}$$

Good correlation was observed between the observed NR6 migration speed in the scaffold variants with different mean pore sizes and both the distance between and density of strut junctions (**Figure 6.28**). The correlation between migration speed and D_{jxn} was expected because D_{jxn} and mean pore size (d) are related by a constant of proportionality. The good correlation between migration speed and the density of strut junctions suggests that microstructural features may play a significant role in influencing cell migration speed and that further study is warranted into this phenomenon.

The CG scaffold system also allowed measurement of the cell-mediated contractile forces generated within the scaffold. Previously, the average cell contraction force generated by dermal fibroblasts within collagen-glycosaminoglycan scaffolds, calculated by measuring the change in the length or thickness of a rectangular scaffold sample when seeded with millions of cells, has been reported to be 1.4 ± 0.2 nN (Freyman, Yannas, et al., 2001). To make this calculation, two significant assumptions were made. The dimensional changes of the rectangular scaffold sample were measured in only one direction, so the average force per cell was calculated using the assumptions that all cells were contracting in the direction that dimensional change was being measured and that all cells were contracting at the same time. The free-floating contraction assay removes the assumption that all cells had to be contracting in only one direction; using this technique, synovial cells and NR6 FBs were estimated to generate average contractile forces of

6.5 ± 0.1 nN and 8.9 ± 0.9 nN, respectively. This calculation still assumes that all cells are contracting at the same time and to the same extent in order to calculate an average force per cell; as expected due to the removal of a critical assumption, the average force per cell calculated using the free-floating assay was larger than that reported using the cell force monitor (1 nN) (Freyman, Yannas, et al., 2001; Freyman, Yannas, et al., 2001).

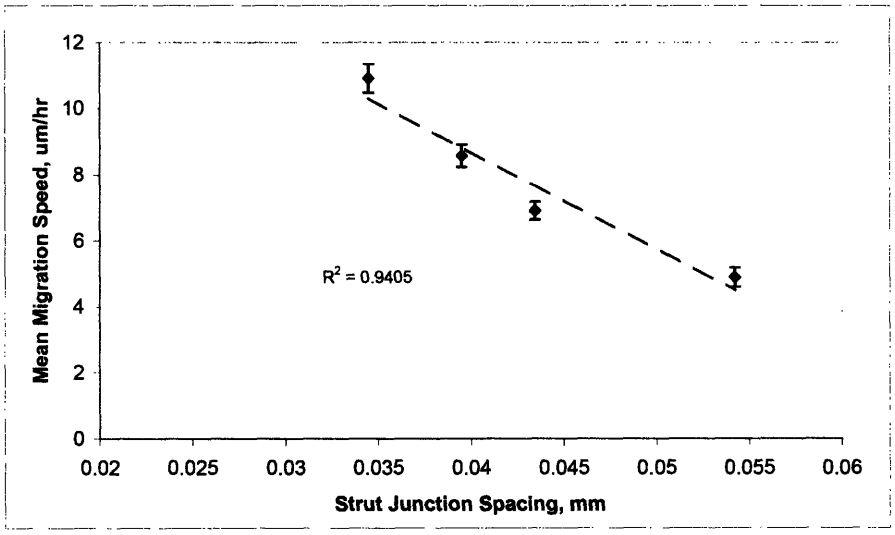

Fig. 6.28a

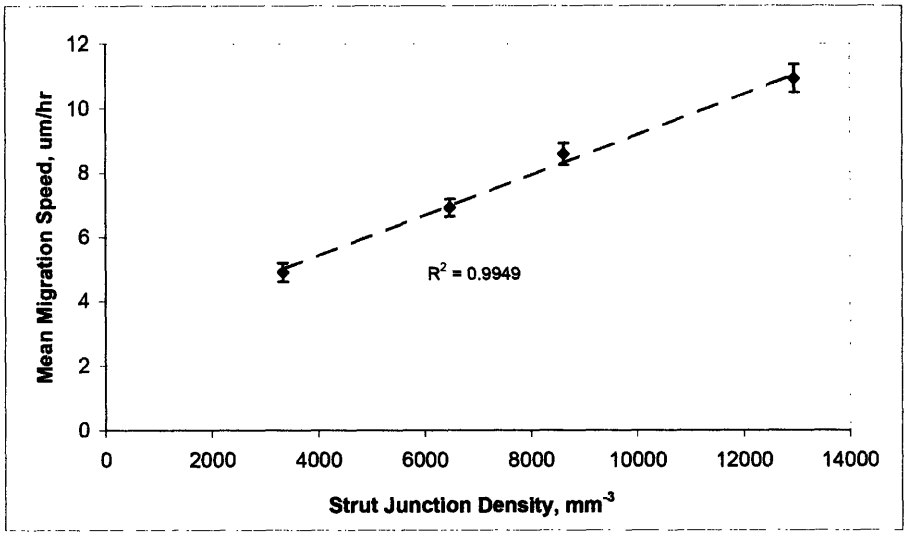

Fig. 6.28b

Figure 6.28. Correlation between observed NR6 FB migration speed with the spacing (Fig. 6.28a) and density of strut junctions (Fig. 6.28b).

The individual cell contraction assay removes both experimental assumptions of the cell force monitor by measuring the contractile force generated by a single cell within the mechanically characterized CG scaffold. Dermal FBs were observed to generate average contractile forces of 26 ± 13 nN (11 – 41 nN); as expected due to the removal of both experimental assumptions, the average force per cell calculated using the individual cell contraction assay was larger than that reported using the cell force monitor (1.4 ± 0.2 nN) (Freyman, Yannas, et al., 2001; Freyman, Yannas, et al., 2001) and the free-floating contraction assay.

Confocal microscopy provides appropriate imaging capabilities to observe cell-mediated scaffold contraction in three-dimensions. Dermal FBs were occasionally observed in an elongated (and assumed contractile) phenotype where the cell was unable to buckle the strut network it was attached to. In this case, the contact point between the cell and the strut (focal adhesion – ligand attachment) was observed to rupture. The internal tension field within the cell was therefore lost, resulting in rapid loss of the elongated phenotype (**Figure 6.29**). While this behavior has been previously noted as a result of light microscopy imaging of FBs within the CG scaffold, confocal microscopy allows improved resolution of this occurrence (**Figure 6.29**). Immediately following failure of the focal adhesion – ligand attachment, the end of the cell processes that just detached from the scaffold exhibits a characteristic focal adhesion pad that is visible under the light microscope and under the confocal microscope. Integration of confocal microscopy with the standardized, characterized CG scaffold variants therefore provide a new technique to not only track cell movement in three-dimensions and observe cell populational behavior, but also to probe individual cell contractile processes, morphological changes, and intercellular activity in three-dimensions in a well-defined extracellular environment.

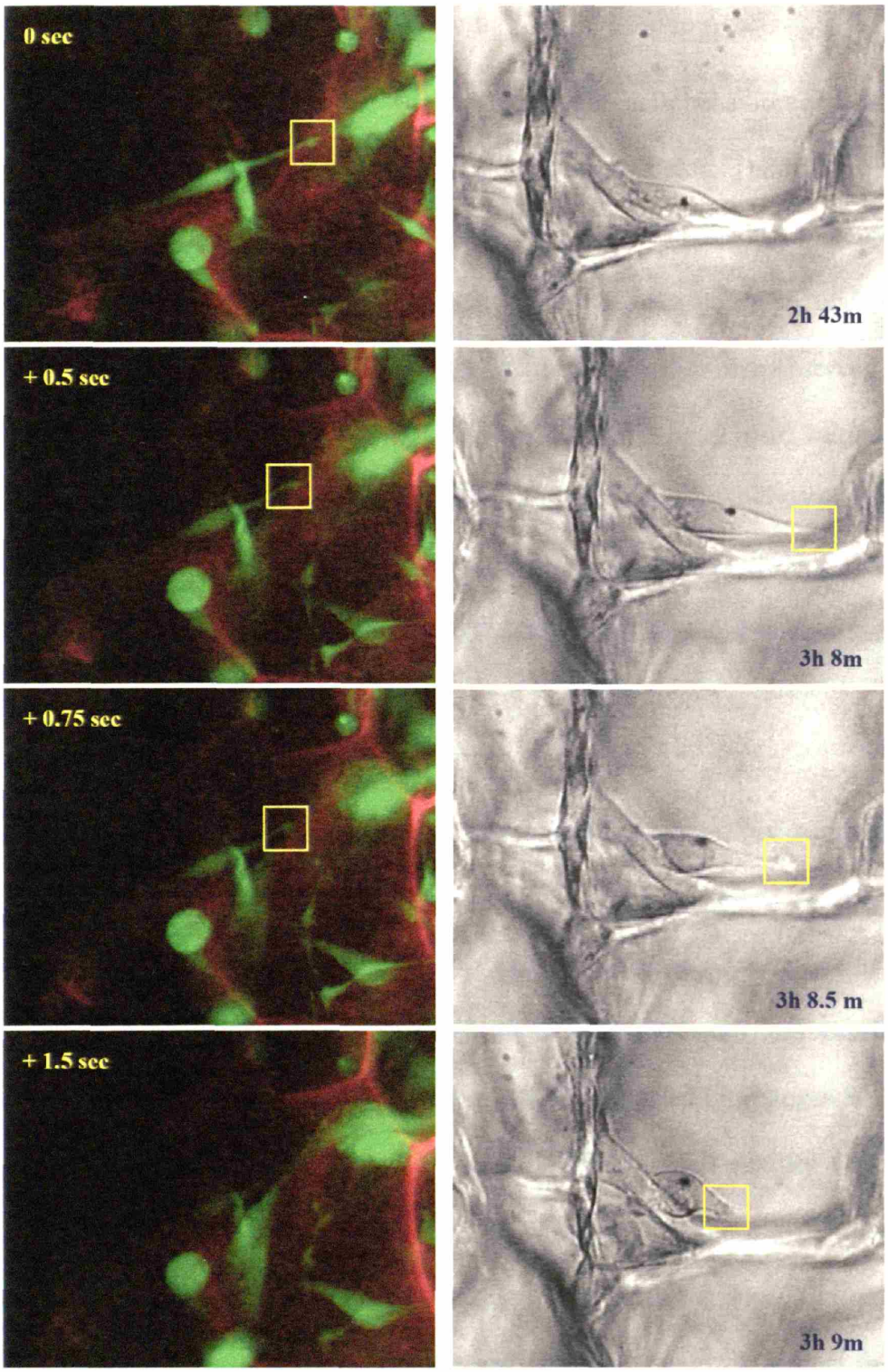

Figure 6.29. Comparison of cell-mediated contraction process resulting in rapid detachment from the scaffold strut due to focal adhesion – ligand rupture using confocal (left) and light (right) microscopy techniques. The associated focal adhesion "pad" is highlighted in both sets of images.

6.5. Conclusions

A robust system has been developed allowing analysis of cell behavior and cell scaffold interactions in a series of well-characterized collagen-GAG scaffolds. The microstructure and stiffness of these CG scaffolds can be independently modified by defined increments, allowing study of the independent effect of scaffold microstructure, stiffness, cell type, and cell seeding density on cell motility. NR6 FBs and DU-145 prostate cancer cells were observed to migrate through the CG scaffold with an average speed between 4 and 13 μm/hour. Migration speeds were of a similar magnitude as those reported for studies of cell motility on 2D membranes (Lo, Wang, et al., 2000) and within other 3D constructs (Zaman, Trapani, et al., In preparation, 2006). A significant effect of scaffold mean pore size, stiffness, cell seeding density, and cell type was observed on cell migration speed.

The significant effect of scaffold mean pore size on the motile fraction, directional persistence, and migration speed was further probed using open-cell foam models to describe the local microstructural features of individual cells. A preliminary explanation of the effect of mean pore size on cell motility was developed, identifying the distance between and density of strut junctions as prominent local microstructural features that are modified by changes in the scaffold mean pore size and which correlate well with the observed effect on cell motility. Strut junctions, as locations within the strut network where more than one strut come together, are a region where the cell can significantly change its morphology from the elongated phenotype typically observed for cells on individual struts to a more spread phenotype. This change in cell shape could have significant effect on overall cell motility. However, further investigation is warranted in order to confirm this conclusion.

The mean contractile force (F_c) generated by individual dermal FBs within the CG scaffold was calculated to range between 11 and 41 nN (F_c = 26 ± 13 nN). The individual cell contraction assay resulted in calculation of larger F_c than the values calculated via the free-floating contraction assay: F_c = 6.5 ± 0.1 nN and F_c = 8.9 ± 0.9 nN for synovial cells and NR6 FBs, respectively. The cell-mediated contractile forces determined using the individual cell contraction assay were also significantly larger than those previously reported in CG scaffolds (F_c = 1.4 ± 0.2 nN) (Freyman, Yannas, et al., 2001). This previous study reported average values calculated from cell populations using the assumption that all cells contracted at the same time and in a single direction. The increased value of the calculated F_c is likely due to the reduced experimental assumptions being made regarding the contractile behavior of a cell population within a three-dimensional substrate by using the free-floating and individual cell contraction assays.

CHAPTER 7. *Conclusions*

7.1. Thesis Conclusions

The key results of the experimental and theoretical methodologies described herein can be summarized as follows:

1. Uniform CG scaffolds with an equiaxed pore structure can be produced via lyophilization with the use of a constant cooling rate technique (Chapter 2). The constant cooling technique establishes a more uniform suspension temperature during solidification compared to the quenching technique due to the high degree of interface resistance developed between the suspension and the freeze dryer. This fabrication process produces a significantly more homogeneous scaffold microstructure. The most uniform scaffolds displayed approximately equiaxed pores. A standard series of CG scaffolds have been fabricated using the constant cooling technique; these scaffolds have a constant relative density and homogeneous pore microstructure with mean pore sizes ranging between 96 and 151 μm.

2. Thermal models have been developed to describe the solidification process related to the fabrication of CG scaffolds via lyophilization (Chapter 3). The first model, describing CG scaffold processing as a conduction-mediated process in a conductive mold with interface resistance and a ramped mold temperature, accurately predicts the local CG suspension solidification time based upon processing conditions. An isothermal coarsening model was then implemented that accurately predicts CG suspension ice crystal size (and hence scaffold mean pore size) based upon the local solidification time of the suspension (either experimentally measured or predicted using the first model). These models correctly describe lyophilization-based CG scaffold fabrication and have since been applied in the fabrication of a new series of collagen-based scaffolds for peripheral nerve (Appendix A) and bone tissue engineering (Appendix B). These models provide valuable insight for manufacture of future scaffolds through predictive modeling of the effects of changes in the fabrication process such as the thickness of the suspension in the mold, the solid content of the suspension, the freezing rate and final freezing temperature, the mold material properties, and the use of nucleation agents.

3. Open-cell foam models have been developed to accurately predict CG scaffold specific surface area and permeability in terms of scaffold mean pore size, relative density, and applied strain (Chapter 4). These results suggest that cellular solids techniques can be used as a predictive model of scaffold specific surface area and permeability for a variety of scaffold architectures under different physiologically-relevant loading conditions. These results also suggest the power of cellular solids modeling techniques utilizing a tetrakaidecahedral unit cell to describe many physical properties of the CG scaffold

cellular structure. Appropriate modeling tools that quantitatively describe scaffold characteristics (*i.e.*, permeability, specific surface area, mechanical properties) in terms of salient microstructural features are advantageous for further advancement in the field of tissue engineering. It appears that open-cell foam models utilizing the tetrakaidecahedral unit cell can accurately model CG scaffolds and have the potential to quantitatively describe many other tissue engineering constructs.

4. CG scaffolds exhibit stress-strain behavior characteristic of low-density, open-cell foams with distinct linear elastic, collapse plateau, and densification regimes (Chapter 5). The structurally isotropic scaffolds were also found to be mechanically isotropic. Further independent control over scaffold stiffness (via post-fabrication crosslinking independent of scaffold microstructure) and microstructure (scaffold pore size independent of stiffness) was observed. In addition to mechanically characterizing the macroscopic scaffold, the Young's modulus (E_s) of the individual struts that define the scaffold microstructure was measured. Good agreement was observed between open-cell foam model predictions of E^*/E_s vs. ρ^*/ρ_s for the lowest density scaffolds; discrepancies between the results and model predictions for higher density CG scaffold variants was suggested to be due to structural heterogeneities in the higher density CG scaffold variants. Besides further validating the use of cellular solids theory to describe the materials and mechanical properties of this CG scaffold system, the most significant aspect of this investigation is that an experimental substrate has been fabricated (Chapters 2 and 3), structurally characterized (Chapters 2 and 4), and mechanically characterized (Chapter 5). Based upon the results of this investigation, the initial local microstructural

and mechanical properties of the extracellular environment surrounding individual cells within the scaffold can be defined and controlled. These characterized scaffold variants provide a standardized framework for a series of *in vitro* and *in vivo* tissue engineering studies, notably a quantitative investigation of the effect of the extracellular environment (mechanics, microstructure) on cell migration and contraction.

5. A robust system has been developed allowing analysis of cell behavior and cell scaffold interactions in a series of well-characterized collagen-GAG scaffolds; the microstructure and stiffness of these CG scaffolds can be independently modified by defined increments, allowing study of the independent effect of scaffold microstructure, stiffness, cell type, and cell seeding density on cell motility (Chapter 5). NR6 FBs and DU-145 prostate cancer cells were observed to migrate through the CG scaffold with an average speed between 4 and 13 μm/hour. Migration speeds were of a similar magnitude as those reported for studies of cell motility on 2D membranes (Lo, Wang, et al., 2000) and within other 3D constructs (Zaman, Trapani, et al., In preparation, 2006). A significant effect of scaffold mean pore size, stiffness, cell seeding density, and cell type was observed on cell migration speed. The significant effect of scaffold mean pore size on the motile fraction, directional persistence, and migration speed was further probed using open-cell foam models to describe the local microstructural features of individual cells. A preliminary explanation of the effect of mean pore size on cell motility was developed, identifying the distance between and density of strut junctions as prominent local microstructural features that are modified by changes in the scaffold mean pore size and which correlate well with the observed effect on cell motility. Strut junctions, as locations within the strut

network where more than one strut come together, are a region where the cell can significantly change its morphology from the elongated phenotype typically observed for cells on individual struts to a more spread phenotype. This change in cell shape could have significant effect on overall cell motility. However, further investigation is warranted in order to confirm this conclusion.

6. The mean contractile force (F_c) generated by cells within the CG scaffold systems was calculated using either a free-floating contraction assay or an individual cell contraction assay (Chapter 6), with the results compared to that previously reported in the literature for dermal fibroblasts in a CG scaffold (F_c = 1.4 ± 0.2 nN) (Freyman, Yannas, et al., 2001). Populations of synovial cells and NR6 fibroblasts in free-floating, unrestrained scaffolds were calculated to generate average contractile forces of F_c = 6.5 ± 0.1 nN and F_c = 8.9 ± 0.9 nN, respectively. Individual dermal fibroblasts within the CG scaffold were calculated to generate individual contractile forces of F_c = 26 ± 13 nN (range: 11 – 41 nN). The individual cell contraction assay resulted in calculation of larger F_c than the F_c values calculated for the free-floating assay; additionally, the calculated cell-mediated contractile forces reported using the individual cell contraction assay were significantly larger than those previously reported in CG scaffolds using the Cell Force Monitor (F_c = 1.4 ± 0.2 nN), even though the same datasets were utilized for both assays. This result is likely due to the reduced experimental assumptions being made concerning the contractile behavior of a cell population within a scaffold by using the individual cell contraction assay because the previous Cell Force Monitor assay reported average values

calculated from cell populations using the assumption that all cells contracted at the same time and in the direction that scaffold deformation was measured.

The synergy of experiments and theoretical analysis provided in this thesis enable creation of new experimental tools for tissue engineering studies. Here, cellular solids theory was used to quantitatively describe the material and mechanical properties of CG scaffolds as well as to further elucidate the salient extracellular features that affect cell behavior. Most significantly, this thesis research has established and characterized a standardized series of collagen scaffolds applicable to a wide variety of tissue engineering applications and has developed techniques for fabricating and adequately characterizing new scaffold variants.

7.2. Future Work

The tools developed and results obtained during this thesis research have suggested a multitude of refinements, new experiments, and future directions for research.

§ At the forefront is expansion of the range of standardized and characterized CG scaffold variants available for use. In particular for future studies of cell behavior in three-dimensions, creating a new class of CG scaffolds with mean pore size on the order of 1 – 50 μm and with higher relative densities (0.005 – 0.05) will be critical. Such scaffolds would act as an ECM analog with a significantly more physiological basis (smaller mean pore sizes and higher densities). Creating such variants require developing new CG suspension mixing strategies and solidification profiles, as well as iterating the characterization protocols (mean pore size, specific surface area, permeability, mechanical properties) described within this thesis.

§ Development of a three-dimensional scaffold structural analysis protocol that will allow rapid interrogation of scaffold microstructural features. The current laboratory standard (Linear Intercept Method: Chapter 2) is experimentally tedious and does not provide much information. While microCT and mercury porosimetry technologies are ill-suited for characterizing non-mineralized – and therefore soft – collagen-based scaffolds, fluorescent labeling combined with 3D imaging technologies such as multi-photon and confocal microscopy as well as digital volumetric imaging provide significantly more analytical power and utility. The scaffold images developed via confocal microscopy in Chapter 6 demonstrate the ability to visualize the strut network at the level of individual struts using such imaging techniques. Such image volumes could then be analyzed to develop information describing scaffold mean pore size, individual strut diameter and length and spatial orientation, and scaffold relative density.

§ Improved imaging techniques will be a significant area for future research and development. In particular, new labeling techniques able to discern intracellular features and that provide for longer imaging times will be an important development. Currently, CMFDA labeled cells have shown a high-degree of phototoxicity (Timp, Hopp, et al., 2005), and traditional fluorophores photobleach rapidly. While the NR6 fibroblasts and DU-145 prostate cancer cells used in this research did not exhibit such phototoxicity, it will be important to develop new labeling techniques in order to perform more in-depth and longer-term studies of cell behavior across a wide-range of cell types. Possible

developments include utilizing a cell line transfected with fluorescent proteins and integration of quantum dot technologies to allow longer-term fluorescent imaging.

§ Increasing the resolution of three-dimensional imaging techniques will be an area of critical importance for future studies of cell behavior within CG scaffolds, particularly when imaging individual cell-scaffold interactions such as focal adhesion-ligand complexes and when imaging intracellular features and mechanisms. Such developments are currently technologically feasible, but were not utilized in this thesis. Use of a higher magnification objective (40x, 67x) and integration of a deconvolution algorithm in order to clean up the z-axis resolution of fluorescent imaging techniques would provide significant improvements in image resolution. Higher resolution images can also be generated by reducing the z-axis spacing between images in the 3D image stack (1 μm spacing was used for this research); such a modification would also improve resolution but would do so at the cost of significantly larger data-sets. For data-sets that already extended into the gigabyte range for 1 μm spacing, such an increase could be significant.

§ A larger field of view will allow study of cell behavior further into the scaffold construct; currently, the z-axis depth of view was limited by the piezo-stage controlling the objective (100 μm) of the confocal microscope. Higher travel piezo stages (500 μm) currently exist for confocal microscopes and could be integrated; multi-photon microscopy techniques could also be utilized, promising significantly deeper fields of view.

§ In order to improve the calculations of the individual cell contraction assay, appropriate protocols need to be developed to use the results of confocal microscopy imaging of cells within the scaffold to generate time-lapse images of strut buckling in three-dimensions. Such a development would require significant post-processing using a three-dimensional image analysis program. Such a development would facilitate improved measurement of the strut geometry (diameter, length, and compound moment of inertia for a non-uniform cylindrical body), the level of loading eccentricity, and would further allow calculation of a significantly improved measure of the individual cell-mediated contractile force.

APPENDIX A. *Fabrication of Novel Scaffolds for Diverse Tissue Engineering Applications I: Tubular Scaffolds with a Radial Pore Microstructure Gradient Fabricated via Spinning*

A.1. Introduction

Scaffolds have been used extensively in a variety of tissue engineering applications to provide a three-dimensional extracellular matrix analog for *in vivo* and *in vitro* studies. Increasingly complex fabrication techniques have been developed to produce scaffolds from biodegradable synthetic polymers or related copolymers (Hubbell, 2000; Freed and Vunjak-Novakovic, 2002; Rutkowski, Miller, et al., 2002; Zhang and Ma, 2002) as well as natural polymers such as several graft copolymers of type I collagen and glycosaminoglycans (GAGs) (Yannas, Lee, et al., 1989; Chamberlain, Yannas, et al., 1998; Butler, Yannas, et al., 1999; Hsu, Spilker, et al., 2000; Freyman, Yannas, et al., 2001). Collagen is a significant constituent of the natural extracellular matrix (ECM) and scaffolds made from collagen have been used very successfully in a wide variety of applications due to a number of useful properties: requisite hemostatic properties, low antigenicity, appropriate mechanical stiffness characteristics, express suitable ligands for cell

attachment, and promotion of cell and tissue attachment and growth (Yannas, 2001; O'Brien, Harley, et al., 2005). The rapidly increasing use of scaffolds has led to the need to better understand the significant role scaffolds play in complex biological processes such as regeneration following severe injury; however, increasingly complex studies of cell behavior within a scaffold and the relative effect of this behavior on clinically significant processes such as regeneration require the fabrication of scaffolds with specific geometries and pore structures. Recently, improved methods for fabrication of collagen-GAG (CG) scaffolds have been detailed where the pore structure homogeneity, mean pore size, and degradation characteristics have been altered and controlled (Chamberlain and Yannas, 1998; Harley, Spilker, et al., 2004; O'Brien, Harley, et al., 2004; Pek, Spector, et al., 2004; O'Brien, Harley, et al., 2005), allowing for the design of specific scaffold architectures at the level of individual pores.

Material, microstructural, and mechanical properties have all been shown to significantly affect scaffold bioactivity – the ability of a scaffold to actively induce or influence specific cell behaviors. Additionally, different three-dimensional environments have been observed to maximize scaffold bioactivity for different cell types and applications (Yannas, 2001; O'Brien, Harley, et al., 2004; O'Brien, Harley, et al., 2005). The diversity of hypothetical functional attributes of a desirable scaffold may in part account for the large variety of scaffold chemical composition and pore structure currently in the literature. However, there is persistent evidence from a wide variety of sources that scaffold permeability and the ability of cells to migrate through a scaffold plays an important role in defining bioactivity (Li, Archibald, et al., 1992; Yannas, 2001).

Following severe injury, peripheral nerves can be induced to regenerate if the transected ends of the nerve are inserted into either end of a bioactive, tubular implant (Chamberlain, Yannas, et al., 1998; Yannas, 2001; Harley, Spilker, et al., 2004). While the use of specific scaffold materials within the tube lumen significantly increases the quality of regeneration, the tube itself is all that is required to induce regeneration and the physical properties of the tube (*i.e.*, porosity, material composition, pore structure, permeability) can significantly affect the quality of regeneration (Li, Archibald, et al., 1992; Chamberlain, Yannas, et al., 1998; Yannas, 2001; Harley, Spilker, et al., 2004). In particular, the protein and cell permeability characteristics of the scaffold significantly affect the quality of regeneration: protein-permeable tubular implants show significantly improved peripheral nerve regeneration compared to protein-impermeable tubular scaffolds (Chamberlain, Yannas, et al., 1998), and cell-permeable tubular implants show significantly improved regeneration compared to impermeable and protein-permeable tubular scaffolds (Jenq and Coggeshall, 1987; Jenq, Jenq, et al., 1987; Aebischer, Guenard, et al., 1988; Aebischer, Salessiotis, et al., 1989; Li, Archibald, et al., 1992; Kim, Connolly, et al., 1993; Rodriguez, Gomez, et al., 1999).

Direct evidence of cell migration through implanted scaffolds and its presumptive effect on peripheral nerve regeneration processes has been observed. Contractile myofibroblasts have been observed in the tube wall of cell-permeable, collagen tubes that induced a superior quality of regeneration (Chamberlain, Yannas, et al., 2000). Although the data did not allow identification of the direction of migration, the presence of myofibroblasts inside the scaffold and their observed absence outside the cell-permeable tube suggest that the cells were migrating outward from the tube lumen (wound site). Myofibroblast migration into and through collagen scaffolds

has also been observed in the study of skin regeneration, where myofibroblast migration into a collagen-GAG scaffold was required for prevention of the coordinated contraction of the wound and for successful induction of skin regeneration after severe injury (Yannas, Lee, et al., 1989). In the absence of an appropriate scaffold structure or when the myofibroblasts were unable to migrate into the scaffold, the myofibroblasts vigorously contracted the wound site with no evidence of regeneration (Troxel, 1994; Yannas, 2001). The known importance of myofibroblast migration through collagen scaffolds for maximal induction of skin regeneration and the observation of myofibroblasts in the tube wall of collagen scaffolds during successful regeneration of peripheral nerves suggest that further study of this phenomenon is required to better understand the process of regeneration.

The objective of this study was to fabricate porous, tubular collagen-based scaffolds that display a gradient in porosity and pore size along the tube radius, a radially-oriented pore distribution, as well as a protein permeable and cell impermeable outer surface to facilitate study of the migration characteristics of myofibroblasts during peripheral nerve regeneration. Creating a tubular scaffold with a gradient in porosity and mean pore size along the tube radius will enable the modulation of cell migration through the scaffold; regions of increased scaffold density and decreased mean pore size will prevent cell migration. A tubular scaffold with a radially aligned pore structure leading from the inner tube surface and a region of high relative density and decreased mean pore size along the outer surface will make the tube cell-permeable from the inner lumen, but cell-impermeable from the outer surface. Such a scaffold structure will facilitate the study of the direction of cell migration during peripheral nerve regeneration. The aim of such a study is development of a scaffold that increases the quality of peripheral nerve regeneration by

modulating myofibroblast migration. The sedimentation fabrication technique detailed here allows production of a wide variety of tubular scaffolds that meet the requirements of a quantitative study of myofibroblast migration during peripheral nerve regeneration.

A.2. Materials and Methods

A.2.1. Fabrication of collagen-glycosaminoglycan (CG) scaffolds via lyophilization

CG scaffolds are fabricated using a freeze-drying (lyophilization) process (Yannas, 2001) where a suspension of collagen and glycosaminoglycans co-precipitated in acetic acid is solidified (frozen), resulting in a continuous, interpenetrating network of ice crystals surrounded by the co-precipitate. Sublimation of the ice crystals produces the highly porous scaffold structure.

The CG suspension was produced by combining microfibrillar, type I collagen (0.5 wt%) isolated from bovine tendon (Integra LifeSciences, Plainsboro, NJ) and chondroitin-6-sulfate (0.05 wt%) isolated from shark cartilage (Sigma-Aldrich Chemical Co., St. Louis, MO) in a solution of 0.05M acetic acid (pH 3.2). The collagen, chondroitin-6-sulfate, and acetic acid were mixed in an overhead blender (IKA Works, Inc., Wilmington, NC); the temperature of the suspension was maintained at 4°C throughout mixing by a cooling system (Brinkman, Westbury, CT) to prevent denaturation of the collagen fibers as a result of the heat generated by mixing. The CG suspension was degassed under vacuum (50 mTorr) to remove air bubbles introduced by mixing and then stored at 4°C until use (O'Brien, Harley, et al., 2004).

A.2.2. Experimental Spinning Procedure

The CG suspension was spun in a cylindrical mold to establish relative component separation (liquid and solid phases); the spinning suspension was then rapidly frozen to lock in place the component separation achieved via spinning, and the frozen solvent phase was removed via sublimation. This technique allows for simple production of a variety of porous tubular structures without the need for complex molds or mandrels to define the tubular structure.

A copper mold used for this experiment (**Figure A.1**) was fabricated using oxygen free copper. Oxygen free copper was used due to its high thermal conductivity, allowing more rapid freezing of the CG suspension and thereby minimizing any remixing of the sedimented CG suspension. The mold was fabricated from a cylindrical bar of copper (Length: 76.2 mm, Diameter: 12.7 mm); an 8.73 mm diameter hole was drilled down the center axis of the cylinder to a depth of 63.5 mm to produce an internal hollow. The opening of the hollow was threaded to allow a threaded copper plug (end cap) to seal the mold hollow. A hardened steel rod was inserted into the opposite end of the cylinder to provide a linkage between the mold and a high-speed rotary tool used to spin the mold about its longitudinal axis. The degassed CG suspension was injected into a PVC tube (O.D.: 7.94 mm, I.D.: 4.76 mm, VWR Scientific, Inc., West Chester, PA) that was sealed on one end by the copper end cap. The opposite end of the PVC tube was sealed with an ultrahigh molecular weight polyethylene (UHMWPE) cap to prevent the CG suspension from spilling during spinning; the capped PVC tube was inserted into the copper mold and screwed in place.

The cylindrical mold was held vertically as it was spun at room temperature using a high-speed rotary tool (Dremel, Robert Bosch Tool Corp, Mt. Prospect, IL) for a specified spinning time (T_s, min.) at a specified angular velocity (R, rpm). After the specified spinning time, the spinning mold was then inserted directly into a bath of liquid nitrogen. The mold continued to spin at the same rate (R) for a specified freezing time (T_f) in the liquid nitrogen bath. The copper mold was then removed from the liquid nitrogen and rotary tool was turned off; the PVC tube with the frozen CG suspension was rapidly removed from the copper mold and placed into a freeze-drier (Genesis, VirTis, Co., Gardiner, NY) with a shelf temperature maintained at –40°C to prevent melting of the sedimented, frozen CG suspension. The end caps were removed and the frozen CG suspension was sublimated in a process that has been previously described to produce a porous CG structure (Yannas, Lee, et al., 1989). Briefly, the frozen CG suspension was sublimated under a vacuum (<100mTorr) at 0°C for 17 hours. Freeze-drying is a well-established process for the fabrication of collagen scaffolds (Loree, Yannas, et al., 1989; Chamberlain and Yannas, 1998; Yannas, 2001; Harley, Spilker, et al., 2004; O'Brien, Harley, et al., 2004; O'Brien, Harley, et al., 2005) where the sublimation step results in the complete removal of the frozen solvent (acetic acid) from the final scaffold structure.

A homologous series of tubular scaffolds was fabricated by producing scaffolds at a constant spinning rate (R = 5000 rpm) and a constant freezing time (T_f = 1 min.), but with variable spinning times (T_s = 0, 1, 3, 5 min) in order to study the effect of the spinning (sedimentation) time on the final structure of the CG scaffold (solid cylindrical vs. tubular). In addition, a separate tubular structure was obtained via a more extreme spinning protocol designed to

produce a large amount of sedimentation (R = 30,000 rpm, T_s = 15 min, T_f = 2 min.). Additional details of the scaffolds fabricated during this experiment are described in **Table A.1**.

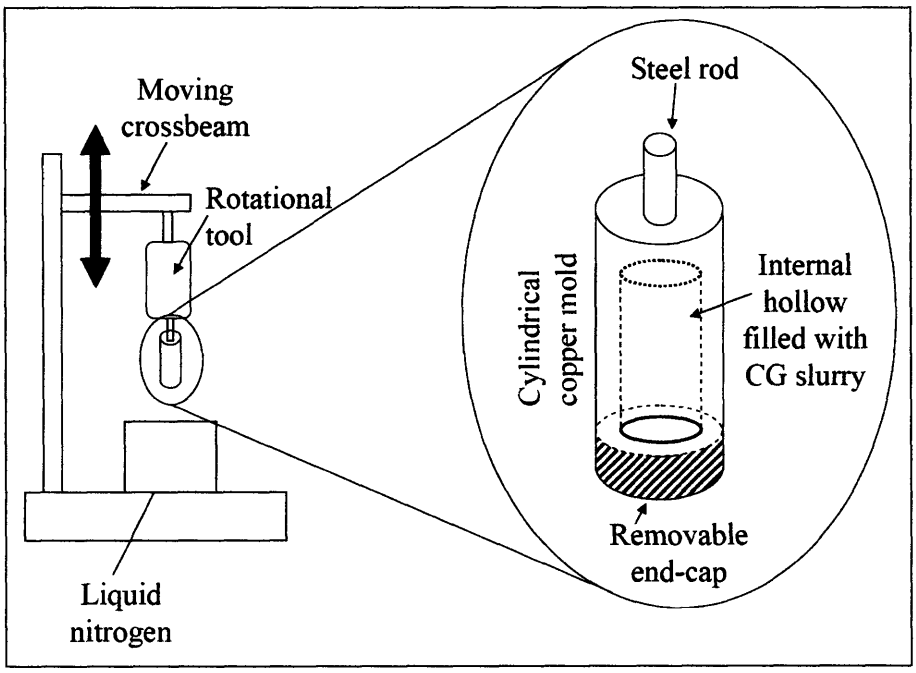

Figure A.1. Schematic of the spinning apparatus.

A.2.3. CG scaffold relative density and specific surface area

The relative density of the tubular scaffolds was calculated from the measured relative density of non-sedimented CG scaffolds (0.006) (O'Brien, Harley, et al., 2005) and the geometry of the resulting sedimented tubular scaffolds. The specific surface area (surface area per unit volume) of the sedimented CG scaffolds was then calculated from the scaffold relative density an. the measured mean pore size. The specific surface area (SA/V) of CG scaffolds can be accurately calculated using an open-cell foam, cellular solids model utilizing a tetrakaidecahedral unit cell (Gibson and Ashby, 1997; O'Brien, Harley, et al., 2005):

Equation A.1. $$\frac{SA}{V} = \frac{10.15}{d}\left(\frac{\rho^*}{\rho_s}\right)^{1/2}$$

A.2.4. CG scaffold crosslinking

It is important to consider the *in vivo* degradation rate (Harley, Spilker, et al., 2004) and stiffness of any scaffold used for tissue engineering applications. In the development of these tubular scaffolds, the structural features of the tube are critical in defining its cell permeable or impermeable nature. Scaffold degradation rate must also be considered because rapid degradation will render a cell impermeable scaffold permeable. However, degradation rate and stiffness can be modified independent of scaffold pore structure via post-fabrication crosslinking intensity: scaffold stiffness increases and degradation rate decreases with increasing crosslink density.

This research has focused on the development of a tubular scaffold with the appropriate structural parameters. Therefore, all CG scaffolds manufactured in this study were crosslinked via a standard dehydrothermal (DHT) process after freeze-drying to strengthen the collagen network by introducing covalent crosslinks between the polypeptide chains of the collagen fibers. Crosslinking was carried out in a vacuum oven (Fisher IsoTemp 201, Fisher Scientific, Boston, MA) at a temperature of 105°C under a vacuum of 50 mTorr for 24 hours (Yannas, Lee, et al., 1989). The degree of crosslinking can be modulated by the length and intensity of the thermal treatment, allowing for fine control over the biodegradation rate of the tube (Yannas, Lee, et al., 1989; Harley, Spilker, et al., 2004). However, collagen tubes treated with the standard DHT process (105°C, 24 hours) have been successfully utilized as peripheral nerve guides. These

scaffolds possessed the required mechanical stiffness and stability for successful surgical implantation and regeneration (Harley, Spilker, et al., 2004). As such, the DHT treatment utilized with this new class of collagen tubes was deemed appropriate for tubular scaffolds to be used to treat peripheral nerve injuries. The high heat and vacuum used during the DHT crosslinking process also serves to sterilize the tubes.

A.2.5. Morphological Analysis

The pore structure of the samples obtained using the spinning technique was analyzed via SEM. Several cross-sections of each tube were visualized using the VP438 Scanning Electron Microscope (Leo, Inc., U.K.) in variable pressure mode (P = 10 Pa) using the backscatter detector; images were acquired at magnifications between 20 and 750x in order to visualize both the gross structure of each tube and the fine pore structure of specific regions of the tube wall. Both the individual pore structure of the scaffold and the gross geometry of the resulting tubular scaffolds are reported.

A.3. Results

Both filled tubes (cylinders) and hollow tubular scaffold structure were obtained by means of the spinning technique; the gross geometrical structures of the scaffolds are reported in **Table A.1** and can be seen in **Figure A.2**. SEM analysis was used to assess the pore structure and gross geometry of the tubular CG scaffolds in this study. Five distinct types scaffold structures have been fabricated and analyzed: R = 5000 rpm; T_s = 0, 1, 3, or 5 min; T_f = 1 min, and R = 30,000

rpm; T_s = 15 min; T_f = 2 min. Two samples from distinct regions of each tube of each device class were analyzed and good experimental reproducibility was observed.

R, rpm	T_s, min	T_f, min	Tube or Cylinder	Tube I.D. ± StDev, mm	Comments
5000	0	1	Cylinder	N/A	Uniform scaffold structure
5000	1	1	Cylinder	N/A	Radially aligned scaffold structure
5000	3	1	Cylinder	N/A	Radially aligned scaffold structure; solid volume fraction of central region lower than scaffold edges
5000	5	1	Tube	2.36 ± 0.01	Tube with radially aligned pores
30,000	15	2	Tube	3.14 ± 0.06	Tube with radially aligned pores

Table A.1. Fabrication conditions and gross morphological structure of the five different types of scaffolds fabricated using the spinning technique. The top four devices are part of a homologous series while the fifth device represents a more severe spinning protocol.

Figure A.2 (a-e) shows cross-sectional SEM images of the five distinct classes of tubular scaffolds (filled or hollow, **Table A.1**) fabricated using the distinct spinning protocols. **Figure A.2a** shows the cross section of a scaffold fabricated by placing the mold directly in liquid nitrogen (T_s = 0 min): a cylindrical (filled) scaffold was produced. **Figure A.2b** (R = 5000 rpm, T_s = 1 min, T_f = 1 min.) shows a cylindrical (filled) scaffold structure without any apparent hollow region in the center; however, a radially aligned pore structure is clearly evident throughout the entire cross-section. **Figure A.2c** (R = 5000 rpm, T_s = 3 min, T_f = 1 min.) again shows a cylindrical (filled) scaffold structure with a radially aligned pore structure but with less structural organization in the central region of the scaffold (lower relative density represented by darker regions under SEM backscatter detectors). **Figure A.2d** (R = 5000 rpm, T_s = 5 min, T_f = 1

min.) shows a tubular scaffold with a well-defined central region (lumen) that is completely devoid of any solid material. The well-defined hollow in the center of the scaffold defines a tubular structure with a uniform inner diameter fabricated without the use of a central mandrel. The radially aligned pore structure observed in scaffolds fabricated with a shorter spinning time is now present through the thickness of the tube wall of this porous tube.

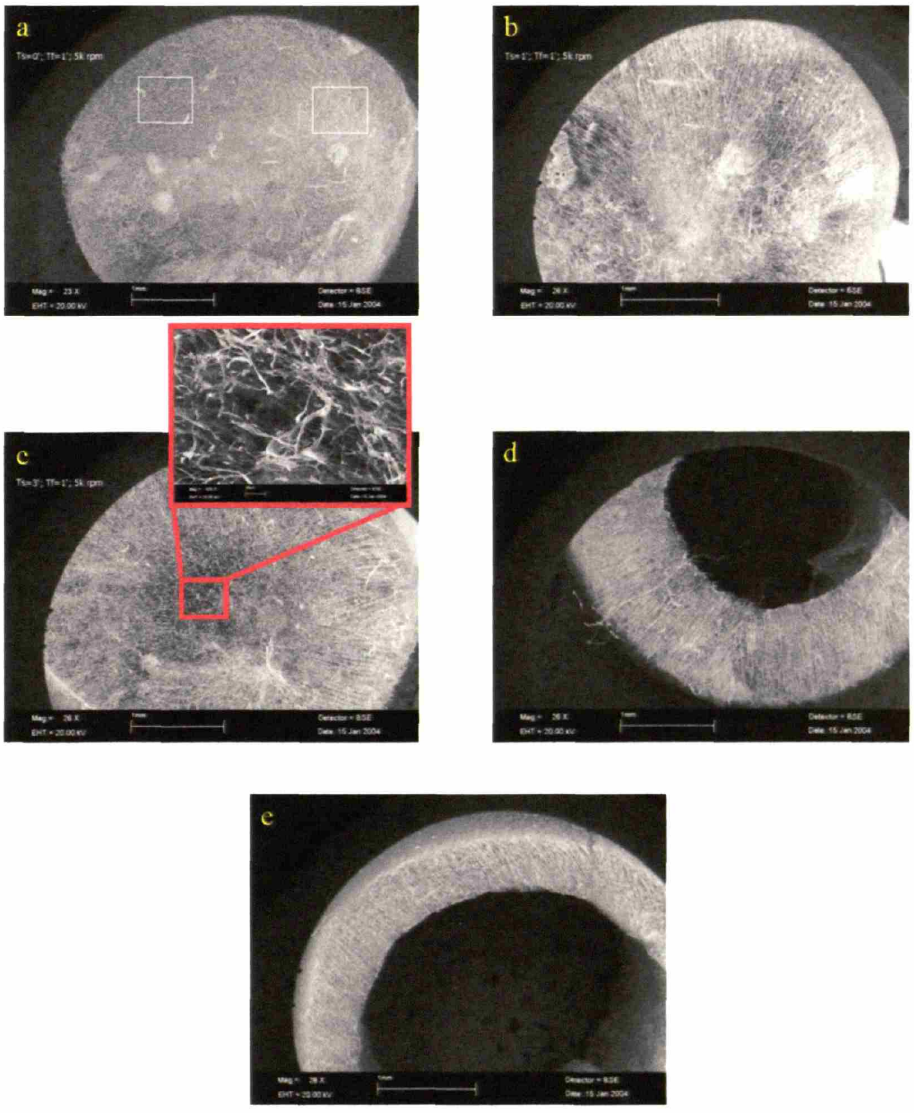

Figure A.2. SEM images of the tube cross section. *a)* Full cross section: R = 0 rpm, T_s = 0 min., T_f = 1 min., *b)* full cross section: R = 5000 rpm, T_s = 1 min., T_f = 1 min., *c)* full cross section and higher magnitude image of the cross section central area: R = 5000 rpm, T_s = 3 min., T_f = 1 min.,

d) bottom half of the cross section: R = 5000 rpm, T_s = 5 min., T_f = 1 min., *e)* upper half of the cross section: R = 30000 rpm, T_s = 15 min., T_f = 2 min.

To increase the sedimentation effect and produce a tubular scaffold with a considerably thinner wall, both the spinning time and velocity were increased (R = 30,000 rpm, T_s = 15 minutes, T_f = 2 minutes). The cross-sectional image of a device fabricated using this technique is shown in **Figure A.2e**. These porous tubes display the well-defined tube lumen and the radially aligned pore structure in the tube walls previously observed with tubes fabricated with lower levels of sedimentation (R = 5000 rpm, T_s = 5 min., T_f = 1 min.); however, the extreme sedimentation that occurred during fabrication has produced a scaffold with radial pore alignment and a radial gradient in pore size and structure.

Figure A.3a shows an SEM image of the entire tube wall of a single scaffold fabricated using the extreme sedimentation process. Additionally, **Figure A.3a**, **A.3b**, A.3c, and **A.3d** show additional SEM images of the inner-most (**Fig. A.3a, A.3b**), middle (**Fig. A.3b, A.3c**), and outer-most (**Fig. A.3d**) regions of the tube walls taken along a constant radial line from a single sample tube to display the distinct regions of pore structure in greater detail. While radially aligned pore channels are evident through the thickness of the tube wall with the bulk of the scaffold displaying a mean pore size of approximately 20 μm (**Fig. A.3b, A.3c**), the pore structure near the outer edge of the tube displays a considerably higher solid volume fraction (brighter regions under backscatter detectors) with a considerably smaller mean pore size (< 5 μm) (**Fig. A.3d**). Additionally, while the majority of the tube wall displays a radially aligned pore structure (**Fig. A.3b, A.3c**), the outer edge of the scaffold displays a non-oriented, amorphous pore structure due to the extreme nature of the sedimentation effect (**Fig. A.3d**).

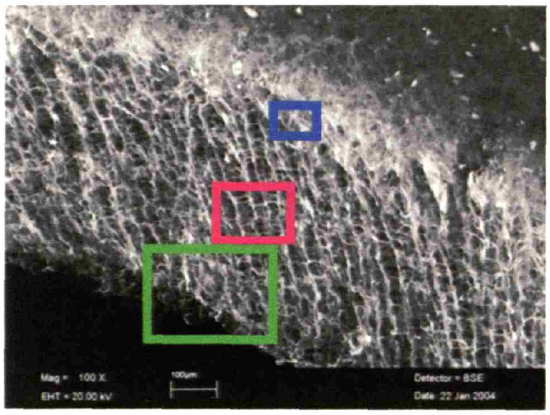

Fig. A.3a

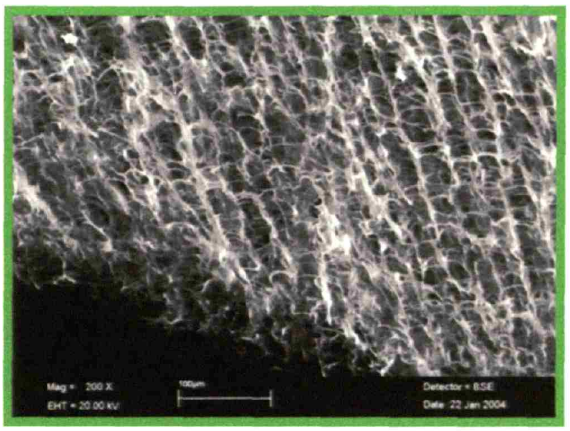

Fig. A.3b

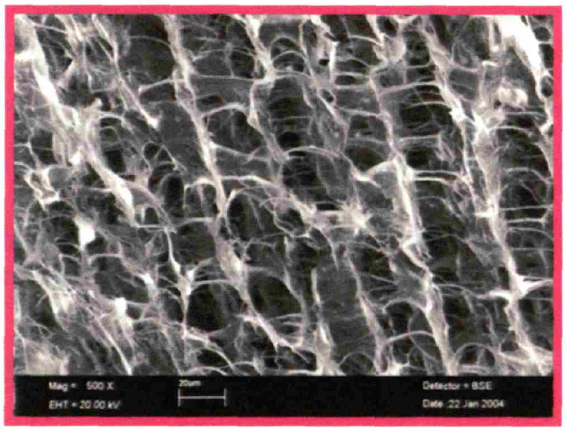

Fig. A.3c

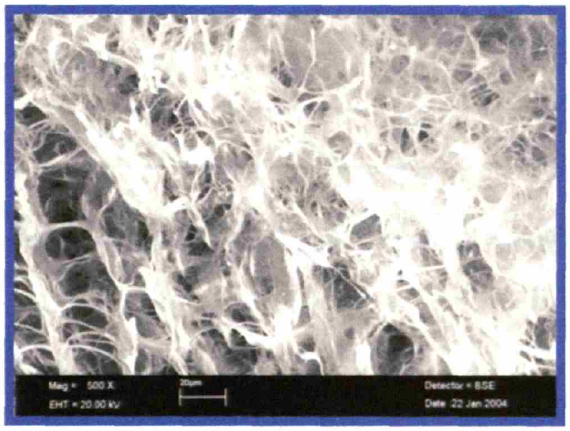

Fig. A.3d

Figure A.3. Cross-sectional SEM images of the tube wall: R = 30000 rpm, T_s = 15 min., T_f = 2 min. (100x) *b)* Higher magnification (200x) image of the internal and central portion of the tube wall, showing the highly aligned pore structure, *c)* Increased magnification (500x) image of the internal portion of the tube wall, *d)* Higher magnification (500x) image of the external portion of the tube wall, showing significantly smaller pores with a greater solid volume fraction.

The relative density and specific surface area of all classes of the sedimented and non-sedimented CG scaffolds is reported in **Table A.2**. While the mean relative density of the cylindrical scaffolds without a central lumen (R = 5000 rpm, T_s = 0, 1, 3 min., T_f = 1 min.) was found to be 0.006, that of the tubular scaffolds was calculated to increase by 30 (R = 5000 rpm, T_s = 5 min., T_f = 1 min.) and 113 (R = 30,000 rpm, T_s = 15 min., T_f = 2 min.) percent. These

calculations represent an average relative density of the entire tube wall. In the case of extreme sedimentation, significantly higher relative densities are expected at the outer tube surface. A similar increase in specific surface area was observed for the two tubular scaffolds compared to the cylindrical scaffolds (**Table A.2**).

R, rpm	T_s, min	T_f, min	Tube I.D. ± StDev, mm	Relative Density	Specific Surface Area, μm^{-1}
5000	0	1	0	0.006	0.039
5000	1	1	0	0.006	0.039
5000	3	1	0	0.006	0.039
5000	5	1	2.36 ± 0.01	0.008	0.045
30,000	15	2	3.14 ± 0.06	0.013	0.057

Table A.2. Relative density and specific surface area of the five different types of scaffolds fabricated using the spinning technique.

A.4. Discussion

For scaffolds produced by submerging the mold into liquid nitrogen and then spinning the mold (R = 5000 rpm, T_s = 0 min, T_f = 1 min.; **Fig. A.2a**), a homogeneous pore structure was observed with no areas of obvious pore alignment, indicating rapid solidification is taking place once the mold is placed in the liquid nitrogen bath. By introducing spinning prior to submersion of the mold into liquid nitrogen, (R = 5000 rpm, T_s = 1 min, T_f = 1 min.; **Fig. A.2b**), a class of scaffolds with a clearly evident radially aligned pore structure throughout the entire cross-section is produced, indicating that spinning is imparting a centrifugal force on the CG suspension. By increasing the spinning time prior to solidification (R = 5000 rpm, T_s = 3 min, T_f = 1 min.; **Fig. A.2c**), the radially aligned pore structure remains evident around the scaffold edges. However,

the central region of the scaffold appears noticeably darker than the outer regions of the scaffold when using the backscatter detectors of the SEM, indicating that there is a decrease in the relative density of the scaffold in the central region and that sedimentation is occurring. Additionally, the pore structure of the central region of the scaffold is not as highly organized and does not present the radially aligned pores seen in the external region of this scaffold or in the internal region of the scaffolds produced with less sedimentation (R = 5000 rpm, T_s = 1 min, T_f = 1 min.). This lack of structural organization in the central region of the scaffold is most likely due to the decrease in the solid density in this region due to sedimentation.

Further increasing the spinning time (R = 5000 rpm, T_s = 5 min, T_f = 1 min.; **Fig. A.2d**) results in sufficient sedimentation to create a tubular scaffold with a well-defined, hollow tube lumen. A radially aligned pore structure remains evident throughout the tube walls of this class of scaffolds, defining radially tracks that could be used as directional guidance cues for cells. However, no radial gradient in pore size or relative density is observed in this class of tubular scaffolds.

Increasing the sedimentation effect (R = 5000 rpm, T_s = 5 min, T_f = 1 min.; **Fig. A.2e, A.3a-d**) results in a tubular scaffold with a larger inner diameter (**Table A.1**) and a radial gradient in mean pore size and relative density through the tube wall. The mean pore size of the scaffold near the inner tube wall (approx. 20 μm: **Fig. A.3b, A.3c**) is considerably larger than the mean pore size observed at the outer tube wall (< 5 μm: **Fig. A.3d**). Additionally, the outer region of the tube wall appears significantly brighter than the inner and central regions of the tube wall when using the backscatter detectors of the SEM (**Fig. A.3a, Fig. A.3c** vs. **Fig. A.3d**, all images taken of the same scaffold with identical settings), indicating that there is a significant increase in

the relative density of the scaffold in the outer region of the tube. This significant difference in pore morphology is attributed to the effect of sedimentation due to spinning. The internal region of the tube wall, with an increased mean pore size (20 μm), an open-cell foam morphology, and radially aligned pore tracks, forms a cell permeable region that may allow cells to migrate into the scaffold from the internal tube lumen. The external region of the tube wall, with a significantly decreased mean pore size (< 5 μm), a predominantly closed-cell foam morphology, and a significantly increased relative density, forms a cell impermeable barrier "membrane." With increased relative density and decreased mean pore size at the outer edge, the tube is cell-impermeable from the outside; however since the outer region is not entirely impermeable (*i.e.*, silicone membrane), it will maintain its protein permeability.

The calculation of relative density and specific surface area for the tubular scaffold showing maximal sedimentation (R = 30,000 rpm, T_s = 15 min., T_f = 2 min.) is not completely valid, however, due to the heterogeneity of the pore structure within the tube wall. Due to the extreme sedimentation observed at the outer edge of the tube, the specific surface area and relative density calculations slightly overestimate the characteristics (specific surface area and relative density) of the majority (inner and central regions) of the tube wall while significantly underestimating the characteristics of the extreme outermost region of the tube wall. As the volume of the highly sedimented region of the scaffold is relatively small compared to that of the entire tube cross-sectional area, the overestimation of the relative density and specific surface area for the vast majority of the tubular scaffold is small. The calculated relative densities and mean pore sizes of the main body (inner and middle region of the tube wall) of the two tubular scaffolds of 0.008 and 0.013 are not large enough to prevent cell migration (O'Brien, Harley, et

al., 2005). Previous research has shown that cell viability increases proportionally with scaffold specific surface area (O'Brien, Harley, et al., 2005); the increased specific surface area of the tubular scaffolds should similarly increase the density of viable cells that can migrate into the tube walls from the central lumen.

A.5. Conclusions

A new fabrication technique for producing cylindrical, porous scaffolds with either a filled or hollow tubular morphology has been developed. This spinning technique allows for a range of scaffold geometries to be fabricated in a reproducible manner from a single mold. During spinning, the solid and liquid phase of the CG suspension underwent differential sedimentation along the cylinder radius due to centrifugal force. Increased sedimentation is observed to occur with increasing velocity (R) and spinning time (T_s), resulting in a scaffold structure with an increasing amount of solid in the external region and ultimately resulting in a hollow tube with a uniform inner diameter of increasing size. A radially-oriented pore distribution is clearly observed in all scaffolds produced via spinning regardless of whether the sedimentation effect is great enough to produce a tube lumen. The radial pore structure is a result of the combined effects of the sedimentation and the heat transfer gradient during freezing that develops in the radial direction due to the rapid immersion of the mold into the liquid nitrogen bath (Loree, Yannas, et al., 1989). By varying the time of spinning and angular velocity, a series of porous scaffolds ranging from a filled, porous cylinder to a highly orientated, porous tube with radially dependent pore structure can be readily manufactured.

For the scaffold produced with the highest degree of sedimentation (R = 30,000 rpm, T_s = 15 minutes, T_f = 2 minutes), a specialized porous tube has been fabricated. With a mean pore size of approximately 20 μm and a relatively high pore volume fraction, the tube walls are cell-permeable from the inner tube lumen into the tube wall. However, with a mean pore size of considerably less than 5 μm and a significantly lower pore volume fraction (higher solid volume fraction), the tube is not cell-permeable from the exterior of the tube into the tube. This structure will be extremely valuable in studying path-dependent cell migration processes such as those seen during peripheral nerve regeneration (**Figure A.4**).

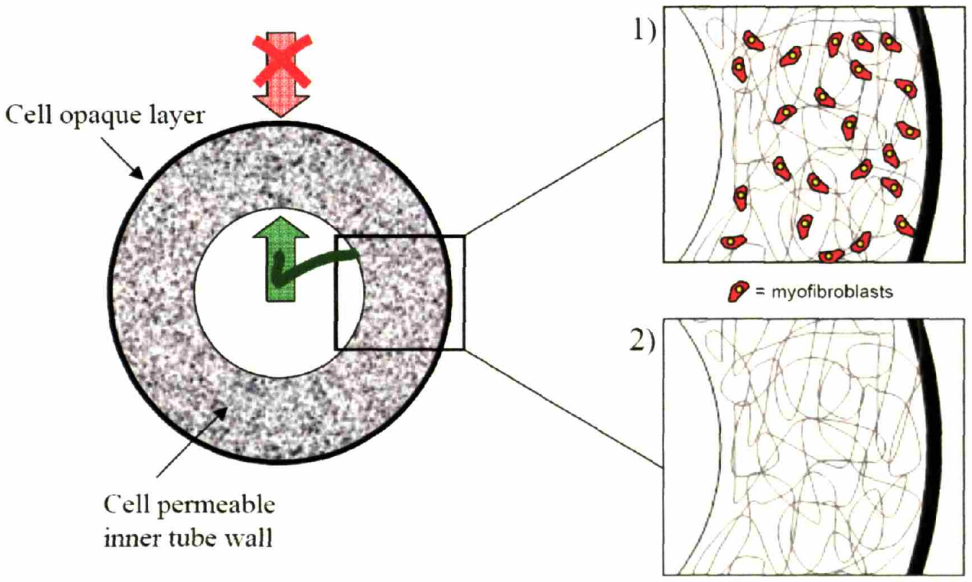

Case 1: MyoFB migration from the tube lumen towards the external edge during peripheral nerve regeneration

Case 2: MyoFB migration from the external region of the tube towards the tube lumen during peripheral nerve regeneration

Figure A.4. Potential outcomes of in vivo study of cell migration during peripheral nerve regeneration.

While currently demonstrated using a two-component CG suspension, this sedimentation technique was designed to work with any multi-component systems where the components display different densities. Under centrifugation, sedimentation of the components will take place and a non-homogeneous distribution of the two (or more) components will be produced. Depending on the relative densities and rheological properties of the system, it is possible to define the extent of interpenetration and/or the complete separation of the components by modulating the time and the velocity of spinning; removal of one component from the bulk defines a pattern of porosity in the remaining component(s).

Future work with this project involves studies of peripheral nerve regeneration, specifically the direction of myofibroblast migration during regeneration and the resultant quality of regeneration as myofibroblast migration is prevented or allowed, as well as development of a mathematical model describing the sedimentation process to allow for more accurate fabrication of specific tube geometries. Another direction of study will be optimizing the scaffold stiffness and degradation parameters for the *in vivo* environment. In addition to the use of the current DHT crosslinking method, increased DHT crosslinking or chemical crosslinking methods can be utilized to significantly slow the process of degradation and increase scaffold stiffness. One such option is the use of a carbodiimide such as 1-ethyl-3-(3-dimethylaminopropyl)carbodiimide (EDAC); such treatment has already been used to regulate the degradation rate of collagen tubes used in peripheral nerve regeneration studies (Harley, Spilker, et al., 2004) and its effect on these new classes of scaffold will be studied.

APPENDIX B. *Fabrication of Novel Scaffolds for Diverse Tissue Engineering Applications II: Fabrication of a mineralized collagen-GAG scaffold*

B.1. Introduction

The unique mechanical properties of bone are derived from its hierarchical structure, in which an extracellular matrix (ECM) comprised of collagen and other organic species such as some glycosaminoglycan content (Grynpas and Hunter, 1988) is reinforced by nanocrystallites of calcium phosphate, providing elasticity and strength (Carter and Spengler, 1978). Since monolithic hydroxyapatite-like mineral materials are inherently brittle, it is not surprising that extensive efforts have gone into the development of materials seeking to mimic bone composition and its complex nanocomposite structure (Kikuchi, Itoh, et al., 2001; Kim, 2001; Rhee, Suetsugu, et al., 2001).

Scaffolds have been used extensively to provide a three-dimensional extracellular matrix analog for *in vivo* and *in vitro* tissue engineering studies. Increasingly complex fabrication techniques

have been developed to produce scaffolds from biodegradable synthetic polymers or related copolymers (*i.e.*, PLLA, PLGA) (Hubbell, 2000; Freed and Vunjak-Novakovic, 2002) as well as natural polymers such as several copolymers of type I collagen and glycosaminoglycans (GAGs) (Yannas, Lee, et al., 1989; Yannas, 2001). Any discussion of the functional requirements for developing porous scaffolds for tissue engineering applications inevitably leads to the example of a benchmark material for soft-tissue (dermal and nerve) regeneration developed by Yannas et al. (Yannas, Lee, et al., 1989; Yannas, 2001). The first and most widely-used of these templates consists of a porous collagen-glycosaminoglycan (GAG) co-precipitate (Yannas, Lee, et al., 1989) with mechanical and physiological properties tailored maximize scaffold bioactivity (Dagalakis, Flink, et al., 1980; Yannas and Burke, 1980; Yannas, Burke, et al., 1980). Scaffold microstructural, mechanical, and materials properties have all been shown to significantly affect scaffold bioactivity – the ability of a scaffold to actively induce or influence specific cell behaviors. The local scaffold microarchitecture defines the environment of the cells within the scaffold; in particular, both the specific surface area (O'Brien, Harley, et al., 2005) and pore interconnectivity (Yannas, 2001) significantly affect scaffold bioactivity by influencing the ability for cells to bind to and populate the scaffold. For bone regeneration scaffolds, a minimum interconnected pore size conducive to cell invasion (~100 μm) has been identified (Hulbert, Young, et al., 1970). Furthermore, high pore volume fraction and specific surface area are thought to be requirements for the effective transfer of nutrients and metabolites (Yannas, 2001). Scaffold mean pore size as well as degradation rate has been observed to significantly influence the adhesion, growth and differentiation of a variety of cell types (Wake, Patrick, et al., 1994; Nehrer, Breinan, et al., 1997; Zeltinger, Sherwood, et al., 2001) and the bioactivity of scaffolds

used for *in vivo* tissue regeneration (Yannas, Lee, et al., 1989; Yannas, 2001; Harley, Spilker, et al., 2004).

In addition to meeting the traditional tissue engineering requirements of low immunogenicity, minimal toxicity, bioresorbability, favorable architecture for cell attachment and adequate mechanical strength, advanced scaffolding materials for skeletal tissue engineering must also seek to interact with their mechanical surroundings to effectively transmit mechanical signals to cells (Guilak, 2002). Mechanical stimuli affects cellular distribution (Eggli, Hunziker, et al., 1988), metabolic activity (Larsson, Aspden, et al., 1991; Vanwanseele, Lucchinetti, et al., 2002), and, ultimately, the mechanical properties of the tissue itself (Swann and Seedhom, 1993). It is generally believed that this relationship is governed by a feedback loop where deformation of the extracellular matrix (ECM) stimulates changes in cell metabolic activity and matrix expression (Carterson and Lowther, 1978).

The *in vivo* and *in vitro* bioactivity of a scaffold is significantly affected by its chemical composition, in addition to its microstructure and its mechanical properties (Yannas, 2001). Producing an appropriate scaffold for bone tissue engineering requires a consideration of the three major constituents of bone: collagen, hydroxyapatite-like mineral, and to a lesser extent, glycosaminoglycans. Collagen is a significant constituent of the natural bone ECM and of successful regeneration templates for a variety of tissues and organs; collagen exhibits requisite hemostatic properties and low antigenicity, expresses suitable ligands to promote cell attachment and growth (Yannas, 2001; Lynn, Yannas, et al., 2004; O'Brien, Harley, et al., 2005). Additionally, the mechanical properties and degradation rate of collagen can be tailored by

altering crosslink density (Yannas and Tobolsky, 1967; Lee, Grodzinsky, et al., 2001; Harley, Spilker, et al., 2004; Harley, Yannas, et al., 2004). Glycosaminoglycans (GAGs) are long, unbranched polysaccharides that do not elicit an immune response. Copolymerization of collagen with GAGs has been observed to increase the stiffness and toughness of collagen (Yannas, Burke, et al., 1975; Yannas, Burke, et al., 1979), and collagen-GAG co-polymer scaffolds have exhibited significantly improved regenerative capacity (Yannas, 2001). While a significant GAG component is not observed in mature bone, GAGs are present in fetal and newborn bone ECM (Grynpas and Hunter, 1988), suggesting the importance of incorporating GAG content into a mineralized scaffold intended to induce bone regeneration. Calcium phosphates are the major constituent of bone, comprising approximately 75% of its dry mass (Lynn, Cameron, et al., 2004). They are responsible for providing much of its mechanical stiffness and strength, and are often the main component of bone tissue engineering constructs.

Lyophilization (freeze-drying) has emerged as a preferred method to fabricate porous collagen-based scaffolds with predominantly open-cell pores and an interconnected porosity (Yannas, 2001). Significant effort has been invested in tailoring freezing rates, mould design and slurry properties to ensure scaffold pore structure homogeneity, and to enable accurate control of pore size, volume fraction, and interconnectivity (Freyman, Yannas, et al., 2001; O'Brien, Harley, et al., 2004; O'Brien, Harley, et al., 2005). In addition to the biochemical benefits of collagen, a major factor contributing to the clinical success of porous collagen scaffolds is their high porosity, providing ample space for cellular invasion, attachment and proliferation, characterized by an open network of, interconnecting pores of controlled size. However, for applications where even minimal load-bearing is necessary, the stiffness of unmineralized collagen scaffolds is

insufficient to maintain their pore structure under loading, even after the application of crosslinking treatments.

Calcium phosphates (CaPs) have long been the focus of extensive research for their potential use for bone tissue engineering (Klein, Driessen, et al., 1983; Doll, Sfeir, et al., 2001; LeGeros, 2002). Their extensive use as bone substitutes has yielded a lucrative commercial market, with products ranging from coatings (Ong and Chan, 2000; Overgaard, 2000) to porous implants (Boden and Schimandle, 1995) to bioactive composites (Bonfield, Grynpas, et al., 1981; Geyer, 1999). Calcium phosphates were originally designed to improve the chemical interactions between a fixed implant and bone. First developed in the early 1980s, the polyethylene/hydroxyapatite (PE/HAp) composite currently marketed as HAPEX™ was designed to combine the superior mechanical stiffness and bone-bonding capacity of HAp with the superior toughness and ductility of PE (Wang, Joseph, et al., 1998). The past 15 years have witnessed the emergence of a vast number of other CaP-based products – including dense bone fillers (Benebassath, Klein, et al., 1994; Hasegawa, Yamamura, et al., 1998; Bohner, 2000), porous implants (Boden and Schimandle, 1995; Moreira-Gonzalez, Jackson, et al., 2003), and advanced CaP-based composites (Bonfield, Grynpas, et al., 1981; Geyer, 1999). When combined with polymeric materials, calcium phosphate composites impart high stiffness and compressive strength. As bone substitute materials, they are biocompatible and have the unique capacity to bond directly to bone.

While the precise mechanisms underlying the bone-bonding capacity of calcium phosphates are still not fully understood, it is largely recognized that by selecting both (i) the precise chemical

composition of the CaP species present and (ii) the mass fraction of each of these species, the manner in which the resultant biomaterial interacts with its environment can be controlled (Lynn, Cameron, et al., 2004; Lynn and Bonfield, 2005). Control of mass fraction, on the other hand, has traditionally been achieved by mechanical mixing of the selected phases. Although this approach has proven highly effective for traditional systems in which pre-fabricated CaP particles can be dry mixed (either with synthetic polymers or with other calcium phosphates), it has proven inadequate to meet the needs of some of the latest applications (Lynn, Cameron, et al., 2004; Lynn and Bonfield, 2005).

The role of precursor phases in the biomineralization process (*i.e.*, apatite, hydroxyapatite, brushite, octacalcium phosphate - OCP) provides particular motivation in the development of constructs for bone tissue engineering. The generic term apatite (Ap) has traditionally been used to refer to the class of calcium phosphate materials with crystal and chemical structure either similar or identical to hydroxyapatite (HAp, $Ca_{10}(PO_4)_6(OH)_2$), and which may or may not contain low-level substitutions of other ionic species into the HAp lattice. One common means of distinguishing similar calcium phosphates is by their calcium to phosphorus ratio (Ca:P). The Ca:P of phase-pure hydroxyapatite, for instance, is 1.67, while that of human bone can range from 1.50 to 1.70 (healthy bone mean: 1.63), depending on age, anatomical location, and disease (Cassella, Garrington, et al., 1995).

Brushite (dicalcium phosphate dehydrate; $CaHPO_4 \cdot 2H_2O$, Ca:P = 1.0), a ubiquitous calcium phosphate found in a number of biological systems, and octacalcium phosphate (OCP, $Ca_8(HPO_4)_2 \cdot (PO_4)_4 \cdot 5H_2O$; Ca:P = 1.33) have both been proposed as precursors to bone mineral

formation *in vivo* (Muenzenberg and Gebhardy, 1973; Johnsson and Nancollas, 1992), and the capacity for hydrolytic conversion of brushite to OCP and conversion of both brushite and OCP to biological apatite is well documented (Suzuki, Nakamura, et al., 1991; Graham and Brown, 1996). Both compounds have been used in orthopedic applications (Driessens, Boltong, et al., 1994; Sasano, Kamakura, et al., 1995).

Considerable interest has been generated recently in collagen-calcium phosphate (CaP) biocomposites for their potential to mimic both the composition and structure of native bone; recent developments have produced some composites with a high degree of nanostructural similarity to bone (Kikuchi, Itoh, et al., 2001).Variation of the CaP phases present in bone substitutes has been shown to significantly influence both implant dissolution and bone apposition rates; thus biocomposites of collagen and various calcium phosphates (brushite (Clarke, Graves, et al., 1993), OCP (Sasano, Kamakura, et al., 1995), HAp (Itoh, Kikuchi, et al., 2001)) have been produced in an attempt to tailor *in vivo* behavior. In an effort to produce porous scaffolds with improved mechanical properties, a limited number of recent efforts have sought to produce freeze-dried scaffolds from collagen/calcium phosphate composites. While these efforts have proven successful in producing open networks of pores sufficiently large for cellular invasion (100-300μm), their methods rely on the presence of a binder phase in the form of either a separate collagen solution (Kikuchi, Ikoma, et al., 2004) or a synthetic polymer (Chen, Ushida, et al., 2000; Chen, Ushida, et al., 2001; Hu, Zhang, et al., 2003; Cui, Zhu, et al., 2004; Liao, Cui, et al., 2004) to prevent settling and phase separation during the freeze-drying process. Furthermore, no efforts to produce porous collagen/CaP composites containing glycosaminoglycans have been reported to date.

In general, collagen-CaP composites have comprised mechanical mixtures of pre-synthesized calcium phosphate particles suspended in a collagenous matrix (Mehlisch, 1989; Mehlisch, Leider, et al., 1990; Hemmerle, Leize, et al., 1995; Sasano, Kamakura, et al., 1995; Ten Huisen, Martin, et al., 1995; Muschler, Negami, et al., 1996). While these have produced encouraging *in vivo* results in some cases (Mehlisch, Leider, et al., 1990; Cornell, Lane, et al., 1991; Sasano, Kamakura, et al., 1995), typically poor matrix bonding and difficulties producing sufficiently small CaP particles resulted in composites with poor mechanical properties and minimal resemblance to natural bone. Here, we produce collagen-CaP composites using a concurrent mapping, titrant-free coprecipitation approach (Lynn, Cameron, et al., 2004). This technique induces precipitation of calcium phosphate crystallites that, under the proper conditions, form with a preferred nanoparticulate orientation to the collagen fibrils with which they are coprecipitated. Although significant attention has been given to the bone-like character of this oriented relationship (Kikuchi, Itoh, et al., 2001; Rhee, Suetsugu, et al., 2001), a key unresolved issue, however, is the lack of systematic means through which the CaP content, and hence the CaP/bioorganic ratio, can be controlled. This issue is particularly important to the mechanical properties of these materials, and thus their capacity for remodeling into healthy bone.

In a previous report, the authors detailed a procedure for simultaneous control of pH and brushite mass yield without the use of titrants (Lynn, Cameron, et al., 2004; Lynn and Bonfield, 2005). The present investigation describes the application of this method to produce porous, freeze-dried scaffolds of collagen, glycosaminoglycan, and calcium phosphate in a manner such that the mean pore size, mechanical properties, and chemical composition (mass fraction CaP,

GAG:collagen ratio, CaP phase) can be reproducibly controlled and varied. Creating such biocomposite scaffolds will enable optimization of a scaffold structure for bone tissue engineering through systematic modulation of scaffold pore microstructure, mechanical properties, and chemical composition.

B.2. Materials and Methods

Here we describe the processing steps required to fabricate porous, mineralized collagen-glycosaminoglycan (CGCaP) scaffolds via freeze-drying. The processing steps for producing the triple co-precipitate CGCaP suspension will first be detailed. The suspension is then freeze dried to form the scaffold; at this stage, the mineral phase in the CGCaP scaffold is brushite. The freeze dried scaffold is crosslinked via dehydrothermal or carbodiimide-based chemistries to strengthen the scaffold network; a hydrolysis step is then utilized to convert the brushite mineral to OCP, a more appropriate biological apatite precursor. The microstructural, compositional, and mechanical properties of the scaffold (*i.e.*, mean pore size, porosity, pore interconnectivity, CaP content phase and mass yield, compressive stress strain response) are then assayed and reported.

B.2.1. Preparation of mineralized collagen-glycosaminoglycan co-polymer suspension

The mineralized collagen-glycosaminoglycan (CGCaP) suspension was produced by combining microfibrillar, type I collagen (1.0 wt%) isolated from bovine tendon (Integra LifeSciences, Plainsboro, NJ) and chondroitin-6-sulfate (0.09 wt%) isolated from shark cartilage (Sigma-Aldrich Chemical Co., St. Louis, MO) in a solution of 0.138 M phosphoric acid (pH 3.2). Reactant ratios were selected using a method for the simultaneous, titrant-free control of pH and

brushite mass yield developed by the authors (Lynn, Cameron, et al., 2004; Lynn and Bonfield, 2005). On the basis of the protocol of Yannas et al. for the production of collagen-bases co-precipitate suspensions (Yannas, Lee, et al., 1989), a target pH of 3.2 was selected. Chondroitin-6-sulphate was added to the collagen slurry at three GAG:collagen mass ratios (0.00, 0.09, 0.18).

The collagen, chondroitin-6-sulfate, and phosphoric acid were mixed at 15,000 rpm in an overhead blender (IKA Works, Inc., Wilmington, NC); the temperature of the suspension was maintained at 4°C throughout mixing by a cooling system (Brinkman, Westbury, CT) to prevent denaturation of the collagen fibers as a result of the heat generated by mixing. After the initial mixing cycle, calcium salts ($Ca(NO_3)_2 \cdot 4H_2O$, $Ca(OH)_2$) were added to the suspension and dispersed via a second mixing step, resulting in the precipitation of a mineral phase – Ca from the added calcium salts and P from the phosphoric acid – with the collagen and glycosaminoglycan phase. Control over CaP phase chemistry (Ca:P ratio 1.00 to 1.67) as well as the bioorganic:mineral content (0 to 80 wt% CaP content) was obtained using a concurrent mapping technique previously described by these authors (Lynn, Cameron, et al., 2004; Lynn and Bonfield, 2005).

B.2.2. Fabrication of CGCaP scaffold via lyophilization

The CGCaP suspension was frozen using a previously described constant cooling rate technique (O'Brien, Harley, et al., 2004; O'Brien, Harley, et al., 2005) to produce a uniform, homogeneous pore structure with approximately equiaxed pores. The degassed CGCaP slurry was poured into a custom polysulfone mould (30 mm x 50mm surface area; 2, 8, or 10 mm deep with a 8mm thick layer of polysulfone between the suspension and the underlying freeze dryer shelf; the mold was

then placed into the chamber of a freeze-dryer (Genesis, VirTis) held at 4°C. The temperature of the freeze-dryer shelf and chamber was cooled to a final freezing temperature of -20°C at a constant rate of 0.2°C/min; the shelf/chamber temperature was then held constant for 480 minutes at T_f to complete the freezing process. The ice phase was then sublimated under vacuum (<100 mTorr) at 25°C for a period of 24 hours to produce the porous mineralized CGCaP scaffolds. The modified temperature condition during sublimation was utilized to speed the sublimation of the frozen phosphoric acid (unreported data) without compromising the collagen integrity.

B.2.3. CGCaP scaffold crosslinking

Crosslinking increases the mechanical strength and decreases the degradation rate of the scaffolds (Yannas and Tobolsky, 1967; Yannas, Burke, et al., 1975; Harley, Spilker, et al., 2004). After the freeze-drying step, the CGCaP scaffolds were crosslinked via either a dehydrothermal or a carbodiimide treatment. Dehydrothermal (DHT) crosslinking strengthens the collagen network by introducing covalent crosslinks between the polypeptide chains of the collagen fibers. DHT crosslinking was carried out in a vacuum oven (Fisher IsoTemp 201, Fisher Scientific, Boston, MA) at a temperature of 105°C under a vacuum of 50 mTorr for 24 hours (Yannas, Lee, et al., 1989).

The water-soluble compound 1-ethyl-3-(3-dimethylaminopropyl)carbodiimide (EDAC) was used to chemically crosslink the composites by way of a modified version of a protocol developed by Olde Damink et al. (Olde Damink, Dijkstra, et al., 1996), further modified by Lee et al. (Lee, Grodzinsky, et al., 2001), Pek et al. (Pek, Spector, et al., 2004), and Vickers et al. (Vickers,

Squitieri, et al., 2006), resulting in the formation of cross-links between the collagen fibers. EDAC acts solely as a catalyst in the crosslinking reaction, allowing the cytotoxic carbodiimide to be completely rinsed from the scaffold following the crosslinking reaction (Lee, Grodzinsky, et al., 2001). Freeze-dried matrices were weighed and the collagen contents of each estimated on the basis of their mass fractions of CaP, reported previously under similar synthesis conditions (Lynn, Cameron, et al., 2004). Scaffolds were then hydrated in 100mL deionized water at room temperature. EDAC (Sigma Aldrich Chemical Co., Steinheim, Germany), stored at –10°C, was dissolved separately in deionized water at a ratio of 6mmol per gram of collagen at room temperature. N-hydroxysuccinimide (NHS, Sigma Aldrich) was added to the same solution at a molar ratio of 5:2. This solution was then added to the water in which the composites were hydrating, and were crosslinked for 2 hours. After crosslinking, matrices were removed and rinsed twice in phosphate buffered saline (PBS), then incubated in fresh PBS for 2 hours.

B.2.4. Hydrolysis of Brushite to OCP

Hydrolytic conversion of the CaP phase of the composites was accomplished by adopting roughly the optimized hydrolysis parameters developed by Heughebaert et al. (Heughebaert, Lebugle, et al., 2000). Scaffolds were immersed in deionized water at 37°C at 40mL per gram of brushite (calculation described in EDAC crosslinking protocol above). The pH of the hydrolysis solution initially decreased due to the likely presence of phosphoric acid residue; the pH was allowed to decrease until a value of $pH < 6.65$ was achieved, after which point manual titration with dilute ammonia (NH_3 91%; BDH; Poole, UK) was performed at hourly intervals, to maintain pH between 6.55 and 6.75.

Scaffolds floated near the surface of the hydrolysis solution; therefore to maintain ion distributions while avoiding damage to scaffold structure, magnetic stirring was applied at the bottom of the reaction vessel at the lowest rate possible (~100rpm). At periodic intervals, scaffolds were removed from the hydrolysis solution, rinsed in deionized water and allowed to dry under a vacuum of <50mTorr for 24 hours at room temperature.

B.2.5. Pore structure characterization via microCT and mercury porosimetry

Mineralized CG scaffolds were analyzed using mercury porosimetry and microCT techniques to determine mean pore size, pore volume fraction, and percent interconnectivity. Cylindrical samples were removed from each mineralized CG scaffold using either an 8 mm diameter dermal biopsy punch (Miltex, Inc., York, PA) or a 9.25 mm diameter trephine blade (Howard Instruments, Inc., Tuscaloosa, AL, USA). MicroCT and mercury porosimetry techniques were then utilized to analyze the pore microstructure; microCT allowed visualization of the uniformity of the mineral distribution while mercury porosimetry allows calculation of the mean pore size and pore volume fraction (Lynn, 2005).

B.2.6. Pore structure characterization and compositional analysis via SEM

Mineralized CG scaffolds were analyzed using SEM analysis to determine mean pore size and distribution of the scaffolds; the mineral content and the spatial distribution of mineral within the scaffolds were determined through SEM analysis using energy dispersive X-ray spectroscopy (EDX). Briefly, 5mm diameter cylindrical samples were cut using a standard biopsy punch (Miltex, Inc.) and mounted on an aluminum sample holder for SEM analysis. SEM analysis was

performed with a Leo VP438 electron microscope (Leo Electron Microscopy, Inc., Thornwood, NY) using both a standard secondary electron detector and a backscatter electron detector under variable pressure mode. Line scan and compositional map data were acquired via EDS for calcium (Ca) and phosphorous (P) content. Scaffold samples were analyzed looking at both the top surface and side face of the scaffold disk to determine spatial distribution of pores and mineral content.

B.2.7. X-ray diffraction analysis of CGCaP co-precipitates

X-ray diffraction (XRD) analysis was performed on the CGCaP scaffold and suspension variants identify the inorganic phases present. Samples were prepared for compositional analysis by breaking each scaffold up into small particles using forceps and a scalpel. This step was performed to ensure that compositional analyses were representative of the average composition of the entire scaffold. All scans were performed using Cu K_α radiation on a Phillips PW3020 2-D diffractometer, with powder specimens mounted on a silicon single crystal. A range of 2° to 50° 2θ was selected to ensure detection of all calcium phosphate species present. A step size of 0.02° 2θ and a dwell time of 10 sec were employed for all measurements. Peaks were attributed to specific compounds by comparison with powder diffraction files (PDF) using Phillips Xpert Plus software.

B.2.8. Mechanical analysis of CGCaP scaffolds

Unidirectional, unconfined compression tests (constant strain rate 0.1% strain/sec) were performed on each scaffold sample. Cylindrical disk samples were cut from sheets of CGCaP

scaffold using a series of cylindrical punches (8 mm diameter dermal biopsy punch, Miltex; 9.25 mm diameter trephine blade, Howard Instruments). Compression tests were performed on both dry and hydrated CGCaP scaffold samples; hydrated scaffold samples were hydrated in a phosphate buffered saline solution (PBS, Sigma Aldrich Chemical Co.) for 12 hours to allow scaffolds to become fully hydrated (Harley, Spilker, et al., 2004).

Mechanical tests were performed using a using a Zwick/Roell Z2.5 static materials tester (Zwick GmbH & Co., Ulm, Germany) at a constant compression rate of 1% strain/sec to a maximum strain of 60% with a 500 N load cell (Part No. BTC-LC0500N.P01, Zwick) sampling at a frequency of 2 Hz. Control of the testing profile (*i.e.*, strain rate, ultimate strain, sampling rate, data collection and storage) was controlled on a PC using the testXpert software package (Zwick). Using the results of this analysis, the Young's modulus, collapse plateau modulus, and collapse stress for the CGCaP scaffold variants was calculated.

B.2.9. Statistical analysis

One-way analysis of variance (ANOVA) and pair wise multiple comparison procedures (Dunn's Method) were used to compare groups of data. Error is reported in figures as the standard deviation (StDev), the standard error of the mean (SEM = $StDev/n^{1/2}$), or as the coefficient of variance (CV = StDev/Mean). A probability value of 95% ($p < 0.05$) was used to determine significance.

B.3. Results

The results from a series of analytical procedures on both the CGCaP suspension and scaffold variants will now be presented. First, compositional analysis of the CGCaP suspensions will be detailed followed by a description of the resultant CG scaffold pore microstructure and mineral distribution. Elemental and mass fraction analysis of the CGCaP will then be described following by the results of initial mechanical characterization of the CGCaP scaffold variants.

B.3.1. pH control over CGCaP suspension

The pH of the CGCaP suspension at each CaP mass fraction and mass ratio of GAG to collagen are shown in **Figure B.1**. The collective average pH for all measurements shown in the figure was 3.23 ± 0.06, illustrating the pH control capacity required of the titrant-free method.

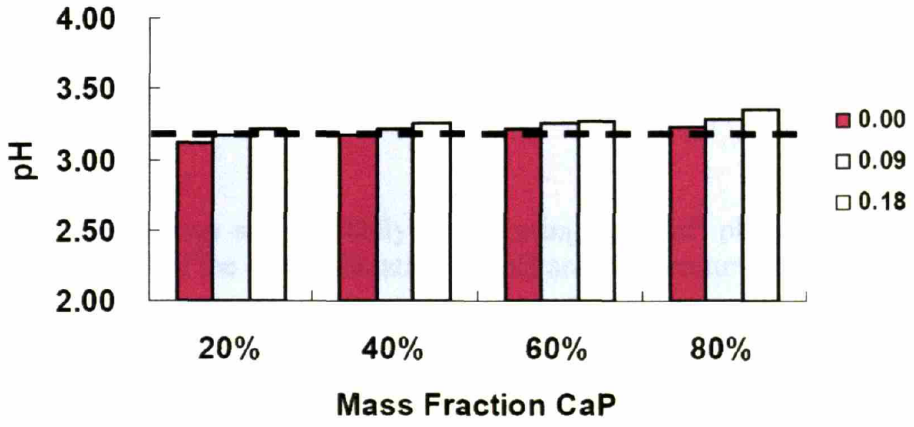

Figure B.1. pH variation of CGCaP suspension due to calcium phosphate (CaP wt% 20, 40, 60, 80%) and GAG content (GAG:collagen mass ratio of 0.00, 0.09, 0.18). The collective average pH for all CGCaP suspension is 3.23 ±0.06, comparable to the target pH of 3.2 (dashed line).

B.3.2. CaP phase within CGCaP triple-co-precipitate suspension

CaP phase mapping was performed via XRD analysis of CaP solutions produced systematically under a wide range of temperatures (10 – 70°C) and pH (2.0 – 8.0). Co-precipitation of CG content takes place at room temperature, pH ~3.2 (Yannas, Lee, et al., 1989); under these conditions, the stable CaP phase obtained is brushite (**Figure B.2**).

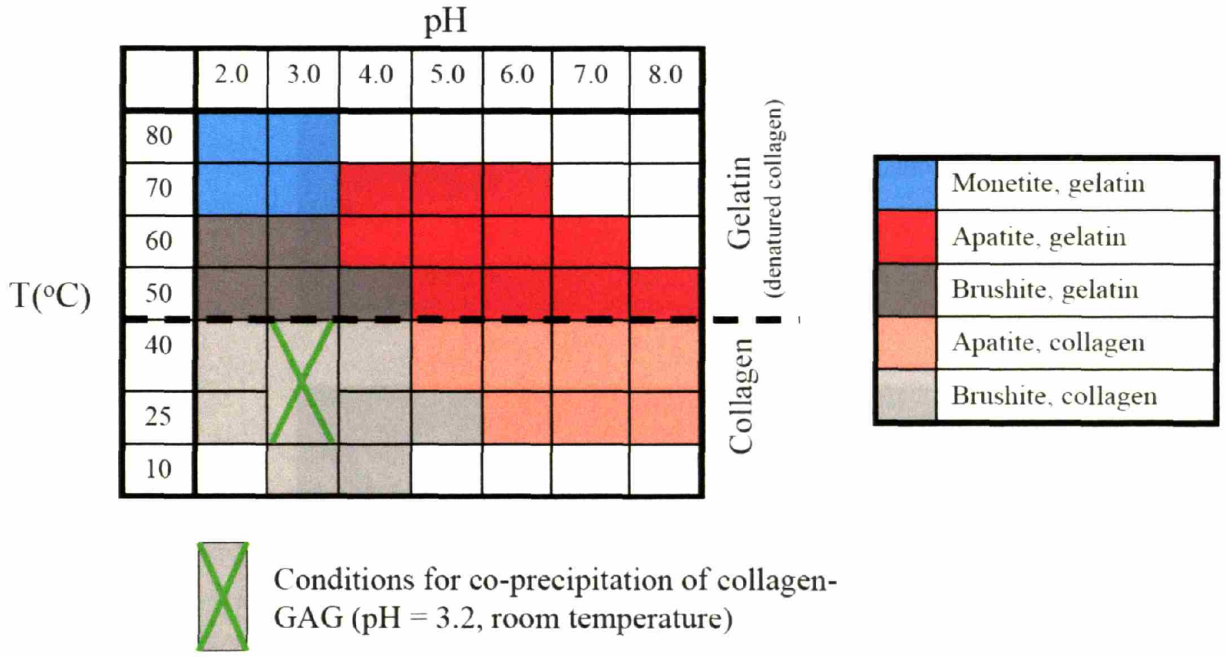

Figure B.2. CaP phase map schematically representing the CaP phase for the CaP/collagen suspension found at each of the 36 combinations of pH and temperature tested.

B.3.3. CGCaP scaffold pore structure

Figure B.3 and **Figure B.4** show SEM and cross-sectional X-ray microtomographic images, respectively, of the CGCaP composite scaffold pore microstructure. A homogeneous, open-cell pore microstructure with interconnected, equiaxed pores is observed throughout the scaffold. X-ray microtomographic analysis indicated that the CGCaP scaffold displayed a pore volume

fraction of 85 ± 3% and a mean pore size of 419 ± 67 μm, appropriate to be used as an ECM for bone. SEM and microCT analysis indicated pore interconnectivity and uniform mineral distribution throughout the scaffold structure.

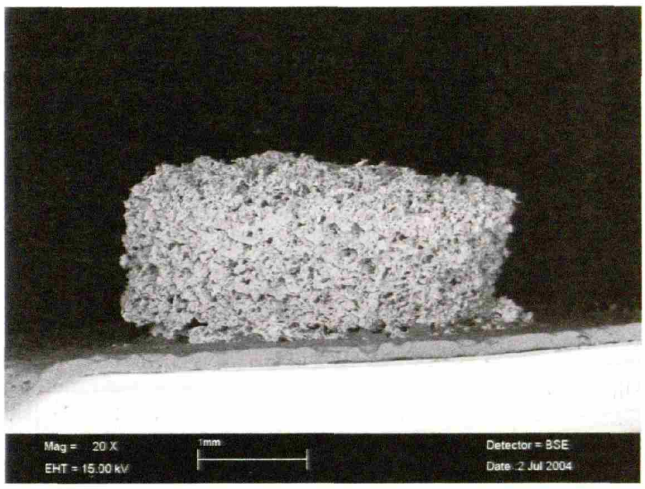

Fig. B.3a

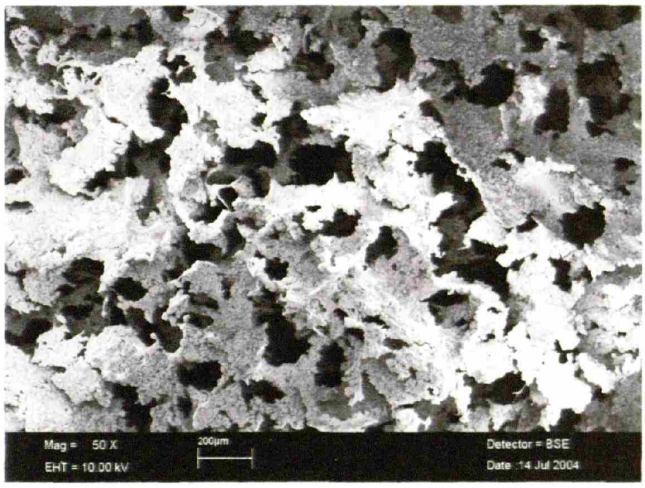

Fig. B.3b

Figure B.3. SEM images of gross scaffold morphology (Fig. B.3a) and local pore microstructure (Fig. B.3b) of the CGCaP scaffold. An open-cell foam-like structure with interconnected pores is observed.

B.3.4. CGCaP scaffold mineral distribution

MicroCT analysis indicated a uniform distribution of mineral content throughout the scaffold structure (**Figure B.4**); EDX analysis of the CGCaP scaffold shows a uniform distribution of both the Ca and P mineral phases throughout the scaffold structure (**Figure B.5**).

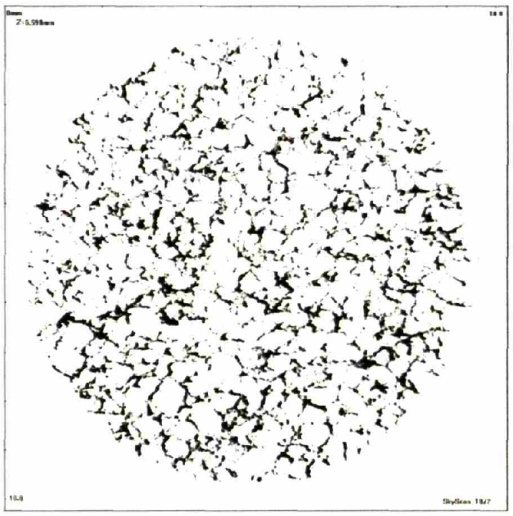

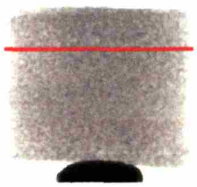

Fig. B.4a

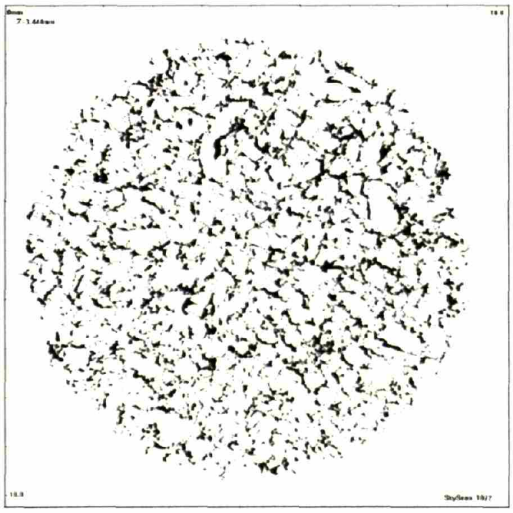

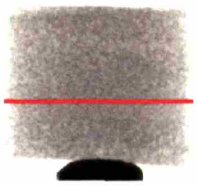

Fig. B.4b

Figure B.4. Cross sectional X-ray microtomographic of the CGCaP scaffold at two distinct locations (Fig. B.4a, B.4b); a homogeneous pore structure and mineral distribution is observed throughout the thickness of an 8.5 mm thick scaffold. Scaffold cross-section diameter: 9.25 mm.

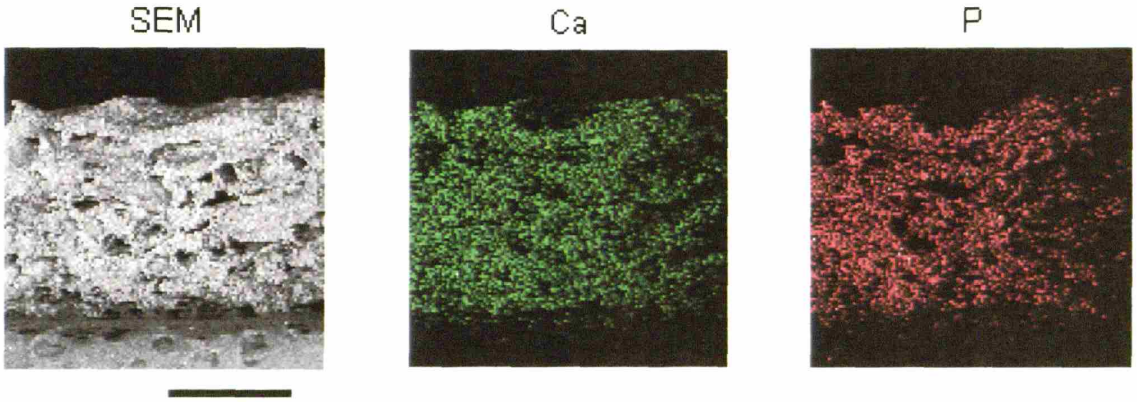

Figure B.5. EDX analysis of scaffold disks show an even distribution of both calcium (Ca) and phosphorous (P) throughout the CGCaP scaffold. Scale bar: 1 mm.

B.3.5. XRD analysis of CGCaP suspension, freeze-dried CGCaP suspension, and CGCaP scaffolds with different cross-linking

Figure B.6 shows the XRD patterns for the CGCaP suspension and freeze-dried CGCaP composites (**Fig. B.6a**) as well as the XRD patterns for the freeze-dried CGCaP composites after three different cross-linking reactions (non-crosslinked, DHT, EDAC, **Fig. B.6b**). There was no significant change in the XRD pattern between the CGCaP suspension and the non-cross-linked composite scaffold. While only minimal changes in the CaP composition of the composites were observed following EDAC crosslinking, the pattern shown in **Figure B.6b** shows that DHT crosslinking induces a nearly perfect, though undesirable, transformation of the brushite phase to monetite. Closer examination of the pattern in **Figure B.6b** reveals that trace amounts of OCP appeared in the brushite during EDAC crosslinking, as indicated by the presence of the characteristic peak at 4.8° 2θ. Due to the induced chemical composition transformation, DHT crosslinking was not utilized for the remainder of this analysis.

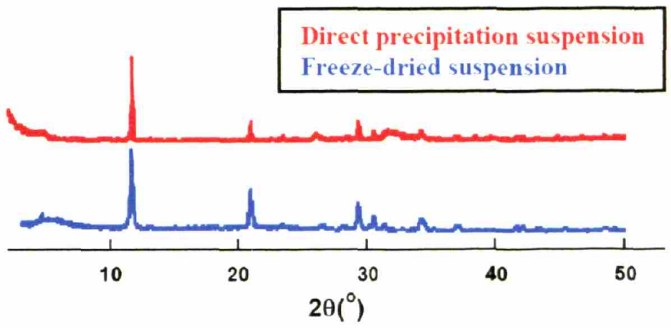

Fig. B.6a

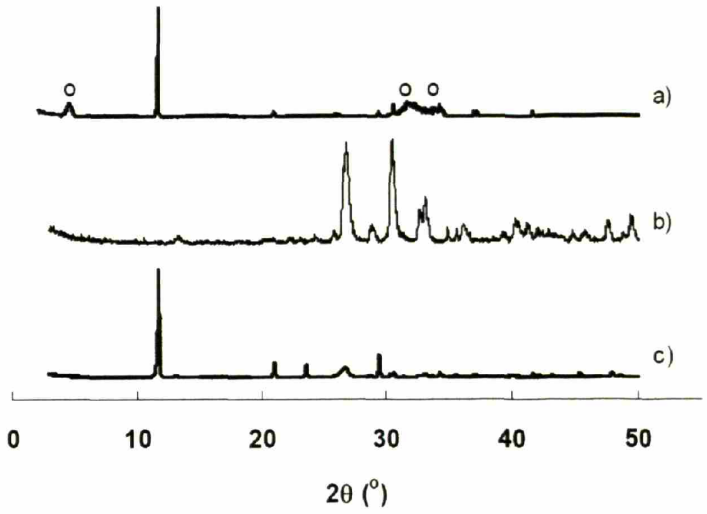

Fig. B.6b

Figure B.6. XRD analysis of CGCaP suspension and freeze-dried CGCaP constructs before and after crosslinking. Fig. B.6a. XRD patterns for brushite content of CaP phase in CGCaP suspension (direct precipitation suspension) and following freeze-drying. No effect of freeze-drying was observed on the mineral content or character. Fig. B.6b. XRD patterns for (i) uncrosslinked CGCaP composites, (ii) EDAC crosslinked and (iii)DHT crosslinked composite scaffolds.. Note that the XRD pattern for the DHT crosslinked composite shows characteristic peaks of monetite with virtually no trace of brushite while EDAC crosslinked composites shows characteristic peaks for brushite and OCP (o), indicating partial hydrolysis has occurred.

B.3.6. Mass fraction of CGCaP suspension and freeze-dried composite scaffold

Predicted and observed (Mean ± StDev) CaP mass fractions (wt %) for both the CGCaP suspension and the freeze-dried composite are shown in **Figure B.7**. The predicted CaP mass fraction gave a good description of the measured values, further validating the concurrent

mapping technique. Average mass fractions for all groups (suspension and composite) were within one standard deviation of their predicted values, with the exception of the 20 and 60wt% CGCaP suspensions, which were marginally lower than predicted.

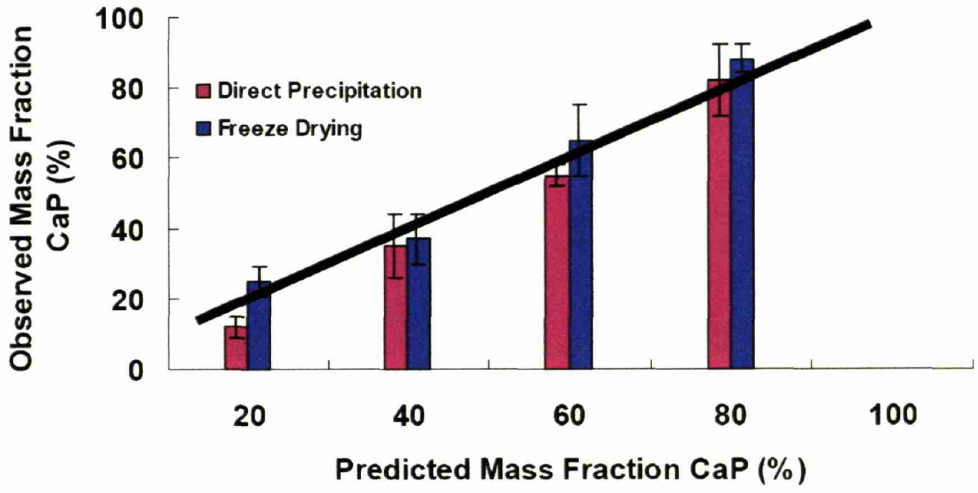

Figure B.7. Observed vs. predicted CaP mass fraction in CGCaP suspension and freeze-dried CGCaP composite.

B.3.7. Hydrolytic conversion of CGCaP composite scaffold CaP phase from brushite to OCP

Figure B.8 shows the progression of the hydrolytic conversion of the EDAC crosslinked matrices over a 48-hour period (**Fig. B.8a**). Progression of the reaction is evidenced by the increased intensity of the characteristic OCP peak at 4.8° 2θ and the concurrent attenuation of the brushite peak at 11.6° 2θ. For scaffolds with varying mass fractions of CaP, full conversion of brushite to OCP required different durations of hydrolysis. **Figure B.8b** illustrates the requisite time to full conversion as a function of mass fraction CaP. The observed increases in time to conversion are thought to be due to the increased density of CaP crystallites within the composites, which may lead to higher local concentrations of ion products from hydrolysis.

There was no consistent trend in the dependence of the time to full conversion on the mass ratio of GAG to collagen.

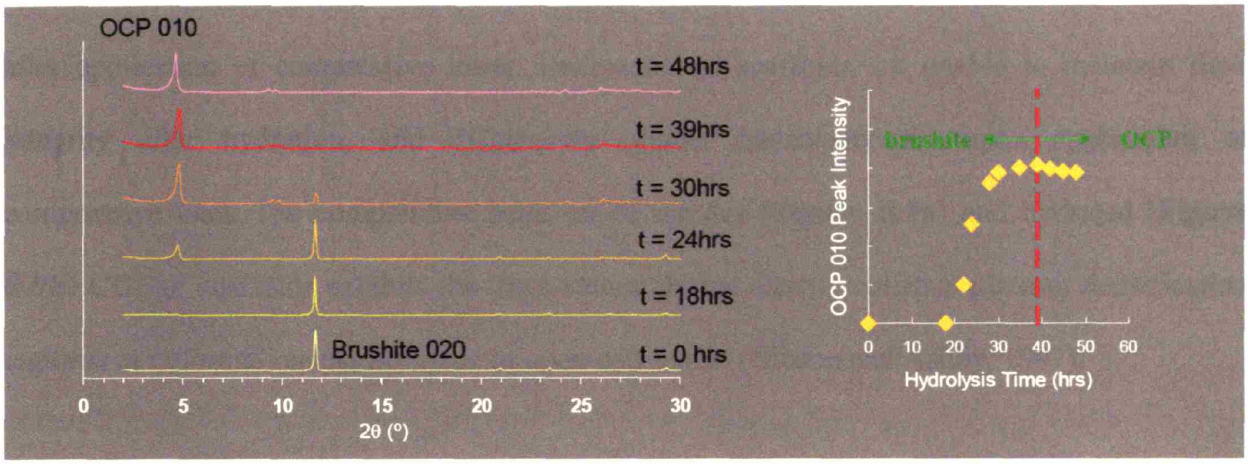

Fig. B.8a

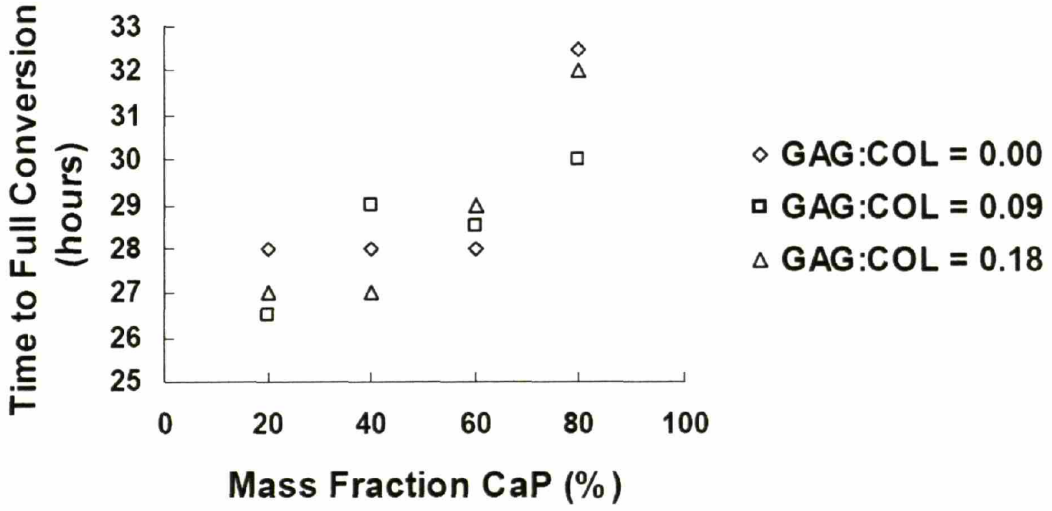

Fig. B.8b

Figure B.8. Conversion of CGCaP composite Ca phase from brushite to OCP. Fig. B.8a. Progression of hydrolytic conversion of EDAC crosslinked CGCAP composite (80% wt% CaP – brushite, GAG:collagen weight ratio 0.09). Fig. B.8b. Time for full conversion of brushite to OCP for all mass fractions of CaP (0 – 80 wt%). Note: Full conversion assessed by extinction of brushite peak at 11.6° 2θ.

B.3.8. Mechanical characterization of CGCaP scaffold

EDAC crosslinking results in CGCaP scaffolds that are sufficiently strong and stiff after hydration to maintain their cohesiveness, shape and pore structure both in the unloaded state, and after application of compressive loads. Uncrosslinked scaffolds are unable to maintain their integrity after hydration, and disintegrate almost instantaneously upon application of compressive load. The compressive behavior of the dry (**Figure B.9a**) and hydrated (**Figure B.9b**) CGCaP scaffolds exhibits the three-stages (linear elastic, collapse plateau, densification regions) of deformation characteristic of open-cell foams (Gibson and Ashby, 1997).

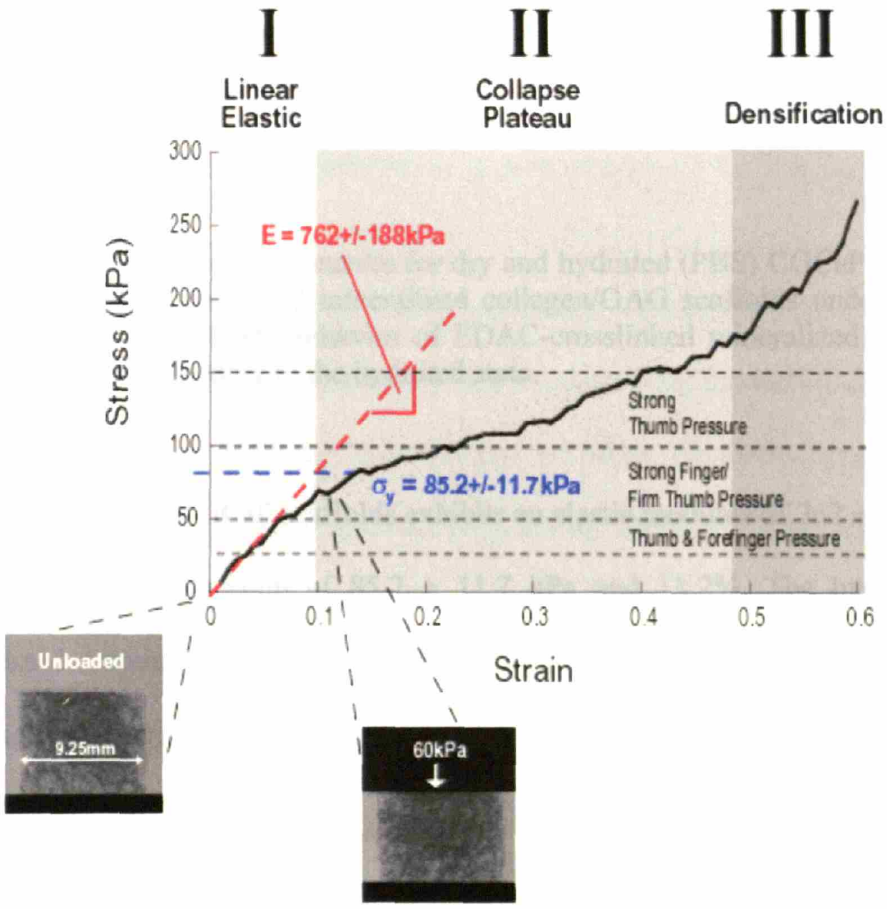

Fig. B.9a

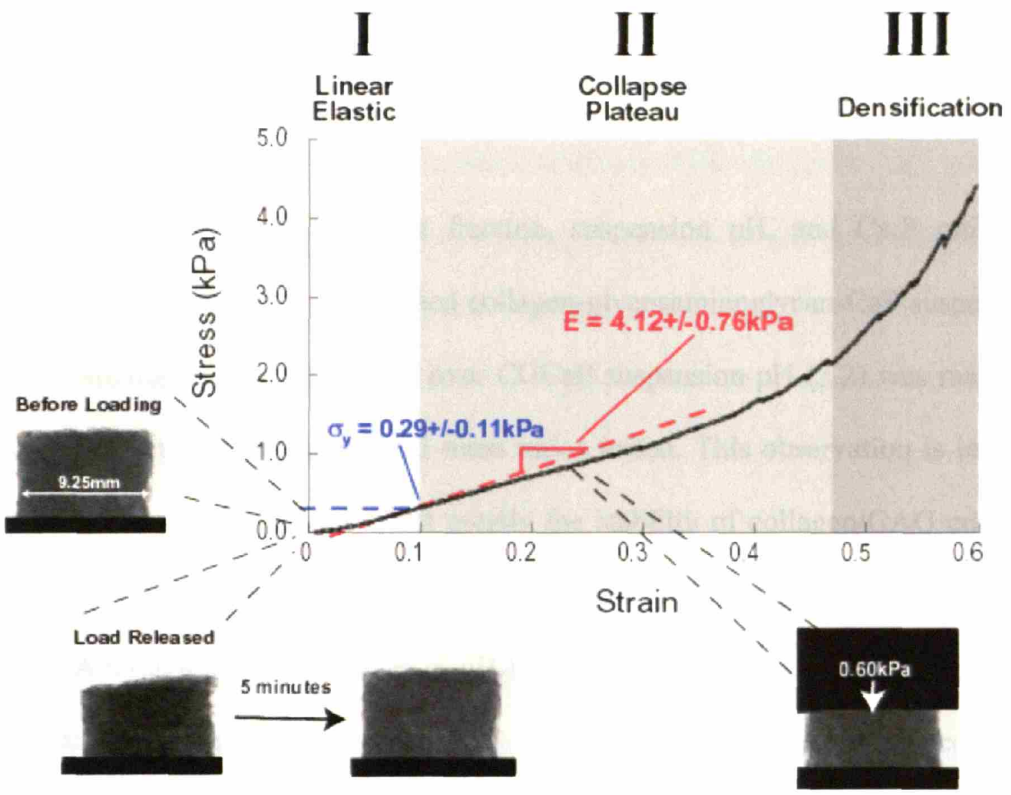

Fig. B.9b

Figure B.9. Compressive stress-strain curves for dry and hydrated (PBS) CGCaP scaffolds. Fig. B.9a. Behavior of EDAC-crosslinked mineralized collagen/GAG scaffolds under compressive loading in the dry state. Fig. B.9b. Behavior of EDAC-crosslinked mineralized collagen/GAG scaffold under compressive loading in the hydrated state.

The dry, EDAC crosslinked CGCaP scaffolds exhibits an elastic modulus of 762 ± 188 kPa and a compressive yield stress and strain of 85.2 ± 11.7 kPa and 11.2%. The hydrated CGCaP scaffolds possessed a compressive elastic modulus (4.12 ± 0.76 kPa) and yield stress (0.29 ± 0.11 kPa), roughly an order of magnitude lower than the corresponding properties of dry scaffolds, and a yield strain of 7%.

B.4. Discussion

Successful control over the CaP weight fraction, suspension pH, and Ca:P ratio has been obtained for the production of a mineralized collagen-glycosaminoglycan-CaP suspension using a concurrent mapping technique. Control over CGCaP suspension pH (3.2) was maintained for all CaP mass fractions and collagen:GAG mass ratios tested. This observation is important for the synthesis, as changes in pH can affect greatly the stability of collagen/GAG coprecipitated complexes and the suspension viscosity, with subsequent effects on pore architecture during freeze-drying. Although a slight increase in pH was observed with increasing GAG to collagen ratio, the observed increase of pH (**Fig. B.1**) was not large enough to induce changes in suspension viscosity or collagen/GAG stability.

Minimal changes were observed in the CaP composition between the CGCaP suspension (brushite, **Fig. B.2**) and the CGCaP composite following freeze-drying and EDAC crosslinking (**Fig. B.6a, B.6b**); however, dehydrothermal treatment following freeze-drying caused a nearly perfect transformation of the brushite to monetite (**Fig. B.6b**). This well known reaction proceeds as a simple dehydration process in which the hydrated layer characteristic of the brushite monoclinic structure is eliminated in favor of the triclinic structure of monetite. Both monetite and brushite are biocompatible and biodegradable, and both are used in biomedical applications; however, only brushite has the capacity to convert to octacalcium phosphate at low temperatures. DHT is thus an unsuitable crosslinking technique for the production of collagen/GAG/OCP biocomposites, while EDAC crosslinking is a more promising candidate.

Excellent agreement was observed between the observed and predicted CaP mass fraction in both the CGCaP suspension and the freeze-dried CGCaP composites (**Figure B.7**), indicating the ability to fabricate mineralized, collagen-based scaffolds with designed CaP content (mass fraction and CaP composition). Concurrent mapping fabrication of CGCaP suspension variants and subsequent freeze-drying to produce a porous, CGCaP scaffold represent arguably the most successful attempt to control the inorganic to organic ratio in a coprecipitated composite documented to date.

Closer examination of the XRD pattern of the freeze-dried, EDAC crosslinked CGCaP composite (**Figure B.6b**) reveals that trace amounts of OCP appeared following crosslinking, as indicated by the presence of the characteristic peak at 4.8° 2θ. Since this reaction is known to occur at varying rates in slightly acidic solutions, it is reasonable to assume that, given the appropriate pH during crosslinking, conversion of the brushite phase to OCP may have occurred simultaneously with crosslinking of the organic phase. Additionally, compared to DHT treatment, EDAC crosslinking results in higher crosslink density, higher compressive stiffness and greater resistance to chondroitinase and collagenase (Pek, Spector, et al., 2004).

Previous investigations of the hydrolysis of brushite in its monolithic form have revealed that full conversion to OCP takes place within 18 hours under the reaction conditions adopted during the present investigation (Heughebaert, Lebugle, et al., 2000). Results shown here indicate that for porous collagen/GAG/brushite composites, complete reaction takes considerably longer, with traces of brushite still present after 24 hours in some of the CGCaP composite variants (**Figure B.8a, B.8b**). This phenomenon may be due to shielding of the calcium phosphate phase by the

organic components of the composite, and may also be affected by lack of adequate ion exchange from the inner to outer portions of the 3-D scaffolds. However, complete conversion of brushite to OCP was observed to take place within 33 hours (**Figure B.8a, B.8b**) for all of the CGCaP suspension variants (variable CaP mass fraction, collagen:GAG ratio).

CGCaP scaffolds with a high degree of pore interconnectivity and a relatively high pore volume fraction (85 ± 3%) were produced via freeze-drying. The homogeneous, open cell microstructure of the CGCaP scaffold, with its interconnected pores (**Figure B.3a, B.3b, B.4a, B.4b**), makes it an ideal candidate for bone tissue engineering applications. The CGCaP scaffold pore structure (Mean pore size: 419 ± 67 μm; Relative Density: 85 ± 3%) allows easy access for cell infiltration and migration and a large scaffold specific surface area for cell binding. It is a stable material produced via a robust fabrication process possessing known compositional, mechanical, and microstructural properties. In addition, uniform distribution of the CaP content was observed throughout the depth of the scaffold (**Figure B.5**), indicating that no phase separation took place between the organic and mineral suspension phases during processing. This result further establishes the validity of the formation of a CGCaP triple-co-precipitate suspension.

Mechanical characterization of the CGCaP scaffolds indicated that the scaffolds (dry and hydrated) behaved as open-cell foams with distinct linear elastic, collapse plateau, and densification regions (**Figure B.9a, B.9b**). While the mechanical properties of these scaffolds was inferior compared to mature, cortical or trabecular bone, the yield strength of the dry CGCaP scaffolds allows them to withstand firm thumb pressure (*i.e.*, during insertion into a defect site)

without deforming permanently. Additionally, after load was removed, the CGCaP scaffold exhibited its elastic nature and returned to its original shape.

B.5. Conclusions

Using the natural structure and composition of bone as a model, a family of novel scaffolds comprising collagen, glycosaminoglycans (GAG), and calcium phosphate (CaP) have been designed and fabricated. A triple co-precipitate solution of collagen, glycosaminoglycans, and CaP (brushite) is produced using a previously described concurrent mapping technique, allowing precise and reproducible control over CaP content (0 to 80 wt%), Ca:P ratio (1.00 to 1.67), CaP phase (brushite), and GAG:collagen ratio. The triple co-precipitate solution is then freeze-dried to produce a CGCaP scaffold with a homogeneous, open-cell microstructure (85 ± 3% porous), with interconnected, equiaxed pores, and a controllable mean pore size (419 ± 67 μm). In addition, the CaP phase (brushite, OCP) can be controlled via a hydrolytic conversion step. Such wide-ranging control of scaffold microstructure, mechanical properties, and composition allows the properties of an implant for bone tissue engineering to be tailored to meet the demands of particular orthopedic applications. These CGCaP scaffolds are also the foundation for the fabrication of layered type I collagen-GAG-CaP and type II collagen-GAG composite scaffolds for osteochondral tissue engineering applications; these layered scaffolds exhibit a "soft" interfacial zone between scaffold layers with a continuous collagen network across the interface mimicking that seen in osteochondral tissue. Fabrication and characterization of such scaffolds will be the subject of a forthcoming publication from our group.

APPENDIX C. *Collagen-GAG Scaffold Fabrication and Characterization Protocols*

C.1. Collagen-Glycosaminoglycan (CG) Suspension Protocol

REFERENCE: (Yannas, Lee, et al., 1989; Chamberlain and Yannas, 1998; O'Brien, Harley, et al., 2004; O'Brien, Harley, et al., 2005)

SUPPLIES

- § 3.6 gm type I microfibrillar bovine tendon collagen (Integra LifeSciences, Inc., Plainsboro, NJ); store at 4°C.
- § 2991.3 ml distilled, deionized water
- § 8.7 ml Glacial Acetic Acid (Mallinckrodt Chemical Co., Paris, KY)
- § 0.32 gm Chondroitin 6-sulfate from shark cartilage (Cat. No. C-4384, Sigma-Aldrich Chemical Co., St. Louis, MO); store at 4°C.

EQUIPMENT

- § Suspension cooling system (Brinkman cooler model RC-2T, Brinkman Co., Westbury, NY)
- § Suspension mixer (Ultra Turrax T18 Overhead blender, IKA Works, Inc., Wilmington, NC)
- § Peristaltic pump (Manostat Cassette Pump, Cat. No. 75-500-000, Manostat, New York, NY)

PROCEDURE

1. Turn on the cooling system (Brinkman model RC-2T) for the blender (Ultra Turrax T18 Overhead blender, IKA Works) and allow the mixing chamber to cool to 4°C (~30 minutes).

2. Prepare a 0.05 M acetic acid (HOAc) (pH 3.2) solution: add 8.7 ml HOAc (Glacial Acetic Acid, Mallinckrodt Chemical Co) to 2991.3 ml of distilled, deionized water in the chemical fume hood. This solution has a shelf life of approximately 1 week.

3. Blend 3.6 gm of microfibrillar bovine tendon collagen with 600 ml of 0.05 M acetic acid at 15,000 rpm (Blender Setting: 3.25) for 90 minutes at 4°C.

4. Prepare the chondroitin 6-sulfate solution: dissolve 0.32 gm chondroitin 6-sulfate (from shark cartilage: Cat. No. C-4384, Sigma-Aldrich) in 120 ml of 0.05 M acetic acid.

5. Calibrate the peristaltic pump (Manostat Cassette Pump, Cat. No. 75-500-000) to 120 ml per 15 minutes.

6. Add the 120 ml chondroitin 6-sulfate solution dropwise to the blending collagen dispersion over 15 minutes using the peristaltic pump, while maintaining the blender at 15,000 rpm (Blender Setting: 3.25) and 4°C.

7. Blend the collagen-GAG suspension an additional 90 minutes at 15,000 rpm (Blender Setting: 3.25) at 4°C.

8. Degas the collagen-GAG suspension in a vacuum flask for 60+ minutes until bubbles are no longer present in the solution.

9. Store the suspension in a capped bottle at 4°C; it will keep for up to four months.

10. If collagen-GAG suspension has been stored for more than one week, re-blend it for fifteen minutes at 10,000rpm (Blender Setting: 2) at 4°C and degas again.

C.2. Collagen-GAG Scaffold Fabrication: Constant Cooling Lyophilization Protocol – Long Version

REFERENCE: (O'Brien, Harley, et al., 2004; O'Brien, Harley, et al., 2005)

SUPPLIES

- § Type I collagen-glycosaminoglycan suspension (67.25 ml/sheet)
- § 5" x 5", 18 gauge 304 stainless steel pan (VirTis Inc., Gardiner, NY)
- § 0.05 M acetic acid

EQUIPMENT

- § Genesis freeze dryer (VirTis)

PROCEDURE

1. Turn on the freeze dryer (VirTis Genesis):
   - » Check that the vacuum oil level is at least 2/3, the oil appears clean, and that the vacuum pump is properly vented (either outside or into a chemical fume hood)
   - » Plug the condenser drain valve and close the condenser and main chamber door
   - » Turn the main ***Power*** switch on
   - » Turn the ***Condenser*** switch on
   - » Set the ***SV*** gauge to 20°C and turn on the ***Freeze*** and ***Heat*** switches

You need to allow approximately 60 minutes for the freeze dryer temperature to stabilize and for the condenser to reach a cold enough temperature to continue.

2. Degas the CG suspension in a vacuum flask (Pressure: ~50 mTorr). Degas approximately twice the required volume to allow appropriate removal of all air bubbles. The length of time needed to degas the suspension varies from 30 – 90 min. depending on the total volume being degassed and the length of time the entire volume of suspension was degassed immediately following mixing.

3. Clean the stainless steel pan (VirTis) with ethanol or 0.05 M acetic acid and wipe the inside with Kim-Wipes to remove all dust and any remaining CG content from the previous run. When cleaning and handling the pan, do not touch the inside of the pan with your bare hands. Use gloves. Allow the pan to air dry.

4. Pipet 67.25 ml of the degassed CG suspension into each pan.

5. Remove any air bubbles introduced into the suspension during the pipetting step using a 200 µl pipette tip. Drag the bubbles to the edge of the pan, allowing them to stick to the edge. Place the pan into the freeze dryer.

6. Check the appropriate program is selected using the Wizard controller. Press the button under ***Program X*** (X = 1 – 12) (Button #1) on the digital display. Select the appropriate program number using the ***Up*** and ***Down*** keys and then press the ***Edit*** key. Check the program variables

(Temperature, Time, Ramp/Hold) against those detailed below. If the progression is incorrect, correct the values. Use the outer two buttons to scroll left or right through the program and the inner two keys to change the value of the selected criteria to match the desired program.

Program 2: Ramp to –40°C. Total time from start to sublimation: ~135 minutes
Mean pore size: 95.9 ± 12.3 μm
Percent porosity: 0.994
Specific surface area (S.A./Vol): 0.00748 μm^{-1}

Freezing Step	Temperature, °C	Time, min	R/H
1 (start)	20	5	H
2 ("ramping")	-40	65	R
3 ("annealing")	-40	> 60	H

Table C.1. Freeze dryer program to fabricate CG scaffolds with a 96 μm mean pore size

Program 3: Ramp to –30°C. Total time from start to sublimation: ~105 minutes
Mean pore size: 109.5 ± 18.3 μm
Percent porosity: 0.994
Specific surface area (S.A./Vol): 0.00655 μm^{-1}

Freezing Step	Temperature, °C	Time, min	R/H
1 (start)	20	5	H
2 ("ramping")	-30	40	R
3 ("annealing")	-30	> 60	H

Table C.2. Freeze dryer program to fabricate CG scaffolds with a 110 μm mean pore size

Program 4: Ramp to –20°C. Total time from start to sublimation: ~90 minutes
Mean pore size: 121.0 ± 22.5 μm
Percent porosity: 0.994
Specific surface area (S.A./Vol): 0.00593 μm^{-1}

Freezing Step	Temperature, °C	Time, min	R/H
1 (start)	20	5	H
2 ("ramping")	-20	30	R
3 ("annealing")	-20	> 60	H

Table C.3. Freeze dryer program to fabricate CG scaffolds with a 121 μm mean pore size

Program 5: Ramp to –10°C. Total time from start to sublimation: ~80 minutes
Mean pore size: 150.5 ± 32.1 μm
Percent porosity: 0.994
Specific surface area (S.A./Vol): 0.00477 μm^{-1}

Freezing Step	Temperature, °C	Time, min	R/H
1 (start)	20	5	H
2 ("ramping")	-10	20	R
3 ("annealing")	-10	> 60	H

Table C.4. Freeze dryer program to fabricate CG scaffolds with a 151 μm mean pore size

NOTE: In all cases, **Step 3** should run for at least 60 minutes, but it is given a longer time in case you are delayed in returning. It is acceptable for that step to run longer than 60 minutes, since the solidification process will be complete by that point.

7. After confirming the program, press the two middle keys on the Wizard together to end the editing step. Select the ***Save*** option from the menu displayed after ending the editing step. The Wizard screen should return to the original screen seen at start-up.

8. Turn off the ***Freeze*** and ***Heat*** buttons, turn the ***Auto*** button on, and press the ***Start*** key. The program should start running. Leave the program to run for the specified length of time.

9. At the end of the 60 minute annealing period, cancel the program. Press the inner two buttons on the wizard controller together, and then when prompted press the outer two keys. Turn off the ***Auto*** switch, then turn on the ***Freeze*** and ***Heat*** switches and set the ***SV*** to the appropriate freezing temperature (-10, -20, -30, or –40°C).

10. Turn on the ***Vacuum*** switch. Make sure the seal on the condenser and main chamber doors is tight and put pressure on the door to the main chamber until a vacuum pressure registers on the Wizard control screen (typically ~1900 mTorr).

11. When the vacuum pressure reaches below 300 mTorr, raise the temperature in the ***SV*** display to 0°C. Allow the freeze dryer to run for 17 hours at 0°C and a pressure <300 mTorr.

12. After 17 hours, raise the value of the ***SV*** control to 20°C. Wait for the chamber temperature to equilibrate to 20°C (temperature displayed in the ***PV*** display). Turn off the ***Vacuum*** switch and turn on the ***Chamber Release*** switch. Wait for the pressure to equilibrate to atmospheric pressure. Remove the pan from the main chamber.

13. Turn off the freeze dryer:
- » Turn off the ***Chamber Release*** switch
- » Turn off the ***Freeze*** and ***Heat*** switches
- » Turn off the ***Condenser*** Switch
- » Turn off the ***Power*** Switch
- » Open the condenser door, unplug the condenser drain line allow condense to drain.

14. Remove the CG scaffold from the pan with gloved hands. Place the scaffold into an aluminum foil packet and store it in a dessicator.

15. Wash the stainless steel pan with ethanol or 0.05 M acetic acid and wipe down with Kim-Wipes to remove any portion of the scaffold that may have torn during removal. Return the pan to storage.

16. Make a notation on the run sheet attached to the front of the freeze dryer in order to keep track of the total number of runs between oil changes. When a row is completely checked off (8 freeze dryer runs), change the oil.

C.3. Collagen-GAG Scaffold Fabrication: Constant Cooling Lyophilization Protocol – Short Version

REFERENCE: (O'Brien, Harley, et al., 2004; O'Brien, Harley, et al., 2005)

SUPPLIES

- § Type I collagen-glycosaminoglycan (CG) suspension (67.25 ml/sheet)
- § 5" x 5", 18 gauge 304 stainless steel pan (VirTis Inc., Gardiner, NY)
- § 0.05 M acetic acid

EQUIPMENT

- § Genesis freeze dryer (VirTis)

PROCEDURE

1. Confirm all parts of the freeze dryer are operational. Turn on the freeze dryer and condenser, set main chamber temperature to 20°C.

2. Degas the CG suspension in a vacuum flask (Pressure: ~50 mTorr). Pipet 67.25 ml of the CG suspension into the pan. Remove any air bubbles introduced into the pan using a 200 µl pipette tip. Place the pan into the freeze dryer.

3. Freeze the CG suspension using a ramping protocol to produce uniform CG scaffolds:
   - » Maintain freeze dryer chamber temperature at 5°C for 5 minutes
   - » Ramp the chamber temperature from 20°C to the final freezing temperature (T_f = -10, -20, -30, -40°C) at a rate of 0.9°C/min.
   - » Maintain the chamber temperature at the final freezing temperature for 60 minutes to allow solidification to complete.

4. Pull a vacuum to start the sublimation process. When the vacuum pressure in the main chamber reaches below 300 mTorr, raise the temperature of the chamber to 0°C. Allow the freeze dryer to run for 17 hours at a temperature of 0°C and a pressure <300 mTorr.

5. After 17 hours, raise the main chamber temperature to 20°C. Wait for the chamber temperature to equilibrate to 20°C. Release the vacuum pressure and remove the scaffold from the freeze dryer.

6. Remove the CG scaffold from the pan with gloved hands. Place the scaffold into an aluminum foil packet and store in a dessicator. Clean pans with 0.05 M acetic acid or ethanol and return them to storage.

7. Make a notation on the run sheet attached to the front of the freeze dryer in order to keep track of the total number of runs between oil changes. When a row is completely checked off (8 freeze dryer runs), change the oil.

C.4. Dehydrothermal Crosslinking Protocol

REFERENCE: (Yannas and Tobolsky, 1967; Yannas, Lee, et al., 1989; Harley, Spilker, et al., 2004)

EQUIPMENT

§ Isotemp vacuum oven (Model 201, Fisher Scientific, Hanover Park, IL)

PROCEDURE

1. Place the collagen-GAG scaffold into an aluminum foil packet. Leave the packet open at the top.

2. Select the appropriate processing conditions. The following processing conditions are those that are typically utilized:

DHT Identifier	Crosslinking Temperature	Crosslinking Time
DHT90/24	90°C	24 hours
DHT105/24 – Lab Standard	105°C	24 hours
DHT120/24	120°C	24 hours
DHt120/48	120°C	48 hours

Table C.5. Typical dehydrothermal crosslinking conditions used on CG scaffolds.

DHT105/24 is the accepted laboratory standard crosslinking technique and is the default crosslinking applied to collagen-GAG scaffolds unless otherwise noted.

3. Place the packet into vacuum oven (Isotemp Model 201, Fisher Scientific) maintained at the desired temperature. Open the "*Vacuum*" knob (turn the knob counterclockwise) and close the "*Purge*" knob (turn the knob clockwise).

4. Turn on the vacuum pump. Wait until the vacuum has been obtained (nearly full scale on the vacuum oven dial).

5. At the end of the processing period, turn off the vacuum and vent the chamber by closing the "Vacuum" knob (clockwise) and opening the "Purge" knob (counterclockwise). Once the vacuum has completely vented, open the vacuum oven door and immediately seal the aluminum foil bag(s). The scaffold is now crosslinked and considered sterile; to maintain sterility, handle the scaffold from this point on using aseptic techniques.

6. Store the scaffold in a dessicator. Crosslinked scaffolds can remain indefinitely in a dessicator prior to use.

C.5. 1-Ethyl-3-(3-Dimethylaminopropyl)Carbodiimide (EDAC) Crosslinking Protocol

REFERENCE: (Olde Damink, Dijkstra, et al., 1996; Lee, Grodzinsky, et al., 2001; Vickers and Spector, 2005; Vickers, Squitieri, et al., 2006)

SUPPLIES

- § 1-ethyl-3-(3-dimethylaminopropyl)carbodiimide (EDAC, Cat. No. E-7750, Sigma-Aldrich Chemical Co., St. Louis, MO); store in a dessicator at -20°C.
- § N-hydroxysuccinimide (NHS, Cat. No. H-7377, Sigma-Aldrich); store in a dessicator at room temperature.
- § Polystyrene cell culture 6-well plate (BD Falcon Multiwell Flat-Bottom Plates, Cat. No. 62406-161, VWR Scientific, Inc., Bridgeport, NJ)
- § Sterile Phosphate Buffered Saline (PBS, Cat. No. 20012-043, Invitrogen, Inc., Carlsbad, CA)

EQUIPMENT

- § Analytical balance (Model No. CP124S, Sartorius AG, Goettingen, Germany)
- § 5, 6, or 8 mm dermal biopsy punch (Miltex, Cat. No. 52441, 52442, 52443, Moore Medical LLC, New Britain, CT)

PROCEDURE

1. Cut the scaffold samples to be crosslinked using a 5, 6, or 8 mm dermal biopsy punch (Miltex) or using a razor blade.

2. Weigh the scaffold samples to determine the average mass of each scaffold sample to be crosslinked ($M_{scaffold}$). To maintain the sterility of the scaffold samples to be used, weigh a series of additional samples that you can remove from the sterile environment for weighing and then discard.

3. For crosslinking scaffold disks, 1 ml of crosslinking solution volume will be required for each disk.

4. Determine the concentrations of EDAC and NHS to be used in the crosslinking solution. This protocol was designed to determine the molar ratio of EDAC:NHS:Carboxylic Acid (where the carboxylic acid groups are on the CG scaffold) based off of the mass of the scaffold samples, the assumption that the scaffolds are entirely composed of collagen, and the observed 1.2 mmol of carboxylic acid (COOH) groups per gram of collagen (Olde Damink, Dijkstra, et al., 1996).

Typical EDAC:NHS:COOH concentrations used to crosslink CG scaffolds are 1:1:5, 5:2:5, and 5:2:1 (primary crosslinking density).

The mass of EDAC (M_{EDAC}) and NHS (M_{NHS}) required for a 5:2:1 EDAC:NHS:COOH solution are calculated here (**Eq. C.1, Eq. C.2**) as an example:

Equation C.1. $$M_{EDAC} = (\#\,samples) \cdot M_{scaffold} \cdot \left(0.0012 \frac{mol_{COOH}}{gm_{collagen}}\right) \cdot \left(\frac{5mol_{EDAC}}{1mol_{COOH}}\right) \cdot \left(\frac{191.7gm_{EDAC}}{1mol_{EDAC}}\right)$$

Equation C.2. $$M_{NHS} = (\#\,samples) \cdot M_{scaffold} \cdot \left(0.0012 \frac{mol_{COOH}}{gm_{collagen}}\right) \cdot \left(\frac{2mol_{NHS}}{1mol_{COOH}}\right) \cdot \left(\frac{116.0gm_{NHS}}{1mol_{NHS}}\right)$$

5. Mix the EDAC and NHS in a half volume (0.5 ml/disk) of sterile PBS (Invitrogen), making a 2X EDAC/NHS solution.

6. Hydrate the scaffolds in a 6 well tissue culture plate (VWR) in the sterile tissue culture hood. Place 5 to 6 scaffold disks in each well and hydrate in a half volume (0.5 ml/disk) of sterile PBS (Invitrogen). Allow the scaffolds to become initially hydrated (~15 minutes)

7. Pipette the half volume of the EDAC/NHS solution (the 2x EDAC/NHS solution in PBS made in step 5) into each well and mix thoroughly.

8. Allow crosslinking to take place for 30 minutes.

9. Remove the EDAC/NHS solution with a pipette and rinse twice with sterile PBS for an additional thirty minutes. Transfer the crosslinked scaffolds to a sealed, sterile container containing sterile PBS for storage.

10. Do not allow the scaffolds to dehydrate once they have been hydrated as this will lead to complete pore collapse

C.6. Type I Collagen-GAG Tubular Scaffold Fabrication Protocol: Spinning Method

REFERENCE: (Harley, Hastings, et al., 2006)

SUPPLIES

- § Type I collagen-GAG suspension
- § Copper mold (**Figure C.1**)
- § PVC tubing, 5 cm length (O.D.: 5/16", I.D.: 3/16) (Cat. No. 60985-520, VWR Scientific, Inc., Bridgeport, NJ)
- § Liquid nitrogen (Airgas, Inc., North Weymouth, MA)

EQUIPMENT

- § Genesis freeze dryer (VirTis, Inc., Gardiner, NY)
- § Dremel high-speed rotary tool (Robert Bosch Tool Corp, Mt. Prospect, IL)

PROCEDURE

1. Degas the CG suspension in vacuum flask (Pressure: ~50 mTorr).

2. Turn on the freeze dryer (Genesis, VirTis). Turn on the condenser and set the chamber temperature to -40°C. Allow the chamber to reach -40°C before continuing.

3. Insert one end of the PVC tube into the threaded bottom cap of the copper mold. Pipet the CG suspension into the PVC tubing. Insert the PVC tube into copper mold and screw the cap shut (**Figure C.1**).

4. Attach the mold to a vertically held Dremel tool (Robert Bosch Tool Corp.). Spin the copper mold using the Dremel tool for a specified length of time (T_s) at a specified rpm setting (R).

5. Insert the spinning mold into a liquid nitrogen bath while maintaining its rotational velocity. Freeze the CG suspension while spinning for a specified freezing time (T_f).

6. Remove the mold from the liquid nitrogen bath and stop the spinning. Quickly remove the PVC tube with the frozen collagen-GAG suspension from the copper jacket and place the PVC tube-frozen CG suspension construct into the freeze dryer.

7. Allow the copper mold to warm up (~15 minutes). Repeat steps 3 to 6 to produce more tubular scaffolds, placing each into the freeze dryer main chamber immediately after freezing to prevent them from melting prior to sublimation.

8. Pull a vacuum in the freeze dryer chamber to start sublimation. When the vacuum pressure in the chamber reaches below 300 mTorr, raise the chamber temperature to 0°C. Allow the freeze dryer to run for 17 hours at a temperature of 0°C and a pressure of <300 mTorr.

9. After 17 hours, raise the chamber temperature to 20°C. Wait for the chamber temperature to equilibrate to 20°C. Release the vacuum pressure and remove the PVC tube from the freeze dryer.

10. Remove the tubular CG scaffold from the PVC tube by slicing the PVC tube with a #15 scalpel or a razor blade along its length. Place the scaffold into an aluminum foil packet and store in a dessicator.

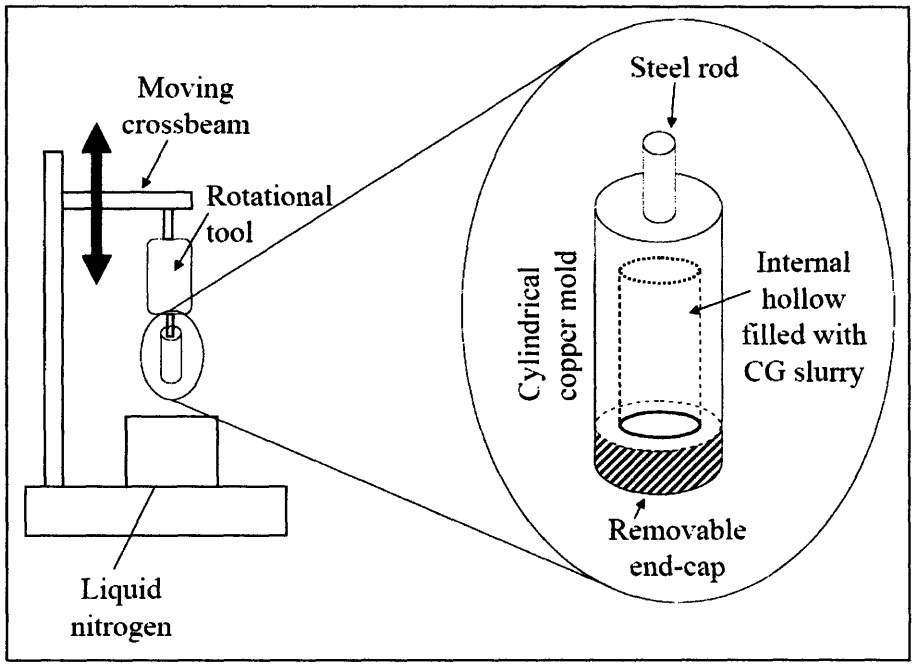

Figure C.1. Schematic of the spinning apparatus used to fabricate tubular CG scaffolds.

C.7. CG Scaffold Glycolmethacrylate Embedding Protocol

REFERENCE: (Freyman, 2001; O'Brien, Harley, et al., 2004; O'Brien, Harley, et al., 2005)

SUPPLIES

- § Plastic embedding mold (Cat. No. 16643A, Polysciences, Inc., Warrington, PA)
- § JB-4 plastic block holders (Cat. No. 15899-50, Polysciences)
- § 10% Neutral buffered formalin (Cat. No. 08379-3.75, Polysciences):
  - 900 ml dH_2O
  - 100 ml 38% formaldehyde
  - 4.0 g monobasic sodium phosphate NaH_2PO_4
  - 8.95 g dibasic sodium phosphate Na_2HPO_4
- § JB-4 A embedding solution:
  - 100 ml JB-4 A monomer solution (Cat. No. 0226A-800, Polysciences)
  - 0.9 g JB-4 A catalyst, (Benzoyl Peroxide, plasticized, Cat. No. 02618-12, Polysciences)
- § JB-4 B embedding solution (Cat. No. 0226B-30, Polysciences)

EQUIPMENT

- § Chemical Fume Hood

PROCEDURE

1. Cut samples from the scaffold for analysis. For analysis of CG scaffold sheets, remove samples from five locations equidistantly spaced through the sheet; for analysis of the longitudinal plane through the scaffold cut 10 x 10 mm square sections, and for analysis of the transverse plane cut 10 x 5 mm rectangular sections.

2. Fix the samples in 10% neutral buffered formalin for 24 – 48 hrs at room temperature

3. Dehydrate the samples in increasing concentrations of ethanol in water as follows (5 min. in each bath): 0% (dH_2O), 50%, 70%, 80%, 95%, 95%, 100%, 100%, 100%

4. Infiltrate the samples with catalyzed JB-4 A solution (Polysciences) at 4°C for 24 h in the chemical fume hood in a sealed vacuum flask. Replace with fresh JB-4 A and place under vacuum for several hours. Hold at 4°C for an additional 24 h in a sealed vacuum flask. If air bubbles are present, repeat vacuum treatment. All infiltration steps should be performed in the fume hood.

5. Mix 25ml of the JB-4 A solution with 1ml of the JB-4 B solution (Polysciences) and pipet ~4 ml into each well of the plastic embedding mold (Polysciences).

6. Place each sample into a well. The JB-4 mixture will polymerize quickly (< 25 min.) so make sure the samples are placed in the proper orientation. The mixture will become progressively browner in color as polymerization proceeds.

7. After the JB-4 mixture becomes viscous enough that the samples do not float, place one plastic stub (Sample block holder, Polysciences) onto each well and place the plastic mold tray in a refrigerator (4°C). Wait overnight for the polymerization to complete.

8. Remove the embedded samples from the mold and store at 4°C until use.

C.8. Sectioning the Embedded CG Scaffold Samples Protocol; Aniline Blue Staining Protocol

REFERENCE: (O'Brien, Harley, et al., 2004; O'Brien, Harley, et al., 2005)

SUPPLIES

- § Aniline Blue
  - 2.5 gm aniline blue (Cat. No. AC40118-0250, Fisher Scientific, Hanover Park, IL)
  - 2 ml glacial acetic acid (Mallinckrodt Chemical Co., Paris, KY)
  - 100 ml distilled water
  - Filter before use
- § 1% Acetic Acid
  - 1 ml glacial acetic acid (Mallinckrodt Chemical Co.)
  - 99 ml distilled water
- § 95%, 100% ethanol
- § Cytoseal 60 (Cat. No. NC9472256, Fisher Scientific)

EQUIPMENT

- § Leica RM2165 microtome (Mannheim, Germany)

PROCEDURE

1. Serially section the embedded CG scaffold samples on a Leica RM2165 microtome (Mannheim, Germany) at a 5μm thickness. Mount each section on a glass microscope slide

2. Dip the slides in the Aniline Blue solution for 2 – 4 minutes.

3. Place the slides into a 1% acetic acid solution for 1 minute.

4. Dip each slide 5-10 times in 95% alcohol until most of background staining goes away.

5. Dip each slide 5-10 times 100% alcohol to complete the rinsing process.

6. Mount each sample with 4 drops of Cytoseal 60 (Fisher Scientific) and coverslip. Try to not introduce air bubbles when placing the coverslip onto the sample.

7. Dry the coverslipped samples laying flat in a chemical fume hood for 1 hour (arbitrary time). Continue to dry the coverslipped samples while laying flat for an additional 2 days on the bench top or in the chemical fume hood.

C.9. CG Scaffold Pore Size Analysis Protocol: Image Acquisition and Linear Intercept Analysis

REFERENCE: (Freyman, 2001; O'Brien, Harley, et al., 2004; O'Brien, Harley, et al., 2005)

EQUIPMENT

- § Inverted optical microscope (Nikon Optiphot, Japan)
- § CCD color video camera (Optronics Engineering, Inc., Goleta, GA)
- § Scion Image analysis software (Scion Corporation, www.scioncorp.com, Frederick, MD)

PROCEDURE

Image Acquisition

1. Visualize the embedded, sectioned, and stained scaffold samples using an optical microscope (Nikon Optiphot).

2. Acquire three digital images from each longitudinal section and two images from each of the smaller transverse section using a CCD color video camera (Optronics Engineering).

Image Editing

1. Open Scion Image. Open each scaffold image and prepare it for pore size analysis.

2. Under the *Options* menu, select "*Threshold.*" Change the threshold values until an optimal image of struts is visible. Clean up any remaining spots with the erase tool. The pore analysis macro will not count any artifact under 5 pixels across, so it is not necessary to remove every stray spot.

3. Under *Process* menu, select "*Make Binary*" under the "*Binary*" sub-menu. This will transform the thresholded image into a permanent binary image. Save the image as an edited *.TIF file.

Pore Analysis

1. Under the *Special* menu in Scion Image, select "*Load macros*", and open the "*pore characterization macros*" file.

2. Set the scale for the analysis using the "*Set Scale*" option in the *Analyze* menu. Under the *Analyze* menu, choose "*Options*" and select the number of significant digits to be displayed after the decimal point to be 5. The microscope scale was calibrated for the microscope-camera assembly in the Mechanical Behavior of Materials laboratory (Prof. Lorna Gibson), rm. 8-102:

Objective Magnification	Known Distance	No. of Pixels
4x	1 mm	325.43
10x	1 mm	838.305
40x	1 μm	2.52787
100x	1 μm	8.3842

Table C.6. Calibration scales for Scion Image for the camera/microscope assembly in 8-102.

3. Select an area of the image to be analyzed using the oval drawing tool. Try to get as much of the viable image enclosed within the curve.

4. Under the "*Special*" menu, run *Linear Intercept*. The distance between the pore walls along lines at various angles emanating from the center of the selected region will be calculated. Next, run the *Plot Intercepts* macro. This macro will transform the average distance between struts along each line into a best-fit ellipse and will calculate linear intercept coefficients C0, C1, and C2 for that ellipse.

5. Transfer CO, C1, and C2 data to an Excel spreadsheet for each scaffold sample. Calculate the minor (*a*) and major (*b*) axes of the best-fit ellipse describing the average CG scaffold pore as well as the aspect ratio using the following equations:

Equation C.3. $$a = \frac{1}{\sqrt{C_0 + \sqrt{C_1^2 + C_2^2}}}$$

Equation C.4. $$b = \sqrt{\frac{\sqrt{C_1^2 + C_2^2}}{C_0 \cdot \sqrt{C_1^2 + C_2^2} + C_2^2 - C_1^2}}$$

Equation C.5. $$AspectRatio = \frac{a}{b}$$

6. Calculate the mean pore diameter (*d*) from the major and minor axes of the best-fit ellipse (**Eq. C.6**). To account for the effects of pores that were not sectioned through their maximal cross-section but rather at an arbitrary angle, the ellipse major and minor axes were corrected by multiplying by 1.5 (Gibson and Ashby, 1997). The mean pore size was calculated from the average radius by multiplying by a factor of 2.

Equation C.6. $$d = 1.5 \cdot 2 \cdot \sqrt{\frac{a^2 + b^2}{2}}$$

Linear Intercept Macro Code:

```
macro 'Linear Intercept'
{This macro measures the linear intercept distance over a giver ROI at intervals of angle
"ThetaStep"}
var
  left,top,width,height,MinDim,nx,ny,i,j,k:integer;
              ThetaStep,NSteps,PI,x1,x2,y1,y2,dy,dx:real;
```

```
 Theta,valx,valy,plength,scale,AspectRatio:real;
  IntLength,LineSum,dummy:real;
 Intercepts:integer;
  switch,indicator:boolean;
  unit:string;
begin
  SetOptions('User1;User2');
  GetRoi(left,top,width,height);
  if width=0 then begin
    PutMessage('Selection required.');
    exit;
  end;
  if width<height then MinDim:=width
    else MinDim:=height;
  PI:=3.141592654;
  GetScale(scale,unit,AspectRatio);
  NSteps:=18;{GetNumber('Enter # steps between 0 and 90 deg.',3,0);}
  ThetaStep:=PI/(2*NSteps);

{block out next line when doing cumulative measurements}

  SetCounter(2*NSteps);
  SetUser1Label('Theta(rad)');
  SetUser2Label('Lx10^3');
  for j:=0 to 2*NSteps-1 do begin
    LineSum:=0;
    Intercepts:=0;
    x1:=left;
    y1:=top;
    Theta:=j*ThetaStep;
   nx:=10*sin(Theta)*width/height;
   ny:=10*abs(cos(Theta));
    for i:=0 to nx do begin
     if Theta=0 then begin
              x1:=left;
              x2:=x1+width;
     end else begin
              x1:=left+(width*i/(nx+1))+width/(2*(nx+1));
              x2:=x1+(height*cos(Theta)/sin(Theta));
            end;
     y2:=top+height;
     if x2>=left+width then begin
        x2:=left+width;
        y2:=y1+(x2-x1)*sin(Theta)/cos(Theta);
     end else if x2<left then begin
                  x2:=left;
```

```
                if Theta>PI/2 then y2:=y1+(x2-x1)*sin(Theta)/cos(Theta);
               end;
   {plength is the length of the line to be drawn in pixels}
   plength:=sqrt(sqr(x2-x1)+sqr((y2-y1)/AspectRatio));
   valx:=x1;
   valy:=y1;
  dx:=(x2-x1)/plength;
  dy:=(y2-y1)/plength;
  switch:=true;
  if plength>=MinDim then begin
  LineSum:=LineSum+(plength/scale);
   for k:=0 to plength do begin
       if GetPixel(x1+k*dx,y1+k*dy)>0
          then indicator:=true
          else indicator:=false;
       if (switch=true) and (indicator=true) then begin
          Intercepts:=Intercepts+1;
          switch:=false;
       end;
       if  (indicator=false) then switch:=true;
     end;
  end;
 end;
for i:=1 to ny do begin
   if Theta<=PI/2 then begin
          x1:=left;
          x2:=left+width
    end else begin
          x1:=left+width;
          x2:=left;
    end;
  y1:=top+height*i/(ny+1);
  y2:=y1+(width*sin(Theta)/abs(cos(Theta)));
   if y2>top+height then begin
     y2:=top+height;
     x2:=x1+((y2-y1)*cos(Theta)/sin(Theta));
   end;
   {plength is the length of the line to be drawn in pixels}
    plength:=sqrt(sqr(x2-x1)+sqr((y2-y1)/AspectRatio));
  valx:=x1;
  valy:=y1;
  dx:=(x2-x1)/plength;
  dy:=(y2-y1)/plength;
  switch:=true;
  if plength>=MinDim then begin
  LineSum:=LineSum+(plength/scale);
```

```
      for k:=0 to plength do begin
          if GetPixel(x1+k*dx,y1+k*dy)>0
             then indicator:=true
             else indicator:=false;
          if (switch=true) and (indicator=true) then begin
             Intercepts:=Intercepts+1;
             switch:=false;
          end;
          if (indicator=false) then switch:=true;
        end;
     end;
    end;{i}
   IntLength:=LineSum/Intercepts;
  dummy:=rUser2[j+1];
  rUser1[j+1]:=180*Theta/PI;

{to do cumulative measurements, type in 'dummy+ before Intlength in the next line}

  rUser2[j+1]:=IntLength*1000;
  end; {j}
  ShowResults;
end;

Macro 'Plot Intercepts'
{This macro plots the linear intercept distance as a function of angle
in cylindrical coordinates
It then finds the best-fit ellipse to a set of linear intercept distance vs. angle data
using multiple linear regression of the equation Y=C0+C1*X+C2*Z, where
Y=1/L^2 , where L is one half the linear intercept distance at Theta
X=cosine(2*Theta),  Z=sine(2*Theta)
C0=(Mii+Mjj)/2 , C1=(Mii-Mjj)/2 , C2=Mij.
The objective is to solve for M11, Mjj, and Mij
The best-fit ellipse it then plotted on top of the linear intercept measurements}

var
  left,top,width,height,X0,Y0,X1,Y1,i,n:integer;
  pscale,aspectRatio,dx1,dx2,dy1,dy2,maxdim:real;
  unit:string;
 sumX,sumY,sumZ,sumXZ,sumXY,sumYZ,sumZsqr,sumXsqr:real;
 C0,C1,C2,Mii,Mjj,Mij,Y,X,Z,PI,Theta1,Theta2,L1,L2:real;

begin
 PI:=3.141592654;
SaveState;
 SetForegroundColor(255);
 SetBackgroundColor(0);
```

```
width:=400;
height:=400;
maxdim:=0;
for i:=1 to rCount do begin
  if rUser2[i]>maxdim then maxdim:=rUser2[i];
end;
pscale:=.8*(width+height)/(2*maxdim);
SetNewSize(width,height);
MakeNewWindow('Linear Intercepts vs. Theta');
SetLineWidth(1);
X0:=(width/2);
Y0:=(height/2);
MakeLineROI(0,Y0,width,Y0);
Fill;
MakeLineROI(X0,0,X0,height);
Fill;
 for i:=1 to rCount do begin
  dx1:=pscale*0.5*rUser2[i]*cos(rUser1[i]*PI/180);
  dy1:=pscale*0.5*rUser2[i]*sin(rUser1[i]*PI/180);
  if i<rCount then begin
    dx2:=pscale*0.5*rUser2[i+1]*cos(rUser1[i+1]*PI/180);
    dy2:=pscale*0.5*rUser2[i+1]*sin(rUser1[i+1]*PI/180);
  end else begin
    dx2:=-pscale*0.5*rUser2[1]*cos(rUser1[1]*PI/180);
    dy2:=-pscale*0.5*rUser2[1]*sin(rUser1[1]*PI/180);
  end;
  MoveTo(X0+dx1,Y0+dy1);
  LineTo(X0+dx2,Y0+dy2);
  MoveTo(X0-dx1,Y0-dy1);
  LineTo(X0-dx2,Y0-dy2);
end;
n:=rCount;
sumX:=0;
sumY:=0;
sumZ:=0;
sumXY:=0;
sumYZ:=0;
sumXZ:=0;
sumZsqr:=0;
sumXsqr:=0;
for i:=1 to n do begin
  Y:=1/(sqr(rUser2[i]/2));
  X:=cos(2*PI*rUser1[i]/180);
  Z:=sin(2*PI*rUser1[i]/180);
  sumX:=sumX+X;
  sumY:=sumY+Y;
```

```
    sumZ:=sumZ+Z;
    sumXY:=sumXY+(X*Y);
    sumYZ:=sumYZ+(Y*Z);
    sumXZ:=sumXZ+(X*Z);
    sumZsqr:=sumZsqr+sqr(Z);
    sumXsqr:=sumXsqr+sqr(X);
  end;
  C1:=((sumXY*sumZsqr)-(sumXZ*sumYZ))/((sumXsqr*sumZsqr)-sqr(sumXZ));
  C2:=((sumYZ*sumXsqr)-(sumXY*sumXZ))/((sumXsqr*sumZsqr)-sqr(sumXZ));
  C0:=(sumY/n)-C1*(sumX/n)-C2*(sumZ/n);
NewTextWindow('Results');
writeln('C0 = ',C0);
writeln('C1 = ',C1);
writeln('C2 = ',C2);
  for i:=1 to rCount do begin
    Theta1:=rUser1[i]*PI/180;
    if i<rCount then Theta2:=rUser1[i+1]*PI/180
     else Theta2:=rUser1[1]*PI/180;
    L1:=1/sqrt(C0+C1*cos(2*Theta1)+C2*sin(2*Theta1));
    L2:=1/sqrt(C0+C1*cos(2*Theta2)+C2*sin(2*Theta2));
    dx1:=pscale*L1*cos(Theta1);
    dy1:=pscale*L1*sin(Theta1);
    if i<rCount then begin
      dx2:=pscale*L2*cos(Theta2);
      dy2:=pscale*L2*sin(Theta2);
     end else begin
      dx2:=-pscale*L2*cos(Theta2);
      dy2:=-pscale*L2*sin(Theta2);
    end;
    MoveTo(X0+dx1,Y0+dy1);
    LineTo(X0+dx2,Y0+dy2);
    MoveTo(X0-dx1,Y0-dy1);
    LineTo(X0-dx2,Y0-dy2);
  end;
end;
```

C.10. CG Scaffold Mechanical Characterization Protocol – Scaffold Mechanical Tester

EQUIPMENT

- § 0.25 N tension-compression load cell (Model No. GSO-25, Error: ± 0.125 mN, Transducer Techniques, Temecula, CA)
- § NanoTest600 Micro/Nanoindenter (MicroMaterials LLC, Wrexham, UK)

SUPPLIES

- § 5, 6, or 8 mm dermal biopsy punch (Miltex, Cat. No. 52441, 52442, or 52443, Moore Medical LLC, New Britain, CT)
- § 16, 18, or 20 mm diameter leather punch (Hollow Punch Set, Boehm, France)
- § Phosphate Buffered Saline (PBS, Cat. No. 20012-043, Invitrogen, Inc., Carlsbad, CA)

PROCEDURE

1. Mount the 0.25 N precision tension-compression load cell (GSO-25, Transducer Techniques, **Figure C.2**) via a custom bracket to the high-precision motor platform of the NanoTest600 Micro/Nanoindenter (MicroMaterials LLC, Wrexham, UK) (**Figure C.3 – Figure C.5**).

2. Fabricate a low-mass compression platten as well as an opposing sample holder from aluminum (Schematics: **Figure C.6 – Figure C.7**). Attach low-mass platen to the load cell.

3. For mechanical characterization of dry CG scaffolds, cut cylindrical disks from the scaffold sheet using a 5, 6, or 8 mm diameter dermal biopsy punch (Miltex).

4. For mechanical characterization of hydrated CG scaffolds cut cylindrical disks from the scaffold sheet using a 16, 18, or 20 mm diameter leather punch (Boehm) whose edges have been sharpened using a metal file. Hydrate the scaffold samples for 12 hours in Phosphate Buffered Saline (PBS, Invitrogen) in order to allow the scaffolds to reach a steady state level of hydration (Harley, 2002).

5. Measure the dimensions of each scaffold sample being tested in order to calculate stress and strain from the load-displacement data.

6. Using the Mico/Nanoindenter motor control software, move the platform (as well as the attached load cell and compression platen) at a defined strain rate (0.1% stain/sec)

7. Acquire load cell data using a custom VI built in LabVIEW (National Instruments, Austin, TX) sampling at a frequency of 5 Hz (**Figure C..8 – Figure C.9**); both load-hold and load-unload cycles were tested. Displacement information was calculated from the known starting position, the defined strain rate, and the measured test time.

8. Correct the displacement values for the defined load cell cantilever deformation under load.

9. Calculate stress and strain from the acquired load-displacement data and the measured scaffold sample dimensions.

10. Determine E^* and $\Delta\sigma/\Delta\varepsilon$ from the linear regions of the linear elastic and collapse plateau regimes. Calculate σ_{el}^* and ε_{el}^* from the intersection of the linear regressions of E^* and $\Delta\sigma/\Delta\varepsilon$.

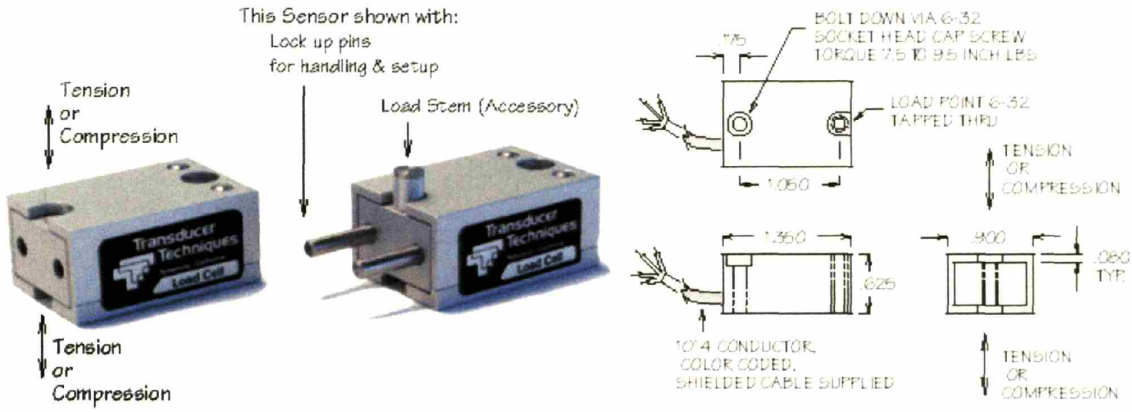

Figure C.2. Image (left) and schematic (right) of the 25 gm load cell used to perform unconfined compression test on the CG scaffold (Images from Transducer Techniques).

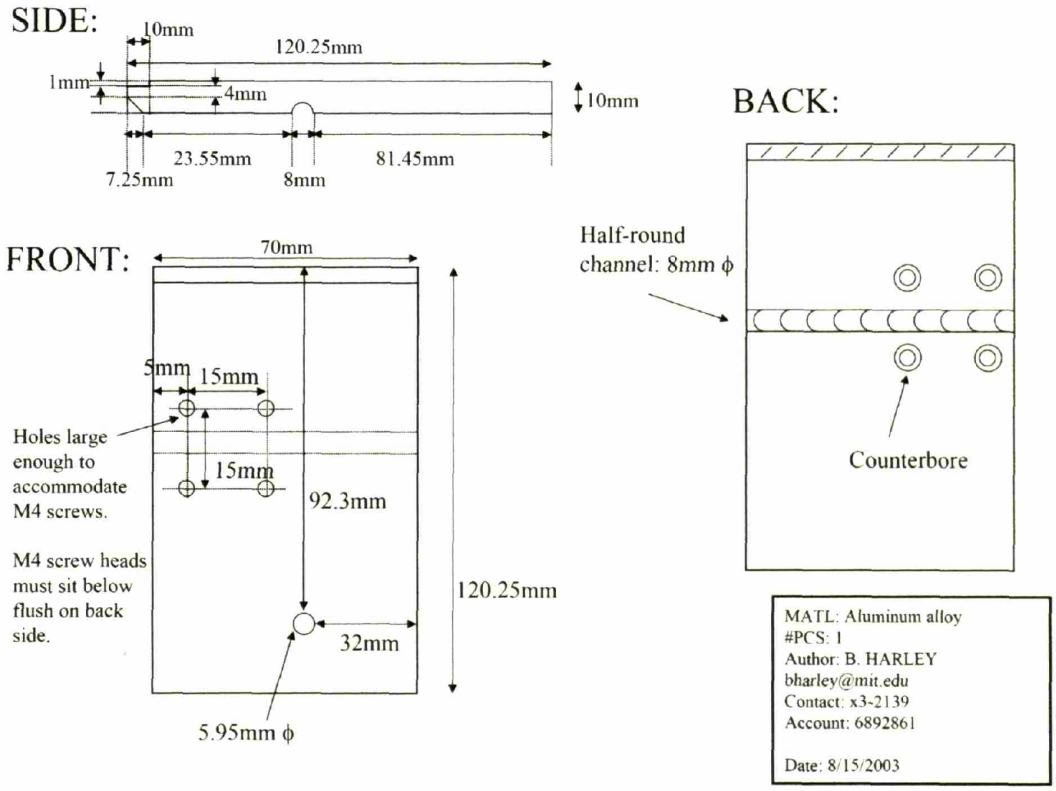

Figure C.3. Schematic of the aluminum bracket that attaches directly to the Micro/Nanoindenter motor stage.

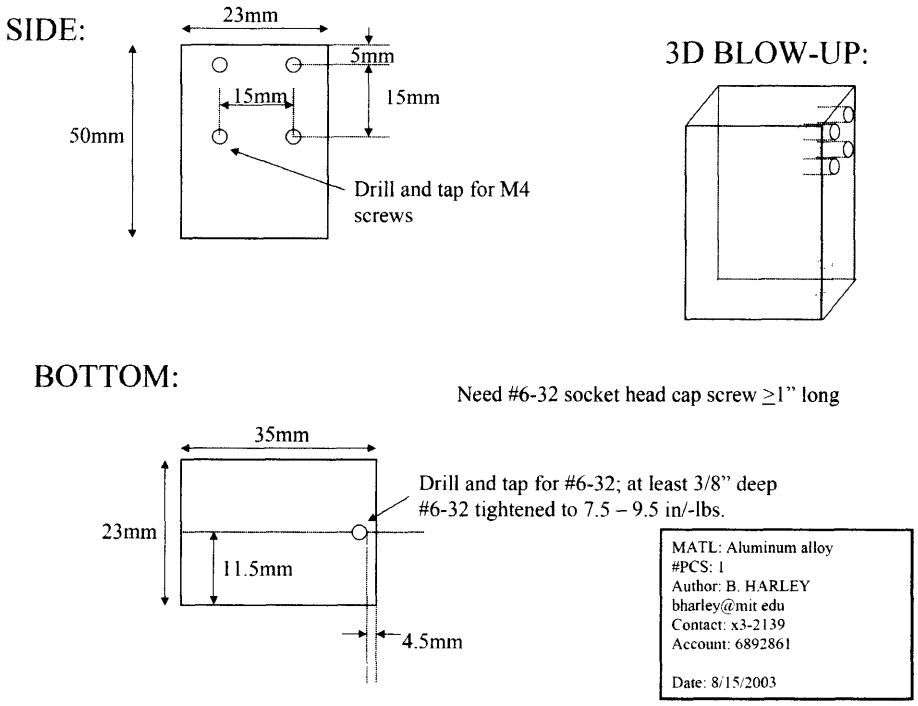

Figure C.4. Schematic of the intermediary bracket that attaches directly to the 25 gm load cell (Transducer Techniques, **Figure C.2**) and to the Micro-Nanoindenter motor stage through the bracket shown in **Figure C.3**.

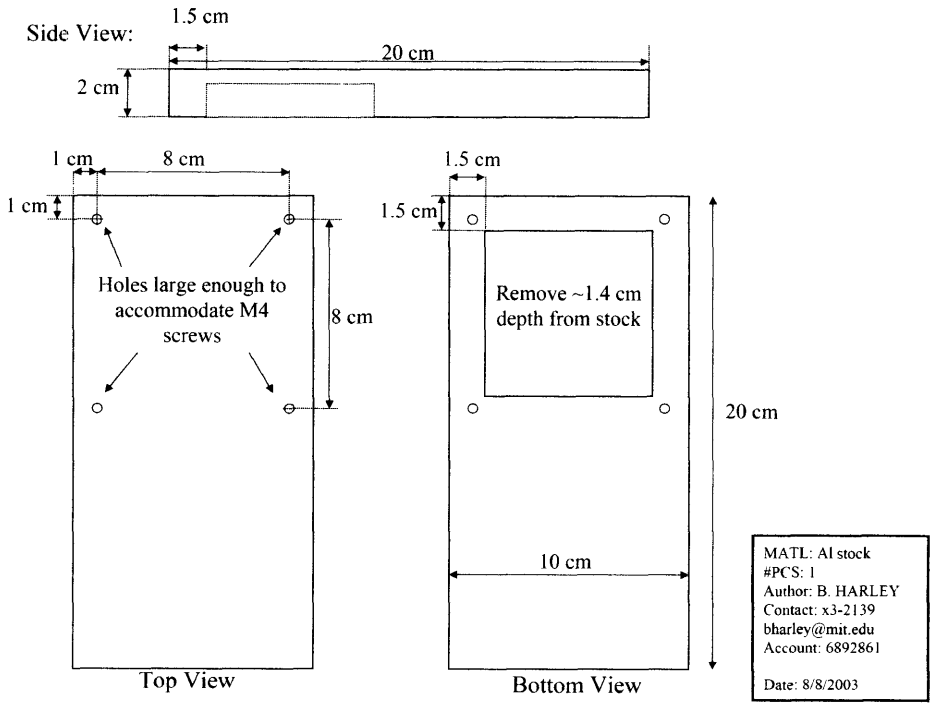

Figure C.5. Schematic of the aluminum base plate that attaches to the base of the Micro/Nanoindenter and provides a stable surface on which to perform mechanical tests.

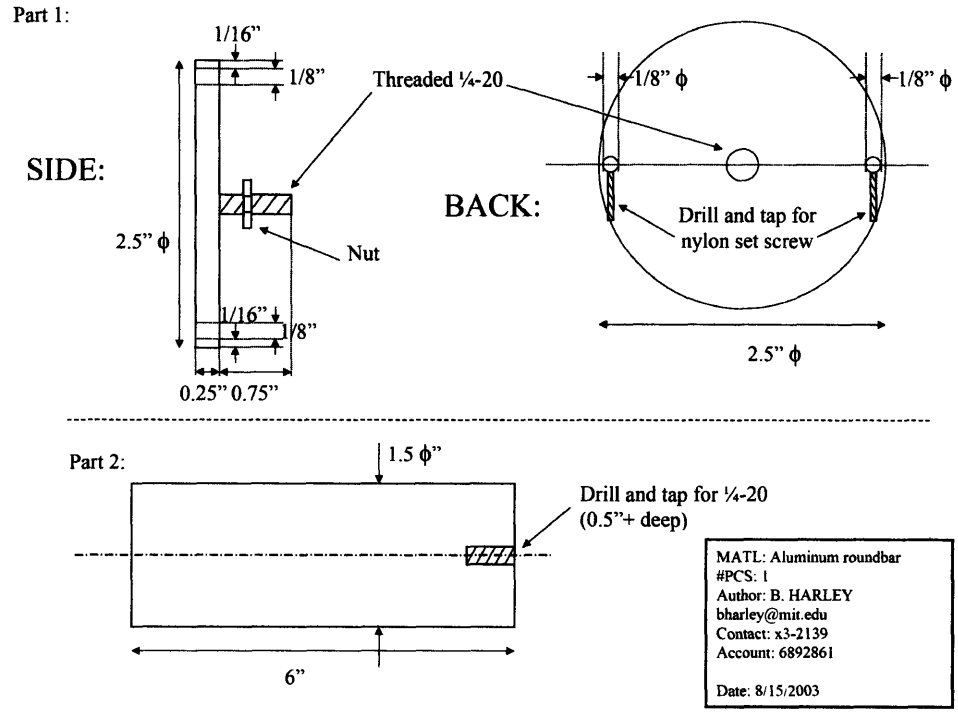

Figure C.6. Schematic of the aluminum sample holder that sits on the base plate (**Figure C.5**) and holds to CG scaffold disk for unconfined compression tests.

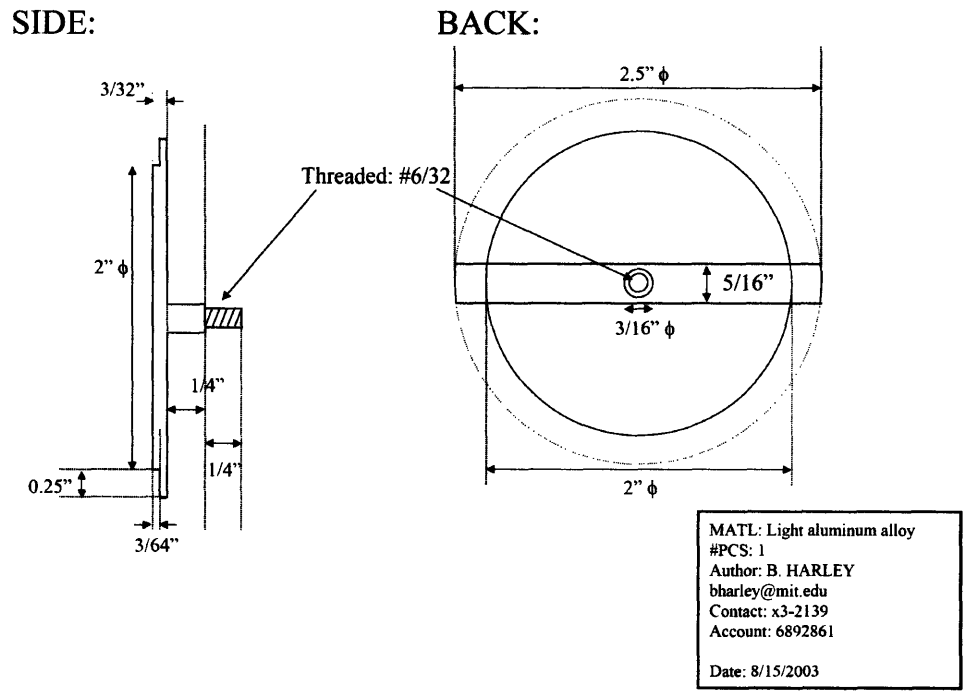

Figure C.7. Schematic of the low-mass compression platten that attaches to the 25 gm load cell and is used to perform unconfined compression tests.

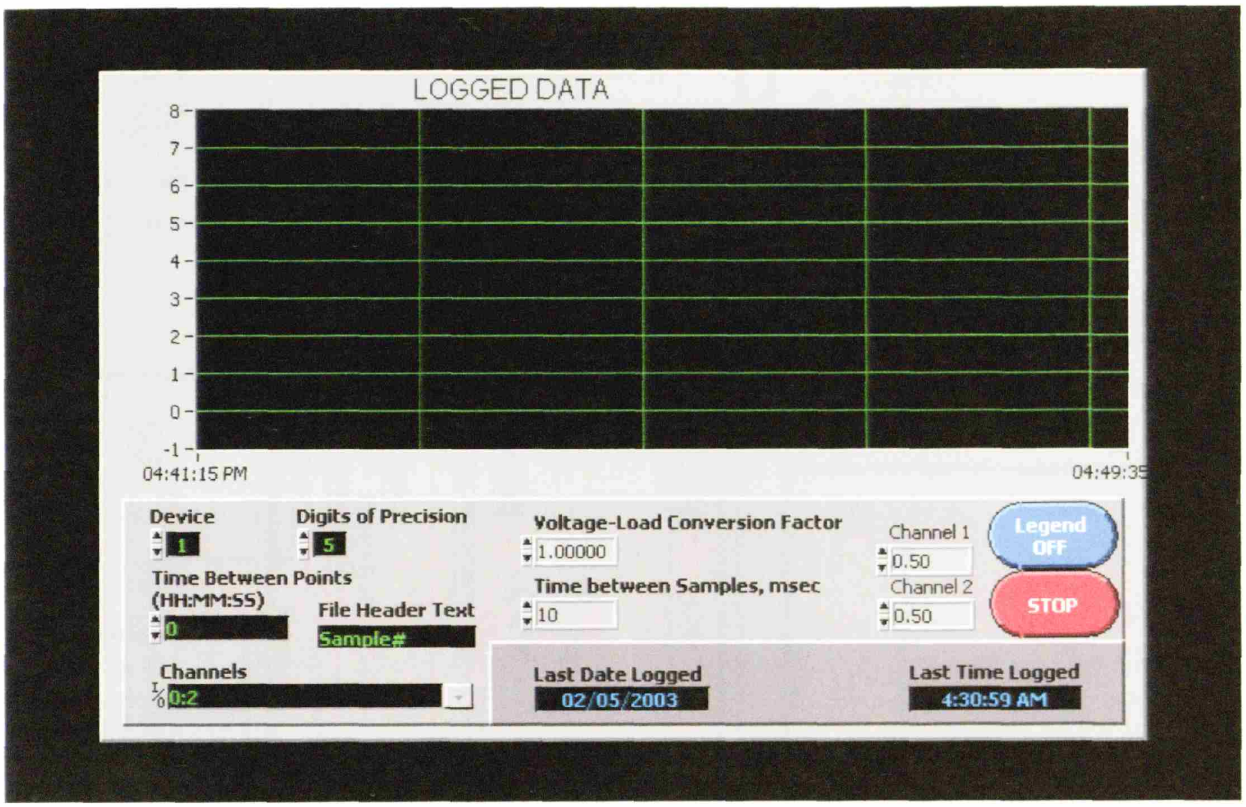

Figure C.8. Front panel of the custom LabVIEW VI used to acquire load data during mechanical characterization of the CG scaffolds using the Micro/Nanoindenter motor stage.

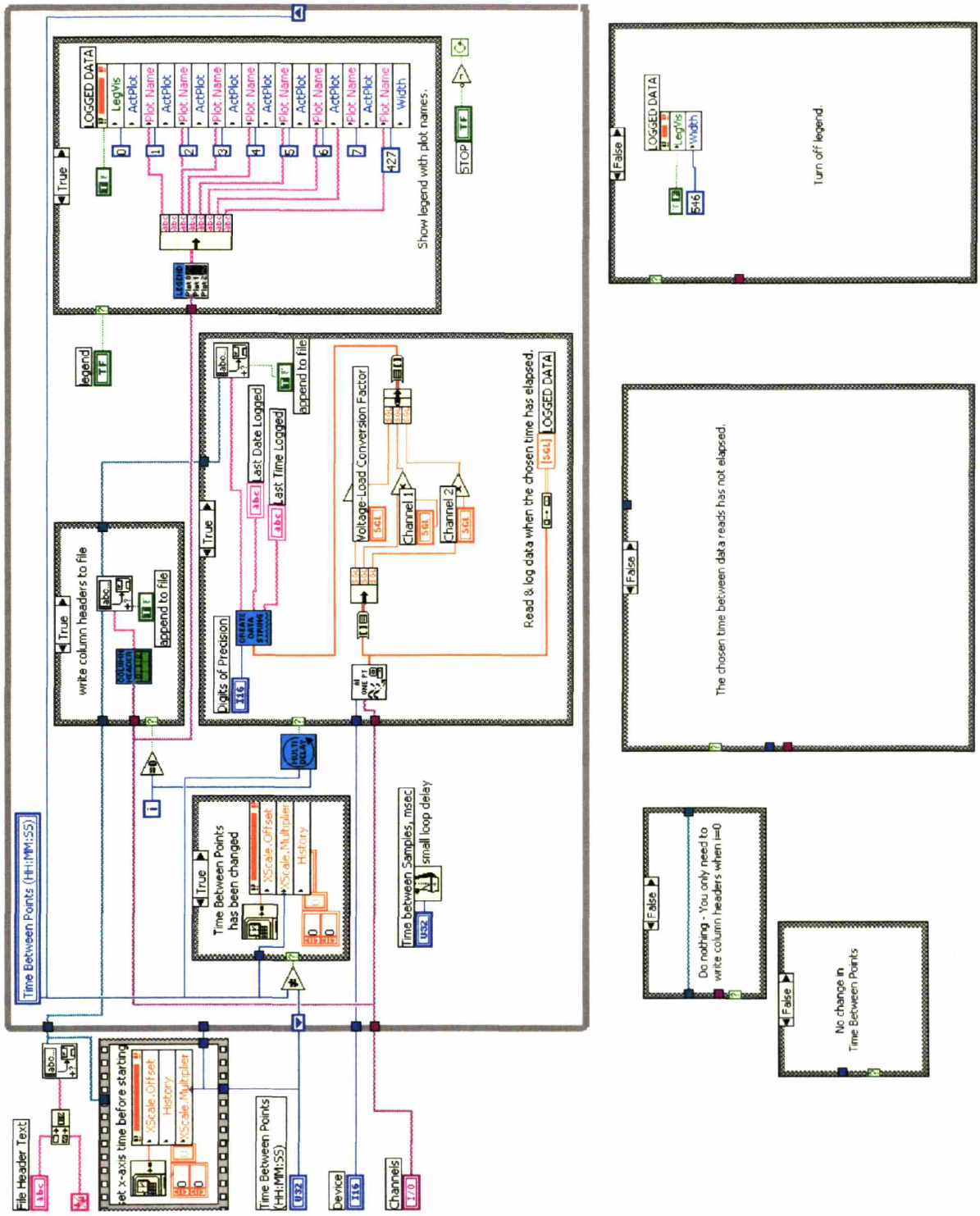

Figure C.9. Rear panel of the custom LabVIEW VI used to acquire load data during mechanical characterization of the CG scaffolds using the Micro/Nanoindenter motor stage.

C.11. CG Scaffold Mechanical Characterization Protocol – Zwick Mechanical Tester

EQUIPMENT

- § Zwick/Roell Mechanical Tester (Model No. Z2.5/TN1S, Zwick GmbH & Co., Ulm, Germany)
- § 20 N load cell (Part No. BTC-LC0020N.P01, Zwick)
- § Video Extensometer software (Correlated Solutions, Inc., West Columbia, SC)
- § High-speed, digital CCD Camera (Retiga 1300, QImaging Corp., Canada)
- § 200 mm lens (Nikon, Japan)

SUPPLIES

- § 6 or 8 mm dermal biopsy punch (Miltex, Cat. No. 52442 or 52443, Moore Medical LLC, New Britain, CT)
- § Phosphate Buffered Saline (PBS, Cat. No. 20012-043, Invitrogen, Inc., Carlsbad, CA)

PROCEDURE

1. Attach the 20 N load cell (Zwick Part No. BTC-LC0020N.P01) to the mechanical tester (Zwick Model No. Z2.5/TN1S). Confirm the connection between the load cell and the testXpert (Zwick) test environment and data acquisition software package.

2. Using the integrated testXpert software package, define the mechanical characterization environment. Save the test environment as a *.ZPV file.

Test type: *Unconfined compression*
Sample geometry: *Cylindrical disk, 6 or 8 mm diameter*
Strain range: *0 – 95% strain*
Loading rate: *0.1% strain/sec, strain controlled*
Sampling frequency: *2 Hz*
Hold time at max strain: *30 seconds*
Unloading rate: *1.0% strain/sec*

3. For mechanical characterization of dry or hydrated CG scaffolds, cut cylindrical disks from the scaffold sheet using a 6 or 8 mm diameter dermal biopsy punch (Miltex). Hydrate the scaffold samples, if necessary, for 12 hours in Phosphate Buffered Saline (PBS, Invitrogen).

4. Measure the dimensions of each scaffold sample being tested in order to calculate stress and strain from the load-displacement data.

5. in order to measure the lateral strains of the scaffold sample under unconfined compression and calculate the Poisson's ratio of the scaffold, set up the high-speed, digital CCD Camera (Retiga 1300, QImaging Corp.) with a 200 mm lens (Nikon) linked to a laptop running the video extensometer software (Correlated Solutions); link the data acquisition laptop to the Zwick mechanical tester so that a lateral strain data point is acquired every time an unconfined compression data point is taken.

6. Using the testXpert control software, perform sequential mechanical tests on a series of CG scaffold samples. Save the data file for each series of tested scaffolds as a *.ZSE file.

7. Export the acquired ***Standard Force*** (N), ***Standard Travel*** (mm), and ***Test Time*** (s) data from the testXpert software package to an Excel spreadsheet. Export the lateral strain data from the video extensometer package to the same spreadsheet.

8. Calculate stress and strain from the acquired force, travel, and time data and the measured scaffold dimensions.

9. Determine E^* and $\Delta\sigma/\Delta\varepsilon$ from the linear regions of the linear elastic and collapse plateau regimes. Calculate σ_{el}^* and ε_{el}^* from the intersection of the linear regressions of E^* and $\Delta\sigma/\Delta\varepsilon$.

10. Determine the Poisson's ratio from the measured vertical and lateral strains in the linear elastic and collapse plateau regimes.

APPENDIX D. *Cell Culture Protocols*

D.1. Incubator Disinfection Protocol

SUPPLIES

- § Steris Staphene spray (Cat. No. 14-415-15, Fisher Scientific, Hanover Park, IL)
- § 70% ethanol

PROCEDURE

1. Shut off the CO_2 tanks and turn off the incubator.

2. Prepare the sterile hood by covering the inside with bench-coat.

3. Cover the chemical fume hood with fresh bench-coat.

4. Disassemble all removable parts from the incubator chamber. Spray all pieces from the incubator inside the chemical fume hood with Staphene (Fisher Scientific). Spray the inside of the incubator with Staphene. Let stand for 15 minutes with the incubator door cracked open ~2 inches.

5. Spray the inside of the incubator with 70% ethanol. Wipe off the excess Staphene with paper towels.

6. Spray all internal pieces of the incubator in the chemical fume hood with 70% ethanol and wipe off the excess Staphene. Spray each part generously with ethanol again and place into the sterile hood to dry: do not wipe anything down. Allow all parts to air dry for 15 – 30 minutes.

7. Spray the inside of the incubator with 70% ethanol and allow all parts to dry for 15 – 30 minutes; do not wipe anything down.

8. Reassemble all internal pieces of the incubator, taking care to move each piece from the sterile hood to the incubator as quickly as possible.

9. Spray the inside of incubator again with 70% ethanol. Shut the door and allow all parts to dry; do not wipe anything down.

10. Turn on the incubator power and open the valves on the CO_2 tanks. Allow the incubator to ventilate with the CO_2 on for 24 hours before using again.

D.2. Complete MEM-α medium for NR6 fibroblasts

REFERENCES: (Chen, Gupta, et al., 1994; Chen, Xie, et al., 1994)
§ Latest recipe revision 01/2002 by L. Richardson

SUPPLIES

Component	Company	Catalog No.	Volume	Concentration
MEM-α	Gibco	11900	875 mL	---
FBS (heat inactivated)	Gibco	16140-071	75 mL	7.5%
L-Glutamine (100x)	Gibco	25030	10.0 mL	2 mM
Pen-Strep	Gibco	15140	10.0 mL	100 U/ml Pen 100 µg/mL Strep
Non-essential AA (100x)	Gibco	11140-050	10.0 mL	0.1 mM
Na-Pyruvate (100x)	Gibco	11360-070	10.0 mL	1 mM
*G418 (35 mg/ml in PBS)	Gibco	11811	10.0 mL	350 µg/mL

Table D.1. MEM-α medium recipe for the parental NR6 fibroblast cell line (without G418 in the medium) or for NR6 fibroblasts expressing WT EGFR (with G418 in the medium).

***NOTE:** The G418 (Geneticin) is the selection antibiotic for cells expressing the WT EGFR. For the parental cell line, omit G418 and make up with MEM-α (add only if using transfected receptor EGFR).

PROCEDURE

Complete Medium:
1. Make 1L MEM-α medium. Combine dH_2O, MEM-α packet, and 2.2 gm $NaHCO_3$ (see MEM-α medium packet).

2. pH the MEM-α medium to 0.1 – 0.3 below the desired final pH of the complete MEM-α medium using NaOH. The pH rises due to the sterile filtering step. Desired final pH range: 7.2 – 7.4.

3. Add the appropriate amounts of FBS, L-glutamine, Penicillin-Streptomycin, Non-essential Amino Acids, and Na-pyruvate as specified in **Table D.1**. Add no Geneticin, making up that volume with MEM-α medium.

4. Sterile filter the complete medium (0.2 µm filter), and store at 4°C.

Serum-Free Medium:
Omit the FBS and make up volume with MEM-α. Add BSA at a concentration of 1 g/L.

General Assay Medium:
Typically use 1% dialyzed FBS (Gibco catalog no. 26300) medium instead of serum-free medium in EGF-related experiments. The cells survive longer and growth factors < ~12,000 Da are dialyzed out. For this medium use 1.0 mL dFBS + 6.5 mL MEM-α in place of 7.5 mL FBS (for 100 mL modified solution). Also add BSA at a concentration of 1 g/L.

Freeze Medium:
60% MEM-α, 30% FBS, 10% DMSO (Use the slow freeze – quick thaw protocol).

D.3. NR6 Fibroblast Thawing Protocol

REFERENCES: (Chen, Gupta, et al., 1994; Chen, Xie, et al., 1994)

SUPPLIES

- § Complete MEM-α medium
- § T75 tissue culture flasks (BD Falcon Tissue Culture Flasks with Vented Cap, Cat. No. BD353136, VWR Scientific, Inc., Bridgeport, NJ)

EQUIPMENT

- § Tabletop centrifuge (Heraeus Labofuge 400, VWR Scientific)

PROCEDURE

1. Place complete MEM-α into the waterbath and warm to 37°C.

2. Remove 1 flask of frozen cells (2 x 10^6 cells/flask in 1 ml freezing medium) from liquid nitrogen storage or the -80°C freezer..

3. Transfer 5 ml of complete MEM-α medium to a 15 ml conical tube.

4. Place the vial containing the frozen cells into the waterbath and allow it to warm until the frozen cell/ medium mass initially starts to melt (you should see the frozen mass begin to glisten)

5. Pipette 1 ml of complete MEM-α medium from the 15 ml conical tube onto the semi-thawed frozen cell mass. Pipette up and down and place medium back into the conical tube.

6. Repeat until the entire 1 ml of frozen cells has been transferred into the 15 ml conical tube.

7. Place the 15 ml conical tube into the centrifuge (Heraeus). Centrifuge the cell solution at 1200 rpm for 5 minutes.

8. Aspirate off the medium supernatant and re-suspend the cell pellet in 6 ml of fresh, complete MEM-α medium.

9. Place 14 ml of complete MEM-α into two T75 flasks (VWR). Place 3 ml of the cell suspension into each flask and swirl gently to distribute the cells.

10. Place the flasks into the incubator. Check for confluence every 24 hours and feed cells every 48 hours.

D.4. NR6 FB Cell Feeding Protocol

REFERENCES: (Chen, Gupta, et al., 1994; Chen, Xie, et al., 1994)

SUPPLIES

§ Complete MEM-α medium

PROCEDURE

1. Warm complete MEM-α medium in a water bath at 37°C.

2. When the medium is warm, wipe the bottle dry with a paper towel and spray with 70% ethanol before placing it into the sterile hood.

3. Remove the old medium from each T75 flask, taking care not to scrape cells with pipette tip.

4. Add 17 ml of complete MEM-α medium into each T75 flask using a sterile pipette tip.

5. Return cells to incubator. Check for confluence every 24 hours and feed cells every 48 hours.

D.5. NR6 FB Cell Passaging Protocol

REFERENCES: (Chen, Gupta, et al., 1994; Chen, Xie, et al., 1994)

SUPPLIES

- § Complete MEM-α medium
- § Sterile Phosphate Buffered Saline (PBS, Cat. No. 20012-043, Invitrogen, Inc., Carlsbad, CA)
- § Trypsin-EDTA (Cat. No. 25300-062, Invitrogen)
- § Trypan Blue (Cat. No. AC18935-0250, Fisher Scientific, Hanover Park, IL)

EQUIPMENT

- § Hausser Phase Contrast Hemacytometer (Cat. No. 02-671-54, Fisher Scientific)
- § Inverted phase contrast microscope (Nikon, Japan)
- § Tabletop centrifuge (Heraeus Labofuge 400, VWR Scientific)

PROCEDURE

1. Warm complete MEM-α medium, sterile PBS (Invitrogen), and 4 ml Trypsin (Invitrogen) per T75 flask to be passaged in a water bath at 37°C.

2. When the medium, PBS, and Trypsin are warm, wipe them dry with paper towel and spray with 70% ethanol before placing in the sterile hood

3. Remove all old medium from each flask, taking care not to scrape the cells with the pipette tip.

4. Add 5 ml of PBS per flask and leave the PBS in the flask to rinse the cells for 30 seconds. Swirl gently to remove any excess medium from the cells.

5. Remove the PBS and add 4 ml of Trypsin per flask. Return the flasks to the incubator for 8 minutes to allow for the cells to detach from the tissue culture plastic (allow the cells to sit for 3 – 4 additional minutes in the incubator if they do not detached after 8 minutes).

6. Add 6 ml of complete medium to each flask to neutralize the Trypsin and to flush cells off of the tissue culture plastic.

7. Remove the Trypsin, additional medium, and cells from the flask and put into a conical tube. Centrifuge the cells at 1200 rpm for 5 minutes.

8. Aspirate off the medium supernatant and add a total of 1 ml of medium to all of the conical tubes, combining the cells into a single 1 ml aliquot.

9. Remove a 20 µl aliquot from the cell suspension.

10. Mix the 20 µl cell suspension aliquot with 20 µl of Trypan Blue (Fisher Scientific). Pipette several times to mix the stain and cell suspension

11. Place a cover slip on the hemacytometer (Fisher) and pipette 20 µl of the stain/cell suspension into the hemacytometer.

12. Cell counts are performed in as many of the nine separate regions of the hemacytometer as is feasible. Average number of cells per region is used to calculate the total cell population. For this calculation, the dilution factor is typically 2 (1:1 ratio of cell suspension to Trypan Blue).

Total Cell Population = (Mean Cells per Region) · Dilution · 10,000 · (Cell Suspension Volume)

13. Add 17 ml complete MEM-α medium to each new T75 flask to be seeded. Add the appropriate volume of the concentrated cell solution to place 5×10^5 cells into each flask.

14. Place the flask(s) into the incubator. Check for confluence every 24 hours and feed cells every 48 hours.

D.6. NR6 FB Cell Freezing Protocol

REFERENCES: (Chen, Gupta, et al., 1994; Chen, Xie, et al., 1994)

SUPPLIES

- § Cell freezing medium (Cat. No. 12648-010, Invitrogen, Inc., Carlsbad, CA)
- § Trypsin-EDTA (Cat. No. 25300-062, Invitrogen)
- § Trypan Blue (Cat. No. AC18935-0250, Fisher Scientific, Hanover Park, IL)
- § DMSO (Cat. No. D2650, Sigma-Aldrich Chemical Co., St. Louis, MO)
- § Fetal Bovine Serum (FBS, Cat. No. 16140-071, Gibco Life Sciences, Carlsbad, CA)

EQUIPMENT

- § Hausser Phase Contrast Hemacytometer (Cat. No. 02-671-54, Fisher Scientific, Hanover Park, IL)
- § Inverted phase contrast microscope (Nikon, Japan)
- § Tabletop centrifuge (Heraeus Labofuge 400, VWR Scientific, Inc., Bridgeport, NJ)

PROCEDURE

1. NR6 fibroblasts can be stored in liquid N_2 or in a -80°C freezer for extended periods of time. Perform the freezing procedure under sterile conditions and warm all solutions to 37°C prior to use to maintain cell viability.

2. Isolate the cell population to be frozen from ~90% confluent flasks using standard cell passaging procedures.

3. Count the cells using standard cell counting procedures defined in Section D.5.

4. Resuspend the cells in the cell freezing medium at a density of 2×10^6 cells/ml. For NR6 fibroblasts the appropriate freezing medium is 60% MEM-α, 30% FBS, and 10% DMSO.

5. Distribute 1 ml of the cells in the freezing medium into each cryovial. Ensure that the cryovials are sealed.

6. Place the cryovials into a Styrofoam container with walls ~15 mm thick and pack the container with cotton gauze. Seal the container with tape and place it into a liquid N_2 dewar.

7. Wait 4 hours for the cell suspension to freeze and then transfer the cryovials to a plastic box in the dewar racks in a liquid N_2 tank or into a -80°C freezer.

D.7. Preparing CMFDA Fluorescent Stain Stock

SUPPLIES

- § CMFDA Fluorescent Stain (Cat. No. C2925, M.W. 464.86 gm/mol, Molecular Probes, Inc., Carlsbad, CA)
- § DMSO (Cat. No. D2650, Sigma-Aldrich Chemical Co., St. Louis, MO)

PROCEDURE

1. Prepare a 10 μM stock of CMFDA (Molecular Probes) in DMSO (Sigma-Aldrich). Add 250 μl DMSO to the 1 mg vial of CMFDA.

2. Aliquot the 10 μM CMFDA stock into 10 μl volumes in individual vials.

3. Store the vials at -20°C until use.

D.8. Preparing Alexa Fluor Fluorescent Stain Stock

SUPPLIES

- § Alexa Fluor 633 Fluorescent Stain (Cat. No. A-20005, M.W. ~1200, gm/mol Molecular Probes, Inc., Carlsbad, CA)
- § DMSO (Cat. No. D2650, Sigma-Aldrich Chemical Co., St. Louis, MO)

PROCEDURE

1. Prepare a 2 µM stock of Alexa Fluor (Molecular Probes) in DMSO (Sigma Aldrich). Add 250 µl DMSO to the 1 mg vial of Alexa Fluor.

2. Aliquot the 2 µM Alexa Fluor stock into 10 µl volumes in individual vials.

3. Store the vials at -20°C until use.

D.9. Alexa Fluor Fluorescently Stained Collagen-GAG Scaffold for Confocal Microscopy

SUPPLIES

- § Alexa Fluor Fluorescent Stain (Molecular Probes Inc., Carlsbad, CA)
- § Sterile Phosphate Buffered Saline (PBS, Cat. No. 20012-043, Invitrogen, Inc., Carlsbad, CA)
- § Polystyrene cell culture 6-well plate (BD Falcon Multiwell Flat-Bottom Plates, Cat. No. 62406-161, VWR Scientific, Inc., Bridgeport, NJ)
- § 6 mm dermal biopsy punch (Miltex, Cat. No. 52442, Moore Medical LLC, New Britain, CT)

PROCEDURE
NOTE: All steps should be done in a sterile manner

1. Cut scaffolds to desired dimension with 6 mm dermal biopsy punch (Miltex).

2. Pre-wet the scaffolds in sterile, warmed (37°C) PBS (Invitrogen). Initially hydrate the scaffold by placing the CG scaffold punches into a standard 6-well plate (VWR), pan-side up. Slowly pipette sterile PBS around the edge of the scaffold disks, allowing capillary action to hydrate the scaffold. Once initial hydration has started, add sterile PBS to the well until the scaffolds are completely immersed. Place the scaffolds into the incubator for ~1 hour to allow hydration to continue.

3. Make a 1:2000 dilution of the 2 μM Alexa Fluor stain in PBS (Invitrogen). Briefly thaw the aliquoted 2 μM Alexa Fluor solution between your fingers and then mix with PBS.

4. Aspirate the PBS from the CG scaffolds. Add the Alexa Fluor:PBS dilution.

5. After 20 minutes, remove the PBS:Alexa Fluor dilution and wash the scaffold disks twice in PBS.

D.10. Seeding CMFDA Fluorescently Stained Cells into Collagen-GAG Scaffolds for Confocal Microscopy

SUPPLIES

- § CMFDA Fluorescent Stain (Cat. No. C2925, Molecular Probes, Inc., Carlsbad, CA)
- § Sterile Phosphate Buffered Saline (PBS, Cat. No. 20012-043, Invitrogen, Inc., Carlsbad, CA)
- § Trypsin-EDTA (Cat. No. 25300-062, Invitrogen)
- § Complete MEM-α cell culture medium
- § Polystyrene cell culture 6-well plate (BD Falcon Multiwell Flat-Bottom Plates, Cat. No. 62406-161, VWR Scientific, Inc., Bridgeport, NJ)
- § Ultra-low Attachment 6-well plate (Corning, Cat. No. 07-200-601 Fisher Scientific, Hanover Park, IL)
- § Sterile filter paper
- § 6 mm dermal biopsy punch (Miltex, Cat. No. 52442, Moore Medical LLC, New Britain, CT)
- § Glass bottom culture dish (Cat. No. P35G-1.5-14-C, MatTek, Corp., Ashland, MA)
- § Trypan Blue (Cat. No. AC18935-0250, Fisher Scientific)

EQUIPMENT

- § Hausser Phase Contrast Hemacytometer (Cat. No. 02-671-54, Fisher Scientific)
- § Inverted phase contrast microscope (Nikon, Japan)
- § Tabletop centrifuge (Heraeus Labofuge 400, VWR Scientific)

PROCEDURE

1. Cut the scaffold into cylindrical disks with the 6 mm dermal biopsy punch (Miltex).

2. Hydrate the scaffold in sterile, warmed (37°C) PBS (Invitrogen). Initially hydrate the scaffold by placing the scaffold disks into a standard 6-well plate (VWR), pan-side up. Slowly pipette the sterile PBS around the edge of the scaffold, allowing capillary action to hydrate the scaffold. Once initial hydration has started, add sterile PBS until the scaffolds are completely immersed. Place the scaffolds in the incubator for ~1 hour to allow hydration to continue.

3. After 20 minutes, start the fluorescent cell staining process in parallel. Thaw the 10 μM CMFDA aliquot (Section D.7) in your hand. Mix the CMFDA stain (10 μl) with complete culture medium (10 ml) at a 1:1000 dilution.

4. Remove the medium from the T75 culture flask (17ml) holding the NR6 fibroblasts to be used for this experiment via aspiration.

5. Add 10 ml of the CMFDA:MEM-α medium to the T75 flask. Place the flask back into the incubator for 20 minutes.

6. Aspirate the CMFDA:MEM-α medium. Add sterile PBS to wash for approximately 30 seconds. Aspirate the PBS and rewash with PBS.
7. Aspirate the PBS. Add 4ml of Trypsin-EDTA (Invitrogen) to the T75 flask and return to the incubator for 8 minutes.

8. Add 6 ml of the complete MEM-α medium to the Trypsin-EDTA in the T75 flask and pipette the entire mixture up and down to remove the cells from flask. Transfer the medium and cells into a 15 ml conical tube (VWR).

9. Centrifuge the 15 ml conical tube for 5 minutes at 1200 rpm.

10. Transfer the scaffolds to complete MEM-α medium for 10 minutes. Fill one well of the 6 well-plate with ~5 ml of complete medium heated to 37°C and place into the incubator for 10 minutes.

11. Aspirate off the supernatant from the 15 ml conical tube after centrifugation. Resuspend the cell pellet in 5 ml of sterile PBS to wash the cells. Remove a 20 µl aliquot to count cell number.

12. Centrifuge the 15 ml conical tube for an additional 5 minutes at 1200 rpm to repellet the cells.

13. Optional step (can be highly irregular). Briefly dry the scaffolds on sterile filter paper (allow enough time for liquid to be drawn out, but do not allow matrices to dry completely).

14. Transfer the scaffolds to an ultra low attachment 6-well plate (Corning), with each scaffold in its own well. Use a micro-pipette to remove as much excess medium from around the scaffold as possible.

15. Aspirate off the PBS supernatant from the 15 ml conical tube after centrifugation. Resuspend the cell pellet in fresh complete MEM-α medium at a 5×10^6 cell/ml concentration (5×10^4 cells per 10 µl)

16. Seed the cells into the scaffold via a micro-pipette. Pipette 10 µl of cell suspension onto one side of each scaffold. Place the seeded scaffold back into the incubator for 10 minutes.

17. After 10 minutes in the incubator, turn each scaffold disk over and pipette another 10 µl of cell solution onto the scaffold (total of 1×10^6 cells per scaffold disk).

18. Return the seeded scaffolds to the incubator for 1 - 2 hours.

19. Add enough complete MEM-α medium to just cover the scaffolds (~1.5 – 2.0 ml). If performing long term culture studies, add additional medium the following day to fill each well (~2.0 ml additional). Maintain in cell culture for the desired period.

20. Prior to confocal imaging of the cell-scaffold construct, transfer the seeded scaffold disk into a glass bottom culture dish (MatTek). Add 1.5 ml of complete MEM-α medium to the culture dish and seal the dish with Parafilm.

D.11. CG Scaffold Digestion via Dispase Protocol

SUPPLIES

- § Sterile Phosphate Buffered Saline (PBS, Cat. No. 20012-043, Invitrogen, Inc., Carlsbad, CA)
- § Dispase (Cat. No. 17105-041, Invitrogen)
- § Trypan Blue (Cat. No. AC18935-0250, Fisher Scientific, Hanover Park, IL)

EQUIPMENT

- § Hausser Phase Contrast Hemacytometer (Cat. No. 02-671-54, Fisher Scientific)
- § Inverted phase contrast microscope (Nikon, Japan)
- § Tabletop centrifuge (Heraeus Labofuge 400, VWR Scientific, Inc., Bridgeport, NJ)

PROCEDURE

1. Place a container of sterile PBS (Invitrogen) into the water bath at 37°C.

2. For each scaffold to be digested, pipette 5 ml of the warmed, sterile PBS into a 15 ml conical tube to be used to rinse the scaffold.

3. For each scaffold to be digested, make a 2.5 ml solution of warmed, sterile PBS with 2.4 U/ml dispase (6 U dispase total) (Invitrogen) in a 15 ml conical tube. NOTE: The scaffolds will digest faster if the dispase solution is pre-warmed (37°C) before you start the digestion.

4. Using foreceps, rinse each scaffold in warmed, sterile PBS by dipping the scaffold into the PBS 10 times.

5. Place each scaffold disk into a separate dispase solution and allow the scaffold to digest in its conical tube in a water bath at 37°C for 20 – 45 minutes, mixing the dispase solution every 5 minutes.

6. Once digested, take an aliquot of the solution and perform the standard cell counting assay (Section D.5) using Trypan blue (Invitrogen). Be sure to note the total volume of the solution prior to counting in order to be able to calculate the total cell number from the cells per ml calculated using the standard cell counting assay.

APPENDIX E. *Confocal Microscopy and Three-Dimensional Image Analysis Protocols*

E.1. Ultraview Live Cell Imager RS3 Confocal Microscope Operation Protocol

EQUIPMENT

- § Ultraview Live Cell Imager RS3 dual spinning disk confocal microscope (PerkinElmer, Wellesley, MA) built on a Zeiss Axiovert 200M bioinverted fluorescent microscope (Carl Zeiss, Inc., Germany)
- § 25x oil-immersion objective (Carl Zeiss)

PROCEDURE

Turning on:

1. On the laser power supply, turn the switch on the circuit-board to 'standby'. Then turn the ignition key to 'on'. Don't touch the on/off switch or the power level.

2. On the shelf above, turn on the RS controller (top box) and the Hamamatsu camera controller (bottom box).

3. On the Yokogawa CSU-21 scan head, turn the key to 'run'.

4. Never move the piezo. Always ensure that any objective slots on the microscope without an objective have dust covers installed.

5. Turn on the microscope (green rocker switch on the right side of the microscope).

6. Install the stage insert correctly. Align the red dot (on the top right) of the insert with the red dot on the frame. Ensure that the stage is stable and not wobbly. Adjust the corner screws where necessary to make it stable.

8. Turn the EXFO lamp on a few minutes before scanning. Never leave it on overnight.

9. Login and start the Ultraview software. Select capture. There should be no errors. If the system fails to connect with the CSU-21, restart everything. If it fails again, ask for help.

10. If sample heating is needed, attach the objective heater to the correct objective and screw it in just tight enough but not too tight. Place the heater (the black box) in the middle and not on the side. Turning the screwdriver counterclockwise tightens the heater strap. Turn on the objective heater box at least an hour before scanning. Make sure the temperature settles at a steady 35.2°C (37°C minus 1.8°C). Always return to this setting if a different setting is used during the experiment. Handle the objective heater very carefully – do not over tighten, do not turn it on before installing it on the objective, and to not force it onto the objective (always loosen it first).

Setting up the sample for scanning:

1. Clean the objective carefully using lens paper. Use a small amount of Zeiss cleaner fluid if necessary. Do not crinkle the lens paper as this will scratch the lens coating. Do not use Kim-

Wipes – these will leave lint on the surface. Apply a drop of oil on the objective to adequately cover the lens tip.

2. Seal the sample with Parafilm. Make sure that no Parafilm is on the bottom of or underneath the plate. Load it securely in place on the stage.

3. Turn the standby switch on the laser off. The amber light will go off.

4. On the left side of the microscope towards the front, the middle button switches from camera to binocular. View the sample using the binocular mode.

5. Never use the 3 buttons right in front of the focus knob on the right side of the microscope.

6. Behind the focus knob on the right side, the top 2 buttons move the objective. Make sure to defocus before using these buttons.

7. The reflector buttons are the bottom two buttons behind the focus knob on the right side. These change the filter positions. There are a total of 5 positions: two are empty, the rest are DAPI, GFP, and Texas Red.

8. Look at the sample using binocular mode and the appropriate filters.

9. When ready to scan, move the light guide to the left direction using the middle button on the left side of the microscope body. Adjust the filter position to one of the empty positions.

TIPS:

- § The objective display on the microscope does not correctly display which objective is being used.
- § For low light transmission imaging, a good starting point is about 3 bars of transmission light. Use the button on the bottom front face of the microscope to make any adjustments.
- § Do not touch the stage or table at any point. This will disrupt the scan.
- § Turn the room lights off to reduce background noise in the image.
- § It is highly advisable to seal your sample with Parafilm to guard against liquid evaporation or spillage onto the objectives and piezo. Avoid getting Parafilm between the bottom surface of the sample and the holder as this will lead to focus drift.

Software

1. You should have already logged in and started the Ultraview software.

2. Make sure you have switched from binocular mode to camera mode and moved the appropriate filters.

3. Define the laser settings by selecting the appropriate wavelengths and dicrotics. Make sure the power level sliders are set to 100% unless you have very bright or sensitive samples.

4. Press the playback button to toggle into the live scanning mode. Do not use the oculars to look at the sample when it is in live mode – there is a risk of laser damage to your eyes.

5. Image control: adjust the exposure and the binning set when you are using pseudocolor vs. grayscale. Pseudocolor shows distortions while grayscale produces a nicer image.

6. Image Display can be adjusted and different palettes selected. This does not adjust the data – only the display during capture.

7. The hardware controller adjusts the piezo. It has a range of 100 μm and a smallest step size of 50 nm. Use this to set the top and bottom positions of the scan as well as the scan intervals in z-stack.

8. Experiment: select the type of dimensionality using the 2D-3D button and the static-time button. Enter delay and total experiment time if doing time-resolved work.

9. Data will be saved in the folder and project selected. Rename it appropriately after collection.

10. Export individual data sets after loading them into the display window. Just selecting them does not work. Use the second icon button in the top left corner of the image display to export. Change the data type to 16 bit and specify the export directory.

11. Upload data files to Kahuna for long term storage.

TIPS:

- § Make sure to press 'enter' after entering in new numbers. The software will not update unless you do this.
- § Don't enter time delays unless you are doing time-resolved work. This will delay the capture of your static image.
- § For 4D work, try collecting a 3D stack first to confirm that everything looks good.

Turning off:

1. Restart the computer.

2. Turn off the EXFO lamp. It cannot be turned on for at least another 30 minutes.

3. Turn off the objective heater and detach it from the objective.

4. Trash any samples into the correct biohazard waste containers.

5. Turn off the microscope and cover it.

6. Turn the Yokogama unit off.

7. Turn the RS controller off.

8. Turn the Hamamatsu box off.

9. Switch the laser to standby.

10. Turn the key to the left to turn it off. The fan takes 5 minutes to turn off. It cannot be turned on for another 30 minutes.

E.2. Three-dimensional Image Analysis Protocol: Imaris XT

EQUIPMENT

- § ImarisXT v4.1 Analytical Image Processing Software (Bitplane AG, Switzerland)
- § High-end desktop workstation. Minimum system requirements:
  - **Hard Drive:** *300+ GB*
  - **Processor:** *3.0+ GHz*
  - **L2 Cache:** *2+ MB*
  - **RAM:** *4+ GB, 667+ MHz*
  - **Operating System:** *Windows XP Professional x64 edition*
  - **Graphics Card:** *512+ MB (High-end graphics card)*
- § External hard drive or network storage space

PROCEDURE

NOTE: A complete user's manual for the ImarisXT software package can be obtained online at the Bitplane AG website (www.bitplane.com).

1. Restart the computer workstation to ensure that all of the RAM is available for running the image analysis software.

2. Open the ImarisXT software package. Open the image stack from a confocal microscopy run using the "*Open*" icon from the toolbar across the top of the screen. This step may take a few minutes. The status of this step will be displayed on a Progress menu bar; do not try to adjust any other settings within Imaris until this step is completed.

3. Confirm the correct time and distance scaling factors are entered for the 4D image sequence. Select the "*Image Properties*" menu under the "*Edit*" tab in the menubar across the top of the screen. Under the "*Geometry*" heading, confirm that the correct voxel size values are entered. For the 25x objective, the correct voxel sizes are: 0.516, 0.516, 1.000.

On the main screen, confirm that the time step between images is correct. Move the slider along the scale at the bottom of the screen and confirm that the time steps in the bottom left hand corner of the image are correct. If not, they can be adjusted in the "*Image Properties*" menu under the "*Geometry*" heading.

Confirm that there is not any drift in the images from time point to time point: select the play button from the toolbar at the bottom of the screen to watch the time sequence. If drift is observed in the first few or last few time points, the data series can be cropped to remove those data points. Select the "Crop Time" menu which can be found under the "*Edit*" tab on the menubar at the top of the screen. Select the start and end of the image sequence ("*From*" and "*To*") in terms of time point number of the new, cropped sequence. Select the "*OK*" tab to crop the sequence.

4. To create the three-dimensional cell volumes at each time point, select the "*Surpass*" button from the menu icons along the top of the screen; select the "*Start with Volume*" tab from the secondary menu that appears. Imaris will then calculate the three-dimensional cell volumes at each time point. This step may take a few minutes; do not try to adjust any other settings within Imaris until this step is completed.

5. Perform volume thresholding on the 3D image volume in order to define the cell volumes. Open the "*Display Adjustment*" menu from the "*Edit*" heading of the menubar at the top of the screen. Adjust the "*Min*" and "*Max*" values in the "*Range – Channel 1*" sub-menu and adjust the "*Threshold*" adjustment toolbar within the "*Volume – Properties*" menu at the upper left corner of the screen to optimize the volume thresholding values. You should end up with a three-dimensional volume filled with distinct blobs corresponding to each cell. Confirm this threshold value is appropriate for the entire time range using the slider at the bottom of the screen. Record the three threshold values used for this image stack in your lab notebook.

6. From the "*Objects*" menu in the toolbar at the left edge of the screen, select the "*Add New Spots*" button. The "*Volume – Properties*" menu above the "*Objects*" menu will change to a "*Spots 1 – Properties*" menu. Within this menu set the "*Minimum Diameter*" to 10 μm and deselect the "*Background Object Subtraction*" tab.

Select the "*Next*" button to start the spot placement algorithm integrated within Imaris. This step may take a few minutes. The status of this step will be displayed on a Progress menu bar; do not try to adjust any other settings within Imaris until this step is completed.

7. Once the spots have been placed in each image in the time sequence, adjust the "*Spot Threshold Value*" in the "*Spots 1 – Properties*" menu in order to optimize the placement of spots in the experimental volume so that one spot is placed within each distinct cell volume throughout the time sequence. Determine the threshold value that best optimizes spot placement throughout the time sequence and record this value in your lab notebook. Select the "*Finish*" button.

8. Select the "*Spots 1*" tab from the "*Objects*" menu. Under the "*Settings*" tab in the "*Spots 1 – Properties*" menu at the top of the menu bar on the left edge of the screen, confirm that the "*Radius Scale*" and "*Rendering Quality*" parameters are set to 1.000 and 0.500, respectively. Under the "Edit" tab, confirm that "*Auto. Depth*" is selected and that the "Diameter" parameter is set to 10 μm.

Under the "*Tracking*" tab, select the "*Autoregressive Motion*" Algorithm and set the "*Maximum Distance*" parameter to 25 μm. Select the "*Create Track*" button to initiate the integrated autoregressive motion spot tracking algorithm within Imaris. This step may take a few minutes. The status of this step will be displayed on a Progress menu bar; do not try to adjust any other settings within Imaris until this step is completed.

9. Once spot tracking has completed, select the "*Spot Track Group 1*" tab from the "*Objects*" menu. Make no changes under the "*Settings*" tab. Under the "*Tracking*" tab, confirm that the correct "*Algorithm*" and "*Maximum Distance*" are selected (Autoregressive motion and 25 μm,

respectively). Make no changes under the "*Tracks*" tab. Under the "*Spots*" tab, confirm that the correct "*Radius Scale*" and "*Rendering Quality*" are selected (1.000 and 0.500, respectively).

Select the "*Statistics*" tab. Imaris will calculate the relevant statistics describing spot movement through the experimental volume during the time sequence. This step may take a few minutes. The status of this step will be displayed on a Progress menu bar; do not try to adjust any other settings within Imaris until this step is completed.

10. Once the statistical calculation process has completed, select the "*Excel*" tab from the "*Spot Track Group 1 – Properties*" menu in the toolbar on the left side of the screen. An Excel spreadsheet will open containing data describing the position of all spots at each time point in Cartesian coordinates, the average spot migration speed, the average step displacement, the total displacement of each spot during migration, and a host of other data.

The criteria that are calculated by the Imaris statistical analysis tool can be specified by adjusting the selections in the "*Statistics*" tab within the "*Preferences*" menu which can be found under the "*Edit*" heading of the menubar at the top of the screen.

11. Movies of cell or spot motion can be made at any point during this analysis from the time sequences of the compressed 2D images, the thresholded 3D volumes, the 3D volumes with the integrated spots, and the spots with or without their individual tracks through 3D space. Simply select the record button (Red dot) from the tool bar at the bottom of the screen. Name the *.MPG file that will be created and under the "*Movie Settings*" specify the "*Compression factor*" and "*Frame rate*" parameters. Typical settings for movies are 80 and 4.0 frames per second for the "*Compression factor*" and "*Frame rate*" parameters, respectively.

Select the "*Save*" tab and make sure to move the cursor off of the live portion of the screen containing the image (*i.e.*, move the tab over one of the toolbars). This step may take a few minutes. Do not try to adjust any other settings within Imaris or open up any other program until this step is completed. Anything appearing over the live portion of the screen will be included in the movie.

12. Once confirming that you have performed all of the analysis you need, shut down Imaris. Do not save the changes to the *.IMS dataset. If you save the changes you will not be able to recover your original dataset. You can recreate the thresholded and adjusted dataset from the original dataset using the volume and spot placement threshold values your recorded.

APPENDIX F. *Material and Equipment Resources*

The following facilities and personnel were utilized during this thesis research:

Fabrication and Crosslinking of CG and CGCaP Scaffolds

Facility: *Fiber and Polymers Laboratory, Rm. 3-315*
Equipment: *Suspension cooling system (Brinkman cooler model RC-2T, Brinkman Co., Westbury, NY)*
Suspension mixer (Ultra Turrax T18 Overhead blender, IKA Works, Inc., Wilmington, NC)
Peristaltic pump (Manostat Cassette Pump, Cat. No. 75-500-000, Manostat, New York, NY)
VirTis Genesis freeze dryer (VirTis, Inc., Gardiner, NY)
Stainless steel molds (VirTis)
Two-channel microprocessor thermocouple (HH22 with type K thermocouples, Omega Engineering, Stamford, CT)
Isotemp vacuum oven (Model 201, Fisher Scientific, Hanover Park, IL)

Facility: *Cambridge Centre for Medical Materials, Cambridge University, UK*
Contact: *Prof. William Bonfield (wb210@cam.ac.uk)*
Dr. Neil Rushton (nr10000@cam.ac.uk)
Dr. Andrew K. Lynn (andrew.k.lynn@orthomimetics.com)

Structural Characterization of CG Scaffold Samples (Pore Size Analysis)

Facility: *Cellular Solids Laboratory, Rm. 16-620*
Equipment: *Glycolmethacrylate embedding equipment and supplies*

Facility: *Edelmann Laboratory, Rm. 4-133*
Equipment: *Leica RM2165 microtome (Mannheim, Germany)*

Facility: *Mechanical Behavior of Materials Laboratory, Rm.8-102*
Equipment: *Inverted optical microscope (Nikon Optiphot, Japan)*
CCD color video camera (Optronics Engineering, Inc., Goleta, GA)

Studies of CG Scaffold Permeability

Facility: *Royal College of Surgeons in Ireland and Trinity College, Dublin Bioengineering Centre, Ireland*
Contact: *Prof. Fergal J. O'Brien (fjobrien@rcsi.ie)*
Equipment: *Custom built device to measure scaffold permeability under applied static strains*

Mechanical Characterization of CG and CGCaP Scaffolds

Facility: *NanoMechanical Technology Laboratory, Rm. 8-114*
Contact: *Alan Schwartzman (alan_s@mit.edu)*
Prof. Krystyn Van Vliet (krystyn@mit.edu)
Equipment: *NanoTest600 Micro/Nanoindenter (MicroMaterials LLC, Wrexham, UK)*
MFP-3D Atomic Force Microscope (WaveMetrics, Inc., Portland, OR)
0.25 N tension-compression load cell (Model No. GSO-25, Transducer Techniques, Temecula, CA)
Custom built LabVIEW VI (National Instruments, Austin, TX)

Facility: *Fiber and Polymers Laboratory, Rm. 3-315*
Contact : *Kristin Myers (kmyers@mit.edu)*
Prof. Simona Socrate (ssocrate@mit.edu)
Equipment: *Zwick/Roell Mechanical Tester (Model No. Z2.5/TN1S, Zwick GmbH & Co., Ulm, Germany)*
20 N load cell (Part No. BTC-LC0020N.P01, Zwick)

SEM and Energy Dispersive X-ray Spectroscopic Analysis of CG and CGCaP Scaffolds

Facility: *Gibson Group SEM facility, Rm. 4-133*
Contact: *Don Galler (dgaller@mit.edu)*
Equipment: *Leo VP438 scanning electron microscope (Leo Electron Microscopy, Inc., Thornwood, NY)*

Cell Culture

Facility: *Cellular Solids Lab, Rm.16-620*
Equipment: *Tabletop centrifuge (Heraeus Labofuge 400, VWR Scientific, Inc., Bridgeport, NJ)*
Hausser Phase Contrast Hemacytometer (Cat. No. 02-671-54, Fisher Scientific, Hanover Park, IL)
Inverted phase contrast microscope (Nikon, Japan)
Water Bath (Sheldon #1212, Cat. No. 14002-368, VWR Scientific)
Hepafilter laminar flow hood

Facility: *Fiber and Polymers Laboratory, Rm. 3-315*
Equipment: *Table top mini-autoclave*

Confocal Microscopy Imaging of Cell Behavior within CG Scaffolds

Facility: NE47 *Bioimaging Facility, Rm. NE47-219*
Contact: *Prof. Paul Matsudaira (matsudaira@wi.mit.edu)*
Dr. James Evans (jgevans@mit.edu)
Equipment: *Ultraview Live Cell Imager RS3 dual spinning disk confocal microscope (PerkinElmer, Wellesley, MA) built on a Zeiss Axiovert 200M bioinverted fluorescent microscope (Carl Zeiss, Inc., Germany)*

Facility: *Gertler Laboratory Bioimaging Facility, Rm. 68-264a*
Contact: *Hyung-Do Kim (hyungdo@mit.edu)*
Prof. Frank Gertler (fgertler@mit.edu)
Equipment: *McBain confocal microscope built on a bioinverted TE2000 microscope (Nikon, Japan)*
MetaMorph Imaging System software (Molecular Devices Corporation, Sunnyvale, CA)

Three-Dimensional Image Analysis and Cell Tracking

Facility: *Cellular Solids Lab, Rm.16-620*
Equipment: *Desktop workstation (Dell)*
Imaris XT site license (Bitplane AG, Switzerland)

APPENDIX G. *References*

1. Aebischer, P., Guenard, V., Winn, S.R., Valentini, R.F. and Galletti, P.M. Blind-ended semipermeable guidance channels support peripheral nerve regeneration in the absence of a distal nerve stump. Brain Res 1988;454:179-187.

2. Aebischer, P., Salessiotis, J.M. and Winn, S.R. Basic fibroblast growth factor released from synthetic guidance channels facilitates regeneration across long nerve gaps. J. Neurosci. Res. 1989;23:282-289.

3. Agrawal, C.M., McKinney, J.S., Lanctot, D. and Athanasiou, K.A. Effects of fluid flow on the in vitro degradation kinetics of biodegradable scaffolds for tissue engineering. Biomaterials 2000;21(23):2443-2452.

4. Allen, H.G. Analysis and design of structural sandwich panels. 1st ed. New York: Pergamon Press; 1969.

5. Andrews, E.W., Gioux, G., Onck, P. and Gibson, L.J. Size effects in ductile cellular solids. Part II: experimental results. International Journal of Mechanical Sciences 2001;43(3):701-713.

6. Assoian, R.K. and Zhu, X. Cell anchorage and the cytoskeleton as partners in growth factor dependent cell cycle progression. Curr. Opin. Cell. Biol. 1997;9(1):93-98.

7. Banks, P.R. and Paquette, D.M. Comparison of three common amine reactive fluorescent probes used for conjugation to biomolecules by capillary zone electrophoresis. Bioconjug Chem 1995;6(4): 447-458.

8. Bansil, R., Yannas, I.V. and Stanley, H.E. Raman-Spectroscopy - Structural Probe of Glycosaminoglycans. Biochimica Et Biophysica Acta 1978;541(4):535-542.

9. Beatty, M.W., Ojha, A.K., Cook, J.L., Alberts, L.R., Mahanna, G.K., Iwasaki, L.R. and Nickel, J.C. Small intestinal submucosa versus salt-extracted polyglycolic acid-poly-L-lactic acid: a comparison of neocartilage formed in two scaffold materials. Tissue Eng. 2002;8(6):955-968.

10. Benebassath, H., Klein, B.Y., Lermer, E., Azoury, R., Rahamim, E., Shlomai, Z. and Sarig, S. An In-Vitro Biocompatibility Study of a New Hydroxyapatite Ceramic HA-SAL1 - Comparison to Bioactive Bone Substitute Ceramics. Cells Mater. 1994;4:37-50.

11. Beningo, K.A., Dembo, M., Kaverina, I., Small, J.V. and Wang, Y.-L. Nascent focal adhesions are responsible for the generation of strong propulsive forces in migrating fibroblasts. Journal of Cell Biology 2001;153(4):881-887.

12. Beningo, K.A. and Wang, Y.-L. Flexible substrata for the detection of cellular traction forces. TRENDS in Cell Biology 2002;12(2):79-84.

13. Blanco, A., Chomski, E., Grabtchak, S., Ibisate, M., John, S., Leonard, S.W., Lopez, C., Meseguer, F., Miguez, H., Mondia, J.P., Ozin, G.A., Toader, O. and van Driel, H.M. Large-scale synthesis of a silicon photonic crystal with a complete three-dimensional bandgap near 1.5 micrometres. Nature 2000;405(6785):437-440.

14. Boden, S.D. and Schimandle, J.H. Biologic Enhancement of Spinal Fusion. Spine 1995;20(24):S113-S123.

15. Bohner, M. Calcium Orthophosphates in Medicine: From Ceramics to Calcium Phosphate Cements. Injury 2000;31(Suppl. 4):37-47.

16. Bonfield, W., Grynpas, M.D., Tully, A.E., Bowman, J. and Abram, J. Hydroxyapatite Reinforced Polyethylene - A Mechanically Compatible Implant Material for Bone Replacement. Biomaterials 1981;2(3):185-186.

17. Borden, M., El-Amin, S.F., Attawia, M. and Laurencin, C.T. Structural and human cellular assessment of a novel microsphere-based tissue engineered scaffold for bone repair. Biomaterials 2003;24(4):597-609.

18. Border, W.A., Noble, N.A. and Ketteler, M. TGF-B: a cytokine mediator of glomerulosclerosis and a target for therapeutic intervention. Kidney Int. Suppl. 1995;49:S59-S61.

19. Brace, W. Permeability from resistivity and pore shape. J Geophys Res 1977;82(23):3343-3349.

20. Brown, R.A., Prajapati, R., McGrouther, D.A., Yannas, I.V. and Eastwood, M. Tensional homeostasis in dermal fibroblasts: Mechanical responses to mechanical loading in three-dimensional substrates. Journal of Cellular Physiology 1998;175(3):323-332.

21. Brown, R.A., Talas, G., Porter, R.A., McGrouther, D.A. and Eastwood, M. Balanced mechanical forces and microtubule contribution to fibroblast contraction. J. Cell Physiol. 1996;169:439-447.

22. Burke, J.F., Yannas, I.V., Quinby, W.C., Bondoc, C.C. and Jung, W.K. Successful Use of a Physiologically Acceptable Artificial Skin in the Treatment of Extensive Burn Injury. Annals of Surgery 1981;194(4):413-428.

23. Butler, C.E., Yannas, I.V., Compton, C.C., Correia, C.A. and Orgill, D.P. Comparison of cultured and uncultured keratinocytes seeded into a collagen-GAG matrix for skin replacements. British Journal of Plastic Surgery 1999;52(2):127-132.

24. Carter, D.R. and Spengler, D.M. Mechanical Properties and Composition of Cortical Bone. Clin. Orthop. Relat. Res. 1978;135:192-217.

25. Carterson, B. and Lowther, D.A. Changes in the Metabolism of the Proteoglycans from Sheep Articular Cartilage in Response to Mechanical Stress. Biochimica et Biophysica Acta 1978;540:412-422.

26. Cassella, J.P., Garrington, N., Stamp, T.C. and Ali, S.Y. An Electron Probe X-Ray Microanalytical Study of Bone Mineral in Osteogenesis Imperfecta. Calcified Tissue Int. 1995;56:118-122.

27. Chamberlain, L.J. and Yannas, I.V. Preparation of collagen-glycosaminoglycan copolymers for tissue regeneration. In: J. R. Morgan and M. L. Yarmush, editors. Methods of Molecular Medicine. Tolowa, NJ: Humana Press; 1998.

28. Chamberlain, L.J., Yannas, I.V., Hsu, H.-P. and Spector, M. Connective tissue response to tubular implants for peripheral nerve regeneration: The role of myofibroblasts. J. Comp. Neurol. 2000;417:415-430.

29. Chamberlain, L.J., Yannas, I.V., Hsu, H.P., Strichartz, G. and Spector, M. Collagen-GAG substrate enhances the quality of nerve regeneration through collagen tubes up to level of autograft. Exp. Neurol. 1998;154(2):315-329.

30. Chang, A.S. and Yannas, I.V. Peripheral Nerve Regeneration. In: G. Adelman, editor. Encyclopedia of Neuroscience. Boston: Birkhauser; 1992. p. 125-126.

31. Chang, A.S., Yannas, I.V., Perutz, S., Loree, H., Sethi, R.R., Krarup, C., Norregaard, T.V., Zervas, N.T. and Silver, J. Electrophysiological study of recovery of peripheral nerves regenerated by a collagen-glycosaminoglycan copolymer matrix. In: R. L. Dunn, editor. Progress in Biomedical Polymers. New York: Plenum Press; 1990. p. 107-119.

32. Chapuis, J.-F., Lucarz-Bietry, A., Agache, P. and Humbert, P. A mechanical study of tense collagen lattices. Eur J Dermatol 1996;6:56-60.

33. Chen, C.S. and Ingber, D.E. Tensegrity and mechanoregulation: from skeleton to cytoskeleton. Osteoarthritis and Cartilage 1999;7:81-94.

34. Chen, G., Ushida, T. and Tateishi, T. Poly(DL-lactic-co-glycolic acid) sponge hybridized with collagen microsponges and deposited apatite particulates. J Biomed Mater Res 2001;57(1):8-14.

35. Chen, G.P., Ushida, T. and Tateishi, T. A Hybrid Sponge of Poly(DL-lactic-co-glycolic acid), Collagen and Apatite. Key Engineering Materials 2000;192-195:753-756.

36. Chen, P., Gupta, K. and Wells, A. Cell movement elicited by epidermal growth factor receptor requires kinase and autophosphorylation but is separable from mitogenesis. J Cell Biol 1994;124(4):547-555.

37. Chen, P., Xie, H., Sekar, M.C., Gupta, K.B. and Wells, A. Epidermal growth factor receptor-mediated cell motility: phospholipase C activity is required, but MAP kinase activity is not sufficient for induced cell movement. J Cell Biol 1994;127(3):847-857.

38. Christensen, J.L., Wright, D.E., Wagers, A.J. and Weissman, I.L. Circulation and chemotaxis of fetal hematopoietic stem cells. PLoS Biol 2004;2(3):E75.

39. Chvapil, M. Collagen sponge: theory and practice of medical applications. J. Biomed. Mater. Res. 1977;11(5):721-741.

40. Claase, M.B., Grijpma, D.W., Mendes, S.C., De Bruijn, J.D. and Feijen, J. Porous PEOT/PBT scaffolds for bone tissue engineering: preparation, characterization, and in vitro bone marrow cell culturing. J. Biomed. Mater. Res. 2003;64A(2):291-300.

41. Clarke, K.I., Graves, S.E., Wong, A.T.C., Triffitt, J.T., Francis, M.J.O. and Czernoszka, J.T. Investigation into the Formation and Mechanical-Properties of a Bioactive Material Based on Collagen and Calcium-Phosphate. J. Mater. Sci. Mater. Med. 1993;4(2):107-110.

42. Comninou, M. and Yannas, I.V. Dependence of Stress-Strain Nonlinearity of Connective Tissues on Geometry of Collagen-Fibers. Journal of Biomechanics 1976;9(7):427-433.

43. Cornell, C.N., Lane, J.M., Chapman, M., Merkow, R., Seligson, D., Henry, S., Gustilo, R. and Vincent, K. Multicenter Trial of Collagraft as Bone Graft Substitute. Journal of Orthopaedic Trauma 1991;5(1):1-8.

44. Cui, K., Zhu, Y., Wang, M.H., Feng, Q.L. and Cui, F.Z. A Porous Scaffold from Bone-Like Powder Loaded in a Collagen- Chitosan Matrix. Journal of Bioactive and Compatible Polymers 2004;19(1):17-31.

45. Cumberledge, S. and Krasnow, M.A. Intercellular signalling in Drosophila segment formation reconstructed in vitro. Nature 1993;363(6429):549-552.

46. Dagalakis, N., Flink, J., Stasikelis, P., Burke, J.F. and Yannas, I.V. Design of an Artificial Skin III: Control of Pore Structure. J Biomed Mater Res 1980;14(4):511-528.

47. Daley, G.Q. Customized human embryonic stem cells. Nat Biotechnol 2005;23(7):826=828.

48. Daley, G.Q., Sandel, M.J. and Moreno, J.D. Stem cell research: science, ethics and policy.. Med Ethics 2005;12(1):5.

49. Delvoye, P., Wiliquet, P., Leveque, J.-L., Nusgens, B.V. and Lapiere, C.M. Measurement of mechanical forces generated by skin fibroblasts embedded in a three-dimensional collagen gel. J Invest Dermatol 1991;97:898-902.

50. Dembo, M. and Wang, Y.-L. Stresses at the cell-to-substrate interface during locomotion of fibroblasts. Biophysical Journal 1999;76:2307-2316.

51. Dickinson, R.B. and Tranquillo, R.T. Optimal Esitmation of Cell Movement Indices from the Statistical Analysis of Cell Tracking Data. Amer. Instit. Chem Eng. J. 1993;39(12):1995-2010.

52. DiMilla, P.A., Barbee, K. and Lauffenburger, D.A. Mathematical model for the effects of adhesion and mechanics on cell migration speed. Biophys J 1991;60(1):15-37.

53. Doillon, C.J., Whyne, C.F., Brandwein, S. and Silver, F.H. Collagen-based wound dressings: control of the pore structure and morphology. J. Biomed. Mater. Res. 1986;20(8):1219-1228.

54. Doll, B., Sfeir, C., Winn, S., Huard, J. and Hollinger, J. Critical Aspects of Tissue-Engineered Therapy for Bone Regeneration. Crit. Rev. Eukaryotic Gene Expression 2001;11:173-198.

55. Driessens, F.C.M., Boltong, M.G., Bermudez, O., Planell, J.A., Ginebra, M.P. and Fernandez, E. Effective Formulations for the Preparation of Calcium-Phosphate Bone Cements. J. Mater. Sci.- Mater. Med. 1994;5(3):164-170.

56. Dunn, G.A. Characterising a kinesis response: time averaged measures of cell speed and directional persistence. Agents Actions Suppl 1983;12:14-33.

57. Eastwood, M., McGrouther, D.A. and Brown, R.A. A culture force monitor for measurement of contraction forces generated in human dermal fibroblast cultures: evidence for cell-matrix mechanical signalling. Biochim. Biophys. Acta. 1994;1201:186-192.

58. Eastwood, M., Mudera, V.C., McGrouther, D.A. and Brown, R.A. Effect of precise mechanical loading on fibroblast populated collagen lattices: morphological changes. Cell Motility and the Cytoskeleton 1998;40:13-21.

59. Eastwood, M., Porter, R., Khan, U., McGrouther, D.A. and Brown, R.A. Quantitative analysis of collagen gel contractile forces generated by dermal fibroblasts and the relationship to cell morphology. J Cell Physiol 1996;166:33-42.

60. Eggli, S., Hunziker, E.B. and Schenck, R.K. Quantitation of Structural Features Characterizing Weight- and Less-Weight-Bearing Regions in Articular Cartilage: A Stereological Analysis of Medial Femoral Condyles in Young Adult Rabbits. Anat. Rec. 1988;222:217-227.

61. Engler, A., Bacakova, L., Newman, C., Hategan, A., Griffin, M. and Discher, D. Substrate compliance versus ligand density in cell on gel responses. Biophys. J. 2004;86:617-628.

62. Ferdman, A.G. and Yannas, I.V. Scattering of light from histologic section: A new method for the analysis of connective tissue. J. Invest. Dermatol. 1993;100:710-716.

63. Fishkind, D.J., Silverman, J.D. and Wang, Y.-L. Function of spindle microtubules in directing cortical movement and actin filament organization in dividing cultures cells. Journal of Cell Science 1996;109:2041-2051.

64. Flemings, M.F. Solidification Processing. New York: New York; 1974.

65. Freed, L.E. and Vunjak-Novakovic, G. Culture environments: Cell-polymer-bioreactor systems. In: R. P. Lanza, editor. Methods of Tissue Engineering. San Diego: Academic Press; 2002. p. 97-111.

66. Freyman, T.M. Development of an In Vitro Model of Contraction by Fibroblasts [Ph.D.]. Cambridge: Dept. of Materials Science and Engineering, Massachusetts Institute of Technology; 2001.

67. Freyman, T.M., Yannas, I.V. and Gibson, L.J. Cellular materials as porous scaffolds for tissue engineering. Prog. Mat. Sci. 2001;46:273-282.

68. Freyman, T.M., Yannas, I.V., Pek, Y.-S., Yokoo, R. and Gibson, L.J. Micromechanics of fibroblast contraction of a collagen-GAG matrix. Experimental Cell Research 2001;269:140-153.

69. Freyman, T.M., Yannas, I.V., Yokoo, R. and Gibson, L.J. Fibroblast contraction of a collagen-GAG matrix. Biomaterials 2001;22(21):2883-2891.

70. Freyman, T.M., Yannas, I.V., Yokoo, R. and Gibson, L.J. Fibroblast contractile force is independent of the stiffness which resists the contraction. Experimental Cell Research 2002;272(2):153-162.

71. Fu, S.Y. and Gordon, T. The cellular and molecular basis of peripheral nerve regeneration. Mol. Neurobiol. 1997;14(67-116).

72. Gage, F.H. Mammalian neural stem cells. Science 2000;287:1433-1438.

73. Gent, A.N. and Rusch, K.C. Permeability of open-cell foamed materials. J. Cell. Plast. 1966;2:46-51.

74. Geyer, G. Materials for Middle Ear Reconstruction. HNO 1999;47(2):77-91.

75. Gibson, L.J. and Ashby, M.F. Cellular Solids: Structure and Properties. In: I. M. Ward, editor. Cambridge Solid State Science Series. Cambridge, U.K.: Cambridge University Press; 1997.

76. Gioux, G., McCormack, T.M. and Gibson, L.J. Failure of aluminum foams under multiaxial loads. Int. J. Mech. Sci. 2000;42:1097-1117.

77. Gordon, P.L., Huang, C., Lord, R.C. and Yannas, I.V. Far-Infrared Spectrum of Collagen. Macromolecules 1974;7(6):954-956.

78. Graham, S. and Brown, P.W. Reactions of Octacalcium Phosphate to Form Hydroxyapatite. J. Cryst. Growth 1996;165(1-2):106-115.

79. Grattoni, C.A., Al-Sharji, H.H., Yang, C., Muggeridge, A.H. and Zimmerman, R.W. Rheology and Permeability of Crosslinked Polyacrylamide Gel. J Colloid Interface Sci 2001;240(2):601-607.

80. Grinnell, F. Fibroblast biology in three-dimensional collagen matrices. Trends Cell Biol. 2003;13:264-269.

81. Grinnell, F., Ho, C.H., Lin, Y.-C. and Skuta, G. Differences in the regulation of fribroblast contraction of floating versus stressed collagen matrices. J. Biol. Chem. 1999;274:918-923.

82. Grynpas, M.D. and Hunter, G.K. Bone mineral and glycosaminoglycans in newborn and mature rabbits. J Bone Miner Res 1988;1988(3):2.

83. Guilak, F. Functional Tissue Engineering - The Role of Biomechanics in Reparative Medicine. Annals of the New York Academy of Sciences 2002;961:193-195.

84. Guo, X.E. and Gibson, L.J. Behavior of intact and damaged honeycombs: a finite element study. International Journal of Mechanical Sciences 1999;41(1):85-105.

85. Haber, R.M., Hanna, W., Ramsay, C.A. and Boxall, L.B. Cicatricial junctional epidermolysis bullosa. J. Am. Acad. Dermatol. 1985;12:836-844.

86. Haddock, S.M., Debes, J.C., Nauman, E.A., Fong, K.E., Arramon, Y.P. and Keaveny, T.M. Structure-function relationships for coralline hydroxyapatite bone substitute. J Biomed Mater Res 1999;47(1):71-78.

87. Harley, B.A. Peripheral nerve regeneration through collagen devices with different in vivo degradation characteristics [M.S.]. Cambridge, MAMassachusetts Institute of Technology; 2002.

88. Harley, B.A. and Flemings, M.F. Quantification of Freeze-drying to Produce Collagen-based Scaffolds for Tissue Engineering Applications: Coarsening-mediated Process. In preparation, 2006.

89. Harley, B.A. and Gibson, L.J. Mechanical Characterization of a Homologous Series of Equiaxed Collagen-GAG Scaffolds. In preparation, 2006.

90. Harley, B.A., Hastings, A.Z., Yannas, I.V. and Sannino, A. Fabricating Tubular Scaffolds with a Radial Pore Size Gradient by a Spinning Technique. Biomaterials 2006;27(6):866-874.

91. Harley, B.A., Lynn, A.K., Wissner-Gross, Z., Bonfield, W., Yannas, I.V. and Gibson, L.J. Design of a Multiphase Osteochondral Scaffold III: Fabrication of a mineralized collagen-GAG scaffold. In preparation, 2006.

92. Harley, B.A., Spilker, M.H., Wu, J.W., Asano, K., Hsu, H.-P., Spector, M. and Yannas, I.V. Optimal degradation rate for collagen chambers used for regeneration of peripheral nerves over long gaps. Cells Tissues Organs 2004;176(1-3):153-165.

93. Harley, B.A., Yannas, I.V. and Gibson, L.J. Fabrication and mechanical characterization of equiaxed collagen-GAG scaffolds. In: Society for Biomaterials; 2004; Sydney, AU; 2004.

94. Harms, B.D., Bassi, G.M., Horwitz, A.R. and Lauffenburger, D.A. Directional persistence of EGF-induced cell migration is associated with stabilization of lamellipodial protrusions. Biophys J 2005;88(2):1479-1488.

95. Hasegawa, K., Yamamura, S. and Dohmae, Y. Enhancing Screw Stability in Osteosynthesis with Hydroxyapatite Granules. Arch. Orthop. Trauma Surg. 1998;117:175-176.

96. Hemmerle, J., Leize, M. and Voegel, J.C. Long-Term Behavior of a Hydroxyapatite Collagen- Glycosaminoglycan Biomaterial Used for Oral-Surgery - A Case-Report. J. Mater. Sci. Mater. Med. 1995;6(6):360-366.

97. Heughebaert, J.C., Lebugle, A., Vu, F. and Phan-Tan-Luu, R. Central Composite Design and Optimization by Multiresponse Analysis of Octacalcium Phosphate Synthesis. Analusis 2000;28(7):571-574.

98. Hillsley, M.V. and Frangos, J.A. Bone tissue engineering: the role of interstitial fluid flow. Biotechnol Bioeng 1994;43(7):573-581.

99. Hobbs, P.V. Ice Physics. Oxford: Clarendon Press; 1974.

100. Hollister, S.J., Maddox, R.D. and Taboas, J.M. Optimal design and fabrication of scaffolds to mimic tissue properties and satisfy biological constraints. Biomaterials 2002;23(20):4095-4103.

101. Howe, A., Aplin, A.E., Alahari, S.K. and Juliano, R.L. Integrin signaling and cell growth control. Curr. Opin. Cell. Biol. 1998;10(2):220-231.

102. Hsu, W.C., Spilker, M.H., Yannas, I.V. and Rubin, P.A. Inhibition of conjunctival scarring and contraction by a porous collagen-glycosaminoglycan implant. Invest. Ophthalmol. Vis. Sci. 2000;41:2404-2411.

103. Hu, Y.Y., Zhang, C., Zhang, S.M., Xiong, Z. and Xu, J.Q. Development of a Porous Poly(L-lactic acid)/Hydroxyapatite/Collagen Scaffold as a BMP Delivery System and its Use in Healing Canine Segmental Bone Defect. J Biomed Mater Res 2003;67A(2):591-598.

104. Huang, C. and Yannas, I.V. Mechanochemical Method for Study of Enzymatic Degradation of Collagen. Abstracts of Papers of the American Chemical Society 1976:64-64.

105. Huang, C. and Yannas, I.V. Mechanochemical studies of enymatic degradation of insoluable collagen fibers. J. Biomed. Mater Res. 1977;8:137-154.

106. Hubbell, J.A. Matrix effects. In: J. Vacanti, editor. Principles of Tissue Engineering. 2nd ed. San Diego: Academic Press; 2000. p. 237-250.

107. Hulbert, S.F., Young, F.A., Mathews, R.S., Klawitter, J.J., Talbert, C.D. and Stelling, F.H. Potential of ceramic materials as permanently implantable skeletal prosthese. J Biomed Mater Res 1970;4(3):433-456.

108. Ikeda, K., Oda, Y., Tomita, K., Nomura, S. and Nakanishi, I. Isolated Schwann cells can synthesize the basement membrane in vitro. J. Electron. Microsc. (Tokyo) 1989;38:230-234.

109. Itoh, S., Kikuchi, M., Takakuda, K., Koyama, Y., Matsumoto, H.N., Ichinose, S., Tanaka, J., Kawauchi, T. and Shinomiya, K. The Biocompatibility and Osteoconductive Activity

of a Novel Hydroxyapatite/Collagen Composite Biomaterial, and its Function as a Carrier of rhBMP-2. J. Biomed. Mater. Res. 2001;54(3):445-453.

110. Jenkins, G., Redwood, K.L., Meadows, L. and Green, M.R. Effect of gel re-organization and tensional force on alpha2-beta1 integrin levels in dermal fibroblasts. FEBS 1999;263:93-103.

111. Jenq, C.-B. and Coggeshall, R.E. Permeable tubes increase the length of the gap that regenerating axons can span. Brain Res 1987;408:239-242.

112. Jenq, C.-B., Jenq, L.L. and Coggeshall, R.E. Nerve regeneration changes with filters of different pore sizes. Exp. Neurol. 1987;97:662-671.

113. Jiang, H. and Grinnell, F. Cell-matrix entanglements and mechanical anchorage of fibroblasts in three-dimensional collagen matrices. Mol. Biol. Cell 2005;16(11):5070-5076.

114. Jiang, P., Bertone, J.F. and Colvin, V.L. A lost-wax approach to monodisperse colloids and their crystals. Science 2001;291(5503):453-457.

115. Johnsson, M.S.A. and Nancollas, G.H. The Role of Brushite and Octacalcium Phosphate in Apatite Formation. Critical Reviews in Oral Biology & Medicine 1992;3(1-2):61-82.

116. Kharait, S., Dhir, R., Lauffenburger, D. and Wells, A. Protein kinase Cd signaling downstream of the EGF receptor mediates migration and invasiveness of prostate cancer cells. Biochem Biophysl Res Commun 2006;343(3):848=856.

117. Kikuchi, M., Ikoma, T., Syoji, D., Matsumoto, H.N., Koyama, Y., Itoh, S., Takakuda, K., Shinomiya, K. and Tanaka, J. Porous Body Preparation of Hydroxyapatite/Collagen Nanocomposites for Bone Tissue Regeneration. Key Engineering Materials 2004;254-156:561-564.

118. Kikuchi, M., Itoh, S., Ichinose, S., Shinomiya, K. and Tanaka, J. Self-Organization Mechanism in a Bone-Like Hydroxyapatite/Collagen Nanocomposite Synthesized In Vitro and its Biological Reaction In Vivo. Biomaterials 2001;22(13):1705-1711.

119. Kim, D.H., Connolly, S.E., Zhao, S., Beuerman, R.W., Voorhies, R.M. and Kline, D.G. Comparison of macropore, semipermeable, and nonpermeable collagen conduits in nerve repair. J. Reconstr. Microsurg. 1993;9:415-420.

120. Kim, H.M. Bioactive Ceramics: Challenges and Perspectives. Journal of the Ceramic Society of Japan 2001;109(4):S49-S57.

121. Klein, C.P., Driessen, A.A., de Groot, K. and van den Hooff, A. Biodegradation Behavior of Various Calcium Phosphate Materials in Bone Tissue. J. Biomed. Mater. Res. 1983;17(5):769-784.

122. Knothe-Tate, M.L. and Knothe, U. An ex vivo model to study transport processes and fluid flow in loaded bone. J Biomech 2000;33(2):247-254.

123. Kodama, H., Amagai, Y., Sudo, H., Kasai, S. and Yamamoto, S. Establishment of a clonal osteogenic cell line from newborn mouse calvaria. Jpn. J. Oral Biol. 1981;23:899-901.

124. Kolodney, M.S. and Wysolmerski, R.B. Isometric contraction by fibroblasts and endothelial cells in tissue culture: a quantitative study. J Cell Biol 1992;117:73-82.

125. Kondo, M., Wagers, A.J., Manz, M.G., Prohaska, S.S., Scherer, D.C., Beilhack, G.F., Shizuru, J.A. and Weissman, I.L. Biology of hematopoietic stem cells and progenitors: implications for clinical application. Annu Rev Immunol 2003;21:759-806.

126. Koo, L.Y., Irvine, D.J., Mayes, A.M., Lauffenburger, D.A. and Griffith, L.G. Co-regulation of cell adhesion by nanoscale RGD organization and mechanical stimulus. J Cell Sci 2002;115(Pt 7):1423-1433.

127. Kraynik, A.M., Reinelt, D.A. and van Swol, F. Structure of random monodisperse foam. Phys. Rev. 2003;67:031403.

128. Kuberka, M., von Heimburg, D., Schoof, H., Heschel, I. and Rau, G. Magnification of the pore size in biodegradable collagen sponges. Int. J. Artif. Organs 2002;25(1):67-73.

129. Kunisaki, S.M., Fuchs, J.R., Kaviani, A., Oh, J.T., LaVan, D.A., Vacanti, J.P., Wilson, J.M. and Fauza, D.O. Diaphragmatic repair through fetal tissue engineering: a comparison between mesenchymal amniocyte- and myoblast-based constructs. J Pediatr Surg 2006;41(1):34-39.

130. Kurz, W. and Fisher, D.J. Fundamentals of Solidification. Switzerland: Transtech Publications; 1989.

131. Lai, W.M. and Mow, V.C. Drag-induced compression of articular cartilage during a permeation experiment. Biorheology 1980;17(1-2):111-123.

132. Lanza, R.P., Cooper, D.K.C. and Chick, W.L. Xenotransplantation. Sci. Am. 1997;July:54-59.

133. Lanza, R.P., Langer, R. and Chick, W.L., editors. Principles of Tissue Engineering. San Diego: Academic Press; 1997.

134. Larsson, T., Aspden, R.M. and Heinegard, D. Effects of Mechanical Load on Cartilage Matrix Biosynthesis In Vitro. Matrix 1991;11:388-394.

135. Lee, C.R., Grodzinsky, A.J. and Spector, M. The effects of crosslinking of collagen-glycosaminoglycan scaffolds on compressive stiffness, chondrocyte-mediated contraction, proliferation, and biosynthesis. Biomaterials 2001;22:3145-3154.

136. LeGeros, R.Z. Properties of Osteoconductive Biomaterials: Calcium Phosphates. Clin. Orthop. Relat. Res. 2002;395:81-98.

137. Lehv, M. and Fitzgerald, P.J. Pancreatic acinar cell regeneration IV: Regeneration after surgical resection. Am. J. Pathol. 1968;53:513-535.

138. Lengerke, C. and Daley, G.Q. Patterning definitive hematopoietic stem cells from embryonic stem cells. Exp Hematol 2005;33(9):971-979.

139. Lerou, P.H. and Daley, G.Q. Therapeutic potential of embryonic stem cells. Blood Rev 2005;19(6):321-331.

140. Levenson, S.M., Geever, E.F., Crowley, L.V., Oates, J.F., Berard, C.W. and Rosen, H. The healing of rat skin wounds. Annals of Surgery 1965;161:293-308.

141. Levick, J.R. Flow through interstitium and other fibrous matrices. Q J Exp Physiol 1987;72(4):409-437.

142. Li, S., De Wijn, J.R., Li, J., Layrolle, P. and De Groot, K. Macroporous biphasic calcium phosphate scaffold with high permeability/porosity ratio. Tissue Eng. 2003;9(3):535-548.

143. Li, S.T., Archibald, S.J., Krarup, C. and Madison, R.D. Peripheral nerve repair with collagen conduits. Clin. Mater. 1992;9(3-4):195-200.

144. Liao, S.S., Cui, F.Z., Zhang, W. and Feng, Q.L. Hierarchically Biomimetic Bone Scaffold Materials: Nano- HA/collagen/PLA Composite. J Biomed Mater Res Part B-Applied Biomaterials 2004;69B(2):158-165.

145. Lin, R.Y., Sullivan, K.M., Argenta, P.A., Meuli, M., Lorenz, H.P. and Adzick, N.S. Exogenous transforming growth factor-B amplifies its own expression and induces scar formation in a model of human fetal skin repair. Ann. Surg. 1995;222:146-154.

146. LiVecchi, A.B., Tombes, R.M. and LaBerge, M. In vitro chondrocyte collagen deposition within porous HDPE: substrate microstructure and wettability effects. J. Biomed. Mater. Res. 1994;28(8):839-850.

147. Lo, C.-M., Wang, H.-B., Dembo, M. and Wang, Y.-L. Cell movement is guided by the rigidity of the substrate. Biophys. J. 2000;79:144-152.

148. Loree, H.M., Yannas, I.V., Mikic, B., Chang, A.S., Perutz, S.M., Norregaard, T.V. and Krarup, C. A freeze-drying process for fabrication of polymeric bridges for peripheral nerve regeneration. In: Proc. 15th Annual Northeast Bioeng. Conf.; 1989; 1989. p. 53-54.

149. Luan, X. and Diekwisch, T.G.H. CP27 affects viability, proliferation, attachment and gene expression in embryonic fibroblasts. Cell Prolif. 2002;35(4):207-219.

150. Lynn, A.K. Design and Development of an Osteochondral Scaffold [Ph.D.]. Cambridge, EnglandCambridge University; 2005.

151. Lynn, A.K. and Bonfield, W. A novel method for the simultaneous, titrant-free control of pH and calcium phosphate mass yield. Acc. Chem. Rev. 2005;38(3):202-207.

152. Lynn, A.K., Cameron, R.E., Best, S.M. and Bonfield, W. Composition-Control of Porous, Coprecipitated Biocomposites of Collagen and Calcium Phosphate. 2004;Not For Submission Until 28th October 2004 (IP Disclosure).

153. Lynn, A.K., Cameron, R.E., Best, S.M., Brooks, R.A., Rushton, N. and Bonfield, W. Phase Mapping: A Novel Design Approach for the Production of Calcium Phosphate-Collagen Biocomposites. Key Eng. Mater. 2004;254-256:593-596.

154. Lynn, A.K., Yannas, I.V. and Bonfield, W. Antigenicity and immunogenicity of collagen. J. Biomed. Mater. Res. B Appl. Biomater. 2004;71(2):343-354.

155. Mamoune, A., Luo, J.H., Lauffenburger, D.A. and Wells, A. Calpain-2 as a target for limiting prostate cancer invasion. Cancer Res 2003;63(15):4632-4640.

156. Mansour, J.M. and Mow, V.C. The permeability of articular cartilage under compressive strain and at high pressures. J Bone Joint Surg Am 1976;58(4):509-516.

157. Maroudas, A. Physicochemical properties of cartilage in the light of ion exchange theory. Biophys J 1968;8(5):575-595.

158. Maroudas, A. and Bullough, P. Permeability of articular cartilage. Nature 1968;219(160):1260-1261.

159. Maroudas, A., Bullough, P., Swanson, S.A. and Freeman, M.A. The permeability of articular cartilage. J Bone Joint Surg Br 1968;50(1):166-177.

160. Martinez-Hernandez, A. Repair, regeneration, and fibrosis. In: a. J. L. F. E. Rubin, editor. Pathology. Philadelphia: J.B. Lippincott; 1988.

161. Mast, B.A., Nelson, J.M. and Krummel, T.M. Tissue repair in the mammalian fetus. In: R. F. D. I.K. Cohen, and W.J. Lindblad (eds.),, editor. Wound Healing. Philadelphia: W.B. Saunders; 1992.

162. Medawar, P.B. The behavior and fate of skin autografts and skin homografts in rabbits. J. Anat 1944;78:176-199.

163. Mehlisch, D.R. Collagen/Hydroxylapatite Implant for Augmenting Deficient Alveolar Ridges: A 24-Month Clinical and Histologic Summary. Oral Surgery, Oral Medicine and Oral Pathology 1989;68:505-514.

164. Mehlisch, D.R., Leider, A.S. and Roberts, W.E. Histologic Evaluation of the Bone-Graft Interface after Mandibular Augmentation with Hydroxylapatite Purified Fibrillar Collagen Composite Implants. Oral Surgery Oral Medicine Oral Pathology Oral Radiology and Endodontics 1990;70(6):685-692.

165. Michel, B. Ice Mechanics. Quebec: Les Presses De L'Universite Laval; 1978.

166. Moreira-Gonzalez, A., Jackson, I.T., Miyawaki, T., DiNick, V. and Yavuzer, R. Augmentation of the Craniomaxillofacial Region Using Porous Hydroxyapatite Granules. Plast. Reconstr. Surg. 2003;111:1808-1817.

167. Muenzenberg, K.J. and Gebhardy, M. Brushite, Octacalcium Phosphate, and Carbonate-Containing Apatite in Bone. Clin. Orthop. Relat. Res. 1973;90:271-273.

168. Mueth, D.M. Measurements of particle dynamics in slow, dense granular Couette flow. Phys Rev E Stat Nonlin Soft Matter Phys 2003;67(1 Pt. 1):011304.

169. Munevar, S., Wang, Y.-L. and Dembo, M. Distinct roles of frontal and rear cell-substrate adhesions in fibrolast migration. Mol. Biol. Cell 2001;12:3947-3954.

170. Muschler, G.F., Negami, S., Hyodo, A., Gaisser, D., Easley, K. and Kambic, H. Evaluation of Collagen Ceramic Composite Graft Materials in a Spinal Fusion Model. Clin. Orthop. Relat. Res. 1996;328:250-260.

171. Nazarian, A. and Muller, R. Time-lapsed microstructural imaging of bone failure behavior. J Biomech 2004;37:55-65.

172. Nehrer, S., Breinan, H.A., Ramappa, A., Young, G., Shortkroff, S., Louie, L.K., Sledge, C.B., Yannas, I.V. and Spector, M. Matrix collagen type and pore size influence behavior of seeded canine chondrocytes. Biomaterials 1997;18(11):769-776.

173. Netti, P.A., Berk, D.A., Swartz, M.A., Grodzinsky, A.J. and Jain, R.K. Role of extracellular matrix assembly in interstitial transport in solid tumors. Cancer Res 2000;60(9):2497-2503.

174. O'Brien, F.J., Harley, B.A., Waller, M.A., Yannas, I.V., Gibson, L.J. and Prendergast, P.J. The effect of pore size on permeability and cell attachment in collagen scaffolds for tissue engineering. Technology and Health Care Submitted, 2005.

175. O'Brien, F.J., Harley, B.A., Yannas, I.V. and Gibson, L.J. Influence of freezing rate on pore structure in freeze-dried collagen-GAG scaffolds. Biomaterials 2004;25(6):1077-1086.

176. O'Brien, F.J., Harley, B.A., Yannas, I.V. and Gibson, L.J. The effect of pore size on cell adhesion in collagen-GAG scaffolds. Biomaterials 2005;26(4):433-441.

177. Olde Damink, L.H.H., Dijkstra, P.J., van Luyn, M.J.A., Van Wachem, P.B., Nieuwenhuis, P. and Feijen, J. Cross-linking of dermal sheep collagen using a water soluble carbodiimide. Biomaterials 1996;17:765-773.

178. Oliver, J. Correlations of structure and function and mechanisms of recovery in acute tubular necrosis. Am. J. Med. 1953;15:535-557.

179. Onck, P.R., Andrews, E.W. and Gibson, L.J. Size effects in ductile cellular solids. Part I: modeling. International Journal of Mechanical Sciences 2001;43(3):681-699.

180. Ong, J.L. and Chan, D.C.N. Hydroxyapatite and Their Use as Coatings in Dental Implants: A Review. Crit. Rev. Biomed. Eng. 2000;28(5-6):667A-707A.

181. Osborne, C.S., Barbenel, J.C., Smith, D., Savakis, M. and Grant, M.H. Investigation into the tensile properties of collagen/chondroitin 6-sulphate gels: the effect of crosslinking agents and diamines. Med Biol Eng Comput 1998;36:129-134.

182. Ott, D. Microporosity and lost-wax investment casting. Metall 1994;48(10):770-774.

183. Overgaard, S. Calcium Phosphate Coatings for Fixation of Bone Implants - Evaluated Mechanically and Histologically by Stereological Methods. Acta Orthop. Scand. 2000;71(6 (Suppl. 297)):1-74.

184. Owan, I., Burr, D.B., Turner, C.H., Qiu, J., Tu, Y., Onyia, J.E. and Duncan, R.L. Mechanotransduction in bone: osteoblasts are more responsive to fluid forces than mechanical strain. Am J Physiol 1997;273(3 Pt. 1):C810-C815.

185. Passegue, E., Wagers, A.J., Giuriato, S., Anderson, W.C. and Weissman, I.L. Global analysis of proliferation and cell cycle gene expression in the regulation of hematopoietic stem and progenitor cell fates. J Exp Med 2005;202(11):1599-1611.

186. Pek, Y.S., Spector, M., Yannas, I.V. and Gibson, L.J. Degradation of a collagen-chondroitin-6-sulfate matrix by collagenase and by chondroitinase. Biomaterials 2004;25(3):473-82.

187. Pelham, J., Robert J. and Wang, Y.-L. Cell locomotion and focal adhesions are regulated by substrate flexibility. Proceedings of the National Academy of Sciences, USA 1997;9:13661-13665.

188. Pelham, J., Robert J. and Wang, Y.-L. High resolution detection of mechanical forces exerted by locomoting fibroblasts on the substrate. Mol. Biol. Cell 1999;10:935-945.

189. Peyton, S.R. and Putnam, A.J. Extracellular matrix rigidity governs smooth muscle cell motility in a biphasic fashion. J. Cell Physiol. 2005;204(1):198-209.

190. Pieper, J.S., Oosterhof, A., Dijkstra, P.J., Veerkamp, J.H. and van Kuppevelt, T.H. Preparation and characterization of porous crosslinked collagneous matrices containing bioavailable chondroitin sulfate. Biomaterials 1999;20:847-858.

191. Pittenger, M.F., Mackay, A.M., Berk, S.C., Jaiswal, R.K., Douglas, R., Mosca, J.D., Morman, M.A., Simonetti, D.W., Craig, S. and Marshak, D.R. Multilineage potential of adult human mesenchymal stem cells. Science 1999;284:143-147.

192. Poirier, D.R. and Geiger, G.H. Transport Phenomena in Materials Processing. Warrendale, PA: The Minerals, Metals & Materials Society; 1994.

193. Prendergast, P.J., Huiskes, R. and Soballe, K. Biophysical stimuli on cells during tissue differentiation at implant interfaces. J Biomech 1997;30(6):539-548.

194. Pruss, R.M.H., H.R. Variants of 3T3 cells lacking mitogenic response to epidermal growth factor. Proc Natl Acad Sci USA 1977;74(9):3918-3921.

195. Rabkin-Aikawa, E., Mayer, J.E. and Schoen, E.J. Heart valve regeneration. In: I. V. Yannas, editor. Regenerative Medicine II. Berlin: Springer; 2005. p. 141-179.

196. Ramanujan, S., Pluen, A., McKee, T.D., Brown, E.B., Boucher, Y. and Jain, R.K. Diffusion and convection in collagen gels: implications for transport in the tumor interstitium. Biophys J 2002;83(3):1650-1660.

197. Rhee, S.H., Suetsugu, Y. and Tanaka, J. Biomimetic Configurational Arrays of Hydroxyapatite Nanocrystals on Bio-organics. Biomaterials 2001;22(21):2843-2847.

198. Rodriguez, F.J., Gomez, N., Perego, G. and Navarro, X. Highly permeable polylactide-caprolactone nerve guides enhance peripheral nerve regeneration through long gaps. Biomaterials 1999;20(16):1489-1500.

199. RoyChowdhury, P. and Kumar, V. Fabrication and evaluation of porous 2,3-dialdehydecellulose membrane as a potential biodegradable tissue-engineering scaffold. J Biomed Mater Res 2006;76A(2):300-309.

200. Rudolph, R., Van de Berg, J. and Ehrlich, P. Wound contraction and scar contracture. In: W. J. Lindblad, editor. Wound Healing. Philadelphia: W.B. Saunders; 1992.

201. Rutkowski, G.E., Miller, C.A. and Mallapragada, S.K. Processing of polymer scaffolds: Solvent casting. In: R. P. Lanza, editor. Methods of Tissue Engineering. San Diego: Academic Press; 2002. p. 681-686.

202. Salem, A.K., Stevens, R., Pearson, R.G., Davies, M.C., Tendler, S.J., Roberts, C.J., Williams, P.M. and Shakesheff, K.M. Interactions of 3T3 fibroblasts and endothelial cells with defined pore features. J. Biomed. Mater. Res. 2002;61(2):212-217.

203. Sander, E.A. and Nauman, E.A. Permeability of musculoskeletal tissues and scaffolding materials: experimental results and theoretical predictions. Crit Rev Biomed Eng 2003;31(1-2):1-26.

204. Sasano, Y., Kamakura, S., Nakamura, M., Suzuki, O., Mizoguchi, I., Akita, H. and Kagayama, M. Subperiosteal Implantation of Octacalcium Phosphate (OCP) Stimulates Both Chondrogenesis and Osteogenesis in the Tibia, but Only Osteogenesis in the Parietal Bone of a Rat. Anat. Rec. 1995;242(1):40-46.

205. Schoof, H., Apel, J., Heschel, I. and Rau, G. Control of pore structure and size in freeze-dried collagen sponges. J. Biomed. Mater. Res. 2001;58(4):352-357.

206. Schulz-Torres, D., Freyman, T.M., Yannas, I.V. and Spector, M. Tendon cell contraction of collagen-GAG matrices in vitro: effect of crosslinking. Biomaterials 2000;21:1607-1619.

207. Sethi, K.K., Yannas, I.V., Mudera, V., Eastwood, M., McFarland, C. and Brown, R.A. Evidence for sequential utilization of fibronectin, vitronectin, and collagen during fibroblast-mediated collagen contraction. Wound Repair and Regeneration 2002;10(6):397-408.

208. Shah, M., Foreman, D.M. and Ferguson, M.W. Neutralisation of TGF-B1 and TGF-B2 or exogenous addition of TGF-B3 to cutaneous rat wounds reduces scarring. J. Cell Sci. 1995;108:985-1002.

209. Sherwood, R.I., Christensen, J.L., Weissman, I.L. and Wagers, A.J. Determinants of skeletal muscle contributions from circulating cells, bone marrow cells, and hematopoietic stem cells. Stem Cells 2004;22(7):1292-1304.

210. Silver, F.H., Yannas, I.V. and Salzman, E.W. Glycosaminoglycan Inhibition of Collagen Induced Platelet-Aggregation. Thrombosis Research 1978;13(2):267-277.

211. Silver, F.H., Yannas, I.V. and Salzman, E.W. Invitro Blood Compatibility of Glycosaminoglycan-Precipitated Collagens. Journal of Biomedical Materials Research 1979;13(5):701-716.

212. Simone, A.E. and Gibson, L.J. Effects of solid distribution on the stiffness and strength of metallic foams. Acta Materialia 1998;46(6):2139-2150.

213. Slack, J.M.W. Stem cells in epithelial tissues. Science 2000;287(1431-1433).

214. Snyder, T.A., Watach, M.J., Litwak, K.N. and Wagner, W.R. Platelet activation, aggregation, and life span in calves implanted with axial flow ventricular assist devices. Ann Thorac Surg 2002;73(6):1933-8.

215. Soller, E.C. In Vitro Pharmacological Inhibition of Myofibroblast Differentiation and Force Generation in a Collagen-GAG Matrix [S.M.]. Cambridge: Mechanical Engineering, Massachusetts Institute of Technology; 2005.

216. Soo, C., Beanes, S.R., Hu, F.-Y., Zhang, X., Catherine Dang, C., Chang, G., Wang, Y., Nishimura, I., Freymiller, E., Longaker, M.T., Lorenz, H.P. and Ting, K. Ontogenetic Transition in Fetal Wound Transforming Growth Factor-B Regulation Correlates with Collagen Organization. Am. J. Pathol. 2003;163(6):2459-2476.

217. Spain, T.L., Agrawal, C.M. and Athanasiou, K.A. New technique to extend the useful life of a biodegradable cartilage implant. Tissue Eng. 1998;4(4):343-352.

218. Spector, M., Heyligers, I. and Roberson, J.R. Porous polymers for biological fixation. Clin. Orth. 1993;235:207-219.

219. Spilker, M.H., Asano, K., Yannas, I.V. and Spector, M. Contraction of collagen-glycosaminoglycan matrices by peripheral nerve cells in vitro. Biomaterials 2001;22(10):1085-1093.

220. Stachowiak, A.N., Bershteyn, A., Tzatzalos, E. and Irvine, D.J. Bioactive hydrogels with an ordewred cellular structure combine interconnected macroporosity and robust mechanical properties. Adv Mater 2005;17(4):399-403.

221. Stemerman, M.B., Spaet, T.H., Pitlick, F., Cintron, J., Lejnieks, I. and Tiell, M.L. Intimal healing. The patterns of reendothelialization and intimal thickening. Am. J. Pathol. 1977;87:125-142.

222. Stenn, K.S. and Malhotra, R. Epithelialization. In: R. F. D. I.K. Cohen, and W.J. Lindblad, editor. Wound Healing. Philadelphia: W. B. Saunders; 1992.

223. Surdez, D., Kunz, B., Wagers, A.J., Weissman, I.L. and Terskikh, A.V. Simple and efficient isolation of hematopoietic stem cells from H2K-zFP transgenic mice. Stem Cells 2005;23(10):1617-1625.

224. Suzuki, O., Nakamura, M., Miyasaka, Y., Kagayama, M. and Sakurai, M. Bone-Formation on Synthetic Precursors of Hydroxyapatite. Tohoku Journal of Experimental Medicine 1991;164(1):37-50.

225. Swann, A.C. and Seedhom, B.B. The Stiffness of Normal Articular Cartilage and the Predominant Acting Stress Levels: Implications for the Aetiology of Osteoarthrosis. British Journal of Rheumatology 1993;32:16-25.

226. Tan, J.L., Tien, J., Pirone, D.M., Gray, D.S., Bhadriraju, K. and Chen, C.S. Cells lying on a bed of microneedles: An approach to isolate mechanical force. Proc. Natl. Acad. Sci. USA 2003;100(4):1484-1489.

227. Ten Huisen, K.S., Martin, R.I., Klimkiewicz, M. and Brown, P.W. Formation and Properties of a Synthetic Bone Composite: Hydroxyapatite-Collagen. J. Biomed. Mater. Res. 1995;29(7):803-810.

228. Thompson, W. On the division of space with minimum partition energy. Phil. Mag. 1887;24:503.

229. Timp, W., Hopp, S., Evans, J.G. and Matsudaira, P. Statistical analysis of phototoxic effects of fluorescent markers on cell motility. In: ASCB; 2005; San Francisco, CA; 2005.

230. Triantafillou, T.C., Zhang, J., Shercliff, T.L., Gibson, L.J. and Ashby, M.F. Failure Surfaces for Cellular Materials under Multiaxial Loads .2. Comparison of Models with Experiment. International Journal of Mechanical Sciences 1989;31(9):665-678.

231. Troxel, K. Delay of skin wound contraction by porous collagen-GAG matrices. Cambridge: Mechanical Engineering, Massachusetts Institute of Technology; 1994.

232. Tsuruga, E., Takita, H., Itoh, H., Wakisaka, Y. and Kuboki, Y. Pore size of porous hydroxyapatite as the cell-substratum controls BMP-induced osteogenesis. J. Biochem. 1996;2:317-324.

233. Udani, V.M., Santarelli, J.G., Yung, Y.C., Wagers, A.J., Cheshier, S.H., Weissman, I.L. and Tse, V. Hematopoietic stem cells give rise to perivascular endothelial-like cells during brain tumor angiogenesis. Stem Cells Dev 2005;14(5):478-486.

234. Uitto, J., Mauviel, A. and McGrath, J. The dermal-epidermal basement membrane zone in cutaneous wound healing. In: R. A. F. Clark, editor. The Molecular and Cellular Biology of Wound Repair. New York: Plenum Press; 1996.

235. Urban, R.M., Jacobs, J.J., Tomlinson, M.J., Gavrilovic, J., Black, J. and Peoc'h, M. Dissemination of wear particles to the liver, spleen, and abdominal lymph nodes of patients with hip and knee replacement. J. Bone Joint Surg. Am. 2000;82(4):457-476.

236. van Tienen, T.G., Heijkants, R.G.J.C., Buma, P., de Groot, J.H., Pennings, A.J. and Veth, R.P.H. Tissue ingrowth and degradation of two biodegradable porous polymers with different porosities and pore sizes. Biomaterials 2002;23(8):1731-1738.

237. Vanwanseele, B., Lucchinetti, E. and Stussi, E. The Effects of Immobilization on the Characteristics of Articular Cartilage: Current Concepts and Future Directions. Osteoarthritis and Cartilage 2002;10:408-419.

238. Veenman, C.J., Reinders, M.J.T. and Backer, E. Resolving Motion Correspondence for Densely Moving Points. IEEE Transactions on Pattern Analysis and Machine Intelligence 2001;23(1):54-72.

239. Vickers, S.M., Johnson, L.L., Zou, L.Q., Yannas, I.V., Gibson, L.J. and Spector, M. Expression of alpha-smooth muscle actin by and contraction of cells derived from synovium. Tissue Eng 2004;10(7-8):1214-1223.

240. Vickers, S.M. and Spector, M. The effects of cross-linking type II collagen-GAG scaffolds on chondrogenesis in vitro. In: Tissue Engineering Society International Conference; 2005; Shanghai, China; 2005.

241. Vickers, S.M., Squitieri, L.S. and Spector, M. The effects of cross-linking type II collagen-GAG scaffolds on chondrogenesis in vitro: Dynamic pore reduction promotes cartilage formation. Tissue Eng. 2006;12(5).

242. Vracko, R. Significance of basal lamina for regeneration of injured lung. Virchows Arch. (Pathol. Anat.) 1972;355:264-274.

243. Wagers, A.J., Christensen, J.L. and Weissman, I.L. Cell fate determination from stem cells. Gen Ther 2002;9(10):606-612.

244. Wagers, A.J. and Weissman, I.L. Plasticity of adult stem cells. Cell 2004;116(5):639-648.

245. Wake, M.C., Patrick, C.W., Jr. and Mikos, A.G. Pore morphology effects on the fibrovascular tissue growth in porous polymer substrates. Cell Transplant. 1994;3(4):339-343.

246. Waller, M.A., McMahon, L.A., O'Brien, F.J., Harley, B.A., Yannas, I.V. and Prendergast, P.J. Effect of pore size on permeability and biophysical stimuli in a collagen-GAG scaffold with uniform porosity. In: Tissue Engineering Society International; 2004; Lausanne, Switzerland; 2004.

247. Wang, H.-B., Dembo, M., Hanks, S.K. and Wang, Y.-L. Focal adhesion kinase is involved in mechanosensing during fibroblast migration. Proc. Natl. Acad. Sci. USA 2001;98(20):11295-11300.

248. Wang, H.-B., Dembo, M. and Wang, Y.-L. Substrate flexibility regulates growth and apoptosis of normal but not transformed cells. Am. J. Physiol. Cell Physiol. 2000;279:C1345-C1350.

249. Wang, M., Joseph, R. and Bonfield, W. Hydroxyapatite-Polyethylene Composites for Bone Substitution: Effects of Ceramic Particle Size and Morphology. Biomaterials 1998;19(24):2357-2366.

250. Wang, N., Butler, J.P. and Ingber, D. Mechanotransduction across the cell surface and through the cytoskeleton. Science 1993;260:1124-1127.

251. Wang, S., Wan, A.C., Xu, X., Gao, S., Mao, H.Q., Leong, K.W. and Yu, H. A new nerve guide conduit material composed of a biodegradable poly(phosphoester). Biomaterials 2001;22(10):157-169.

252. Wang, Y., Yates, F., Naveiras, O., Ernst, P. and Daley, G.Q. Embryonic stem cell-derived hematopoietic stem cells. Proc Natl Acad Sci USA 2005;102(52):19081-19086.

253. Ware, M.F., Wells, A. and Lauffenburger, D.A. Epidermal growth factor alters fibroblast migration speed and directional persistence reciprocally and in a matrix-dependent manner. J Cell Sci 1998;111(16):2423-2432.

254. Westinghouse_Savannah_River_Company. Wind Climate Analyses for National Weather Service Stations in the Southeast USA. Aiken, SC: U.S. Department of Energy, DE-AC09-96SR18500; 2002. Report No.: DE-AC09-96SR18500.

255. Wickelgren, I. Muscling transplants in mice,. Science 1996;273:33.

256. Willert, H.G. Reactions of the articular capsule to wear products of artificial joint prostheses. J. Biomed. Mater. Res. 1977;11(2):157-164.

257. Williams, R.E. Space-filling polyhedron: its relation to aggregates of soap bubbles, plant cells and metal crystallites. Science 1968;161:276-277.

258. Woodley, D.T., Peterson, H.D., Herzog, S.R., Stricklin, G.P., Burgeson, R.E., Briggaman, R.A., Cronce, D.J. and O'Keefe, E.J. Burn wounds resurfaced by cultured epidermal autografts show abnormal reconstitution of anchoring fibrils. JAMA 1988;259:2566-2571.

259. Yannas, I.V. Collagen and gelatin in the solid state. Rev. Macromol. Chem. 1972:49B-104B.

260. Yannas, I.V. Biologically-Active Analogs of the Extracellular-Matrix - Artificial Skin and Nerves. Angewandte Chemie-International Edition in English 1990;29(1):20-35.

261. Yannas, I.V. Models of organ regeneration processes induced by templates. In: A. D. Cherrington, editor. Bioartificial Organs: Ann. N.Y. Acad. Sci.; 1997. p. 280-293.

262. Yannas, I.V. Tissue and Organ Regeneration in Adults. New York: Springer-Verlag; 2001.

263. Yannas, I.V. and Burke, J.F. Design of an Artificial Skin I: Basic Design Principles. J Biomed Mater Res 1980;14(1):65-81.

264. Yannas, I.V., Burke, J.F., Gordon, P.L., Huang, C. and Rubenstein, R.H. Design of an Artificial Skin II: Control of Chemical-Composition. J Biomed Mater Res 1980;14(2):107-132.

265. Yannas, I.V., Burke, J.F., Huang, C. and Gordon, P.L. Correlation of in vivo collagen degradation rate with in vitro measurements. J Biomed Mater Res 1975;9(6):623-628.

266. Yannas, I.V., Burke, J.F., Huang, C. and Gordon, P.L. Suppression of in vivo degradability and of immunogenicity of collagen by reaction with glycosaminoglycans. Polym. Prepr. Am. Chem. Soc. 1975;16(2):209-214.

267. Yannas, I.V., Burke, J.F., Huang, C. and Gordon, P.L. Suppression of Invivo Degradability and of Immunogenicity of Collagen by Reaction with Glycosaminoglycans. Abstracts of Papers of the American Chemical Society 1975;170(AUG24):56-56.

268. Yannas, I.V., Burke, J.F., Umbreit, M. and Stasikelis, P. Progress in Design of an Artificial Skin. Federation Proceedings 1979;38(3):988-988.

269. Yannas, I.V. and Huang, C. Fracture of tendon collagen. J. Polym. Sci. 1972;10:577-584.

270. Yannas, I.V., Lee, E., Orgill, D.P., Skrabut, E.M. and Murphy, G.F. Synthesis and characterization of a model extracellular matrix that induces partial regeneration of adult mammalian skin. Proc. Natl. Acad. Sci. USA 1989;86(3):933-937.

271. Yannas, I.V. and Silver, F. Thromboresistant Analogs of Vascular Tissue. Abstracts of Papers of the American Chemical Society 1975;170(AUG24):122-122.

272. Yannas, I.V. and Tobolsky, A.V. Cross linking of gelatine by dehydration. Nature 1967;215(100):509-510.

273. Yeung, T., Georges, P.C., Flanagan, L.A., Marg, B., Ortiz, M., Funaki, M., Zahir, N., Ming, W., Weaver, V. and Janmey, P.A. Effects of substrate stiffness on cell morphology, cytoskeletal structure, and adhesion. Cell Motil. Cytoskeleton 2005;60:24-34.

274. Yin, Y., Lu, Y., Gates, B. and Xia, Y. Template-assisted self-assembly: a practical route to complex aggregates of monodispersed colloids with well-defined sizes, shapes, and structures. J Am Chem Soc 2001;123(36):8718-8729.

275. Zaman, M.H., Kamm, R.D., Matsudaira, P. and Lauffenburger, D.A. Computational model for cell migration in three-dimensional matrices. Biophys. J. 2005;89:1389-1397.

276. Zaman, M.H., Matsudaira, P. and Lauffenburger, D.A. Understanding effects of MMPs and matrix organization on persistence and translational speed in 3D cell migration. In preparation, 2006.

277. Zaman, M.H., Trapani, L.M., Siemeski, A., Kamm, R.D., Wells, A., Lauffenburger, D.A. and Matsudaira, P. Migration of tumor cells in three-dimensional matrices is governed by matrix stiffness along with cell-matrix adhesion. In preparation, 2006.

278. Zeltinger, J., Sherwood, J.K., Graham, D.A., Mueller, R. and Griffith, L.G. Effect of pore size and void fraction on cellular adhesion, proliferation, and matrix deposition. Tissue Eng 2001;7(5):557-72.

279. Zhang, R. and Ma, P.X. Processing of polymer scaffolds: Phase separation. In: R. P. Lanza, editor. Methods of Tissue Engineering. San Diego: Academic Press; 2002. p. 97-111.

280. Zhang, Y.-Z., Olson, N., Mao, F., Roth, B. and Haugland, R.P. FASEB J 1992;6:A1835.

281. Zmora, S., Glicklis, R. and Cohen, S. Tailoring the pore architecture in 3-D alginate scaffolds by controlling the freezing regime during fabrication. Biomaterials 2002;23(20):4087-4094.

282. Znati, C.A., Rosenstein, M., McKee, T.D., Brown, E., Turner, D., Bloomer, W.D., Watkins, S., Jain, R.K. and Boucher, Y. Irradiation reduces interstitial fluid transport and increases the collagen content in tumors. Clin Cancer Res 2003;9(15):5508-5513.